Faculty of Science and Engineering
Department of Applied Geology

Impactors and the Impacted: Analytical Techniques to Identify and Understand the Impact Evolution of Extraterrestrial Materials

Lucy Victoria Forman

This thesis is presented for the degree of
Doctor of Philosophy
of
Curtin University

March 2017

DECLARATION

To the best of my knowledge and belief this thesis contains no material previously published by any other person except where due acknowledgment has been made. This thesis contains no material which has been accepted for the award of any other degree or diploma in any university.

The author acknowledges that copyright of published works contained within this thesis resides with the copyright holder(s) of those works. I warrant that I have obtained, where necessary, permission from the copyright owners to use any third-party copyright material reproduced in the thesis (e.g. questionnaires, artwork, unpublished letters), or to use any of my own published work (e.g. journal articles) in which the copyright is held by another party (e.g. publisher, co-author).

Signed: 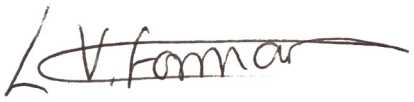 Date: 17.3.17

ABSTRACT

Impacts are a vital and frequently-occurring evolutionary process throughout our Solar System. From the micro-scale collisions between particles of dust at the dawn of the Solar System, to the repeated heavy impacts on the lunar surface 3.5 Ga ago, to the collisions within the asteroid belt creating meteorites, all planetary bodies experience this process. Understanding how the conditions and effects of such impact events result in the geological features observed in extraterrestrial samples, is key to piecing together the evolutionary history of impacts within our Solar System.

Gentle accretionary processes at the beginning of the Solar System resulted in the formation of highly porous planetary bodies, specifically asteroids. Such high porosities are no longer present in the relicts recovered from asteroids as meteorites, therefore some type of compactional mechanism is responsible for creating the low-porosity, lithified meteorites in global collections. Furthermore, not all meteorites exhibit strong shock characteristics, therefore the driving mechanism for compaction must be of low-intensity.

Impact-induced compaction is the most viable and likely porosity-reducing mechanism, based upon the frequency of impacts within the Solar System on both spatial and temporal scales, and the heat and pressure generated in such events, but it is yet to be substantially assessed using evidence from physical samples- meteorites. Low-intensity impacts between highly-porous bodies would result in large and heterogeneous temperature excursions as pores collapse, due to interaction with the propagating shockwave through the porous medium, based on numerical simulation predictions. Large and non-porous chondrules are predicted to remain relatively cool during the compaction process, whilst matrix grains, surrounded

by abundant pores, experience large temperature excursions due to collapse of abundant pore spaces. Vast temperature excursions and stress heterogeneities are predicted across the medium as the propagating shockwave interacts with the various chondritic components, however little evidence of this impact-induced compaction process has been identified within meteorite samples, which is one of the topics addressed by the research presented in this thesis.

Testing of these simulation predictions on samples that have undergone limited thermal and aqueous alteration prior to asteroid compaction is paramount; secondary processes can generate complex micro-textures and deformation features, which may be indiscernible from those textures generated by the compaction process that we wish to investigate. A carbonaceous chondrite of the Vigarano subclass (CV), the Allende meteorite, is examined in Chapters 2 & 3 for this reason. Electron backscatter diffraction (EBSD) imaging of chondrules and matrix regions in this sample revealed several compaction-related characteristics; three different chondrules all displayed a small amount of crystal-plastic deformation (<7-8°) that was concentrated at the chondrule edges, but no deformation was observed in their interiors. Matrix grains from four different regions exhibited deformation textures throughout entire grains, and of a higher degree (up to 20°) than observed within the chondrules. We attribute this to the heterogeneous distribution of heat during the compaction event; matrix grains are predicted to heat up disproportionately to chondrule grains owing to the greater number of heat-producing collapsing pores in matrix regions. Furthermore, low-angle boundaries within the matrix grains aligned across the sample, further confirming these textures resulted from a compressional event.

Further microtextural investigations of this sample are discussed in Chapter 3. A large area EBSD map (8 mm^2 at a step size of 0.5 μm) of the Allende sample allowed for meso- and micro-scale observations to be made simultaneously. This map is one of the largest EBSD datasets to have ever been collected of an extraterrestrial material, and represents a significant advance in the field of meteoritics and the application of EBSD techniques to such materials. Crystallographic preferred orientation (CPO) analyses of ~80 250μm x 250 μm regions of matrix revealed heterogeneous CPOs in <a> of the olivine grains, with varied orientations and intensities throughout the sample. The relationship between distance from chondrules, or other mechanically strong components, such as amoeboid olivine aggregates (AOAs), and CPO generation is quite clear; matrix regions proximal to chondrule edges have the strongest CPOs, and these are consistently orientated such that the matrix grains lie parallel to the chondrule edges. In regions furthest from chondrules, CPOs were not observed, or were much weaker, and generally formed a CPO with <a> aligned such that the longest

physical axis of the grains lie parallel to the polished surface of the sample (Chapter 3, Fig. 3.2). At the meso-scale where grains across the sample are considered collectively and local heterogeneities are averaged, a weak CPO in <a> of the olivine matrix grains aligns with the y-axis of the sample thin section, meaning grains are elongate parallel to the x-axis. This allowed for the directionality of compaction to be determined as parallel to the y-direction of the sample. The heterogeneities of the CPO at the micro-scale represent grain realignment during the impact event to reduce the space occupied parallel to the propagating shockwave. Matrix olivine grains have flattened against strong and larger components of the sample, as has been observed in Allende, whereas the matrix olivine grains further from chondrules have physically re-oriented according to the direction of the shockwave. The configuration of the CPOs within Allende can only have formed due to impact-induced compaction. The work in Chapters 2 & 3 therefore provide strong observational evidence to support this mechanism of compaction and porosity reduction of asteroids, and should be verified by examining other petrologic type 3 meteorites.

The extensive studies of Allende discussed here and in previous work can only provide part of the history of the asteroid of origin, or parent body, of the CV meteorites. These microtextures can also vary as a function of surmised depth on the parent body. The parent body of the CV class is presumed to have experienced limited but variable aqueous and thermal alteration, based upon observations from CV class meteorites from previous studies, which utilised a variety of geochemical characteristics and thermometry techniques. This variability is surmised to result from differing locations of origin on the parent body, both as a function of depth (and therefore temperature) and laterally around the asteroid (and potentially the type of alteration). Typically, the geochemistry of olivine grains is described for the purposes of meteorite classification, as it is a fundamental step in determining the class the sample should belong to. However grain morphology, which is predicted to have a moderate link to aqueous alteration and potentially thermal alteration, has not been as extensively investigated. Chapter 4 therefore encompasses a morphologic and crystallographic comparative study of the matrices of three CV chondrites of the CV_{oxA}, CV_{oxB} and CV_{red} subclasses. The work discussed here determined that increased grain size and aspect ratio are positively correlated to the degree of aqueous alteration the sample has undergone. These characteristics apply most highly to the matrix grains of the Allende meteorite, which have experienced the highest temperatures of all CV chondrites in global CV collections. The sample with the most equant grains, Kaba, is documented to have experienced the lowest temperatures but moderate aqueous alteration, in prior studies. However, the reduced CV chondrite, Vigarano, contains elongate but the smallest grains of the three samples, and yet has also experienced low temperatures, comparable to

those experienced by Kaba. A definite interplay between grain morphology and alteration is therefore present and explored in Chapter 4.

These observations are considered in terms of CPO generation as a function of depth during the early asteroid compaction process. Allende contains the clearest and strongest crystallographic preferred orientation (CPO), whilst Kaba's matrix grains form a moderate CPO. Conversely, Vigarano does not appear to have a substantial CPO within the matrix. Based on predicted alteration temperatures, Allende originated from the deepest location of the three samples examined. Within this context, the microtextures observed therefore appear to increase with depth on the parent body, however the morphology of these grains likely plays an important role in textural formation; elongate grains preserve stronger CPOs because the process of grain reorientation would be most pronounced in matrix grains with significantly differing crystallographic dimensions. Kaba has the most equant grains, which is likely why the CPO produced is only moderate when compared with Allende. However, despite the elongate grains of Vigarano, it is classed as a breccia, and therefore the compactional textures may have been overprinted with reworking or residual thermal metamorphism following impact-induced compaction. We conclude that aqueous alteration is likely the primary control for grain growth in terms of size and how euhedral the grains are, but that thermal alteration may dictate how elongate the grains grow to become. Allende originates from the greatest depth on the parent body if products of aqueous alteration and thermal history are suitable indicators, and whilst Kaba and Vigarano likely originated from a shallower but similar depth, we deduce that they came from a different lateral location on the parent body to account for the variance in alteration characteristics. This interplay between impact-induced compaction effects and grain morphology is one that should be explored with other CV chondrites in future work.

Collisions into fully-evolved planetary bodies, such as Earth, are typically understood through examination of the ejecta produced by the impact event, or the impact crater produced by the projectile, amongst other indirect consequences of the event. One of the most significant and well-known impact events on Earth occurred at the close of the Cretaceous period and the beginning of the Paleogene ~65 Ma ago, and is hence referred to as the K-Pg impact. The K-Pg impact ejecta and debris were deposited globally following the catastrophic collision at Chicxulub, Mexico, which is surmised to have led to the demise of the dinosaur population. Material from this impact was transported ballistically, via the ejecta cloud, and also dispersed by atmospheric processes following re-entry of ejecta material into the Earth's atmopshere. This boundary layer is highly enriched in platinum group elements (PGEs), specifically Ir, relative to terrestrial values, signifying this material originated from the projectile. Identification and evaluation of the host phase(s) for these elements can inform our understanding of these

cataclysmic impacts, however scientific efforts up until now have failed to identify the carrier phase(s), and consequently the processing of the PGE elements subsequent to the K-Pg impact event remains poorly understood.

In this work, a variety of techniques were employed at a range of scales to identify the form of the Ir within the ejecta layer at sites <4000 km from the impact site (Chapter 5). Given the distance the material was transported from the impact site, ejecta cloud processes would have been involved in debris transport, therefore ejecta cloud conditions can be constrained based on inferences drawn from this material. The Woodside Creek sample, from New Zealand, which was at a paleodistance of ~14,000 km at the time of impact, has a bulk Ir concentration of ~30 ppb. Our analyses indicate that the Ir is enriched within the FeO (~4 ppm) and amphibole phases (~6 ppm) based on laser-ablation inductively-coupled-plasma mass-spectrometry (LA-ICP-MS) mapping.

In Archean impact layers, Ir typically forms PGE alloy nuggets with other highly siderophile elements. However, feature mapping of the entire sample areas and TEM analyses of the FeO phase within the Woodside Creek sample, did not identify PGE nano-nuggets smaller than ~45 nm or greater than ~100 nm. The bulk concentration of Ir within the K-Pg samples is low in comparison to similar impact layers of Archaean age, where abundant PGE micro-nuggets have been observed. Therefore, if present, only a small number of nuggets would exist within the K-Pg layer, and sampling effects may have resulted in examination of a TEM lamella devoid of such nuggets. The K-Pg impact ejecta cloud that resulted in the Woodside Creek layer is interpreted to have been highly oxidising due to the vapourisation of the volatile-rich target material during the impact by prior modelling studies. Consequently, the Ir may have been oxidised during ejecta transport and would be disseminated throughout the FeO phase. Future TEM analyses of all phases associated with Ir may therefore constrain the form of Ir within the carrier phase(s), to further understand the impact cloud processing mechanisms after this impact event.

The work described and explored in this thesis examines a projectile on Earth and primitive impacted materials from asteroids, and demonstrate the wealth of comprehension to be gained from detailed microstructural examination of these materials. The works contained within this thesis have provided new insights into mechanisms of the earliest grain modification processes, asteroid compaction, and collisions into fully-evolved planetary bodies and the kind of processing of the ejecta that follows a collision event. This, therefore, contributes significantly to scientific knowledge over a range of fields in meteoritic and planetary sciences, extending beyond those discussed in each chapter, and highlights the gaps in our scientific understanding that future research should aim to resolve.

For Linda, Stephen and Anna: for making me the person I am today, I dedicate this thesis to each of you.

I want to make sure we use all our talent, not just 25 percent. Don't let anyone rob you of your imagination, your creativity, or your curiosity. It's your place in the world; it's your life. Go on and do all you can with it, and make it the life you want to live.

-Mae C. Jemison

Courage is like — it's a habitus, a habit, a virtue: you get it by courageous acts. It's like you learn to swim by swimming. You learn courage by couraging.

-Marie M. Daly

I am among those who think that science has great beauty. A scientist in his laboratory is not only a technician: he is also a child placed before natural phenomena which impress him like a fairy tale. We should not allow it to be believed that all scientific progress can be reduced to mechanisms, machines, gearings, even though such machinery has its own beauty.

-Marie Curie

Happiness can be found, even in the darkest of times, if one only remembers to turn on the light.

-J. K. Rowling

I solemnely swear I am up to no good.

-J. K. Rowling

ACKNOWLEDGEMENTS

Curtin University- For allowing me to complete my PhD here, providing me with HDR funding, and a fun and supportive environment to work in.

Australian Research Council- This work was funded by the ARC via their Arc Laureate fellowship programme, awarded to my primary supervisor, Prof. Phil Bland.

Department of Applied Geology- The staff and students that I have encountered in my time as a PhD student have been supportive, kind and accepting and encouraging of my bright and colourful clothing choices. Thanks for the coffee and laughs when I needed it.

Curtin University Counselling Services- Without this service I would not have completed my studies. I learnt a huge deal about myself, my motivations, how my mind works and how to improve it to enjoy life to the fullest and happiest extent I can.

Prof. Phil Bland- Eternal thanks for having faith in me to do super cute and fun science things with you. I could never have guessed when I first met you in 2008 that I would be joining your team in Perth to start a new and very exciting adventure four and a half years later. Thank you so much for your endless encouragement, support and positivity. I have learnt a huge amount from you and look forward to continuing to work on projects with you.

Dr. Nick Timms- For teaching me all you have about microstructure, deformation, EBSD fun and general structural geology, I can't express how grateful I am. It has formed an integral part of my PhD, and I couldn't have gotten anywhere without your assistance and persistence in furthering my understanding. Thanks also for your fab comments on all of my manuscripts, and sorry for bugging you so often!

Dr. Gretchen Benedix-Bland- You are incredibly inspiring to me as a scientist and a person. You have achieved so much in various fields and I hope that one day I can say something similar. Thanks for the support, insight, scientific understanding, chats, tea, and providing me with a place to rest my head when needed. I'm super excited that you'd like to keep me around for the near-future to do exciting research, so thank you!

Alex & Libby Bland- For cuddles, constant fun, always trying your best in our lessons and rekindling my love for Harry Potter. Thank you for welcoming me into your lives and giving me a place where spontaneous singing is always acceptable :).

My parents, Linda & Steve- I love you both so much. Thank you for adapting, being unbelievably supportive, putting up with me being so far away, going above and beyond for me, and not only that, for encouraging me to go and be the best version of myself possible. I model myself in what I see in you both. You are truly inspiring to me. I hope I've made you proud in what I have done so far, and I will continue to try and make you proud to have me as your daughter :).

My sister, Anna- My first friend in life. The person who taught me to talk louder than you, longer than you, and who taught me to share (or forced me?!). I adore you and everything about you. I am far from you, and sometimes I'm not able to be there for you, but I will always look to you when I am lost. Thanks for your patience and listening to my internal monologue on more than one occasion :P.

My favourite coffee drinker and dear friend, Meg- Who knew that living together for a month could have created our friendship?! You get me and my quirkiness and for that I am so grateful. Thank you for the giggles, wisdom, 6- hour chats, cake, letting me look after Sassypants, and all the support you provide me with. I'll get round to reading your novel now!

My dear friend and proto-doctor, Luke- What a journey we have had. I am so proud to call you my best friend, colleague and soon-to-be international collaborator. Thank you for your unending support and faith in what I do and how I do it. Thank you for providing me with a safe space to say stupid science fails and for kindly correcting me when it was due. Thanks for helping me understand things (nuggets, I'm looking at you!), joining me for coffee on the hammocks and being someone I can confide in and look to for energy and positivity. You will never truly know how much you have provided me with. May our research collaborations continue forever :D.

My fiancé, Keith- My love, my light, my joy. Thank you for choosing me. Thank you for being patient during all the times I stayed late at the office (especially towards the end), for cleaning for me, feeding me, picking me up when I was tired and protecting me from life's harder days. Thank you for understanding when I needed me-time, and thank you for giving me space to create and be the louder version of myself. For all the questions, ideas, and comments about the Solar System and asteroids- I love you all the more. Thanks for being such an important part of my life journey. I look forward to supporting you in the same way (and laughing when you grumble) when you work towards your doctorate <3.

TABLE OF CONTENTS

LIST OF FIRST AUTHOR PUBLICATIONS INCLUDED AS PART OF THE THESIS (APPENDIX A)

A1: Hidden Secrets of Deformation: Impact-induced Compaction Within a CV Chondrite

L. V. Forman, P. A. Bland, N. E. Timms, G. S. Collins, T. M. Davison, F. J. Ciesla, G. K. Benedix, L. Daly, P. W. Trimby, L. Yang, S. P. Ringer.

2016, Earth and Planetary Science Letters, v. 452, p.133-145.

A2: Defining the mechanism for compaction of the CV chondrite parent body

L. V. Forman, P. A. Bland, N. E. Timms, L. Daly, G. K. Benedix, P. W. Trimby, G. S. Collins, and T. M. Davison.

2017, Geology, v. 45, no. 6, p. 559-562.

LIST OF FIRST AUTHOR PUBLICATIONS RELEVANT TO THE THESIS (APPENDIX B)

B1: Defining the Crystallographic Fingerprint of Extraterrestrial Treasures

L. V. Forman, P. A. Bland, N. E. Timms, L. Daly, G. K. Benedix & P. W. Trimby.

2016, 79th Annual Meeting of the Meteoritical Society, Abstract 6264.

B2: Recovering the Primordial History of Chondrites in Unprecedented Detail using Massive EBSD Datasets

L. V. Forman, P. A. Bland, N. E. Timms, L. Daly, G. S. Collins, T. M. Davison, P. W. Trimby & S. P. Ringer.

2015, 78th Annual Meeting of the Meteoritical Society, Abstract 5086.

B3: Impact-Induced Compaction in CV Chondrites: Exploring a Hidden Record with EBSD

L. V. Forman, P. A. Bland, N. E. Timms, & G. K. Benedix.

2014, 77th Annual Meeting of the Meteoritical Society, Abstract 5303.

B4: Constraining the Compositional Variety of Impactors at 1AU Over the Last ~3.5 Ga: In Situ Identification and Analysis of >200 Meteoritic Grains in a Lunar Soil.

L. V. Forman, P. A. Bland, K. A. Dyl, L. Daly, C. G. Ryan & J. Paxman.

2014, 45th Lunar and Planetary Science Conference, Abstract 2680.

B5: Impact-Induced Compaction in CV Chondrites: Exploring a Hidden Record with EBSD

L. V. Forman, P. A. Bland, N. E. Timms & G. K. Benedix.

2015, 14th Australian Space Research Conference.

LIST OF CO-AUTHORED PUBLICATIONS RELEVANT TO THE THESIS (APPENDIX C)

C1: In Situ Analysis of Refractory Metal Nuggets in Carbonaceous Chondrites

L. Daly, P. A. Bland, K. A. Dyl, L. V. Forman, K. A. Evans, P. W. Trimby, S. Moody, L. Yang, H. Liu, S. P. Ringer and C. G. Ryan.

2016, Geochimica et Cosmochimica Acta, in press.

C2: Composition of Refractory Metal Nuggets: Implications for Their Origins

L. Daly, P. A. Bland, K. A. Dyl, L. V. Forman, P. W. Trimby, S. Moody, L. Yang, H. Liu, A. La Fontaine, and J. M. Cairney.

2016, 47th Lunar & Planetary Science Conference, Abstract 1880.

C3: Atom Probe Tomography and Its Application to Refractory Metal Nuggets

L. Daly, P. A. Bland, L. V. Forman, S. M. Reddy, W. D. Rickard, D. W. Saxey, A. La Fontaine, L. Yang, P. W. Trimby, J. M. Cairney and S. P. Ringer.

2016, 79th Annual Meeting of the Meteoritical Society, Abstract 6241.

C4: Mineralogy and Petrology of the Murrili Meteorite

G. K. Benedix, L. V. Forman, L. Daly, R. C. Greenwood, I. A. Franchi, J. M. Friedrich, M. M. Meier, C. Maden, H. Busemann, J. C. Welten and M. W. Caffee.

2016, 79th Annual Meeting of the Meteoritical Society, Abstract 6237.

C5: In Situ Analysis of Refractory Metal Nugget Crystallography Providing Clues to Early Solar System Events

L. Daly, P. A. Bland, L. V. Forman, P. W. Trimby, S. Moody, L. Yang, H. Liu, S. P. Ringer, and M. Saunders.

2015, 78th Annual Meeting of the Meteoritical Society, Abstract 5061.

C6: Catching a Falling Star (or Meteorite)- Fireball Camera Networks in the 21st Century

P. A. Bland, G. K. Benedix and the Desert Fireball Network Team.

June 2015, Elements Magazine.

C7: A New Unequilibrated Chondrite Lithology Discovered in the Murchison CM2 Meteorite.

G. K. Benedix, S. S. Russell, L. V. Forman, A. W. R. Bevan and P. A. Bland.

2015, 46th Lunar and Planetary Science Conference, Abstract 1143.

C8: Crystallography of Refractory Metal Nuggets Identified Within Ca-Al-Rich Inclusions, Chondrules and Matrix of Carbonaceous Chondrites.

L. Daly, P. A. Bland, K. A. Dyl, L. V. Forman, P. W. Trimby, S. Moody, and S. P. Ringer.

2014, 77th Annual Meeting of the Meteoritical Society, Abstract 5207.

C9: In Situ Analysis of Refractory Metal Alloys in Carbonaceous Chondrites: Implications for Early Solar System Processes

L. Daly, P. A. Bland, K. A. Dyl, L. V. Forman,and C. G. Ryan.

2014, 45th Lunar & Planetary Science Conference, Abstract 2071.

LIST OF FIGURES

Supplementary Figures

LIST OF TABLES

LIST OF ABBREVIATIONS USED IN THIS THESIS

2D	Two- dimensional
3D	Three- dimensional
AOA	Amoeboid Olivine Aggregate
APM	Atom Probe Microscopy
BSE	Backscattered Electron
CAI	Ca-Al-Rich Inclusion
CC	Carbonaceous Chondrite
CI	Carbonaceous Chondrite Type Ivuna
CM	Carbonaceous Chondrite Type Mighei
CPO	Crystallographic Preferred Orientation
cps	Counts per Second
CV	Carbonaceous Chondrite Type Vigarano
CV_{oxA}	- Oxidised Type A
CV_{oxB}	- Oxidised Type B
CV_{red}	- Reduced
CV3	- Petrologic Type 3
DR	Data Repository
EBSD	Electron Backscatter Diffraction
EDS	Energy Dispersive X-ray Spectroscopy
Fa	Fayalite
FIB	Focussed Ion Beam
Fo	Forsterite
GIS	Gas Injection System
HIP	Hot Isostatic Pressing
HSE	Highly Siderophile Element
IIC	Impact-induced Compaction

K-Pg	Creatceous- Paleogene
LAB	Low Angle Boundary
LA-ICP-MS	Laser Ablation Inductively Coupled Plasma Mass Spectrometry
m.u.d.	Mean Uniform Density
RMN	Refractory Metal Nugget
SE	Secondary Electron
SEM	Scanning Electron Microscope
SPO	Shape Preferred Orientation
TEM	Transmission Electron Microscopy
TIMA	Tescan Integrated Mineral Analyser
TKD	Transmission Kikuchi Diffraction
XRF	X-ray Fluorescence Microscopy

Chapter 1

Thesis Introduction

L. V. Forman

Department of Applied Geology, Curtin University, GPO Box U1987, Perth, WA 6845, Australia

INTRODUCTION

Impacts are a fundamental driver across all time periods for the evolution of our solar system and beyond. From the very beginning of a planetary system, impacts between loosely bound particles are the cause for planetary growth, accretion and evolution (O'Keefe and Ahrens, 1977; Matsui, 1986; Matsui and Abe, 1986; Scott et al., 1989; Chyba, 1990; Cintala, 1992; Metzler et al., 1995; Keil et al., 1997; Scott, 2002; Chambers, 2004; Strom et al., 2005; Asphaug et al., 2006; Cuzzi and Weidenschilling, 2006; Weidenschilling and Cuzzi, 2006; Weidenschilling, 2011; Chambers, 2013), inducing compaction (Davison et al., 2010; Davison et al., 2012; Bland et al., 2014; Davison et al., 2016), seismic activity and plate tectonics (Richardson et al., 2005; O'Neill et al., 2016), hydrothermal activity (Ames et al., 1998; Kring, 2002; Naumov, 2002; Osinski et al., 2005; Abramov and Kring, 2007; Pirajno, 2009; Schwenzer and Kring, 2009; Marzo et al., 2010; Kirsimäe and Osinski, 2013; Osinski et al., 2013) and the destruction of planetary bodies in their entirety (Keil et al., 1994; Kring, 2002). The Moon is known to have experienced impacts of varying size; the heavily cratered lunar surface is clear evidence of collisional events from the last ~3.5 billion years (Shoemaker, 1972; Morgan et al., 1974; Wasson et al., 1975; Ryder, 1990; Kring, 2002). Similarly, Earth shows the scars of both large and relatively small impacts (e.g. Wolfe Creek, Western Australia; Meteor Crater, Arizona, US; Chixculub Crater, Mexico) however, the process of plate tectonics limits the age of impact structures that are observable on the Earth's surface today. In this thesis, I explore impactors and impacted materials from various perspectives; compaction of porous planetary bodies in the early Solar System, and the processing of impactor debris following a catastrophic impact on Earth 65 Ma ago. Meteorites provide a window into the complex beginnings and lifetime of our Solar System, and are therefore ideal samples to explore the expansive record of impact driven planetary evolution over the last ~4.5 Ga.

1. IMPACTED MATERIALS

1.1 METEORITES & CLASSIFICATION

Meteorites arguably provide the only record of early solar system formation and processing to create the planetary system we observe today (e.g. Grossman and Larimer, 1974; Macdougall et al., 1984; McSween et al., 1988; Podosek and Swindle, 1988; Ryder, 1990; Brenker et al., 2000; Scott, 2002; Scott and Krot, 2003; Krot et al., 2005; Weidenschilling and Cuzzi, 2006; Davison et al., 2013; Gillet and Goresy, 2013). Condensation of mineral phases, planetary accretion, lithification, fragmentation, aqueous and thermal alteration and impact events on other planetary bodies are just some of the processes that are can be evaluated through examination of extraterrestrial

materials (Macdougall et al., 1984; Anders and Grevesse, 1989; Keller and Buseck, 1990; Weinbruch et al., 1994; Krot et al., 1995; Rubin, 1997; Papike, 1998; Britt et al., 2002; Cuzzi and Weidenschilling, 2006; Huss et al., 2006; Rubin et al., 2007; Weidenschilling, 2011; Gillet and Goresy, 2013; Hanna et al., 2015). Meteorites originate from asteroids, planets, moons and potentially comets, so we can gain a unique understanding of geological variation within the solar system, from the geochemical and primary, secondary and tertiary processing perspectives (Hutchison, 2004). The first three Chapters (2, 3 & 4) succeeding this introduction examine primitive meteorites to comprehend early asteroid formation and the primary compaction process.

There are three broad classifications of these rocks; stony, stony-iron and iron meteorites, with further sub-classifications within each group (Sears and Dodd, 1988; Weisberg et al., 2006). The studies in Chapters 2, 3 & 4 of this thesis focus on stony meteorites, and more specifically chondrites, which are so called owing to the typical presence of spherical, glassy components named chondrules (with the exception of petrologic type 1 chondrites), and are composed predominantly of silicates (Hewins, 1997; Scott and Krot, 2003; Hutchison, 2004). Chondrites are the most primitive type of meteorite, and therefore offer the best insight into early solar system formation out of all meteorite types (Scott et al., 1988; Brearley and Jones, 1998; Scott and Krot, 2003). The chondrite group is split into five subgroups; carbonaceous, ordinary, enstatite, R-group and K-group. Each subgroup contains meteorites with broadly similar characteristics, for example the proportion of chondrules or matrix in a sample, or similar oxidation states (Van Schmus and Wood, 1967; Kallemeyn and Wasson, 1981; Sears and Dodd, 1988; Brearley and Jones, 1998; Weisberg et al., 2006). Carbonaceous chondrites are complex and arguably the most interesting of the chondrites; in addition to sub-millimetre ferromagnesian chondrules and fine-grained (<10 μm) interstitial matrix grains also seen in other chondrite groups, carbonaceous chondrites often contain abundant amoeboid olivine aggregates (AOAs) and calcium-aluminium-rich inclusions (CAIs), which are the result of high temperature (>1500 °C (Hutchison, 2004)) nebular processes such as condensation, melting and evaporation (Grossman and Larimer, 1974; Scott et al., 1988; Sears and Dodd, 1988; Brearley and Jones, 1998; Scott and Krot, 2003; Krot et al., 2005; Weisberg et al., 2006). As this is a highly variable subset of meteorites, further sub-classifications are used to identify meteorites with similar cosmochemical and textural properties (Scott et al., 1988; Scott and Krot, 2003; Weisberg et al., 2006).

1.1.1 Secondary Alteration & Metamorphism

The petrologic type of a meteorite denotes the type and degree of secondary alteration it has experienced, which is noted as a number from 1-6 (Van Schmus and Wood, 1967). Aqueous alteration is shown by the presence of hydrous phases within the

meteorite, such as phyllosilicates (Rubin et al., 2007), sharply defined chondrules (type 2-3) or no chondrules (type 1), opaque fine-grained matrix grains, and no secondary feldpsars (Van Schmus and Wood, 1967; Sears and Dodd, 1988; Brearley and Jones, 1998; Hutchison, 2004). The alteration is noted as petrologic types 1-3, with 1 being the most aqueously altered (Van Schmus and Wood, 1967; Sears and Dodd, 1988). Aqueous alteration is most likely to have occurred as a secondary process on the parent body, where fluids from melting ice were mobilized due to a low-temperature heating event (Brearley and Jones, 1998; Hutchison, 2004). Various dating methods (e.g. Mn-Cr chronometry, Rb-Sr, I-Xe chronometry, ^{26}Al decay, and ^{40}Ar-^{39}Ar dating) imply this process occurred approximately 10-15 Ma after the first CAIs formed (Endress et al., 1996) and continued for 10s of Mas.

The alternate style of secondary alteration is thermal metamorphism. Using the petrological notation, this is displayed as a type 3-6, with 6 being the most thermally altered (Van Schmus and Wood, 1967; Sears and Dodd, 1988). Some samples that have experienced very high metamorphic temperatures (>950 °C (Hutchison, 2004)) exceed this classification and are deemed a type 7 by some researchers e.g. Shaw (L7) meteorite, Watson 012 (H7) or the Uden meteorite (LL7) (Dodd et al., 1975; McSween and Patchen, 1989; Noronha and Friedrich, 2014; Tait et al., 2014). However, the addition of type 7 to the classification is not supported by all in the planetary community. Thermal metamorphism is recognised by a coarsening of matrix grains with increased temperature (600 - 950 °C (Hutchison, 2004)), degraded chondrule outlines and textural variation across chondrules, low distinction between chondrule and matrix grains, very low water content (<1.5 wt%), crystalline chondrule mesostases and overall textural and chemical equilibration of the meteorite with increased petrologic type (Van Schmus and Wood, 1967; Sears and Dodd, 1988; Brearley and Jones, 1998; Hutchison, 2004). Thermal metamorphism is likely to have begun prior to any periods of aqueous alteration, approximately 4-6 Ma after CAI formation, and continued for 10s Ma after, as based on the presence of radiogenic ^{26}Mg (Zinner and Gopel, 1992; Zinner and Göpel, 2002), data from the Pb-Pb and ^{129}I systems (Swindle et al., 1991; Göpel et al., 1994), and data from the ^{40}Ar-^{39}Ar system (Turner, 1988). Logically, such processing would make any primitive textures and structures challenging to examine.

The mid-point of the classification system- petrologic type 3- is reserved for primitive samples that have experienced very limited thermal and aqueous alteration (Van Schmus and Wood, 1967; Hutchison, 2004; Weisberg et al., 2006). It is vital that these type 3 meteorites are used to understand the earliest of solar system processes, as overprinting of early textures and microstructures is likely to occur in meteorites that have experienced extensive secondary alteration. Even where

alteration has occurred prior to the process of interest, such as asteroidal compaction, it is simpler to interpret textures of relatively unaltered samples rather than rocks that have experienced a high amount of alteration. All CV chondrites are classified between types 3.0 and 3.3 (Guimon et al., 1995; Brearley and Jones, 1998) meaning limited secondary thermal and aqueous alteration textures are present, hence their worth in understanding the earliest of nebular and solar system processes. For example, Allende (CV3.2) has experienced the highest metamorphic temperatures of all CV chondrites (<~800 K) (Weinbruch et al., 1994; Bonal et al., 2006; Huss et al., 2006; Cody et al., 2008) as determined by Raman spectra analyses, olivine-spinel thermometry, and Fe/Mg interdiffusion in olivine. Some meteorites from other classes have experienced over 1200 K (Cody et al., 2008) during thermal metamorphism, and so in context Allende has experienced relatively low temperatures. Allende also shows evidence of minimal aqueous alteration, such as abundant secondary Ca-Fe-rich pyroxenes (e.g. Krot et al., 1995; Krot et al., 1998), but it is still regarded as a relatively primitive meteorite by the planetary community. It is for this reason that Allende is the focus of Chapters 2 & 3, which explore the early compaction of asteroids.

1.1.2 Shock processing

Another secondary, or in some cases tertiary (Doyle et al., 2015), process when subsequent to thermal metamorphism or aqueous alteration, is that of shock processing. Impacts into a planetary body or asteroid are very common and their effects have been well documented in meteorite samples and terrestrial rocks (e.g. Dodd and Jarosewich, 1979; Stöffler et al., 1991; Bischoff and Stöffler, 1992; Scott et al., 1992; Scott, 2002). The shock stage of a meteorite is expressed as a number from 1-6, where 6 is the highest shock stage we have observed to date (Dodd and Jarosewich, 1979; Stöffler et al., 1991; Scott et al., 1992). Shock may be exhibited in a meteorite in many different ways, dependent on the type of material the impacted asteroid or planet was initially composed of (Stöffler et al., 1991; Scott et al., 1992; Bland et al., 2011; Beitz et al., 2013; Davison et al., 2016). Typical shock features into a pre-compacted planetary medium include, but are not limited to; undulose extinction of olivine, mosaicism of olivine grains, melt pockets and veins, planar fractures, planar deformation features, and whole rock melting (Stöffler et al., 1988; Stöffler et al., 1991; Langenhorst, 2002; Hutchison, 2004; Ferrière and Osinski, 2013; Gillet and Goresy, 2013). A meteorite with a shock stage of 6 for example, would contain abundant melt pockets, shock melted glass, the presence of ringwoodite- a high pressure polymorph of olivine- and localized opaque shock veins, all of which occur at shock pressures between 75 and 90 GPa (Stöffler et al., 1991; Scott et al., 1992; Rubin et al., 2007). This kind of shock processing from impacts into low-porosity materials may skew interpretations of textures and structures from other solar system processes of interest,

therefore only low-shock meteorites (S1-2) are investigated in Chapters 2-4.

It is essential to also consider impacts into porous media, as the above classification and associated features apply to shock effects generated due to impact into lithified, non-porous rocks (Stöffler et al., 1991; Scott et al., 1992). Compaction of porous material generates large and widespread heating due to pore collapse within relatively low velocity impact scenarios (Davison et al., 2012; Bland et al., 2014; Davison et al., 2016). Chapters 2 & 3 explore asteroid compaction from an initially high-porosity body, therefore the effect of pore collapse is highly significant.

1.2 CV CHONDRITES

CV chondrites are carbonaceous chondrites of great similarity to the subclass 'type' meteorite, Vigarano, and are specifically investigated in Chapters 2-4. CVs contain olivines with widely varying compositions from grain to grain owing to the vast differences in degree of equilibration (Brearley and Jones, 1998; Hutchison, 2004). Olivine compositions usually lie in the range $Fa_{10\text{-}85}$ (Brearley and Jones, 1998). CVs also have a typical carbon content of <1.05 wt%, and a water content of <3.5 wt% (Guimon et al., 1995; Brearley and Jones, 1998; Hutchison, 2004). Their bulk chemistry reveals this class has the highest Ca/Si, Al/Si and Mg/Si ratios of all chondrites (Kallemeyn and Wasson, 1981; Wasson and Kallemeyn, 1988; Hutchison, 2004). CVs also contain the largest chondrules, at an average of 1 mm diameter (Hewins, 1997; Brearley and Jones, 1998; Scott and Krot, 2003; Hutchison, 2004). Chondrites of the CV class typically contain ~40 vol% fine-grained matrix, 45 vol% chondrules, 10 vol% CAIs and between 1 and 5 vol% metal (Wasson and Kallemeyn, 1988; Brearley and Jones, 1998; Scott and Krot, 2003).

Several large falls and finds of samples belonging to this subclass (e.g. Allende, Vigarano) have highlighted some distinct disparities within the CV population. This has resulted in further classification into three sub-types; oxidized type A (CV_{oxA}, Allende-type), oxidized type B (CV_{oxB}, Bali-type) and reduced (CV_{red}) (Weisberg et al., 1997; Weisberg et al., 2006). The three groups are distinguishable based on the following: matrix/chondrule ratios are CV_{red} 0.5-0.6, CV_{oxA} 0.6-0.7, and CV_{oxB} 0.7-1.2 whilst metal/magnetite ratios increase in the reverse order (Weisberg et al., 1997; Weisberg et al., 2006). CV_{oxA} samples are more thermally altered than CV_{oxB}, as they only contain minor phyllosilicates, matrix grains are typically coarse and comprise mainly ferrous olivine laths ($Fa_{40\text{-}60}$). CV_{oxB} samples contain many hydrous phyllosilicates due to the high amounts of aqueous alteration they have experienced, and comprise comparatively fine grains of ferrous olivine in the matrix (Weisberg et al., 1997; Weisberg et al., 2006). The reduced subclass contains samples that have been thermally altered, but to a lesser extent than CV_{oxA} as evidenced by the finer grains and fewer secondary minerals, such as sodalite and nepheline (Weisberg et al., 2006).

CV chondrites are all predicted to originate from the same parent body (Brearley and Jones, 1998; Krot et al., 1998; Weisberg et al., 2006), based upon similarities in oxygen isotope measurements (Weisberg et al., 2006), and the extensive microanalytical studies of Krot et al., (e.g. 1995; 1998; 2004) led to the discovery that the significant differences between the subgroups likely arose from secondary alteration on the parent body (Krot et al., 1998). Chapter 4 investigates the morphological and crystallographic differences between the matrices of one CV chondrite from each sub-type, and the relevant implications of parent body processes are discussed there.

1.3 ASTEROID COMPACTION AND LITHIFICATION

Planetary bodies accreted from a nebula of small (<~1 mm), dust-sized particles that had condensed from the nebula gas in the very early solar system. Over a period several million years, planetary bodies were accreted (Amelin et al., 2002; Cuzzi et al., 2005; Russell et al., 2006; Weidenschilling and Cuzzi, 2006) but maintained the high volume of pore spaces between dust particles (Beitz et al., 2013). Porosity at this time is surmised to be >~65% (Blum, 2004; Ormel et al., 2008; Bland et al., 2011; Beitz et al., 2013) based on filling factors of the dust agglomerates in the accretion disk. The asteroids we observe in our solar system, and the meteoritic samples we receive from small planetary bodies no longer possess such high levels of porosity (Brearley and Jones, 1998; Britt et al., 2002; Hutchison, 2004; Macke et al., 2011), although variance between and within meteorite classes has been well documented (Consolmagno et al., 2008; Macke et al., 2011). The porosities of carbonaceous chondrites do not directly correlate to shock stage, which is assigned based on evidence of traditional impacts into compacted media (see section 1.1.1.2) (Stöffler et al., 1991; Scott et al., 1992; Consolmagno et al., 2008; Bland et al., 2014). Therefore, another early process, which does not necessarily generate traditional shock features, must have acted to compact the parent body (Blum, 2004; Bland et al., 2014). The process by which asteroids were compacted to meteoritic porosities is still in debate, and Chapters 2, 3 and 4 explore the microscopic evidence of this in depth.

Impact-induced compaction as a driver for lithification is best supported by the microtextural evidence (Bland et al., 2011; Forman et al., 2016) and large-scale physical constraints, such as the low-gravity generated by small asteroids (Blum, 2004; Weidenschilling and Cuzzi, 2006). This process involves frequent but low-velocity impacts between highly porous bodies, causing gradual compaction and subsequent lithification of the rocky body (Blum, 2004; Bland et al., 2014; Davison et al., 2016). There is a distinct lack of traditional shock features in the majority of chondrites, and recent numerical modelling has highlighted why this may be the case (Davison et al., 2010; e.g. Bland et al., 2014; Davison et al., 2016).

Earlier shock classification systems were calibrated using low-porosity, homogenous rocks (Stöffler et al., 1991; Scott et al., 1992) and were therefore unsuitable to use as a proxy for initially uncompacted, highly porous planetary bodies. Numerical simulations detailing the predicted response of bimodal media with different porosities to impacts of varying velocities have indicated how evidence of impact-induced compaction may be identified in primitive meteorites at the meso-scale (Davison et al., 2010; Bland et al., 2011; Davison et al., 2012; Bland et al., 2014; Davison et al., 2014; Davison et al., 2016). Large, mechanically strong chondrules are surrounded by porous, fine-grained, mechanically weak matrix regions. Upon impact, the simulation shows abundant pore collapse in matrix regions, with associated pressure and temperature peaks far exceeding those experienced by the non-porous chondrules (Davison et al., 2012; Bland et al., 2014; Davison et al., 2016). The heterogeneous introduction of heat in low-velocity impact scenarios implies varied textural and structural evidence is likely to be observed within the meteorites; chondrules, having experienced limited temperature (max. of 330 °C at 1 km/s impact velocity (Bland et al., 2014)) and pressure increases relative to matrix grains, are very unlikely to have any 'traditional' shock features. Conversely, fine-grained matrix grains are likely to be crystal-plastically deformed (expanded upon in section 1.1.4), and may have been physically aligned due to the shock wave propagating through the medium and generating heat due to pore collapse (Davison et al., 2016). Furthermore, the shock wave is predicted to have interacted constructively and destructively as it encountered chondrules (mechanically robust) and high porosity matrix regions (comparatively weak) resulting in non-uniform temperatures and associated deformation between matrix regions (Bland et al., 2014; Davison et al., 2016). Microstructural and textural studies to assess potential evidence of this process is examined in Chapters 2 & 3.

Alternative compaction and lithification theories have received some support from numerical simulations and microscopy studies. Low-temperature gravitational compaction was proposed by Fujimara et al., (1983) whereby lithostatic forces, powered by gravitational means generated by the asteroid, would gradually compact the porous material over ~1 Ma, to create a lithified, low-porosity rocky asteroid. Gravitational calculations have since revealed that small planetary bodies would have insufficient gravitational force to overcome the strength of the porous body (Blum, 2004; Weidenschilling and Cuzzi, 2006), and cold compaction does not agree with deformation features that have been observed within carbonaceous chondrites (Bland et al., 2011; Forman et al., 2016).

Compaction via radioactive heating of ^{26}Al has also received some support in recent years (e.g. Henke et al., 2012; Gail et al., 2015), and is termed hot isostatic pressing (HIP). This involves a two-phase system,

whereby cold gravity-driven compaction is followed by a heating event powered by the radiogenic decay of ^{26}Al on the parent body. This is predicted to compact the body over ~1 Ma, as the heat is expected to induce sintering of the matrix and chondrule grains, thereby reducing the porosity of the material. However, the amount of heating that is predicted to be required for compaction exceeds that of the peak temperatures that have been measured for many carbonaceous chondrites (Bonal et al., 2006; Cody et al., 2008; Henke et al., 2012; Gail et al., 2015). There are no chondrites that have a porosity above ~40% (Consolmagno et al., 1998; Consolmagno et al., 2008), and therefore regardless of the variations in porosity between and within meteorite classes, some degree of compaction has occurred on all planetary bodies. Given the high temperatures required for this process to occur, and little evidence of such temperatures being achieved in most carbonaceous chondrites, this compaction process has not received the same support as impact-induced compaction amongst researchers. All three process are discussed in the context of microstructural and textural properties of the CV chondrite Allende in Chapters 2 & 3, and are considered on the planetary scale with three CV chondrites in Chapter 4.

1.4 CRYSTAL-PLASTIC DEFORMATION OF IMPACTED MATERIALS

Grains respond to compaction in various ways, dependent upon the conditions under which the compaction occurs (Ashby and Verrall, 1977; Schwenn and Goetze, 1978; Twiss and Moores, 2006). We can therefore use deformation features as a tracer for the temperatures and pressures of the parent

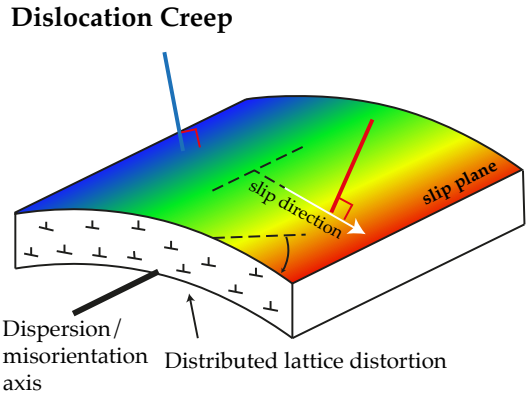

Figure 1.1: *Dislocation creep within a crystal to generate a distorted crystal lattice. Dislocations migrate along slip planes in the slip direction indicated around the dispersion axis. Slightly different crystallographic orientations would be measured at the blue and red lines, and therefore deformation due to dislocation creep can be quantified. If multiple dislocations migrate along parallel slip planes, this can be termed a slip system.*

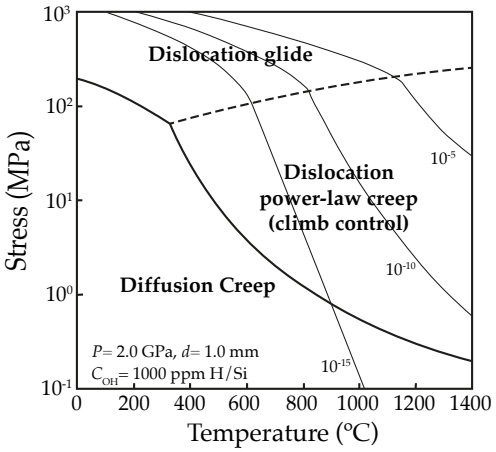

Figure 1.2: *Deformation mechanism map for olivine at a grain size of 1.0 mm. The dominant deformation process in olivine is dictated by the temperature and differential stresses present. Variations occur when considering different grain sizes, however the general configuration of the map here still applies. After Katayama, 2009.*

body at the time of compaction, which constrains the likely compacting process, as explored in Chapters 2 and 3.

Crystal structures deform in response to an applied stress, and the type of deformation is typically a function of the temperature of the material at the time. In Chapters 2 and 3, crystal-plastic deformation is explored; this type of deformation requires heat to be activated, and is a ductile deformation feature, meaning the crystal bends to accommodate the applied stress (e.g. Fig. 1.1). Chapters 2 and 3 investigate deformation of olivine.

One of the dominant deformation schemes of olivine at low temperatures is dislocation creep (Fig. 1.1 & 1.2). Dislocations within the crystal structure migrate along a number of slip-planes within the well-defined slip-systems of olivine. This results in grain shape modification and a strained crystal, unless dislocations migrate to grain boundaries (Fig. 1.1), and it is activated by heat and pressure. Dislocation glide occurs at low temperatures and high shear stresses, whereby a glide plane through the crystal lattice allows for bond switching along the plane, to result in ductile deformation of the crystal lattice (Twiss and Moores, 2006; Katayama, 2009). When a number of parallel glide planes with the same slip vector are activated, this constitutes a slip-system (Nicolas et al., 1973; Nicolas and Poirier, 1976; Ashby and Verrall, 1977; Twiss and Moores, 2006; Katayama, 2009). Dislocations will predictably meet and interact with one another if multiple slip systems are operating at the same time and in different directions. In this case, dislocation glide becomes more difficult, as intersecting dislocations inhibit the process, which is called work hardening. This serves to halt dislocation migration (Twiss and Moores, 2006).

At higher temperatures and comparatively lower differential stresses, dislocation climb may be activated (Ashby and Verrall, 1977; Goetze and Poirier, 1978; Twiss and Moores, 2006; Katayama, 2009). This allows for edge dislocations to migrate, or climb, to an adjacent glide plane. It is necessary for an atom to move from one half-plane to another during this process, which creates internal

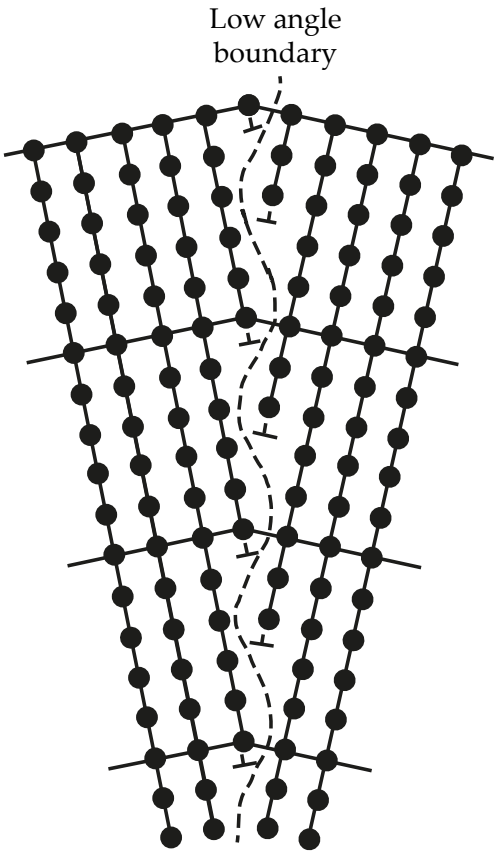

Figure 1.3: *Example of migration of alike dislocations to form a dislocation wall or low-angle boundary within a crystal. After Twiss & Moores, 2006.*

strain within the crystal lattice (Twiss and Moores, 2006), however climb is the slowest process of the two mechanisms mentioned. Where dislocation glide is mitigated by work hardening, climb enables dislocations to migrate through the crystal lattice once more, and can result in strain recovery where dislocations can be annihilated if two with opposing signs meet. It is common for edge dislocations of the same sign to collect into a dislocation wall (Fig. 1.3) or a low-angle boundary, as this is the lowest energy configuration after dislocation climb has occurred (Twiss and Moores, 2006). This wall or low-angle boundary separates the two parts of the crystal which now have marginally different crystal orientations due to dislocation accumulation (Twiss and Moores, 2006), and can be detected using electron backscatter diffraction (EBSD); a microanalytical technique that is used in Chapters 2-4.

Where dislocation creep has occurred throughout a sample along a single or number of slip systems, a microfabric or crystallographic preferred orientation may be formed. Crystals rotate to a preferred orientation as a direct result of dislocation slip along well-defined slip planes within the grains (Twiss and Moores, 2006). Different slip systems dominate under different temperature and pressure conditions, and also vary with the addition of water (Fig. 1.4) (Carter and Ave'Lallemant, 1970; Fliervoet et al., 1999; Twiss and Moores, 2006; Karato et al., 2008). These slip systems are discussed in Chapter 2 in relation to the formation conditions of microfabrics in the Allende meteorite.

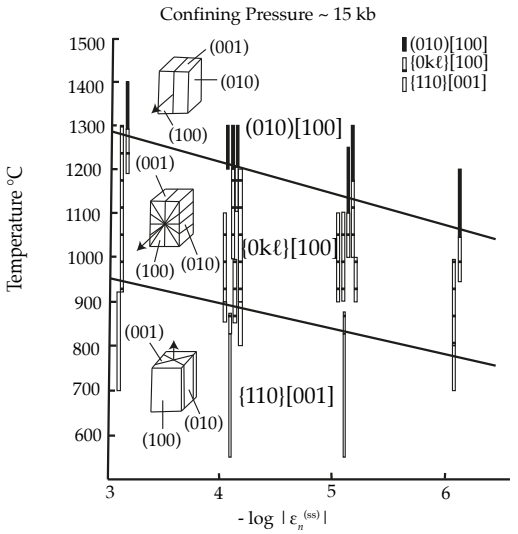

Figure 1.4: *Graph showing slip systems determined by experiment, as a function of strain rate and temperature. Each bar represents a different set of conditions that the respective slip systems have operated under. () indicate Miller indices of specific slip planes, {} refer to all slip planes symmetrically related to the specified slip plane, and [] indicate the coordinates of specific slip directions. Cube models represent olivine crystals, with respective dominant slip planes and slip directions (arrows) indicated (Twiss and Moores, 2006). After Carter & Ave'Lallement, 1970.*

1.5 ANALYTICAL TECHNIQUES FOR UNDERSTANDING IMPACTED MATERIALS

1.5.1 Electron backscatter diffraction (EBSD)

Porous media that have undergone compaction are unlikely to show traditional shock features given the surmised low velocity of the impacts (Davison et al., 2016) and subsequent absence of macro-scale brittle deformation that may be observed in impacted non-porous media. Traditional optical microscopy techniques are therefore unsuited to detect the microtextures and

structures that are expected from early impacts. As compaction, regardless of the process, is predicted to result in temperature changes (Henke et al., 2012; Bland et al., 2014; Gail et al., 2015; Davison et al., 2016), grain re-orientation, and brittle or crystal-plastic grain deformation (e.g. Fujimura et al., 1983; Bland et al., 2014; Gail et al., 2015; Hanna et al., 2015), a technique which examines the crystallography, structures and textures within a sample must be used.

Electron backscatter diffraction (EBSD) analysis allows for the identification of crystal structures based on the diffraction patterns produced when electrons are incident on the sample or crystal surfaces. Minerals or phases are easily identified (Humphreys, 2004) with relatively little additional input, in a regular scanning electron microscope (SEM) (Prior et al., 1996; Trimby and Prior, 1999; Trimby et al., 2002) using the Oxford Instruments software package, AZtec. Samples are required to be flat, which typically requires mechanical polishing, but may be in thin or thick section format. This imaging technique determines the crystallographic orientations of each of the imaged pixels based upon the diffraction pattern orientations, and each pixel is then colour-coded to reflect the orientation in terms of the three Euler angles (- ϕ2, -Φ, -ϕ1 which are red, blue and green respectively) (Fig. 1.5a) (Humphreys, 2004; Groeber et al., 2009). This data is displayed and further reduced using the Channel 5.12 software package. Here, the software can be used to noise reduce the dataset based on user-

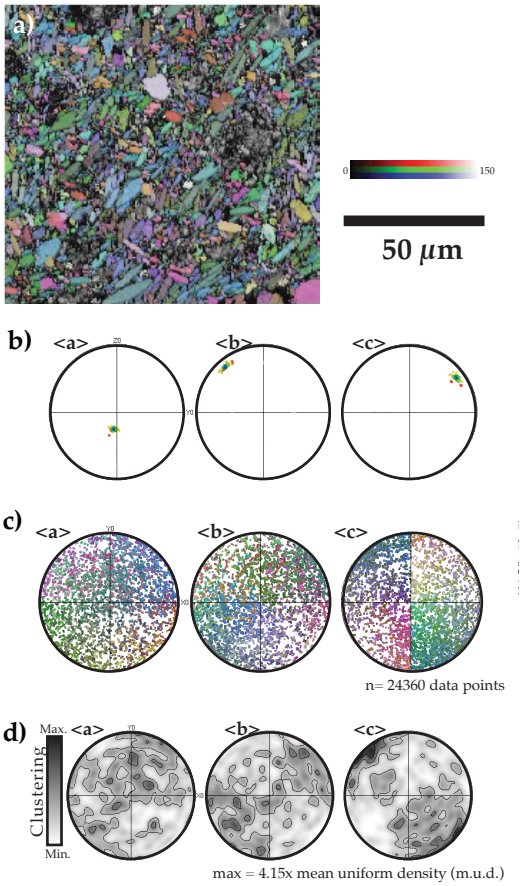

Figure 1.5: *Workflow of EBSD data reduction and processing. A) Euler map, presenting each grain colour-coded to reflect the orientation in terms of the three euler angles. Euler map is overlain onto the band contrast map, where lighter regions indicate a well-indexed grain, and darker regions indicate a poorly indexed grain. B) Data from a single grain is presented on three lower-hemisphere, equal area plots, showing the <a>, <b> and <c> crystallographic axis for olivine. The variation in colour of the data indicates this grain has experienced deformation, and therefore slip system analysis can be used to determine the plane of slip, and slip direction (e.g. Fig. 1.1). C) One point per grain, from all grains in the region of (a) presented on lower hemisphere, equal area plots, colour coded to match the euler map. D) Data from (c) is contoured to identify any crystallographic preferred orientations (CPO) in the data. High density regions are shaded black, with a maximum density of 4.15x mean uniform density (m.u.d.). In this case the CPO is in the <c> axis.*

specified parameters, detect grain boundaries and therefore infer separate grains, detect low-angle intragrain boundaries and changes in crystallographic orientation across a grain due to crystal-plastic deformation, and calculate grain sizes and shapes based on a choice of user-selected parameters.

The crystallographic orientation data from each pixel or grain of the EBSD analysis may then be displayed on lower-hemisphere,

Figure 1.6: *Schematic of how EBSD data is displayed onto lower hemisphere, equal area plots. Each crystal of olivine has three primary crystallographic axes; <a>, <b> and <c> (a). These are displayed on the lower-hemisphere plots according to where the three primary crystallographic axis would intersect the bowl shape (b). If grains are oriented randomly (c), crystallographic axes do not cluster and therefore have a low m.u.d. If grains are somewhat aligned (d), the crystallographic axes plot in similar regions, and CPOs can be identified from the contoured data.*

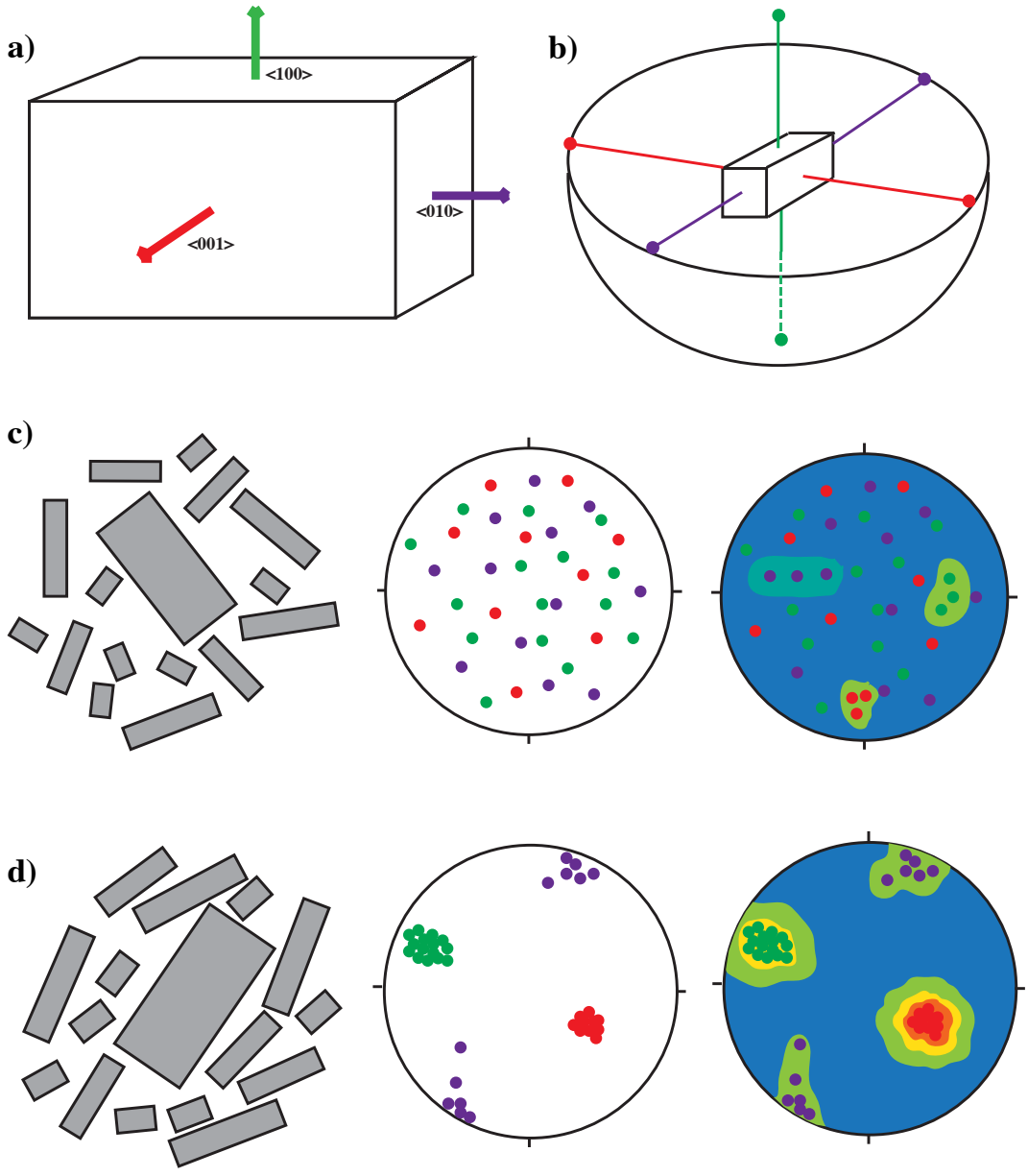

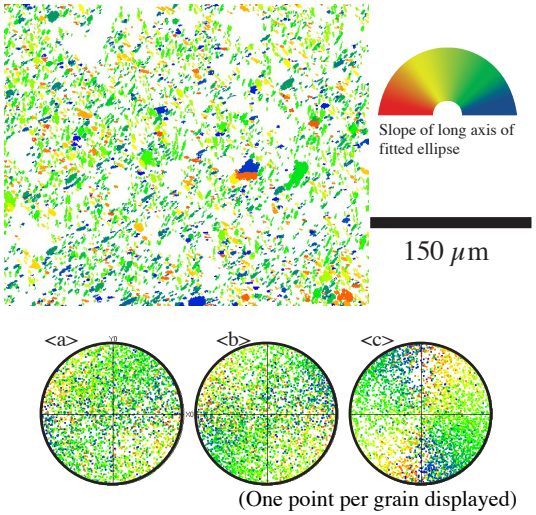

Figure 1.7: *Slope (orientation) of long axis of ellipse map is presented. Data can be displayed on lower hemisphere, equal area plots in the same colour scheme to allow for any relationships to be identified, such as shape preferred orientations (SPOs). Here, the vertically oriented grains (yellow-green) appear to have a <c> axis that is predominantly perpendicular to the long axis of the ellipse, implying the <c> axis is not the long axis of the crystals.*

equal area plots (pole figures) in the map/sample reference frame of x-y-z; a schematic to demonstrate the workflow of this is shown in Fig. 1.6. Pole figures are colour coded according to the map of the data they display so comparisons can easily be made. Chapters 2, 3 & 4 examine the olivine grains within the meteorites, therefore the a=<100>, b=<010> and c=<001> axis are plotted (Fig 1.5). Single grains, one point per grain, as well as subsets of the data can be displayed to suit the purpose of the required analysis (Fig. 1.5). The display of single grains (Fig. 1.5b) enables the user to identify intragrain deformation through examining the Euler colouration of the displayed points, and may also be used to compare orientations of different phases, or perform slip system analysis for deformed grains. One point per grain (Fig. 1.5c) allows for the entire dataset to be compared, but not biased by larger grains that contain many more measured points or pixels; this is typically useful when identifying crystallographic preferred orientations or fabrics (Groeber et al., 2009). In this case, the pole figure data are typically contoured for data density (Fig. 1.5d), which gives a measure of CPO intensity, in terms of the mean uniform density (m.u.d.).

Grain statistics, such as diameter (circle-equivalent, long ellipse axis or short ellipse axis), grain area, grain elongation (aspect ratio) or grain slope can be quantified within the Channel 5.12 software package. Maps can be modified to present grains based upon any of the aforementioned parameters, and such data can subsequently be displayed as pole figures and colour coded accordingly to identify any orientation and morphologic correlations (e.g. Fig. 1.7, where grain slope is presented).

As data collection of this technique is performed using electron-opaque samples, there are resolution limitations to consider that may not be ideal for the sample to be analysed. Users specify the step-size of the data collection, or the dataset resolution, prior to mapping the sample, which is reliable to a lower limit of ~0.1 μm for most EBSD instrumentation.

1.5.2 Transmission kikuchi diffraction (TKD)

TKD uses the same principles to image a sample, and obtain and analyse the dataset as with EBSD, but at a much finer scale.

TKD uses regular EBSD instrumentation but with electron transparent samples to enable mapping at spatial resolutions of <10 nm (Trimby, 2012; Trimby et al., 2014). This requires the use of a SEM. Sample preparation is somewhat different, and is fully outlined in Chapter 2.3. Data interpretation and analysis is done using the same software packages and in the same manner as described above. TKD is therefore an excellent tool for high-resolution mapping and identifying structures and textures at the nano scale, and may be directly compared with micro-meso scale features identified using EBSD.

2. SEARCHING FOR THE PROGENITORS OF IMPACTORS: A CASE STUDY OF A TERRESTRIAL SETTING

2.1 IMPACT PROCESSES

Very small to catastrophic impacts happen regularly throughout our solar system (Michel and Morbidelli, 2013). The frequency of the impact typically depends upon the impactor size; the larger the impact, the rarer its occurrence (Michel and Morbidelli, 2013). When an impactor encounters a rocky target body, the size of said impactor, the target lithology and atmospheric conditions all typically dictate how the material is dispersed (Pierazzo and Melosh, 2000; Collins et al., 2012; Melosh, 2012; Collins et al., 2013).

Upon contact, a shock wave propagates downwards and accelerates through the planetary body, acting to compact, melt, and shock the target rock (Melosh, 2012) due to the sudden injection of pressure from the projectile's momentum. At this time, highly shocked surface materials on the target body at the edge of the projectile may be 'jetted' out of the impact crater at high velocity (Melosh, 2012). A release wave, known as the rarefaction wave, also travels upwards through the projectile, compressing it, followed by a downwards decompression shockwave, which may result in partial or full melting or vapourisation of the projectile owing to the large amount of heat generated during compression (Collins et al., 2012; Melosh, 2012; Collins et al., 2013). Numerical simulations indicate that higher impact angles

typically lead to an increased proportion of vapourised projectile material (Pierazzo and Melosh, 2000; Osinski and Pierazzo, 2012). Conversely, smaller projectiles travelling at lower velocities, and at lower impact angles are predicted to generate less heat, and less of the projectile would be vapourised (Pierazzo and Melosh, 2000; Osinski and Pierazzo, 2012). The style of impact crater on the target body can also be used to remotely infer physical properties of the planetary body- for example the impact craters on the asteroid 253-Mathilde can't be constrained by impact cratering simulations based on terrestrial and lunar impacts (Cheng and Barnouin-Jha, 1999; Housen et al., 1999; Housen and Holsapple, 2003). Mathilde was therefore inferred to have an unusually high porosity to describe the behavior of the surface to impact (Housen et al., 1999; Housen and Holsapple, 2003; Housen and Holsapple, 2011).

In the instance of large, crater-inducing projectiles, the type of atmospheric conditions present on the target body can affect how materials are preserved or redistributed (Goldin and Melosh, 2007; Housen and Holsapple, 2011). Direct native remnants of the projectile may be deposited close to the impact site, whilst more catastrophic impacts may result in wide-spread ejecta distribution from the impact site of both the target rocks and native and melted/vapourised projectile (Artemieva and Morgan, 2007; Goldin and Melosh, 2007; Artemieva and Morgan, 2011; Housen and Holsapple, 2011; Goderis et al., 2012). Both instances may provide information as to the type of projectile, the lithology and porosity of the target body, and atmospheric conditions at the time of impact (Housen and Holsapple, 2003; Artemieva and Morgan, 2007; Housen and Holsapple, 2011).

Examination of the geochemistry of a projectile or relicts can offer an insight into the planetary origin and processing history of the parent body, in a similar way to smaller meteorite falls and finds (e.g. Goderis et al., 2012; Goderis et al., 2013). Lithologies from throughout our solar system contain distinct and relatively well-established fingerprints of their parent planetary body; for example, oxygen isotope studies are able to separate terrestrial, lunar, martian, and asteroidal lithologies due to their differing oxygen isotope signatures based on the location of formation in the solar system (Clayton and Mayeda, 1983; Lodders, 1997; Franchi et al., 1999; Spicuzza et al., 2007). Other techniques, both non-destructive and destructive, can also be used to determine what meteorite class a fragment belongs to, or place constraints on the temperature and pressure the fragment may have experienced (e.g. Swindle et al., 1991; Agee et al., 1995; Krot and Scott, 1995). The potential applications of detecting exogenous material using geochemical constraints are described in the following section, and the techniques used for exogenous fragment identification are outlined in section 2.3.

2.2 EARTH: CRETACEOUS-PALEOGENE (K-PG) BOUNDARY CLAYS

Extraterrestrial material falls to the Earth's surface on a very regular basis (Grieve and Pesonen, 1992; Michel and Morbidelli, 2013). Over the course of the Earth's history, some large and catastrophic impact events have altered the evolution of life, such as the impact event ~65 Ma ago (e.g. Arenillas et al., 2006; Renne et al., 2013), which is believed to have led to the demise of the dinosaur population through direct and indirect causes relating to the impact event (Alvarez et al., 1980; Alvarez et al., 1990). The crater associated with the event – the Chicxulub crater- is located in the Gulf of Mexico and a large proportion of it is underwater (Smit and Hertogen, 1980; Hildebrand et al., 1991; Pope et al., 1991; Warner et al., 1997; Smit, 1999; Arenillas et al., 2006; Gulick et al., 2013).

The K-Pg boundary, formerly the K-T boundary (Cretaceous-Tertiary), is a thin layer of rock which formed at the close of the Cretaceous Period and the beginning of the Paleogene Period. Radiometric $^{40}Ar/^{39}Ar$ dating techniques indicate this layer formed at 66.043 Ma (Renne et al., 2013). The alteration to the nomenclature of the boundary layer arose as the 'Tertiary' is no longer recognized as a formal geochronological unit (Gradstein et al., 2004). At the K-Pg boundary worldwide, an enrichment in highly siderophile elements, notably iridium, was first detected by Alvarez et al., (1980) and noted by many afterwards (e.g. Ganapathy et al., 1981; Schmitz et al., 1988; Alvarez et al., 1990; Elliot et al., 1994; Evans et al., 1994; Shukolyukov and Lugmair, 1998a; Shukolyukov and Lugmair, 1998b; Glikson and Allen, 2004; Quitte et al., 2007; Osawa et al., 2009). As iridium is refractory as well as siderophile, such concentrations are highly unlikely to be found on the Earth's surface (Alvarez et al., 1980; Lodders, 2003). Upon the discovery of the Chicxulub impact crater, dating techniques identified the synchronicity of the impact crater and iridium-rich boundary layer, and alongside impact debris and shocked minerals, deemed the two were related (Hildebrand et al., 1991; Pope et al., 1991; Hildebrand and Stansberry, 1992). The Chicxulub crater is over ~200 km in diameter and represents one of the largest terrestrial impacts recorded to date (Grieve et al., 1995; Warner et al., 1997; Pierazzo and Artemieva, 2012; Michel and Morbidelli, 2013), which may be the primary reason for the global-scale evidence (Pope et al., 1991; Pierazzo and Artemieva, 2012). Geochemical examination of the highly siderophile elements of impact ejecta at many K-Pg boundary sites indicate the projectile was a carbonaceous chondrite (Smit, 1999; Goderis et al., 2013), and numerical simulations modelling the distribution of impact ejecta imply the projectile was between 10 and 14.4 km in diameter (Warner et al., 1997; Pierazzo et al., 1998; Morgan, 2008).

Material found to originate from the projectile at distal ejecta locations are primarily comprised of vapourised and re-condensed fragments that were expelled from the impact site high into the atmosphere within the ejecta

cloud (Ebel and Grossman, 2005; Wittmann et al., 2007; Artemieva and Morgan, 2009). Owing to the large temperatures predicted, much of the ejecta cloud would have been vapour and over time this cloud dissipated and condensed, and debris fallout resulted in the global K-Pg impact ejecta layer (Ebel and Grossman, 2005; Artemieva and Morgan, 2007; Artemieva and Shuvalov, 2008; Artemieva and Morgan, 2009). The distal layers are between 2-4 mm in thickness (Smit and Hertogen, 1980; Smit, 1999; Schulte et al., 2010), and contain abundant platinum group elements (PGEs) (Alvarez et al., 1980; Alvarez et al., 1990; Artemieva and Morgan, 2007; Goldin and Melosh, 2007; Artemieva and Morgan, 2009; Artemieva and Morgan, 2011; Goderis et al., 2013). Chapter 5 examines the K-Pg layers from sites greater than 4000 km from the impact location, to identify the host mineral of the iridium in situ- doing so aids in understanding how the condensation and interactions occurred within the impact cloud, and also helps constrain the temperatures within the impact ejecta cloud and geochemical conditions of the Earth's atmosphere at the time of impact and condensation. The techniques described in the following section (2.3) were all employed to facilitate in situ identification of the iridium within the boundary clays- something that has yet to be achieved for the K-Pg boundary clays.

2.3 LOOKING FOR A NEEDLE IN A HAYSTACK: ANALYTICAL TECHNIQUES FOR IN SITU GEOCHEMICAL ANALYSIS OF EXTRATERRESTRIAL AND TERRESTRIAL MATERIALS

2.3.1 Backscatter electron (BSE) & energy dispersive spectrometry (EDS) imaging

Backscatter electron (BSE) imaging requires a scanning electron microscope (SEM) and specifically in this thesis a field emission SEM, whereby electrons that are fired at the sample surface interact with the top portion of the sample, and are then emitted as backscattered electrons (BSEs) (Lyman et al., 1990). The detector forms an image of the sample based upon the BSEs; this is a greyscale image, where materials of differing density can be identified. Bright regions are associated with higher atomic number elements such as Fe, Ir, Zr, and Os. Darker regions conversely show the locations of low density material, and often lighter elements such as Mg, Na and C. This technique is useful for a broad-scale examination of a full sample to identify any interesting and typically heavy elements for further investigation with quantitative techniques.

Energy dispersive spectrometry (EDS) imaging also uses an SEM, with the addition of the AZtec software package from Oxford Instruments. EDS measures the concentration of x-rays emitted of varying energies (Fitzgerald et al., 1968; Newbury, 2002; Goldstein et al., 2012a), when sample particles are excited by electrons in the SEM chamber.

All elements of interest (not including H and He) produce unique x-ray energies allowing for element identification and quantification using the energy spectra produced by the EDS measurement equipment (Newbury, 2002). Ideally, EDS instrumentation can detect photon energies between 0.1 keV- 100 keV, which encompasses most major and minor element energies (Newbury, 2002; Goldstein et al., 2012a). EDS is well-suited to examining the elemental distribution across a sample, but it can be time consuming to obtain a full elemental map with sufficient accuracy. If the elemental composition of the meteoritic material is known, or if it has an affinity to a major element, EDS imaging can provide the spatial context for further investigation with other high-resolution imaging techniques. Once again, the resolution of such imaging is dictated by the capabilities of the SEM used.

2.3.2 X-ray fluorescence (XRF) synchrotron imaging

XRF imaging works in a very similar manner to EDS, however it is conducted at a synchrotron facility, and therefore excellent spatial resolution is attained (~2 μm/pixel) and it has much greater detection sensitivities (Ryan et al., 2010). XRF imaging typically uses a high beam voltage of 18.5 keV, and so a larger volume of the sample is measured when compared with traditional imaging techniques such as EDS, and x-rays can penetrate up to ~100 μm into a sample before interacting with the material (Goldstein et al., 2012b; Dyl et al., 2014). This allows for mineral phases at depth to be detected (Dyl et al., 2014). This very high energy beam also enables mapping of trace elements, such as Ir, Pt, and Os (Ryan et al., 2010). The XRF technique has energy sensitivities between 3.3-19.9 keV, and has a high energy resolution of 300-400 eV, detecting 25 elements down to the 10 ppm scale (Fisher et al., 2014), making it ideal to identify very small or low concentration trace elements, such as iridium and platinum. The elemental spectra can be used to accurately quantify elemental abundances within the sample in any specified region, however some limitations arise where energy peaks begin to overlap, but correct data reduction practices reduce the likelihood of this occurring (Ryan et al., 2010; Fisher et al., 2014).

XRF using the synchrotron often requires less time to acquire elemental maps when compared with EDS. The improvement in spatial and energy resolutions, and elemental quantification accuracy make this technique invaluable for detecting small, low elemental concentration exogenous materials, specifically in the case of trace elements (Ryan et al., 2010; Fisher et al., 2014).

2.3.3 Tescan integrated mineral analyser (TIMA) mapping

The TIMA mapping technique integrates BSEs and EDS data collectively in a field emission SEM to directly identify mineral phases. Typically, a step size of 2 μm is used for the EDS data collection. Grain boundaries can be identified easily with the combination of data, and then individual grains are assigned a mineral phase based

upon an appropriate spectrum match with pre-identified minerals in the software. The obvious issue here is that minerals unknown to the system may be present and this requires manual mineral identification based on the elemental spectrum collected with EDS. Given the ease of mineral identification and abundance measurement where minerals are identified successfully, this technique is good to use prior to LA-ICP-MS analysis, so that appropriate and reliable data reduction can be applied. The images produced can also serve to provide mineralogical context for minerals or elements of interest, that are likely to occur with more major minerals or elements and have already been detected using the TIMA.

2.3.4 Laser ablation inductively-coupled plasma mass spectrometry (LA-ICP-MS)

LA-ICP-MS is a destructive technique whereby the material of interest is irradiated with an ultraviolet (UV) beam from a laser, and the resultant laser-induced elemental vapour is transported via an inert gas flow to the inductively-coupled plasma. Here, it is decomposed and ionised, and then analysed via mass spectrometry which relies upon the mass of the particle to identify the isotopes present (Arrowsmith, 1987; Jarvis and Williams, 1993; Perkins et al., 1993; Liu et al., 2013). This method usually requires appropriate known standards to be run in the instrument to calibrate the unknown sample results, although standard-less analyses have been achieved to some accuracy (e.g. Liu et al., 2008). It can be used to create a map, or to do single spot analyses, and is very useful in determining abundances and distributions of major, minor and trace elements of interest (Jarvis and Williams, 1993; Perkins et al., 1993), such as Fe, Mg, Cu, Ni, Pb, Ir, Re, Os etc. Analysis using LA-ICP-MS typically has a detection limit of 0.05-10 μg/g, which is an improvement upon the detection limit of XRF techniques (Jarvis and Williams, 1993; Perkins et al., 1993). This technique also uses mass spectrometry, and so does not encounter the same energy peak overlaps as in XRF analyses, but it does suffer from isobaric and polyatomic interference from ion overlaps with a similar mass/charge ratio. Fortunately however, ^{193}Ir does not have any significant overlap with phases reported in the boundary samples, and therefore this should not pose a setback. Data reduction is performed based upon existing mineralogical information, so this technique is difficult to use alone for the context required here. In addition, data reduction can be modified according to different minerals, but multi-mineralogical samples are complex to display on a single map whilst also being correctly spatially calibrated to the correct mineral. This technique has an excellent detection limit (ppb level) (Jarvis and Williams, 1993; Perkins et al., 1993; Liu et al., 2013) suited to the predicted concentrations of Ir or other HSEs for example, however the complexity in imaging multiple mineralogies in one map means the location of the elemental abundances may not be as accurately correlated to other images when compared to alternate techniques.

2.3.5 Focussed ion beam (FIB) and transmission electron microscopy (TEM)

Samples can be prepared for TEM by removing a slice of a material from a thin or thick section, using a focused ion beam (FIB). This process is described in depth in Chapter 5. The wedge of the sample is thinned until it reaches electron transparency (~ 100 nm) and may then be investigated using a TEM at unprecedentednano-scale magnification (e.g. Lee et al., 2003; Garvie and Buseck, 2004; Bleiner et al., 2006). Electrons are fired at the sample and interact with the material when passing through. These interactions are dictated by material properties, such as density, resulting in a high-resolution density map of the sample, similar to a BSE image. This is commonly used in association with EDS to obtain elemental distribution and identify density and compositional relationships.

Given the size of TEM slice, this is commonly the final stage of looking for small particles in a sample as identification of an area of interest is required using one of the broad-scale aforementioned techniques. It is beneficial for examining very small nuggets or particles, and is therefore used as the final step in the study described in Chapter 5.

3. CHAPTER SUMMARIES

CHAPTER 2: HIDDEN SECRETS OF DEFORMATION- IMPACT-INDUCED COMPACTION WITHIN A CV CHONDRITE

This paper was published in the journal of Earth and Planetary Sciences on 15th October 2016. Here, the initial use of EBSD techniques to explore microstructural features within the CV meteorite Allende is detailed. This chapter highlights microstructural deformation features resulting from planetary compaction via impact in the early solar system, by examining the primitive and relatively unaltered meteorite. Both chondrules and matrix regions were examined, and results were compared against predictions of impact-induced compaction numerical simulations, to confirm deformation features closely correlated with the anticipated heat and pressure distributions.

CHAPTER 3: DEFINING THE MECHANISM FOR COMPACTION OF THE CV PARENT BODY

This paper has been submitted to Geology and at the time of thesis submission was in press. Building upon the work of Chapter 2, textural and microstructural features at the micro and meso scales are investigated in the same meteorite, Allende, to look for evidence of the larger-scale features potentially resulting from impact-induced compaction. One of the largest EBSD datasets to have ever been collected is shown and analysed to understand how this meteorite responded

texturally to early compaction. Similar microstructural analyses of the chondrule grains as in Chapter 2 were performed to provide additional directionality to the compression orientation of the sample; textural and microstructural observations are consistent with one another, and we therefore conclude they were generated during the same compressional process. Other compaction processes such as gravitational compaction and hot isostatic pressing are considered, however it is most viable for impact-induced compaction to produce the textures observed within the context of this sample.

CHAPTER 4: A MORPHOLOGIC & CRYSTALLOGRAPHIC COMPARISON OF CV CHONDRITE MATRICES

This paper has been prepared for publication in Meteoritics & Planetary Science and at the time of submission was in preparation. The olivine matrices of three CV chondrites, Allende, Kaba and Vigarano, are examined to determine the signature matrix grain of each meteorite, in terms of morphology and crystallography. Grain size and shape data were obtained from multiple EBSD datasets containing ~10,000 grains for each sample, and the average grain diameter (circle equivalent), aspect ratio and area were calculated. The matrices are also defined in terms of their textural properties; crystallographic preferred orientations (CPOs) and shape preferred orientations (SPOs) signify how strongly coupled the grain shape and any present microfabrics are, and also indicate how much each sample has been affected by compaction to produce the CPO. Each meteorite is commonly referred to based upon the geochemical composition of the olivine grains, and so the morphologic and crystallographic data are complimentary to the well-established geochemical analysis. The three CV chondrites studied in this section are all primitive and are believed to have originated from the same parent body; CPOs and grain morphology may therefore be used to constrain conditions on the target body during early compaction-related impacts, based on distance from the impacted surface, and understand how this relates to the variance in alteration between the CV chondrite samples.

CHAPTER 5: RELICTS OF AN IMPACTOR: SEARCHING FOR THE IRIDIUM CARRIER WITHIN THE DISTAL K-PG BOUNDARY CLAYS

This paper has been prepared for submission to Geochimica et Cosmochimica Acta and at the time of submission was in preparation. This manuscript examines impacts in a terrestrial setting, focussing on one of the most catastrophic impacts in the Earth's history- the K-Pg boundary extinction impact event- which occurred ~65 Ma ago. Dispersion of the projectile material created an enrichment in platinum group elements, most notably iridium, in boundary clays worldwide that has been detected through bulk geochemical analysis. In this chapter, we examine 5 boundary clay samples from

various distal ejecta sites around Europe and New Zealand to identify the specific carrier phase of iridium within the clays, which has not been successfully achieved in prior work. The nature of the iridium and what elements it is associated with has implications for interactions within the impact cloud and with the Earth's atmosphere, and may be used to better constrain current numerical simulations of impact ejecta transport.

4. SUMMARY

The aims of this thesis involve examining the effects of impact into different types of target materials, which represents the evolution of impacts over time within our solar system, and could be extended to other, solar systems of similar make-up. Each study involves the use of numerous analytical techniques to arrive at well-informed conclusions to the research questions asked. What kind of microstructures are present in primitive meteorites that pertain to compactional impacts between highly porous bodies? What textural response can be observed within those meteorites? How do such structures and textures evolve between samples from the same parent body? Impacts into early porous bodies leave evidence that few have found within meteorites; Chapters 2, 3 & 4 explore such evidence thoroughly, and assess the similarities between numerical modelling predictions of the compaction process with the physical microstructural and textural features observed. As the solar system evolved, impacts continued to affect a lot of the lithified planetary bodies, such as asteroids, moons, and planets. Finally, impacts into highly evolved and lithified planets, like the Earth, can produce similar remnants as on the well-studied lunar surface. However, the processing such remnants undergo, specifically on Earth, offer an insight into the planetary conditions at the time of impact; the target lithology, porosity, atmospheric temperature and composition may all be inferred from different kinds of impact ejecta. Chapter 5 consequently considers: what is the host phase of the abundant iridium in the distal K-Pg boundary clays, and what can therefore be inferred regarding the ejecta plume, projectile material transport and atmospheric conditions at the time?

5. REFERENCES

Abramov, O., and Kring, D.A., 2007, Numerical modeling of impact-induced hydrothermal activity at the Chicxulub crater: Meteoritics & Planetary Science, v. 42, no. 1, p. 93–112.

Agee, C.B., Li, J., Shannon, M.C., and Circone, S., 1995, Pressure-temperature phase diagram for the Allende meteorite: Journal of Geophysical Research: Solid Earth, v. 100, no. B9, p. 725–740.

Alvarez, F., Alvarez, W., Asaro, H.V., and Michel, L.W., 1980, Extraterrestrial cause for the Cretaceous-Tertiary extinction: Science, v. 208, no. 4448, p. 1095–1108.

Alvarez, W., Asaro, H.V., and Montanari, A., 1990, Iridium profile for 10 million years across the Cretaceous-Tertiary boundary at Gubbio (Italy): Science, v. 250, no. 4988, p. 1700–1702.

Amelin, Y., Krot, A.N., Hutcheon, I.D., and Ulyanov, A.A., 2002, Lead Isotopic Ages of Chondrules and Calcium-Aluminum-Rich Inclusions: Science, v. 297, no. 5587, p. 1678–1683.

Ames, D.E., Watkinson, D.H., and Parrish, R.R., 1998, Dating of a regional hydrothermal system induced by the 1850 Ma Sudbury impact event: Geology, v. 26, no. 5, p. 447–450.

Anders, E., and Grevesse, N., 1989, Abundances of the elements: Meteoritic and solar: Geochimica et Cosmochimica Acta, v. 53, p. 197–214.

Arenillas, I., Arz, J.A., Grajales-Nishimura, J.M., Murillo-Muñetón, G., Alvarez, W., Camargo-Zanoguera, A., Molina, E., and Rosales-Domínguez, C., 2006, Chicxulub impact event is Cretaceous/Paleogene boundary in age: New micropaleontological evidence: Earth and Planetary Science Letters, v. 249, no. 3-4, p. 241–257.

Arrowsmith, P., 1987, Laser ablation of solids for elemental analysis by inductively coupled plasma mass spectrometry: Analytical Chemistry, v. 59, p. 1437–1444.

Artemieva, N., and Morgan, J., 2007, Distal Ejecta from the Chicxulub-Numerical Model: Lunar and Planetary Science Conference, v. 38, no. 1338, p. 1543.

Artemieva, N., and Morgan, J., 2011, Global Ejecta from Chicxulub: Spherules, Shocked Quartz and More: Lunar and Planetary Science Conference, v. 42, p. 1180–1181.

Artemieva, N., and Morgan, J., 2009, Modeling the formation of the K--Pg boundary layer: Icarus, v. 201, no. 2, p. 768–780.

Artemieva, N.A., and Shuvalov, V.V., 2008, Numerical simulation of high-velocity impact ejecta following falls of comets and asteroids onto the Moon: Solar System Research, v. 42, no. 4, p. 351–356.

Ashby, M.F., and Verrall, R.A., 1977, Deformation Maps for Olivine: American Geophysical Union, v. 58, no. 6, p. 512–512.

Asphaug, E., Agnor, C.B., and Williams, Q., 2006, Hit-and-run planetary collisions: Nature, v. 439, no. 7073, p. 155–160.

Beitz, E., Güttler, C., Nakamura, A.M., Tsuchiyama, A., and Blum, J., 2013, Experiments on the consolidation of chondrites and the formation of dense rims around chondrules: Icarus, v. 225, no. 1, p. 558–569.

Bischoff, A., and Stöffler, D., 1992, Shock metamorphism as a fundamental process in the evolution of planetary bodies: information from meteorites: European Journal of Mineralogy, v. 4, no. 4, p. 707–755.

Bland, P.A., Collins, G.S., Davison, T.M., Abreu, N.M., Ciesla, F.J., Muxworthy, A.R., and Moore, J., 2014, Pressure–temperature evolution of primordial solar system solids during impact-induced compaction: Nature Communications, v. 5, p. 5451.

Bland, P.A., Howard, L.E., Prior, D.J., Wheeler, J., Hough, R.M., and Dyl, K.A., 2011, Earliest rock fabric formed in the Solar System preserved in a chondrule rim: Nature Geoscience, v. 4,

no. 4, p. 244–247.

Bleiner, D., Macrì, M., Gasser, P., Sautter, V., and Maras, A., 2006, FIB, TEM and LA–ICPMS investigations on melt inclusions in Martian meteorites—Analytical capabilities and geochemical insights: Talanta, v. 68, no. 5, p. 1623–1631.

Blum, J., 2004, Grain growth and coagulation: ASP Conference Series, v. 309, p. 369–391.

Bonal, L., Quirico, E., Bourot-Denise, M., and Montagnac, G., 2006, Determination of the petrologic type of CV3 chondrites by Raman spectroscopy of included organic matter: Geochimica et Cosmochimica Acta, v. 70, no. 7, p. 1849–1863.

Brearley, A.J., and Jones, R.H., 1998, Chondritic meteorites: Reviews in Mineralogy and Geochemistry, v. 36, no. 1, p. 3.1–3.198.

Brenker, F.E., Palme, H., and Klerner, S., 2000, Evidence for solar nebula signatures in the matrix of the Allende meteorite: Earth and Planetary Science Letters, v. 178, no. 3-4, p. 185–194.

Britt, D.T., Yeomans, D., Housen, K., and Consolmagno, G., 2002, Asteroid density, porosity, and structure, in Bottke, W.F., Jr, Cellino, A., Paolicchi, P., and Binzel, R.P.B. eds., University of Arizona Press, p. 485–500.

Carter, N.L., and Ave'Lallemant, H.G., 1970, High Temperature Flow of Dunite and Peridotite: Geological Society of America Bulletin, v. 81, no. 8, p. 2181–2202.

Chambers, J.E., 2013, Late-stage planetary accretion including hit-and-run collisions and fragmentation: Icarus, v. 224, no. 1, p. 43–56.

Chambers, J.E., 2004, Planetary accretion in the inner Solar System: Earth and Planetary Science Letters, v. 223, no. 3-4, p. 241–252.

Cheng, A.F., and Barnouin-Jha, O.S., 1999, Giant Craters on Mathilde: Icarus, v. 140, no. 1, p. 34–48.

Chyba, C.F., 1990, Impact Delivery and Erosion of Planetary Oceans in the Early Inner Solar-System: Nature, v. 343, no. 6254, p. 129–133.

Cintala, M.J., 1992, Impact-induced thermal effects in the lunar and Mercurian regoliths: Journal of Geophysical Research: Solid Earth, v. 97, no. E1, p. 947–973.

Clayton, R.N., and Mayeda, T.K., 1983, Oxygen isotopes in eucrites, shergottites, nakhlites, and chassignites: Earth and Planetary Science Letters, v. 62, no. 1, p. 1–6.

Cody, G.D., Alexander, C.M.O., Yabuta, H., Kilcoyne, A.L.D., Araki, T., Ade, H., Dera, P., Fogel, M., Militzer, B., and Mysen, B.O., 2008, Organic thermometry for chondritic parent bodies: Earth and Planetary Science Letters, v. 272, no. 1-2, p. 446–455.

Collins, G.S., Melosh, H.J., and Osinski, G.R., 2012, The Impact-Cratering Process: v. 8, no. 1, p. 25–30.

Collins, G.S., Wünnemann, K., Artemieva, N., and Pierazzo, E., 2013, Numerical Modelling of Impact Processes, in Osinski, G.R. and Pierazzo, E. eds., The Contact and Compression Stage of Impact Cratering, Blackwell Publishing Ltd., Chichester, UK, p. 254–270.

Consolmagno, G.J., Britt, D.T., and Macke, R.J., 2008, The significance of meteorite density and porosity: Chemie der Erde-Geochemistry, v. 68, no. 1, p. 1–29.

Consolmagno, G.J., Britt, D.T., and Stoll, C.P., 1998, The porosities of ordinary chondrites: Models and interpretation: Meteoritics & Planetary Science, v. 33, no. 6, p. 1221–1229.

Cuzzi, J.N., and Weidenschilling, S.J., 2006, Particle-gas dynamics and primary accretion, in McSween, H.Y. and Lauretta, D.S. eds., Meteorites and the Early Solar System II, University of Arizona Press, University of Arizona, Tuscon, p. 353–381.

Cuzzi, J.N., Ciesla, F.J., Petaev, M.I., and Krot, A.N., 2005, Nebula evolution of thermally processed

solids: Reconciling models and meteorites: Chondrites and the Protoplanetary Disk, v. 341, p. 732–773.

Davison, T.M., Ciesla, F.J., and Collins, G.S., 2012, Post-impact thermal evolution of porous planetesimals: Geochimica et Cosmochimica Acta, v. 95, p. 252–269.

Davison, T.M., Collins, G.S., and Bland, P.A., 2016, Mesoscale modeling of impact compaction of primitive solar system solids: The Astrophysical Journal, v. 821, no. 1, p. 68.

Davison, T.M., Collins, G.S., and Bland, P.A., 2014, Mesoscale Numerical Modeling of Compaction of Primitive Solar System Solids in Low-Velocity Collisions: Lunar and Planetary Science Conference, v. 45, p. 2718.

Davison, T.M., Collins, G.S., and Ciesla, F.J., 2010, Numerical modelling of heating in porous planetesimal collisions: Icarus, v. 208, no. 1, p. 468–481.

Davison, T.M., O'Brien, D.P., Ciesla, F.J., and Collins, G.S., 2013, The early impact histories of meteorite parent bodies: Meteoritics & Planetary Science, v. 48, no. 10, p. 1894–1918.

Dodd, R.T., and Jarosewich, E., 1979, Incipient Melting in and Shock Classification of L-Group Chondrites: Earth and Planetary Science Letters, v. 44, no. 2, p. 335–340.

Dodd, R.T., Grover, J.E., and Brown, G.E., 1975, Pyroxenes in the Shaw (L-7) chondrite: Geochimica et Cosmochimica Acta, v. 39, no. 12, p. 1585–1594.

Doyle, P.M., Jogo, K., Nagashima, K., Krot, A.N., Wakita, S., Ciesla, F.J., and Hutcheon, I.D., 2015, Early aqueous activity on the ordinary and carbonaceous chondrite parent bodies recorded by fayalite: Nature Communications, v. 6, p. 7444.

Dyl, K.A., Cleverley, J.S., Bland, P.A., Ryan, C.G., Fisher, L.A., and Hough, R.M., 2014, Quantified, whole section trace element mapping of carbonaceous chondrites by Synchrotron X-ray Fluorescence Microscopy: 1. CV meteorites: Geochimica et Cosmochimica Acta, v. 134, p. 100–119.

Ebel, D.S., and Grossman, L., 2005, Spinel-bearing spherules condensed from the Chicxulub impact-vapor plume: Geology, v. 33, no. 4, p. 293–296.

Elliot, D.H., Askin, R.A., Kyte, F.T., and Zinsmeister, W.J., 1994, Iridium and dinocysts at the Cretaceous-Tertiary boundary on Seymour Island, Antarctica: Implications for the K-T event: Geology, v. 22, no. 8, p. 675–678.

Endress, M., Zinner, E., and Bischoff, A., 1996, Early aqueous activity on primitive meteorite parent bodies: Nature, v. 379, no. 6567, p. 701–703.

Evans, N.J., Ahrens, T.J., McInnes, B., and Gregoire, D.C., 1994, New evidence for primary fractionation of ruthenium and iridium in the Chicxulub ejecta cloud: New Developments Regarding the KT Event and Other Catastrophes in Earth History, v. 825, p. 34–36.

Ferrière, L., and Osinski, G.R., 2013, Shock Metamorphism: John Wiley & Sons, Ltd, Chichester, UK.

Fisher, L.A., Fougerouse, D., Cleverley, J.S., Ryan, C.G., Micklethwaite, S., Halfpenny, A., Hough, R.M., Gee, M., Paterson, D., Howard, D.L., and Spiers, K., 2014, Quantified, multi-scale X-ray fluorescence element mapping using the Maia detector array: application to mineral deposit studies: Mineralium Deposita, v. 50, no. 6, p. 665–674.

Fitzgerald, R., Keil, K., and Heinrich, K.F.J., 1968, Solid-State Energy-Dispersion Spectrometer for Electron-Microprobe X-ray Analysis: Science, v. 159, no. 3814, p. 528–530.

Fliervoet, T.F., Drury, M.R., and Chopra, P.N., 1999, Crystallographic preferred orientations and misorientations in some olivine rocks deformed by diffusion or dislocation creep: Tectonophysics, v. 303, no. 1-4, p. 1–27.

Forman, L.V., Bland, P.A., Timms, N.E., Collins, G.S., Davison, T.M., Ciesla, F.J., Benedix, G.K., Daly, L., Trimby, P.W., Yang, L., and Ringer, S.P., 2016, Hidden secrets of deformation: Impact-induced compaction within a CV chondrite: Earth and Planetary Science Letters, v. 452, p. 133–145.

Franchi, I.A., Wright, I.P., Sexton, A.S., and Pillinger, C.T., 1999, The oxygen-isotopic composition of Earth and Mars: Meteoritics & Planetary Science, v. 34, no. 4, p. 657–661.

Fujimura, A., Kato, M., and Kumazawa, M., 1983, Preferred orientation of phyllosilicate [001] in matrix of Murchison meteorite and possible mechanisms of generating the oriented texture in chondrites: Earth and Planetary Science Letters, v. 66, p. 25–32.

Gail, H.-P., Henke, S., and Trieloff, M., 2015, Thermal evolution and sintering of chondritic planetesimals - II. Improved treatment of the compaction process: Astronomy & Astrophysics, v. 576, p. A60.

Ganapathy, R., Gartner, S., and Jiang, M., 1981, Iridium anomaly at the Cretaceous-Tertiary boundary in Texas: Earth and Planetary Science Letters, v. 54, no. 3, p. 393–396.

Garvie, L.A.J., and Buseck, P.R., 2004, Nanosized carbon-rich grains in carbonaceous chondrite meteorites: Earth and Planetary Science Letters, v. 224, no. 3-4, p. 431–439.

Gillet, P., and Goresy, El, A., 2013, Shock Events in the Solar System: The Message from Minerals in Terrestrial Planets and Asteroids: Annual Review of Earth and Planetary Sciences, v. 41, no. 1, p. 257–285.

Glikson, A., and Allen, C., 2004, Iridium anomalies and fractionated siderophile element patterns in impact ejecta, Brockman Iron Formation, Hamersley Basin, Western Australia: evidence for a major asteroid impact in simatic crustal regions of the early Proterozoic earth: Earth and Planetary Science Letters, v. 220, no. 3-4, p. 247–264.

Goderis, S., Paquay, F., and Claeys, P., 2012, Projectile Identification in Terrestrial Impact Structures and Ejecta Material, in Osinski, G.R. and Pierazzo, E. eds., The Contact and Compression Stage of Impact Cratering, Processes and Products, Blackwell Publishing Ltd., Chichester, UK, p. 223–239.

Goderis, S., Tagle, R., Belza, J., Smit, J., Montanari, A., Vanhaecke, F., Erzinger, J., and Claeys, P., 2013, Reevaluation of siderophile element abundances and ratios across the Cretaceous–Paleogene (K–Pg) boundary: Implications for the nature of the projectile: Geochimica et Cosmochimica Acta, v. 120, p. 417–446.

Goetze, C., and Poirier, J.P., 1978, The Mechanisms of Creep in Olivine [and Discussion]: Philosophical Transactions of the Royal Society of London A: Mathematical, Physical and Engineering Sciences, v. 288, no. 1350, p. 99–119.

Goldin, T.J., and Melosh, H.J., 2007, Interactions Between Chicxulub Ejecta and the Atmosphere: The Deposition of the K/T Double Layer: Lunar and Planetary Institute Science Conference Abstracts, v. 38, p. 2114–2115.

Goldstein, J., Newbury, D.E., and Williams, D.B., 2012a, X-Ray Spectrometry in Electron Beam Instruments: Springer Science & Business Media.

Goldstein, J., Newbury, D.E., Joy, D.C., Lyman, C.E., Echlin, P., Lifshin, E., Sawyer, L., and Michael, J.R., 2012b, Scanning Electron Microscopy and X-ray Microanalysis: Springer Science & Business Media.

Göpel, C., Manhès, G., and Allègre, C.J., 1994, U-Pb systematics of phosphates from equilibrated ordinary chondrites: Earth and Planetary Science Letters, v. 121, no. 1-2, p. 153–171.

Gradstein, F.M., Ogg, J.G., and Smith, A.G., 2004, A geologic time scale: Newsletters on

Stratigraphy, v. 45, no. 2, p. 171–188.

Grieve, R., Rupert, J., Smith, J., and Therriault, A., 1995, The record of terrestrial impact cratering: GSA Today, v. 5, no. 10, p. 189.

Grieve, R.A.F., and Pesonen, L.J., 1992, The terrestrial impact cratering record: Tectonophysics, v. 216, no. 1-2, p. 1–30.

Groeber, M.A., Rowenhorst, D.J., and Uchic, M.D., 2009, Collection, Processing, and Analysis of Three-Dimensional EBSD Data Sets, in Schwartz, A.J., Kumar, M., Adams, B.L., and Field, D.P. eds., Electron Backscatter Diffraction in Materials Science, Springer Science & Business Media, Boston, MA, p. 123–137.

Grossman, L., and Larimer, J.W., 1974, Early chemical history of the solar system: Reviews of Geophysics, v. 12, no. 1, p. 71–101.

Guimon, R.K., Symes, S.J.K., Sears, D.W.G., and Benoit, P.H., 1995, Chemical and physical studies of type 3 chondrites XII: The metamorphic history of CV chondrites and their components: Meteoritics & Planetary Science, v. 30, no. 6, p. 704–714.

Gulick, S.P.S., Christeson, G.L., Barton, P.J., Grieve, R.A.F., Morgan, J.V., and Urrutia Fucugauchi, J., 2013, Geophysical Characterisation of the Chicxulub Impact Crater: Reviews of Geophysics, v. 51, no. 1, p. 31–52.

Hanna, R.D., Ketcham, R.A., Zolensky, M., and Behr, W.M., 2015, Impact-induced brittle deformation, porosity loss, and aqueous alteration in the Murchison CM chondrite: Geochimica et Cosmochimica Acta, v. 171, p. 256–282.

Henke, S., Gail, H.P., Trieloff, M., Schwarz, W.H., and Kleine, T., 2012, Thermal evolution and sintering of chondritic planetesimals: Astronomy & Astrophysics, v. 537, p. A45.

Hewins, R.H., 1997, Chondrules: Annual Review of Earth and Planetary Sciences, v. 25, no. 1, p. 61–83.

Hildebrand, A.R., and Stansberry, J.A., 1992, K/T boundary ejecta distribution predicts size and location of Chicxulub crater: Lunar and Planetary Science Conference, v. 23, p. 537.

Hildebrand, A.R., Penfield, G.T., Kring, D.A., Pilkington, M., Camargo Z, A., Jacobsen, S.B., and Boynton, W.V., 1991, Chicxulub Crater: A possible Cretaceous/Tertiary boundary impact crater on the Yucatán Peninsula, Mexico: Geology, v. 19, no. 9, p. 867–871.

Housen, K.R., and Holsapple, K.A., 2011, Ejecta from impact craters: Icarus, v. 211, no. 1, p. 856–875,.

Housen, K.R., and Holsapple, K.A., 2003, Impact cratering on porous asteroids: Icarus, v. 163, no. 1, p. 102–119.

Housen, K.R., Holsapple, K.A., and Voss, M.E., 1999, Compaction as the origin of the unusual craters on the asteroid Mathilde: Nature, v. 402, no. 6758, p. 155–157.

Humphreys, F.J., 2004, Characterisation of fine-scale microstructures by electron backscatter diffraction (EBSD): Scripta materialia, v. 51, no. 8, p. 771–776.

Huss, G.R., Rubin, A.E., and Grossman, J.N., 2006, Thermal metamorphism in chondrites, in McSween, H.Y. and Lauretta, D.S. eds., Meteorites and the Early Solar System II, University of Arizona, Tuscon, Arizona, p. 567–586.

Hutchison, R., 2004, Meteorites: Cambridge University Press, Cambridge.

Jarvis, K.E., and Williams, J.G., 1993, Laser ablation inductively coupled plasma mass spectrometry (LA-ICP-MS): a rapid technique for the direct, quantitative determination of major, trace and rare-earth elements in geological samples: Chemical Geology, v. 106, no. 3-4, p. 251–262.

Kallemeyn, G.W., and Wasson, J.T., 1981, The compositional classification of chondrites—I. The carbonaceous chondrite groups: Geochimica et Cosmochimica Acta, v. 45, no.

7, p. 1217–1230.

Karato, S.-I., Jung, H., Katayama, I., and Skemer, P., 2008, Geodynamic Significance of Seismic Anisotropy of the Upper Mantle: New Insights from Laboratory Studies: Annual Review of Earth and Planetary Sciences, v. 36, no. 1, p. 59–95.

Katayama, I., 2009, Thin anisotropic layer in the mantle wedge beneath northeast Japan: Geology, v. 37, no. 3, p. 211–214.

Keil, K., Haack, H., and Scott, E.R.D., 1994, Catastrophic fragmentation of asteroids: evidence from meteorites: Planetary and Space Science, v. 42, no. 12, p. 1109–1122.

Keil, K., Stöffler, D., Love, S.G., and Scott, E.R.D., 1997, Constraints on the role of impact heating and melting in asteroids: Meteoritics & Planetary Science, v. 32, no. 3, p. 349–363.

Keller, L.P., and Buseck, P.R., 1990, Aqueous alteration in the Kaba CV3 carbonaceous chondrite: Geochimica et Cosmochimica Acta, v. 54, no. 7, p. 2113–2120.

Kirsimäe, K., and Osinski, G.R., 2013, Impact-Induced Hydrothermal Activity, in The Contact and Compression Stage of Impact Cratering, Blackwell Publishing Ltd., Chichester, UK, p. 76–89.

Kring, D.A., 2002, Cataclysmic bombardment throughout the inner solar system 3.9–4.0 Ga: Journal of Geophysical Research, v. 107, no. E2, p. 4.1–4.6.

Krot, A.N., and Scott, E.R.D., 1995, Alteration of CV3 carbonaceous chondrites: Parent body vs. nebular processes: Lunar and Planetary Science Conference, v. 26, p. 803.

Krot, A.N., Petaev, M.I., Scott, E.R.D., Choi, B.G., Zolensky, M.E., and Keil, K., 1998, Progressive alteration in CV3 chondrites: More evidence for asteroidal alteration: Meteoritics & Planetary Science, v. 33, no. 5, p. 1065–1085.

Krot, A.N., Scott, E.R.D., and Zolensky, M.E., 1995, Mineralogical and chemical modification of components in CV3 chondrites: Nebular or asteroidal processing?: Meteoritics & Planetary Science, v. 30, no. 6, p. 748–775.

Krot, A.N., Yurimoto, H., Hutcheon, I.D., and MacPherson, G.J., 2005, Chronology of the early Solar System from chondrule-bearing calcium-aluminium-rich inclusions: Nature, v. 434, no. 7036, p. 998–1001.

Langenhorst, F., 2002, Shock metamorphism of some minerals: Basic introduction and microstructural observations: Bulletin of the Czech Geological Survey, v. 77, no. 4, p. 265–282.

Lee, M.R., Bland, P.A., and Graham, G., 2003, Preparation of TEM samples by focused ion beam (FIB) techniques: applications to the study of clays and phyllosilicates in meteorites: Mineralogical Magazine, v. 67, no. 3, p. 581–592.

Liu, Y., Hu, Z., Gao, S., Günther, D., Xu, J., Gao, C., and Chen, H., 2008, In situ analysis of major and trace elements of anhydrous minerals by LA-ICP-MS without applying an internal standard: Chemical Geology, v. 257, no. 1-2, p. 34–43.

Liu, Y., Hu, Z., Li, M., and Gao, S., 2013, Applications of LA-ICP-MS in the elemental analyses of geological samples: Chinese Science Bulletin, v. 58, no. 32, p. 3863–3878.

Lodders, K., 1997, An Oxygen Isotope Model for the Composition of Mars: Icarus, v. 126, no. 2, p. 373–394.

Lodders, K., 2003, Solar System Abundances and Condensation Temperatures of the Elements: The Astrophysical Journal, v. 591, no. 2, p. 1220–1247.

Lyman, C.E., Goldstein, J.I., Romig, A.D., Jr, Echlin, P., Joy, D.C., Newbury, D.E., Williams, D.B., Armstrong, J.T., Fiori, C.E., Lifshin, E., and Peters, K.-R., 1990, Backscattered Electron Imaging, in Scanning Electron Microscopy, X-Ray Microanalysis, and Analytical Electron

Microscopy, Springer US, New York, USA, p. 51–54.

Macdougall, J.D., Lugmair, G.W., and Kerridge, J.F., 1984, Early Solar System aqueous activity: Sr isotope evidence from the Orgueil CI meteorite: Nature, v. 307, no. 5948, p. 249–251.

Macke, R.J., Britt, D.T., and Consolmagno, G.J., 2011, Density, porosity, and magnetic susceptibility of achondritic meteorites: Meteoritics & Planetary Science, v. 46, no. 2, p. 311–326.

Marzo, G.A., Davila, A.F., Tornabene, L.L., Dohm, J.M., Fairén, A.G., Gross, C., Kneissl, T., Bishop, J.L., Roush, T.L., and McKay, C.P., 2010, Evidence for Hesperian impact-induced hydrothermalism on Mars: Icarus, v. 208, no. 2, p. 667–683.

Matsui, T., 1986, Evolution of an impact-induced atmosphere and magma ocean on the accreting Earth: Nature, v. 319, p. 303–305.

Matsui, T., and Abe, Y., 1986, Impact-induced atmospheres and oceans on Earth and Venus: Nature, v. 322, no. 6079, p. 526–528.

McSween, H.Y., and Patchen, A.D., 1989, Pyroxene thermobarometry in LL-group chondrites and implications for parent body metamorphism: Meteoritics & Planetary Science, v. 24, no. 4, p. 219–226.

McSween, H.Y., Sears, D., and Dodd, R., 1988, Thermal Metamorphism, in Kerridge, J.F. and Matthews, M.S. eds., Meteorites and the Early Solar System, Tucson, p. 102–113.

Melosh, H.J., 2012, The Contact and Compression Stage of Impact Cratering, in Osinski, G.R. and Pierazzo, E. eds., The Contact and Compression Stage of Impact Cratering, Blackwell Publishing Ltd., Chichester, UK, p. 32–42.

Metzler, K., Bobe, K.D., Palme, H., Spettel, B., and Stöffler, D., 1995, Thermal and impact metamorphism on the HED parent asteroid: Planetary and Space Science, v. 43, no. 3-4, p. 499–525.

Michel, P., and Morbidelli, A., 2013, Population of Impactors and the Impact Cratering Rate in the Inner Solar System, in Osinski, G.R. and Pierazzo, E. eds., The Contact and Compression Stage of Impact Cratering, John Wiley & Sons, Ltd, Chichester, UK, p. 21–31.

Morgan, J.V., 2008, Comment on "Determining Chondritic Impactor Size from the Marine Osmium Isotope Record": Science, v. 321, no. 5893, p. 1158a.

Morgan, W., Ganapathy, R., Higuchi, H., and Anders, E., 1974, Lunar basins: characterization of projectiles, from meteorite trace elements in highland samples.: Moon, v. 11, p. 424–425.

Naumov, M.V., 2002, Impact-Generated Hydrothermal Systems: Data from Popigai, Kara, and Puchezh-Katunki Impact Structures, in Plado, J. and Pesonen, L.J. eds., Impacts in Precambrian Shields, Impact Studies, Springer Berlin Heidelberg, Berlin, Heidelberg, p. 117–171.

Newbury, D.E., 2002, Energy-Dispersive Spectrometry: John Wiley & Sons, Inc., Hoboken, NJ, USA.

Nicolas, A., and Poirier, J.P., 1976, Crystalline Plasticity and Solid State Flow in Metamorphic Rocks: John Wiley & Sons, London & New York.

Nicolas, A., Boudier, F., and Boullier, A.M., 1973, Mechanisms of flow in naturally and experimentally deformed peridotites: American Journal of Science, v. 273, p. 853–876.

Noronha, B.A., and Friedrich, J.M., 2014, Chemical compositions and classification of five thermally altered carbonaceous chondrites: Meteoritics & Planetary Science, v. 49, no. 8, p. 1494–1504.

O'Keefe, J.D., and Ahrens, T.J., 1977, Impact-induced energy partitioning, melting, and vaporization on terrestrial planets: Lunar and Planetary Science Conference, v. 8, p. 3357–3374.

O'Neill, C., Marchi, S., Zhang, S., and Bottke, B.,

2016, Impact-driven tectonism in the Hadean: Lunar and Planetary Science Conference, v. 47, p. 2733.

Ormel, C.W., Cuzzi, J.N., and Tielens, A.G.G.M., 2008, Co-Accretion of Chondrules and Dust in the Solar Nebula: The Astrophysical Journal, v. 679, no. 2, p. 1588–1610.

Osawa, T., Hatsukawa, Y., Keisuke, N., Koizumi, M., Oshima, M., Toh, Y., Kimura, A., and Furutaka, K., 2009, Iridium concentration and noble gas composition of Cretaceous-Tertiary boundary clay from Stevns Klint, Denmark: Geochemical Journal, v. 43, no. 6, p. 415–422.

Osinski, G.R., and Pierazzo, E., 2012, Impact Cratering Processes and Products: John Wiley & Sons.

Osinski, G.R., Lee, P., Parnell, J., Spray, J.G., and Baron, M., 2005, A case study of impact-induced hydrothermal activity: The Haughton impact structure, Devon Island, Canadian High Arctic: Meteoritics & Planetary Science, v. 40, no. 12, p. 1859–1877.

Osinski, G.R., Tornabene, L.L., Banerjee, N.R., Cockell, C.S., Flemming, R., Izawa, M.R.M., McCutcheon, J., Parnell, J., Preston, L.J., Pickersgill, A.E., Pontefract, A., Sapers, H.M., and Southam, G., 2013, Impact-generated hydrothermal systems on Earth and Mars: Icarus, v. 224, no. 2, p. 347–363.

Papike, J.J., 1998, Comparative planetary mineralogy; chemistry of melt-derived pyroxene, feldspar, and olivine: Reviews in Mineralogy and Geochemistry, v. 36, p. 7.1–7.11.

Perkins, W.T., Pearce, N.J.G., and Jeffries, T.E., 1993, Laser ablation inductively coupled plasma mass spectrometry: A new technique for the determination of trace and ultra-trace elements in silicates: Geochimica et Cosmochimica Acta, v. 57, no. 2, p. 475–482.

Pierazzo, E., and Artemieva, N., 2012, Local and Global Environmental Effects of Impacts on Earth: v. 8, no. 1, p. 55–60.

Pierazzo, E., and Melosh, H.J., 2000, Hydrocode modeling of oblique impacts: The fate of the projectile: Meteoritics & Planetary Science, v. 35, no. 1, p. 117–130.

Pierazzo, E., Kring, D.A., and Melosh, H.J., 1998, Hydrocode simulation of the Chicxulub impact event and the production of climatically active gases: Journal of Geophysical Research: Solid Earth, v. 103, no. E12, p. 607–625.

Pirajno, F., 2009, Hydrothermal Processes Associated with Meteorite Impacts, in Hydrothermal Processes and Mineral Systems, Springer Netherlands, Dordrecht, p. 1097–1130.

Podosek, F.A., and Swindle, T.D., 1988, Extinct radionuclides, in Kerridge, J.F. and Matthews, M.S. eds., Meteorites and the Early Solar System, University of Arizona Press, Tuscon, Arizona, p. 1093–1113.

Pope, K.O., Ocampo, A.C., and Duller, C.E., 1991, Mexican site for K/T impact crater?: Nature, v. 351, no. 6322, p. 105.

Prior, D.J., Trimby, P.W., Weber, U.D., and Dingley, D.J., 1996, Orientation contrast imaging of microstructures in rocks using forescatter detectors in the scanning electron microscope: Mineralogical Magazine, v. 60, no. 403, p. 859–869.

Quitte, G., Robin, E., Levasseur, S., Capmas, F., Rocchia, R., Birck, J.-L., and AlleGre, C.J., 2007, Osmium, tungsten, and chromium isotopes in sediments and in Ni-rich spinel at the K-T boundary: Signature of a chondritic impactor: Meteoritics & Planetary Science, v. 42, no. 9, p. 1567–1580.

Renne, P.R., Deino, A.L., Hilgen, F.J., Kuiper, K.F., Mark, D.F., Mitchell, W.S.I., Morgan, L.E., Mundil, R., and Smit, J., 2013, Time Scales of Critical Events Around the Cretaceous-Paleogene Boundary: Science, v. 339, no. 6120, p. 684–687.

Richardson, J., Melosh, H., Greenberg, R., and O'Brien, D., 2005, The global effects of impact-induced seismic activity on fractured asteroid

surface morphology: Icarus, v. 179, no. 2, p. 325–349.

Rubin, A.E., 1997, Mineralogy of meteorite groups: Meteoritics & Planetary Science, v. 32, no. 2, p. 231–247.

Rubin, A.E., Trigo-Rodríguez, J.M., Huber, H., and Wasson, J.T., 2007, Progressive aqueous alteration of CM carbonaceous chondrites: Geochimica et Cosmochimica Acta, v. 71, no. 9, p. 2361–2382.

Russell, S.S., Hartmann, L., Cuzzi, J., and Krot, A.N., 2006, Timescales of the solar protoplanetary disk, in Lauretta, D.S. and McSween, H.Y. eds., Meteorites and the Early Solar System II, University of Arizona Press, p. 233–251.

Ryan, C.G., Siddons, D.P., Kirkham, R., and Dunn, P.A., 2010, The new Maia detector system: methods for high definition trace element imaging of natural material: AIP Conference Proceedings, v. 1221, no. 9, p. 10–17.

Ryder, G., 1990, Lunar samples, lunar accretion and the early bombardment of the Moon: Eos, Transactions American Geophysical Union, v. 71, no. 10, p. 313–323.

Schmitz, B., Andersson, P., and Dahl, J., 1988, Iridium, sulfur isotopes and rare earth elements in the Cretaceous-Tertiary boundary clay at Stevns Klint, Denmark: Geochimica et Cosmochimica Acta, v. 52, no. 1, p. 229–236.

Schulte P., Alegret L., Arenillas I., Arz J. A., Barton P. J., Bown P. R., Bralower T. J., Christeson G. L., Claeys P., Cockell C. S., Collins G. S., Deutsch A., Goldin T. J., Goto K., Grajales-Nishimura J. M., Grieve R. A. F., Gulick S. P. S., Johnson K. R., Kiessling W., Koeberl C., Kring D. A., MacLeod K. G., Matsui T., Melosh J., Montanari A., Morgan J. V., Neal C. R., Nichols D. J., Norris R. D., Pierazzo E., Ravizza G., Rebolledo Vieyra M., Reimold W. U., Robin E., Salge T., Speijer R. P., Sweet A. R., Urrutia-Fucugauchi J., Vajda V., Whalen M. T. and Willumsen P. S., 2010, The Chicxulub Asteroid Impact and Mass Extinction at the Cretaceous-Paleogene Boundary: Science, v. 327, no. 5970, p. 1214–1218.

Schwenn, M.B., and Goetze, C., 1978, Creep of olivine during hot-pressing: Tectonophysics, v. 48, no. 1-2, p. 41–60.

Schwenzer, S.P., and Kring, D.A., 2009, Impact-generated hydrothermal systems capable of forming phyllosilicates on Noachian Mars: Geology, v. 37, no. 12, p. 1091–1094.

Scott, E.R.D., 2002, Meteorite evidence for the accretion and collisional evolution of asteroids: Asteroids, v. 3, p. 697–709.

Scott, E.R.D., and Krot, A.N., 2003, Chondrites and their Components: Treatise on geochemistry, v. 1, p. 7.01–7.72.

Scott, E.R.D., Barber, D.J., Alexander, C.M., Hutchinson, R., and Peck, J.A., 1988, Primitive material surviving in chondrites - Matrix, in Sears, D. and Dodd, R.T. eds., Meteorites and the Early Solar System, University of Arizona Press, Tuscon, Arizona, p. 718–745.

Scott, E.R.D., Keil, K., and Stöffler, D., 1992, Shock Metamorphism of Carbonaceous Chondrites: Geochimica et Cosmochimica Acta, v. 56, no. 12, p. 4281–4293.

Scott, E.R.D., Taylor, G.J., Newsom, H.E., Herbert, F., and Zolensky, M., 1989, Chemical, thermal and impact processing of asteroids, in Binzel, R.P.B., Gehrels, T., and Matthews, M.S. eds., Asteroids II, Asteroids II, Tuscon, Arizona, p. 701–739.

Sears, D., and Dodd, R.T., 1988, Overview and Classification of Meteorites, in Kerridge, J.F. and Matthews, M.S. eds., Meteorites and the Early Solar System, University of Arizona Press, Tuscon, Arizona, p. 3–31.

Shoemaker, E.M., 1972, Cratering history and early evolution of the moon: Lunar and Planetary Science Conference Proceedings, v. 3, p. 696–698.

Shukolyukov, A., and Lugmair, G.W., 1998a,

Chromium in the Cretaceous-Tertiary boundary layer: first isotopic evidence for an impactor and its type: Meteoritics and Planetary Science, v. 33, no. 4, p. A144.

Shukolyukov, A., and Lugmair, G.W., 1998b, Isotopic Evidence for the Cretaceous-Tertiary Impactor and Its Type: Science, v. 282, no. 5390, p. 927–930.

Smit, J., 1999, The global stratigraphy of the Cretaceous-Tertiary boundary impact ejecta: Annual Review of Earth and Planetary Sciences, v. 27, no. 1, p. 75–113.

Smit, J., and Hertogen, J., 1980, An extraterrestrial event at the Cretaceous-Tertiary boundary: Nature, v. 285, no. 5762.

Spicuzza, M.J., Day, J.M.D., Taylor, L.A., and Valley, J.W., 2007, Oxygen isotope constraints on the origin and differentiation of the Moon: Earth and Planetary Science Letters, v. 253, no. 1-2, p. 254–265.

Stöffler, D., Bischoff, A., Buchwald, V., and Rubin, A.E., 1988, Shock effects in meteorites, in Kerridge, J.F. and Matthews, M.S. eds., Meteorites and the Early Solar System, University of Arizona Press, p. 165–202.

Stöffler, D., Keil, K., and Scott, E.R.D., 1991, Shock Metamorphism of Ordinary Chondrites: Geochimica et Cosmochimica Acta, v. 55, no. 12, p. 3845–3867.

Strom, R.G., Malhotra, R., Ito, T., Yoshida, F., and Kring, D.A., 2005, The origin of planetary impactors in the inner solar system: Science, v. 309, p. 1847–1850.

Swindle, T.D., Caffee, M.W., Hohenberg, C.M., Lindstrom, M.M., and Taylor, G.J., 1991, Iodine-xenon studies of petrographically and chemically characterized Chainpur chondrules: Geochimica et Cosmochimica Acta, v. 55, no. 3, p. 861–880.

Tait, A.W., Tomkins, A.G., Godel, B.M., Wilson, S.A., and Hasalova, P., 2014, Investigation of the H7 ordinary chondrite, Watson 012: Implications for recognition and classification of Type 7 meteorites: Geochimica et Cosmochimica Acta, v. 134, p. 175–196.

Trimby, P., Day, A., Mehnert, K., and Schmidt, N.H., 2002, Is fast mapping good mapping? A review of the benefits of high-speed orientation mapping using electron backscatter diffraction: Journal of Microscopy, v. 205, no. 3, p. 259–269.

Trimby, P.W., 2012, Orientation mapping of nanostructured materials using transmission Kikuchi diffraction in the scanning electron microscope: Ultramicroscopy, v. 120, p. 16–24.

Trimby, P.W., and Prior, D.J., 1999, Microstructural imaging techniques: a comparison between light and scanning electron microscopy: Tectonophysics, v. 303, no. 1-4, p. 71–81.

Trimby, P.W., Cao, Y., Chen, Z., Han, S., Hemker, K.J., Lian, J., Liao, X., Rottmann, P., Samudrala, S., Sun, J., Wang, J.T., Wheeler, J., and Cairney, J.M., 2014, Characterizing deformed ultrafine-grained and nanocrystalline materials using transmission Kikuchi diffraction in a scanning electron microscope: Acta Materialia, v. 62, p. 69–80.

Turner, G., 1988, Dating of secondary events, in Kerridge, J.F. and Matthews, M.S. eds., Meteorites and the Early Solar System, University of Arizona Press, Tuscon, Arizona, p. 276–288.

Twiss, R.J., and Moores, E.M., 2006, Structural Geology: W. H. Freeman.

Van Schmus, W.R., and Wood, J.A., 1967, A chemical-petrologic classification for the chondritic meteorites: Geochimica et Cosmochimica Acta, v. 31, no. 5, p. 747–765.

Warner M., Morgan J., the Chicxulub Working Group, Brittan J., Buffler R., Camargo A., Christeson G., Denton P., Hildebrand A., Hobbs R., Macintyre H., Mackenzie G., Maguire P., Marin L., Nakamura Y., Pilkington M., Sharpton V., Snyder D., Suarez G. and Trejo A., 1997, Size

and morphology of the Chicxulub impact crater: Nature, v. 390, no. 6659, p. 472–476.

Wasson, J.T., and Kallemeyn, G.W., 1988, Compositions of chondrites: Philosophical Transactions of the Royal Society of London, v. 325, no. 325, p. 535–544.

Wasson, J.T., Boynton, W.V., Chou, C.-L., and Baedecker, P.A., 1975, Compositional evidence regarding the influx of interplanetary materials onto the lunar surface: The Moon, v. 13, no. 1-3, p. 121–141.

Weidenschilling, S.J., 2011, Initial sizes of planetesimals and accretion of the asteroids: Icarus, v. 214, no. 2, p. 671–684.

Weidenschilling, S.J., and Cuzzi, J.N., 2006, Accretion dynamics and timescales: Relation to chondrites, in Lauretta, D.S. and McSween, H.Y. eds., Meteorites and the Early Solar System II, University of Arizona, Tuscon, Arizona, p. 473–485.

Weinbruch, S., Armstrong, J., and Palme, H., 1994, Constraints on the thermal history of the Allende parent body as derived from olivine-spinel thermometry and Fe/Mg interdiffusion in olivine: Geochimica et Cosmochimica Acta, v. 58, no. 2, p. 1019–1030.

Weisberg, M.K., McCoy, T.J., and Krot, A.N., 2006, Systematics and Evaluation of Meteorite Classification, in Lauretta, D.S. and McSween, H.Y. eds., Meteorites and the Early Solar System II, Tuscon, Arizona, p. 19–52.

Weisberg, M.K., Prinz, M., and Clayton, R.N., 1997, CV3 chondrites: Three subgroups, not two: Meteoritics and Planetary Science, v. 32, no. 4, p. A138–A139.

Wittmann, A., Kenkmann, T., Hecht, L., and Stöffler, D., 2007, Reconstruction of the Chicxulub ejecta plume from its deposits in drill core Yaxcopoil-1: Geological Society of America Bulletin, v. 119, no. 9-10, p. 1151–1167.

Zinner, E., and Gopel, C., 1992, Evidence for ^{26}Al in feldspars from the H4 chondrite Ste. Marguerite: Meteoritics, v. 27, no. 3, p. 311.

Zinner, E., and Göpel, C., 2002, Aluminum-26 in H4 chondrites: Implications for its production and its usefulness as a fine-scale chronometer for early solar system events: Meteoritics & Planetary Science, v. 37, no. 7, p. 1001–1013.

Chapter 2

Hidden Secrets of Deformation: Impact-Induced Compaction within a CV Chondrite

The following chapter has been published in EARTH AND PLANETARY SCIENCE LETTERS. The original format has been modified for the purposes of this thesis, but all content remains the same. The original, formatted and published version can be found in Appendix A1.

L. V. Forman[1], P. A. Bland[1], N. E. Timms[1], G. S. Collins[2], T. M. Davison[2], F. J. Ciesla[3], G. K. Benedix[1], L. Daly[1], P. W. Trimby[4], L. Yang[4], and S. P. Ringer[5], 2016, Hidden secrets of deformation: Impact-induced compaction within a CV chondrite: Earth and Planetary Science Letters, v. 452, p.133-145.

[1]Department of Applied Geology, Curtin University, GPO Box U1987, Perth, WA 6845, Australia

[2]Royal School of Mines, Department of Earth Science & Engineering, Imperial College London, Prince Consort Road, South Kensington, SW7 2BJ, United Kingdom

[3]Department of the Geophysical Sciences, The University of Chicago, 5734 South Ellis Avenue, Chicago, IL 60637, USA

[4]Australian Centre for Microscopy and Microanalysis, The University of Sydney, NSW, 2006, Australia

[5]Australian Institute for Nanoscale Science and Technology, and School of Aerospace, Mechanical and Mechatronic Engineering, The University of Sydney, NSW, 2006, Australia

1. ABSTRACT

The CV3 Allende is one of the most extensively studied meteorites in worldwide collections. It is currently classified as S1—essentially unshocked—using the classification scheme of Stöffler et al. (1991), however recent modelling suggests the low porosity observed in Allende indicates the body should have undergone compaction-related deformation. In this study, we detail previously undetected evidence of impact through use of Electron Backscatter Diffraction mapping to identify deformation microstructures in chondrules, AOAs and matrix grains. Our results demonstrate that forsterite-rich chondrules commonly preserve crystal-plastic microstructures (particularly at their margins); that low-angle boundaries in deformed matrix grains of olivine have a preferred orientation; and that disparities in deformation occur between chondrules, surrounding and non-adjacent matrix grains. We find heterogeneous compaction effects present throughout the matrix, consistent with a highly porous initial material. Given the spatial distribution of these crystal-plastic deformation microstructures, we suggest that this is evidence that Allende has undergone impact-induced compaction from an initially heterogeneous and porous parent body. We suggest that current shock classifications (Stöffler et al., 1991) relying upon data from chondrule interiors do not constrain the complete shock history of a sample.

2. INTRODUCTION

Planetary systems evolve from a molecular cloud comprised of dust (condensed minerals and presolar grains) and gas, to a protoplanetary disk, where most of the mass is concentrated in the 'mid-plane' of that disk. Turbulence allows for gas and particle clumping and accretion of the dust into centimetre- to metre-sized bodies (Cuzzi and Weidenschilling, 2006). Interactions with the gas and collisions lead these solids to grow and accumulate into planetesimals measuring 10 s to 100 s of kilometers in diameter. As this accumulation must be relatively gentle to ensure sticking and adhesion among the components, primordial planetesimals formed in this way would preserve large pore spaces in between each component, resulting in very high porosities (>65%) (Blum, 2003 and Weidenschilling and Cuzzi, 2006).

Planetary evolution from these primordial objects to the asteroids that we see today requires that porosity be greatly reduced, as evidenced by the worldwide collection of meteorites that comprises comparatively low-porosity rocks. A number of mechanisms for porosity reduction and weak fabric development have been suggested, including metamorphism and expansion/contraction cycles (Stacey et al., 1961 and Zolensky et al., 1997), accretional compaction (Cain et al., 1986), gravitational compaction (Fujimara et al., 1983) and sedimentation; perhaps the two most plausible mechanisms being

compaction from lithostatic overburden (Cain et al., 1986) and impacts (Scott, 2002, Sharp and DeCarli, 2006, Davison et al., 2010, Beitz et al., 2013 and Bland et al., 2014). It is apparent that the gravity field of even relatively large planetesimals would be insufficient and to generate the required lithostatic pressure to cause sufficient compaction that could adequately explain the low porosities of meteorites (Weidenschilling and Cuzzi, 2006 and Friedrich et al., 2014). The anisotropy of magnetic susceptibility (AMS) studies done by Gattacceca et al. (2005) conclude that dynamic compaction via impacts is the most likely mechanism for fabric development and therefore porosity reduction, which is also supported by a wide number of findings within meteorite collections; low (but variable) porosities throughout a given sample; heterogeneous porosities within the same chondrite group; subtle mineral deformation microstructures; widespread planar fabrics; and localised melt pockets within matrix (Nakamura et al., 1992, Consolmagno et al., 1998, Brenker et al., 2000, Cuzzi et al., 2008 and Johansen et al., 2009). Such evidence is not unique to carbonaceous chondrites; it is also present in ordinary chondrites, in the form of high-pressure polymorphism, vitrification of silicate minerals and deformation of olivine grains (Rubin, 2004). Recent work on the CM meteorite Murchison has also revealed porosity loss was induced by impact and predicted a pre-compaction bulk porosity of up to ~50% (Hanna et al., 2015). Further support for the occurrence of impacts on early highly porous bodies is found in Housen et al.'s work (1999) regarding impact-cratering on the asteroid Mathilde; an unusual lack of blanket ejecta around prominent craters indicate the impacts that produced them occurred when the body was highly porous. Other studies also argue that impacts on such a large scale may destroy the target body if the porosity was not sufficiently high and the impact direct; the pores allow the target to sustain the impacts without being disrupted and oblique impacts lead to less ejecta and the crater morphologies present on Mathilde (Housen et al., 1999, Cheng and Barnouin-Jha, 1999 and Housen and Holsapple, 2011). Impact-induced compaction is therefore discussed in depth with relation to the research outlined in this paper.

Evidence of impact shock is routinely observed in current meteorite collections and a shock level is assigned to each meteorite (Stöffler et al., 1991, Scott et al., 1992 and Sharp and DeCarli, 2006). The approach taken by Stöffler et al. (1991) uses published data from impact experiments on low-porosity and homogeneous terrestrial rocks, lunar rocks and single crystals, taking these materials as analogues for low-porosity, H, L and LL ordinary chondrites. A set of shock metamorphic features seen in analogue materials are used to calibrate the peak pressure experienced for that meteorite, and determine a shock level. This classification is based upon the largest of grains in any sample (Stöffler et al., 1991 and Scott et al.,

1992), meaning only a few larger grains are considered. Allende, the sample of study in this paper, is identified as an S1- virtually unshocked- and is expected to have experienced no more than 5 GPa in peak shock pressure (Scott et al., 1992). The samples and procedures used in the early study may not be ideal for several reasons: meteorites are not homogeneous materials, and grain size plays an important role in determining the shock reaction of a grain, especially when pore space is considered (Davison et al., 2010). Most importantly, the experimental impact studies that underpin the Stöffler et al. (1991) and Scott et al. (1992) approach are concerned with impacts into low- or zero-porosity targets and, by extension, impacts into compacted planetesimals. Therefore, this approach may not be suitable for approximating impacts into highly porous primordial objects.

Recent numerical models consider more complex scenarios, concerned with impacts into uncompacted porous planetesimals, bimodal material and mixed compositions of the target body. Davison et al. (2010) model shock propagation through homogeneous, porous planetesimals and find high porosity to be positively related to higher impact-generated temperatures on an asteroidal scale. Similar numerical simulations have highlighted the importance of pore collapse in the target body upon impact, which generates large amounts of heat, allowing the whole medium to experience elevated temperatures and potential melting (Consolmagno et al., 1998, Davison et al., 2010 and Davison et al., 2014). Further improvements were made to these models to acknowledge the small-scale and complex material properties of primitive bodies: chondrites are essentially bimodal mixtures of porous, fine-grained matrix and large chondrules without intercrystalline porosity (Bland et al., 2011, Bland et al., 2014 and Davison et al., 2014). In an impact compaction simulation with a bulk shock pressure of only ~1 GPa, the bulk post-shock temperature was ≈425 K, but the matrix was heated to ≈530 K from an initial temperature of 300 K, whereas chondrules were heated by only a few degrees (Bland et al., 2014). Heating occurs at chondrule edges adjacent to initially porous areas of matrix, and at the edges of closely spaced chondrules, and pressure distribution within chondrules is also not uniform; chondrule edges are predicted to experience higher pressures than chondrule interiors. Porosity in matrix also varies, with high-porosity regions observed in the lee of chondrules. Petrologic evidence of these features has yet to be identified, but the models give an indication of how a bimodal heterogeneous material may react upon impact.

In light of the models described above (Davison et al., 2010 and Bland et al., 2014), the shock pressure aspect of Allende's impact history may simply be absent from large, resilient chondrules. Allende is a well-studied sample that contains approximately 40% matrix (Macke et al., 2011), and has a measured bulk porosity of 22%. Recent fabric analysis has inferred that ~50% pore volume

reduction has occurred in Allende via impact (Bland et al., 2011 and Hanna et al., 2015), but this is unlikely to be homogeneous throughout any sample. Assuming initial matrix porosity in the >65% range, this implies a pre-compaction matrix:chondrule volume ratio of >2:1. Numerical simulations that exposed such a chondrule–matrix mixture to a ~1 GPa shock wave reproduced the observed bulk and matrix porosity in Allende, and suggest that localised heating by heterogeneous pore collapse may have been a significant process.

In this study we explore the possibility that matrix grains and chondrules responded differently to planetary compaction. We establish how the microanalytical and textural study of this meteorite holds interesting implications about the evolution of the parent body of Allende.

3. APPROACH AND METHODS

In this study we analysed a thin section of Allende. The initial imaging of this sample was conducted at the X-Ray Fluorescence Beamline (XRF) at the Australian Synchrotron facilities in Melbourne. Here, 25 element maps were collected for the entire sample in under 10 h (Fig. 2.1). These were compared with the collected Energy Dispersive Spectroscopy (EDS) data for accuracy of elemental distribution throughout the sample, in addition to monitoring any instrumental drift. The Maia detector on this beamline had an energy sensitivity in the range of 3.3–19.9 keV, encompassed a number of major elements with an energy resolution of 300–400 eV, and in this case, produced maps with a spatial resolution of 2 μm per pixel. Elements were detected in the spectra processing stage and so were not required beforehand for the imaging to occur. In addition, the Maia detector was able to detect elements at the 10–100 ppm scale – commonly lower than other traditional imaging techniques (Fisher et al., 2014). Owing to the high-energy beam in use (18.5 keV), this technique sampled a larger depth than other traditional imaging techniques, and so data collected represented an average of the volume sampled (Dyl et al., 2014). Further information regarding this imaging technique can be found in the Analytical Methods section of Dyl et al. (2014). This map was used as a means of identifying areas of interest for further Secondary Electron (SE), Backscatter Electron (BSE), EDS and Electron Backscatter Diffraction (EBSD) analyses. Ten regions encompassing chondrules, Amoeboid Olivine Aggregates (AOAs) and matrix grains were mapped using a variety of imaging techniques, utilising the Tescan Mira3 FESEM, at the John de Laeter centre at Curtin University, Western Australia. It is important to note that all maps were taken in the same physical orientation in the SEM, allowing for direct and accurate comparisons of crystallographic features between sites.

Standard Secondary Electron (SE) and Back-Scattered Electron (BSE) images were collected at a voltage of 20 keV, a beam intensity of 17, an aperture size of 30 μm and a working distance between 10 and 15 mm. These images were used to define regions

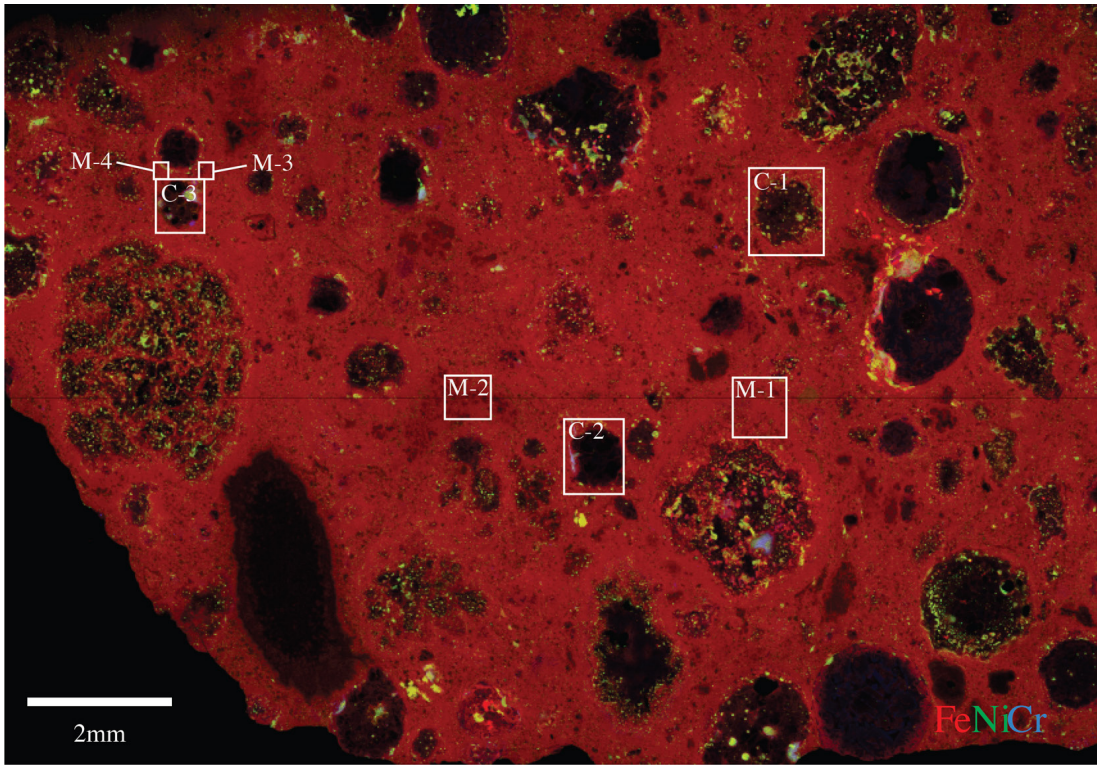

Fig. 2.1: *X-Ray Flourescence Synchrotron map of a thin section of the Allende meteorite. Chondrule and matrix sites to be discussed are shown (C = chondrule/AOA, M = matrix). Note that M-1, M-3 and M-4 are proximal to a chondrule or AOA, and M-2 is in an area devoid of chondrules, AOAs and CAIs.*

of interest for further analysis and image collection.

Electron Backscatter Diffraction (EBSD) was the primary technique used in the study. EBSD enabled mapping of the crystallographic orientation of grains in a thin section, both in relation to crystallographic axes and neighbouring grains. Automated and simultaneous EBSD and EDS maps were generated using Oxford Instruments' Aztec acquisition system, using a fixed x and y step size for each site in a user-defined grid, varying between 0.1 µm and 8 µm, dependant upon the grain size distribution at each particular site. This approach generated a dataset with high spatial resolution whilst also being

Site	Type	Step size (µm)	Imaging threshold (µm)	Number of points	Mean Angular Deviation (MAD) (°)	Acc. voltage (keV)	Forsterite indexed (%)	Not indexed (%)
C-1	Chondrule	0.5	2	77284	0.38		82.5	16.0
C-2	Chondrule	2	8	172125	0.60		45.8	49.8
C-3	AOA	0.81	3.6	2403310	0.53		36.3	63.2
M-1	Matrix	0.1	0.4	130732	0.68	20	48.9	49.0
M-2	Matrix	0.12	0.48	2314956	0.67		37.2	59.3
M-3	Matrix	0.2	0.8	122760	0.67		36.55	52.87
M-4	Matrix	0.35	1.4	35708	0.80		37.9	57.1

Table 2.1: *EBSD and SEM imaging parameters used for imaging at each of the chondrule, AOA and matrix sites in this sample of Allende.*

time-efficient. Table 2.1 shows the conditions under which the maps were collected at each site. SE images were obtained to confirm that topographic features present in or around chondrules did not bias the EBSD data and interpretation.

Allende was found to contain abundant matrix grains at the sub-micrometre scale, and so greater spatial resolution was required for accurate analysis of the smaller grains. The Transmission Kikuchi Diffraction (TKD) technique utilised electron transparent samples in the SEM, coupled with conventional EBSD instrumentation, resulting in an order of magnitude improvement in spatial resolution compared to EBSD (sub 10 nm – Trimby et al., 2014). A transmission electron microscope (TEM) foil was extracted containing a sectional view of a chondrule rim and adjacent matrix material. The sample was created using a focused ion beam (FIB) SEM (Carl Zeiss Auriga) at the Australian Centre for Microscopy & Microanalysis (ACMM), Sydney. To protect the sample from gallium beam damage a platinum layer was deposited and the sample lifted out using a Kleindiek micromanipulator. The section was mounted on a molybdenum grid using platinum welds and the sample was further thinned to 100 nm. The TEM foil was analysed using TKD and EDS on a Carl Zeiss Ultra Plus FEG SEM at the ACMM, Sydney. TKD and EDS data were acquired using an Oxford Instruments AZtec system with a Nordlys-Nano EBSD detector and an X-Max 20 mm2 SDD EDS detector and with an accelerating voltage of 30 kV.

EBSD data were processed using the Oxford Instruments HKL software package Channel 5.12, generating crystallographic orientation maps, phase maps and pole figure plots that were compared across each site. In this process, noise reduction and data processing were done in a very similar manner to that described in Watt et al. (2006); isolated misindexed data points were removed using a wildspike correction, and all non-indexed points infilled to a six nearest-neighbour extrapolation. Grains were detected in each map based upon crystallographic orientation, and using a misorientation angle of at least 10° between two adjacent pixels to identify grain boundaries. Grains with diameters less than four times the step size were removed to allow for reliable data interpretation, which also removed misindexed points. Grain orientation data from the entirety of each map were plotted on to lower hemisphere, equal area projections as one point per grain to avoid grain size related bias during contouring. In this study, we focused on olivine grains to enable a direct comparison with shock-level studies. Although compositions across the olivine solid-solution can be found in Allende, there was little variation in their crystal structure: EBSD does not discriminate between olivine sub-types, and so all EBSD patterns from olivine were successfully indexed using the 'forsterite' match unit in the HKL database (indexing statistics are given for each region of interest in Table 1).

Low-angle boundaries (LABs) can form

due to a number of mechanisms. Both orientation selective dissolution and grain growth in a vein setting may result in grains of similar orientation forming apparent low-angle sub-grain boundaries where their edges meet. Neither of these mechanisms are likely given the primitive nature of Allende. LABs can also be a geometric consequence of grain impingement between two similarly-orientated grains (Wheeler et al., 2001). Where grains preserve crystallographic variations that cannot be attributed to fractures, it was assumed that they were deformed crystal-plastically (via dislocation creep and recovery). Dislocation slip systems were then inferred assuming pure tilt boundary geometry, whereby an orthogonal relationship exists between the rotation axis of low-angle boundaries, pole to the dominant dislocation slip plane and slip direction (e.g. Prior et al. 2002) combined with cumulative dispersion of crystallographic poles in each grain. As the rotation axes did not lie in the plane perpendicular to the LAB trace, we can infer these boundaries formed due to tilt and did not show evidence of twist-boundary formation. Further information regarding this test can be found in the methods section of Gray (2013). LAB planes were inferred from traces in map view and contain misorientation axes. Axes of misorientation were identified based upon axes of pole dispersions in lower hemisphere plots. The related slip systems were then inferred using geometric criteria: a slip-system is composed of both a slip plane and direction; the pole to the slip plane is contained within the low-angle boundary with the misorientation axis, and the slip direction is perpendicular to that plane.

The numerical simulations described by Bland et al. (2014) provided peak and post-shock stress (pressure), temperature and porosity distributions for numerous impactor velocity and initial matrix/chondrule abundance scenarios. To compare more directly the data from our study with the simulation predictions, shear strain distribution maps were produced from the simulation outputs. The tracer particle positions in the simulations were used to derive the second invariant of the total strain tensor using the method described by Bowling (2015). This invariant measure of shear deformation includes the net elastic plus plastic strain at the end of the simulations (i.e., the finite strains). As the elastic–plastic rheological model used in the numerical simulations to represent the chondrules and matrix incorporates a yield strength that is pressure, strain and temperature dependent, it can describe (very approximately) both brittle (low pressure) and ductile (high pressure) deformation. In reality, olivine rheology is more complex in detail, and involves anisotropic elastic and plastic properties. Furthermore, as the matrix of fine grains and interstitial pore space is treated as a uniform continuum in the simulations, we note that the strain in the matrix is the bulk strain of the grains and the pore spaces, which will be largely accommodated by grain

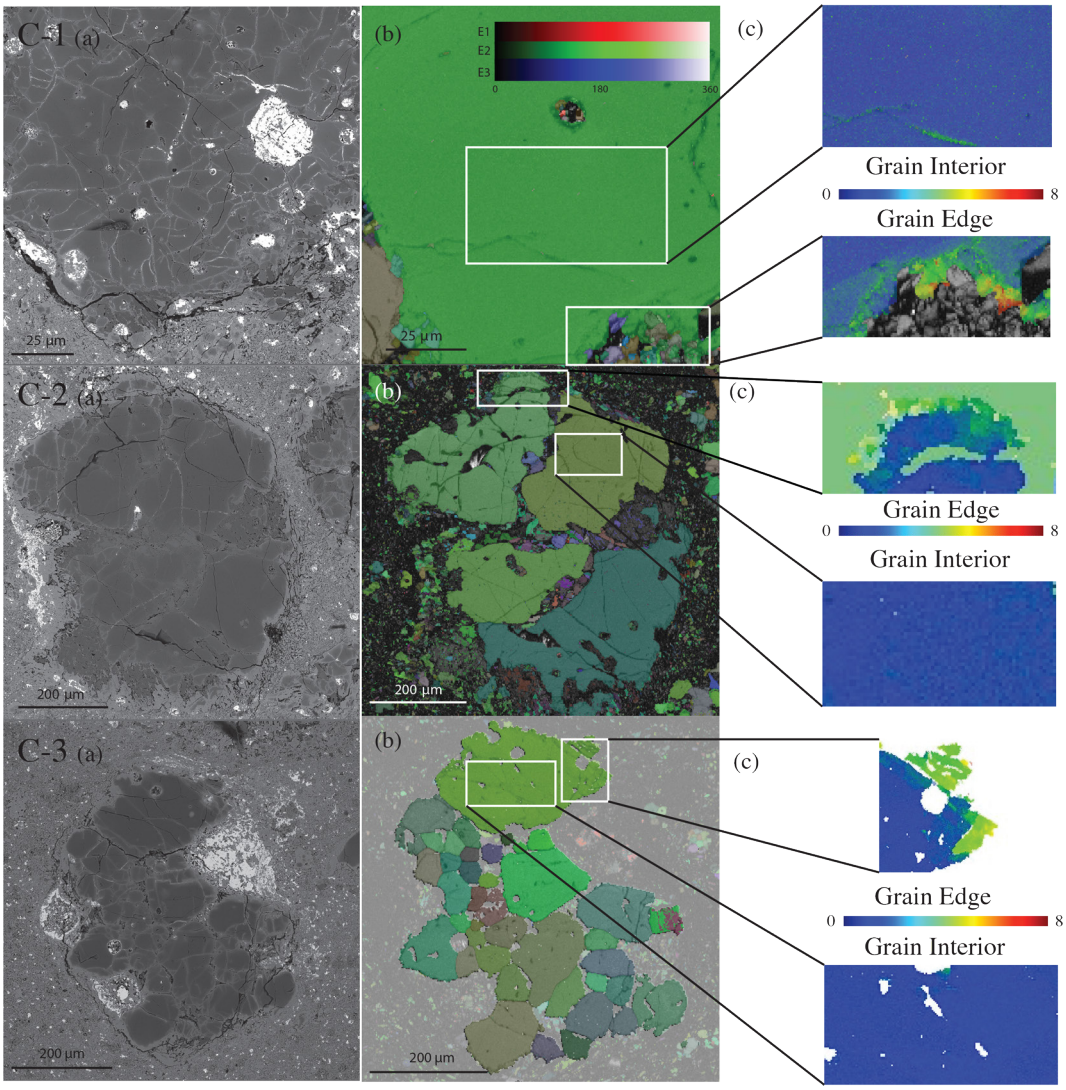

***Fig.* 2.2:** *Chondrule/AOA sites C-1, C-2 and C-3 respectively. (a) Backscatter Electron (BSE) images, (b) Euler maps of each site, showing the orientation of each grain in terms of the three Euler angles, and (c) texture component maps showing a vast increase in deformation at grain edges when compared to grain interiors (scale bar is shown in degrees °).*

rearrangement and pore collapse, rather than permanent deformation of individual matrix grains: i.e., 'details' of the strain in individual matrix grains is not resolved. Despite these limitations we expect the qualitative distribution of shear strain observed in the numerical simulations to provide an informative comparison with permanent strain derived from our crystallographic orientation analysis.

4. RESULTS & ANALYSIS

Olivine in the chondrules in Allende was commonly Mg-rich, i.e., forsteritic, whereas matrix olivine was more Fe-rich, i.e., fayalitic (Fig. 2.1). Prior studies calculate proportions of chondrule and matrix to be approximately 60% and 40% respectively (McSween, 1979 and Macke et al., 2011). The chondrules,

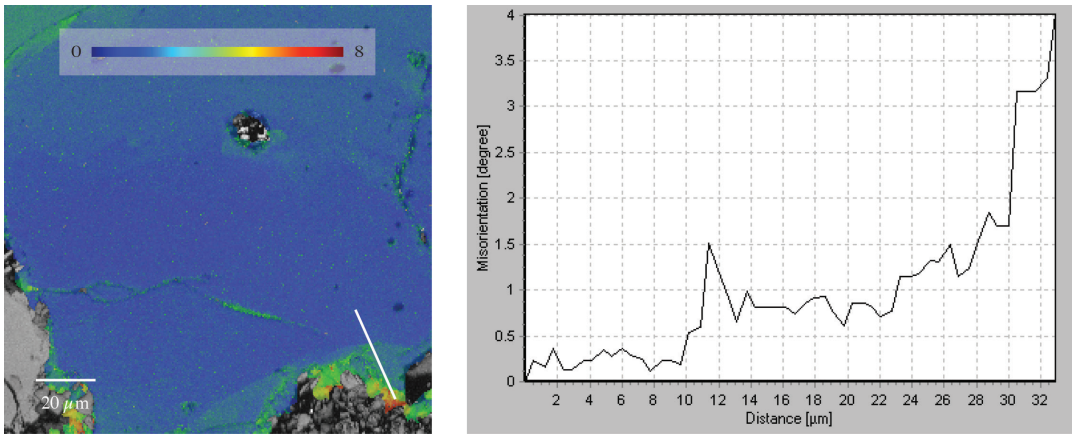

Fig. 2.3: *(a) Map of texture component for chondrule at C-1. White transect line is shown through lower outer edge of the chondrule. (b) Misorientation profile for the white transect line in (a) demonstrates the gradual increase in orientation deviation in an outwards direction from the innermost point of the transect. This confirms the outer edges of chondrules deform gradually and cumulatively from the inner to outer points along the transect.*

AOAs and Calcium–Aluminium Inclusions (CAIs) were also weakly elongate as is shown in Fig. 2.1. Within the 1.28 cm^2 sample area of our sample, we observed a large variation in matrix grain size (Supplementary Figs. 1–4). EBSD analyses resolved forsterite, diopside, and enstatite, which have been recorded previously (Stöffler et al., 1991). As expected, this sample was highly texturally heterogeneous, containing different chondrule types and a wide range of matrix grain shapes and sizes. We found no evidence of high-pressure polymorphs, such as ringwoodite, that would indicate high shock pressures.

4.1. Chondrules and AOAs

Three chondrule and AOA sites were examined (Fig. 2.2), and are collectively referred to as 'chondrule sites' from this point forward. For each site, a 'cumulative misorientation map' was generated such that each datapoint was coloured for the minimum mismatch in crystallographic orientation (minimum misorientation) from a user-specified point within the grain (all sites, Fig. 2.2c). These maps resolved misorientations to a precision based upon the fit quality of the indexing solutions (mean angular deviation (MAD), Table 2.1) in each map, which were typically reliable down to approximately 0.5° in this study. Each of the chondrules showed very little or no internal deformation in their interior: up to a maximum of 1° in the central parts of the grains. However, the outer 10–30 μm of the chondrule and outermost AOA grains commonly preserved up to 6° of progressive, cumulative misorientation that did not relate to brittle fractures (all sites, Fig. 2.2c and Fig. 2.3). This relationship is visible in the local misorientation maps, where each pixel was coloured to reflect mean misorientation with the eight nearest neighbour data points (Fig. 2.4). Fig. 2.3 and Fig. 2.4 show that

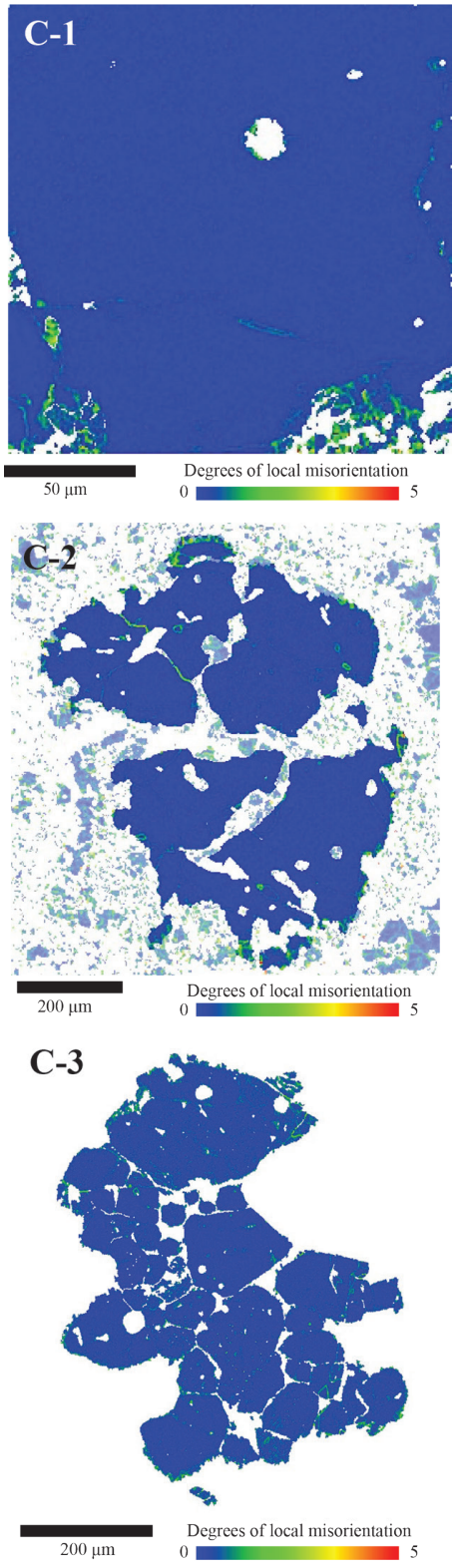

Fig. 2.4: *Local misorientation maps of the chondrule/AOA sites. Each pixel is colour coded to reflect its degree of misorientation from the* surrounding *8 pixels.*

progressive crystallographic misorientations at the edges of the grains are accommodated by many relatively planar LABs, parallel to the grain edge. Fig. 2.3 demonstrates the deformation at C-1 is cumulative and begins in the outer 30 µm of the grain, reaching maximum deformation at the edge (7–8°). Not only were the highest degrees of strain at the grain edges at each site, but LABs were also generally concentrated at the top and bottom, and to the right of the chondrules and AOA, as indicated by the continuous, cumulative strain at the margins of chondrule C-1, for example (Figs. 2.2b, 2.2c, 2.3 and 2.4).

4.2. Matrix grains

Maps of crystallographic orientation for olivine at the four matrix sites are shown in Fig. 2.5. Grain size and shape maps and distribution histograms are presented in Supplementary Figs. 2.1–2.4, and matrix grains measured in the TKD section are shown in Fig. 2.6. It is clear a variety of grain sizes are present; between 0.1 µm and 50 µm. The grains were chiefly subhedral and lath-shaped, characterised as having an aspect ratio greater than 2:1 in 2D. A wide range of intragrain misorientation characteristics were observed at a very fine scale in matrix grains; up to 20° of internal deformation across a 20 µm grain was recorded at site M-2, with as little as 2° internal deformation across a selection of grains at site M-1 (Fig. 2.5 and Fig. 2.6). Whilst a wide range of values were recorded, average internal deformation was high, with the majority of values in the 8–15° range. It is important to note that in contrast

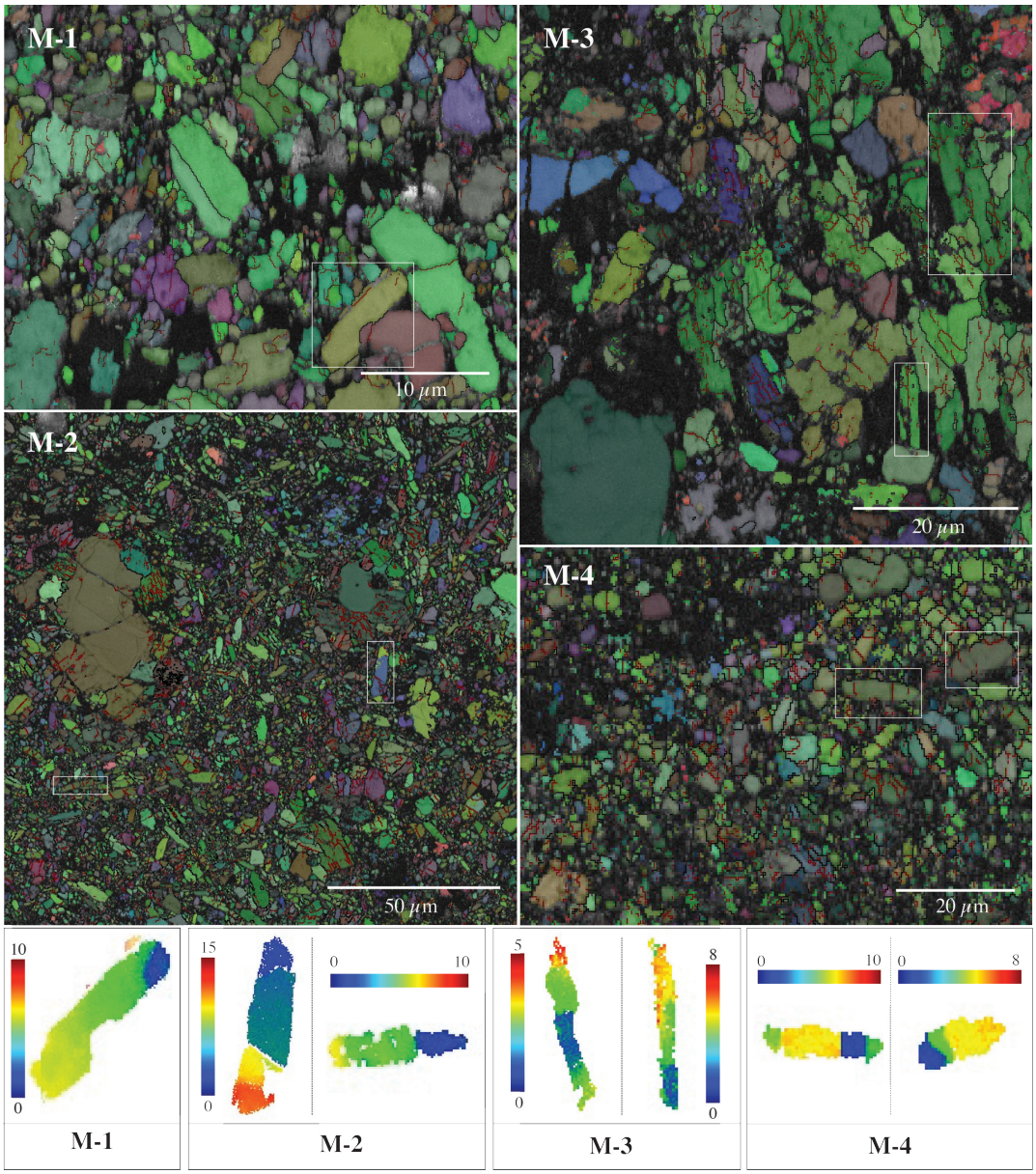

Fig. 2.5: *Four matrix sites (M-1–4) shown using Euler maps. White boxes in each image refer to laths displayed in lower panel; texture maps of individual grains demonstrate the extent of deformation that has occurred throughout the full length of the grain. Scale bar shows degrees (°) of deformation from pre-defined unstrained point of grain (blue region).*

to chondrules, intragrain deformation was observed throughout the full length of the matrix grains, and the magnitude of deformation is consistently greater in all cases.

At sites M-1 and M-3, the trace of planar LAB orientations were measured relative to the map x–y reference frame plotted onto rose diagrams (Fig. 2.7). The rose plots reveal a dominant trend of the LABs, preferentially aligned with map y direction (i.e., circa 0° and 180° in Fig. 2.7). This is significant because aligned LABs indicate a relatively consistent applied stress field at

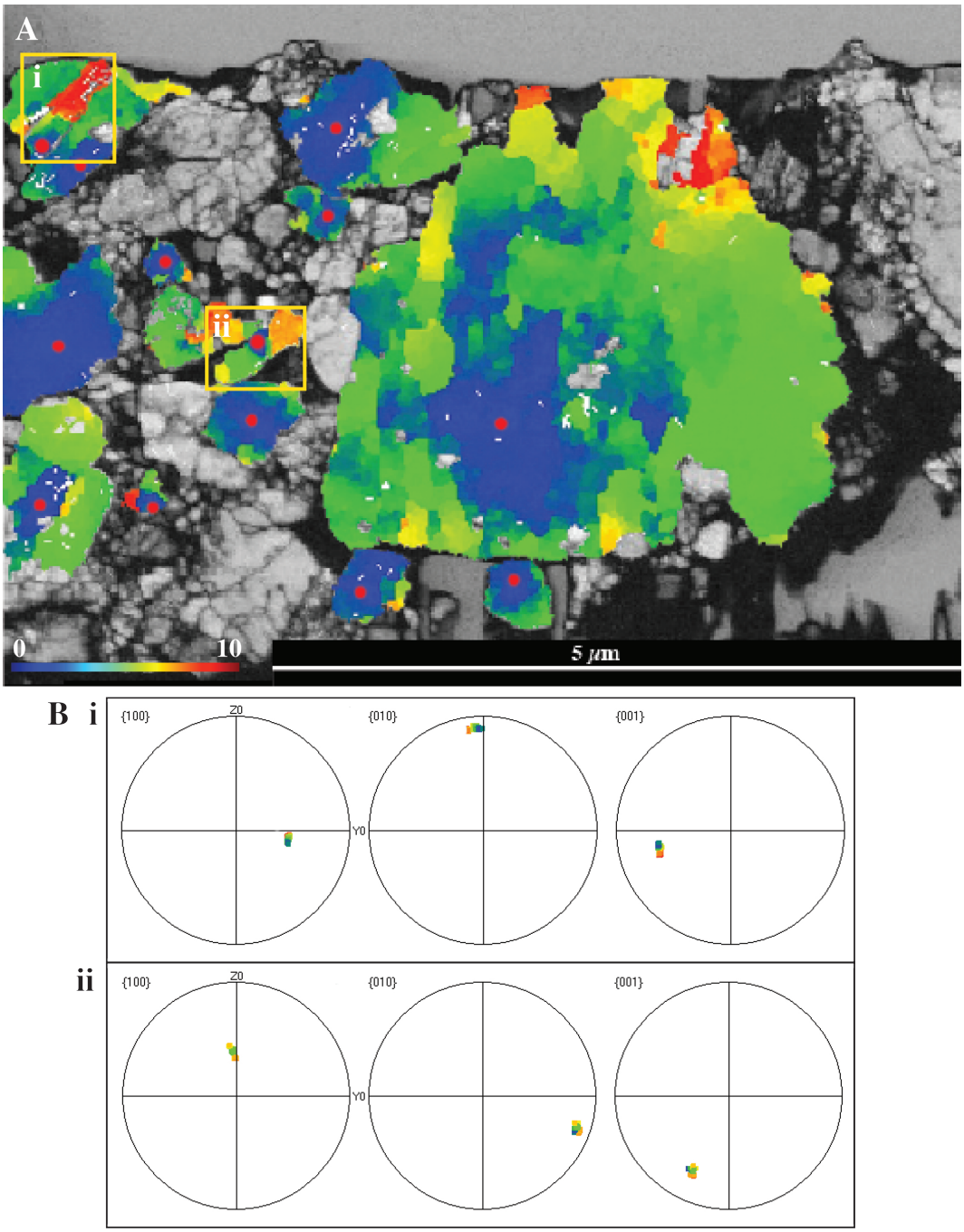

Fig. 2.6: *EBSD image of a TKD section of Allende (A). Greyscale image is the band contrast map, indicating the quality of the patterns obtained in imaging by the brightness of the colours (i.e. white/light greys = good band contrast and pattern quality). Colour overlay demonstrates the amount of crystallographic orientation deviation in degrees from user-defined reference points (red dots) in selected grains. Lower-hemisphere, equal area plots show dispersion of each crystallographic axis within the grain (B).*

the scale of the observations, such as those produced in controlled olivine deformation experiments by Kohlstedt and Goetze (1974). The spatial density of low-angle boundaries

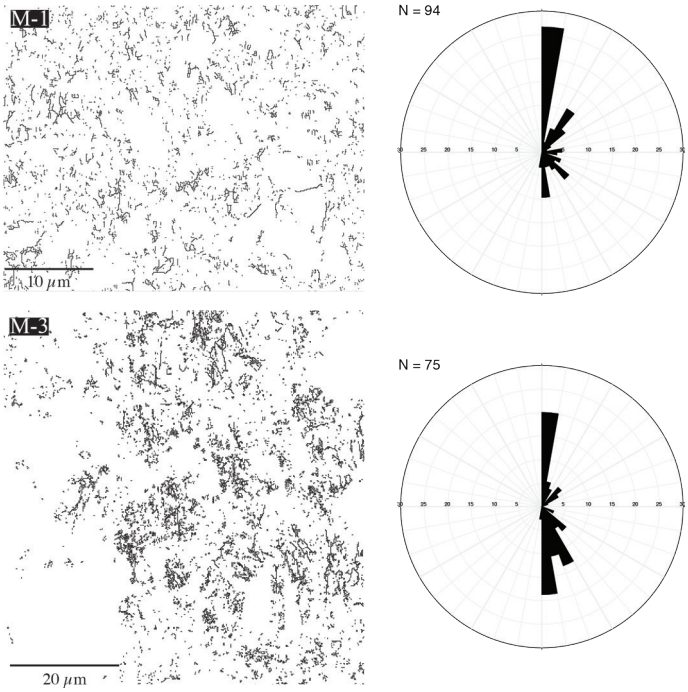

Fig. 2.7: *Low-angle boundaries (1°–10°) are presented for matrix sites M-1 and M-3 on the left. The orientations of these boundaries are plotted onto rose diagrams on the right, demonstrating the preferential orientation for both sites is roughly N–S, or at 0° and 180°.*

was more consistent throughout the matrix grains when compared with chondrule sites; where chondrules and AOAs have a higher density of LABs at their edges, those found in matrix grains were not confined to the grain edges and were present throughout the grain area (Fig. 2.5 and Fig. 2.6). This is consistent with findings of experimentally stressed olivine crystals; undulose extinction along the grains indicates multiple, similarly oriented low-angle boundaries are present, accommodating changes in crystallographic orientation (Kohlstedt and Goetze, 1974 and Fliervoet et al., 1999).

The matrix sites also presented a range of porosities. In some locations, grains appeared very compact with an extremely low porosity (e.g. M-2), whereas areas of M-1 and M-4 appeared more porous with lower indexing rates over the whole region-quantification of this porosity is currently a work in progress. It is important to recall that images at each site were collected at different image resolutions, allowing for maximum efficiency and coverage whilst maintaining the high indexing ratios (Table 2.1). As some grains were smaller than the specified step-size for imaging each site, this may have resulted in non-indexing of those grains, making the EBSD-inferred porosity of the region incorrect. In light of this, secondary electron images were obtained (Supplementary Fig. 2.5) for each matrix site, and these confirmed and qualified the porosity variations implied in the EBSD maps.

4.3. Slip systems

Based upon the misorientation axes observed from the EBSD maps we have

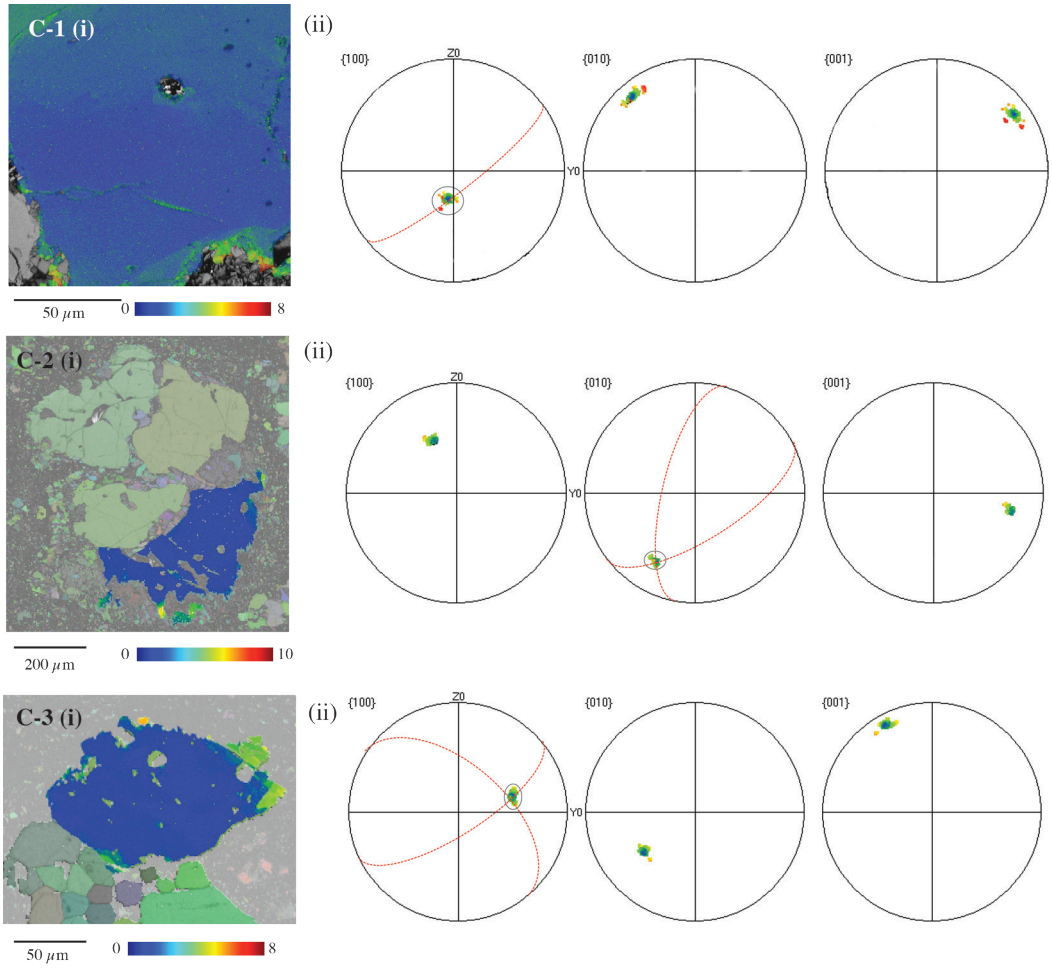

Fig. 2.8: *Texture component maps of Chondrule/AOA site C-1, C-2 and C-3 (i). This demonstrates the degrees of rotation in Euler angles from a central, unstrained point within the presented grain. This data is plotted on lower hemisphere, equal area, stereographic projections (ii). At each site the orientation of the low-angle boundaries is shown on the equal area plots as red lines for each highlighted grain in the maps. At site C-1 and C-3, the misorientation axis is the [100] axis, and at C-2 the misorientation axis is [010]. At sites C-2 and C-3 two sets of low-angle boundaries are observed and cause a two-way dispersion in the data.*

inferred the likely slip-systems that have contributed to the LABs in chondrules, AOA grains and matrix grains including those within the TKD data. C-1 and C-3 had a misorientation axis of the [100] (a-axis), while C-2 had misorientation along the [010] (b-axis) (Fig. 2.8). Matrix grains largely had misorientation axes of [010] (b-axis) whilst one examined grain at M-3 had a misorientation axis of [100] (a-axis). EBSD, BSE and SE images indicated that the LABs occur within grains and so it was assumed they result from intragrain plasticity, which would have required high stresses. Chondrule site C-3 (Fig. 2.7c) displayed evidence of two different slip systems; the misorientation axis was [100] in both cases, but one slip system comprised slip in the [001] direction along the (010) plane, and the other involved slip in the [010] direction along the (001) plane. A variety

of slip systems were inferred across each of the sites; of the 9 examples found, matrix slip systems were most commonly (001)[100] (slip in the (001) direction along the [100] plane), with occurrences of other common systems at each site. Chondrule grain slip systems were more widely varied and include (001)[010], (001)[100] and (010)[100] throughout the sites.

4.4. Strain distribution observations

The qualitative distribution of strain observed in chondrules and matrix is consistent with numerical simulations results (Fig. 2.9). In the simulated chondrules, the predicted mean strain is low, but localised near their margins for 1.0 and 1.5 km/s cases (Figs. 2.9a and b), whereas strain is higher and distributed throughout the chondrules for the 2 km/s case (Fig. 2.9c). In all simulated impactor velocity scenarios, the matrix strain is always higher than within the chondrules, with an increase in mean strain with impactor velocity (Fig. 2.9). Strain in the matrix is typically more intensely developed immediately adjacent to the chondrules, most commonly with an eccentric distribution and asymmetric strain shadows (Fig. 2.9). All of the simulations predict strong gradients in matrix strain over the micrometre scale (Fig. 2.9).

5. DISCUSSION

Previous work has shown that Allende has a weak but prominent fabric throughout, with an alignment of the short <100> axis of fayalitic olivine grains (Watt et al., 2006). Our study confirmed the weak fabric, albeit with varying alignments (Supplementary Figs. 2.1–4 and 6). Chondrules, AOAs, CAIs and larger grains are elongate in the vertical orientation, indicative of a horizontal compaction orientation in the plane of the images (Fig. 2.1). However, we also observed a significant difference in spatial distribution and density of deformation between chondrule and matrix olivines: an absence of deformation

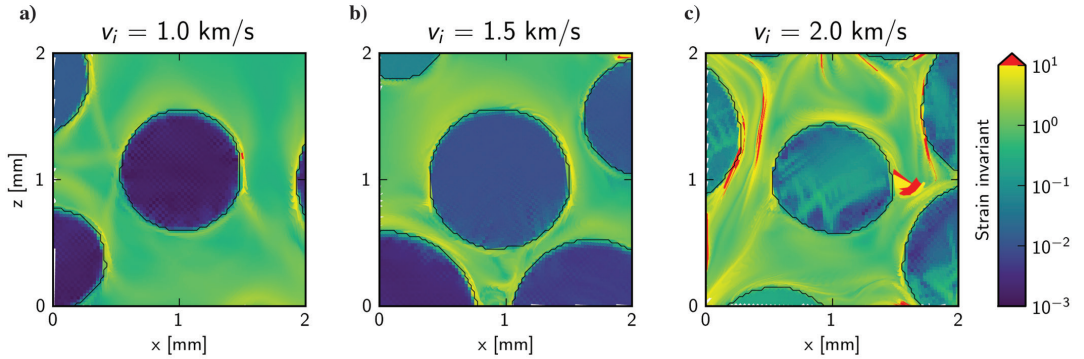

2.9: *Finite invariant shear strain distribution maps derived from numerical simulations for three impact speeds: a) v = 1.0 km/s; b) 1.5 km/s; c) 2.0 km/s, which generate bulk shock pressures of approximately 1, 1.7 and 3 GPa, respectively. In these simulations chondrules are treated as single grains and the matrix of fine grains and pore space is treated as a continuum. Hence, while simulated strains in the chondrules are expected to be comparable to those observed inside chondrule grains, the strain distribution within the matrix is the bulk strain of both matrix grains and pore space combined and is not directly comparable to strain observed in individual matrix grains.*

of chondrule interiors, minor crystal-plastic deformation at the edges of chondrule grains (up to 6° misorientation ductile strain in the outer 20 μm of these grain edges), and moderate yet heterogeneous crystal-plastic deformation throughout matrix grains (e.g., 20° misorientation along the length of a 20 μm grain). The low-angle boundaries in the matrix grains also have a preferential alignment (their traces are vertical in the plane of the images) whereas those in the chondrules rims are generally parallel to the edge of the grains (Fig. 2.7).

A large portion of the deformation of chondrule grain edges is concentrated at the top, bottom and to the right of the chondrules. Further to this, deformation is absent on the left and less prominent on the right of these grains when compared with the top and bottom areas. Coupled with an absence of matrix grain deformation to the left of such grains, a compressional 'shadow' has been generated. It is possible that compaction of pores against the boundary of the grain normal to the compacting direction generated enough heat such that these areas of the grains were compressed but show no evidence of strain. The top and bottom of the chondrules may not have experienced the same degree of compaction and, therefore, less pore collapse and subsequent heating would have occurred (Davison et al., 2010). Here, there may not have been sufficient heat to deform these regions without strain being evident. However, the lack of evidence for melting observed at this scale indicates this may not be the case, and therefore other possibilities, such as shear heating, should be considered. Given that the presence of strain 'shadows' on the left side of the larger grains, it is probable that a similar shadow would be evident in the matrix as a higher porosity relative to surrounding matrix areas. Whilst the sample has lost a large portion of it's initial porosity (~50%), the compaction process is very unlikely to generate uniformly low porosities throughout the matrix due to the bimodal grain size distribution of the material, and therefore porosity heterogeneities are to be expected.

The microstructural analysis clearly shows that deformation was spatially heterogeneous, and indicative that Allende experienced locally heterogeneous (stress, temperature) conditions. Olivine deforms crystal-plastically in response to stress at high temperatures. This is achieved by the activity of several possible dislocation slip systems, and it is well established that distinct slip systems operate in different environmental conditions (e.g. stress, temperature, H2O activity) for terrestrially deformed olivine (Karato et al., 2008). Operation of different slip systems produces different types of crystallographic fabric, which can be identified by trends in clustering in lower-hemisphere, equal-area plots of the EBSD data (Karato et al., 2008). Therefore, quantification of fabrics may be used to infer temperature and pressure conditions at the time of fabric generation. Using this approach, we can deduce that the variable slip-systems identified within

the chondrules and AOA probably reflected heterogeneous stress and temperature conditions throughout the sample. Most slip systems within matrix grains are indicative of deformation under dry and low-moderate stress conditions, with some variation to higher-stress slip systems (Karato et al., 2008). M-1 and M-2 presented a weak A-type fabric when compared with Karato et al.'s (2008) classification system, where M-3 displayed a D-type fabric. The fabric types indicated high temperatures (>1470 K) and low stresses (0–350 MPa) at sites M-1 and M-2, and moderate temperature (1200–1470 K) and stress (>350 MPa) conditions at M-3 (Karato et al., 2008). Sites M-1 and M-2 were situated away from chondrules, whereas M-3 was very close to and between two chondrules and so higher stresses may be expected. However, the lack of high-pressure phases and mosaicism of LABs in the sample limit the shock pressures at time of deformation to below 10 GPa (Langenhorst, 2002). There has been some speculation that the presence of pores prior to compaction allows for higher-temperature slip-systems to activate in olivine when compared with zero-porosity samples (Goetze and Poirier, 1978). Therefore, it is possible that higher-temperature slip-systems may have activated in highly porous regions of the sample.

The microstructures observed in this sample of Allende and other evidence can be used to evaluate several different models for the compaction of Allende. An early theory highlighted a static force, such as burial compaction due to gravity, as a possible source of compression (Fujimara et al., 1983). The microstructural features we have observed in this study do not indicate that this is the compaction mechanism; the asymmetry in large grain deformation indicates localised compaction from one direction, not multiple directions. The slip systems that activated within the grains are widely varied, but some require heating beyond 1450 °C; in the case of lithostatic compaction, heating is expected to be continuous for the duration of the slow compaction process as pores are continuously destroyed. If temperatures of 1450 °C were achieved for any length of time, widespread melting would have occurred, which has not been observed. A lack of overprinting in the microstructures also implies all structural features were generated at the same time; compaction due to lithostatic forces would result in microstructures forming over longer time periods, and therefore we might expect to see cross-cutting deformation relationships. At a larger scale, Allende's tensile strength is approximately 28 MPa in its currently compressed form (Svetsov et al., 1995). This strength may be surpassed in the centre of a planetary body with a radius greater than approximately 300 km and, therefore, lithostatic pressure may result in the compaction observed if Allende sampled the centre of a planetary body. However, this mechanism is unable to explain the asymmetry of deformation in the chondrules and distribution of porosity and crystal-plasticity in the matrix grains. Porosity reduction under these conditions should

have orthorhombic symmetry. Overburden-related stresses in small planetary bodies are unlikely to be high enough to activate slip systems responsible for the observed fabrics in the matrix olivine in Allende. Furthermore, Allende is a primitive meteorite of petrologic type 3, and if it originates from the centre of a planetary body, it would not remain in a primitive state. A number of CO, CR and CM meteorites have lower porosities than Allende (Macke et al., 2011), and so if the same principle applies to their deep origin on their respective parent bodies, many asteroids would have been completely destroyed to create a number of meteorites in our collections. The oxidised CV subclass (e.g. Allende) is significantly less compacted than the reduced CV subclass (20% porosity compared with ~5% porosity) (Macke et al., 2011), but the oxidised samples present significantly higher metamorphism. We would expect the inverse relationship to be evident where lithostatic overburden forces are dominant. There are currently asteroids in our solar system that appear to be of low bulk density when compared with their likely meteorite equivalents (Britt et al., 2002); this suggests that these bodies are still highly porous, and so a planet-wide compaction process is further unlikely. Gravitational compressional forces generate gradual and continuous heating and were likely involved in the early heating of the body and initial stages of lithification. Therefore, we believe that it is improbable that lithostatic overburden could have generated the compressional microstructures, but possibly contributed to overall lithification.

Consequently, we consider the case of dynamic and rapid compressional forces during impact events in the creation of the aforementioned microstructures. The asymmetric distribution of strain (i.e., crystal-plastic deformation and porosity reduction) around chondrules and AOA grains, and highly heterogeneous stresses and temperatures inferred from operative slip systems are consistent with numerical simulations of impacts at these scales (Davison et al., 2010, Davison et al., 2014 and Bland et al., 2014). We observed a varied yet generally greater intensity of deformation in small matrix grains when compared with large chondrule and AOA grains; given a rapid loss of pore space upon compaction generates a temperature increase, the matrix would likely experience more heat than chondrules, and consequently would be more deformed relative to the large low-porosity grains. The preferential orientation of LAB planes and crystallographic preferred orientation in the matrix grains can be readily explained by differential heating between chondrules and matrix during a single moderate-strong impact event, which would consequently reduce bulk porosity. Microstructural evidence also indicates an instantaneous and rapid compressional force is responsible.

Allende has a lack of macrostructure shock features that previously suggested it was unaffected by impact, however as a result

of porosity loss, any further impacts post-compaction are unlikely to cause substantial compression or generate compaction-related shock features (Sharp and DeCarli, 2006, Davison et al., 2010 and Bland et al., 2014). Compaction via impact is a much simpler scenario when compared with lithostatic overburden; it is unlikely that a large number of asteroids were completely destroyed to produce the samples in our vast meteorite collections, and low-velocity collisions into small planetary bodies are much more common and easier to achieve (Housen and Holsapple, 2011 and Beitz et al., 2013). At a planetary scale, samples originating closer to the asteroid surface would show more evidence of metamorphism when compared with samples at depth on the parent body following impact processing; this is reflected in the properties of oxidised and reduced CV class meteorites, where higher porosities and significant metamorphism are observed in oxidised samples compared with reduced samples. In situ evidence of impacts into highly porous bodies has been found on C-type asteroid Mathilde; whilst CV meteorites may not originate from C-type asteroids (Bell, 1988), the principal of impacts into early, highly porous bodies is well supported by this prior research (Housen et al., 1999, Cheng and Barnouin-Jha, 1999 and Housen and Holsapple, 2011). Furthermore, conclusions from impact compaction studies that correlate compaction pressures with overall shock stages for each carbonaceous chondrite class support our findings (Weidenschilling and Cuzzi, 2006; Beitz et al., 2013).

Shock wave attenuation into a polymineralic and porous media has been shown to induce shear heating at grain boundary contacts (Gillet and Goresy, 2013). We predict Allende to have experienced no more than 10 GPa based on the absence of high-pressure polymorphs and mosaicism in the olivine grains. At this pressure, we expect that Allende would have begun to melt at 1600 °C, but at lower pressures heating to 1150 °C could have induced melting (Agee et al., 1995). The microstructural features presented indicate that these grains did not experience such temperatures, but shear heating may have been more pronounced at the grain boundaries, resulting in grain sintering, lithification and strengthening of Allende. The geometry of deformation seen in the matrix does show potential evidence of shear processing (Fig. 2.5), whereby LABs parallel to the direction of compression have formed. Additionally, the lower edges of C-1 and C-3 (Fig. 2.2) appear fragmented from the rest of the surrounding material, which could indicate that shear-induced disaggregation has occurred. Experiments examining the sintering behaviour of olivine have found that it is favoured where a fine-grained (micrometre-scale) aggregate is rapidly heated to high T: an analogous scenario to that encountered by a high porosity matrix during impact-induced compacxtion (Cooper and Kohlstedt, 1984). Weak evidence of this can be found in Allende (Fig. 2.6), where grains

have a higher amount of deformation at their contact margin. However, understanding the intricacies of lithification in this sample is beyond the scope of this paper and should be examined at higher resolution in future work.

The local and regional pressure and temperature anomalies over distances of 10–100 μm can be attributed to interactions of shock waves in the bimodal, porous medium, resulting in heterogeneous deformation. The simulations described by Bland et al. (2014) reveal that low-velocity impacts of 2 km/s in a material of 70% matrix, 30% chondrule result in peak pressures in chondrules of ≈6.5 GPa, but with predicted post-shock heating temperatures of 370 K in chondrules, and 1100 K in the matrix. These models also yield large disparities in peak pressure between matrix and chondrules; chondrule interiors realistically experience 4–5 GPa, chondrule edges approximately up to 8 GPa, and over only 100 μm within the matrix, a pressure range of 7–18 GPa may arise (Bland et al., 2014). Whilst peak pressures cannot be directly compared with our data, comparisons with the modelled first order approximations of corresponding strain distribution are more analogous. Acknowledging the limitations of the simulations to be able to capture the complexity of olivine rheology exactly, the strain in the modelled 1.0 km/s and 1.5 km/s scenarios (<2 GPa bulk shock pressure) show the strongest similarity to the observed chondrule deformation from EBSD mapping (Fig. 2.2, Fig. 2.3 and Fig. 2.4). First-order predictions of the higher intensity strain in the matrix are also consistent with observations from EBSD mapping (Fig. 2.5 and Fig. 2.6). These outcomes suggest the modelling accurately predicts the response of a bimodal sample to compression and we infer impacts are responsible for the petrographic features described.

6. CONCLUSIONS

EBSD analysis in this study of Allende has revealed the following:

1. Crystal-plastic deformation at the margins of chondrule grains, commonly with an asymmetric distribution (in the context of all figures shown).

2. A lack of crystal-plastic deformation within chondrule interiors (<1°).

3. High degrees of crystal-plastic deformation throughout matrix olivine grains (up to 20° of misorientation). This deformation was spatially heterogeneous, with asymmetric zones of intense deformation close to chondrules.

4. A dominance of LABs in matrix olivine grains with strongly preferred boundary plane orientations in the reference frame of the sample surface.

We conclude Allende has been compacted via impact processing. Planar shock modelling shows a low impact velocity of a few km/s into a 50% bulk porosity target material is sufficient to produce the features present. The effect of the temperature difference between the two components following impact is large and significant; however, such expected low pressures (1–1.3 GPa, Bland et al., 2014) are unlikely to have produced

petrographic shock evidence traditionally observed in chondrules. Matrix grains are the key to understanding the magnitude of the compaction-inducing impact, as they show preservation of compaction-related deformation and provide a more accurate representation of peak temperatures and stresses.

7. ACKNOWLEDGMENTS

This work was funded by the Australian Research Council via their Australian Laureate Fellowship programme (FL110100074) (PAB). This research was supported by the Curtin International Postgraduate Research Scholarship awarded to LF and LD, and GKB acknowledges support from Curtin University via their Research Fellowship scheme. GSC and TMD acknowledge funding from the UK Science and Technology Facilities Council STFC grant ST/J001260/1. The authors would also like to acknowledge the technical assistance and use of facilities at John de Laeter Microscopy centre, at Curtin University; the Australian Synchrotron XFM beamline, and the University of Sydney node of the Australian Microscopy & Microanalysis Research Facility: Sydney Microscopy & Microanalysis. The authors would like to thank the handling editor and anonymous reviewer for their constructive comments in the review process.

8. REFERENCES

Beitz E., Guettler, C., Nakamura, A. M., Tsuchiyama, A., & Blum, J. (2013). Experiments on The Consolidation Of Chondrites and the Formation of Dense Rims Around Chondrules. Icarus, 225(1), 558–569.

Bland P. A., Howard, L. E., Prior, D. J., Wheeler, J., Hough, R. M., & Dyl, K. A. (2011). Earliest Rock Fabric Formed in the Solar System Preserved in a Chondrule Rim. Nature Geoscience, 4(4), 244–247.

Bland P. A., Collins, G. S., Davison, T. M., Abreu, N. M., Ciesla, F. J., Muxworthy, A. R., & Moore, J. (2014b). Pressure–Temperature Evolution of Primordial Solar System Solids During Impact-Induced Compaction. Nature Communications, 5, 5451.

Blum J. (2003) The Structure of Planetesimals in the Solar Nebula (abstract #5152) Meteoritics & Planetary Science 38 (Suppl.):A83

Bowling T. J. (2015). Global Surface Modification of Asteroid 4 Vesta Following the Rheasilvia Impact. PhD Thesis. Purdue University.

Brenker F. E., Palme H. & Klerner S. (2000) Evidence for Solar Nebula Signatures in the Matrix of the Allende Meteorite. Earth & Planetary Science Letters, 178, 185-194.

Cain P. M., McSween H. Y. & Woodward N. B. (1986). Structural Deformation of the Leoville Chondrite. Earth & Planetary Science Letters, 77, 165–175.

Consolmagno G. J., Britt, D. T., & Stoll, C. P. (1998). The Porosities of Ordinary Chondrites: Models and Interpretation. Meteoritics & Planetary Science, 33(6), 1221–1229. Consolmagno G. J. & Britt D. T. (2004) Meteoritical Evidence and Constraints on Asteroid Impacts and Disruption. Planetary Space Science, 52, 1119-1128.

Cuzzi J. N. and Weidenschilling S. J. (2006) Particle-Gas Dynamics and Primary Accretion. In Meteorites and the Early Solar System II (D. S. Lauretta and H. Y. McSween Jr., eds.), Univ. of Arizona, Tucson, 353-381.

Cuzzi J. N., Hogan R. C., & Shariff K. (2008). Toward Planetesimals: Dense Chondrule Clumps in the Protoplanetary Nebula. The Astrophysical Journal, 687, 1432.

Davison T. M., Ciesla F. J., & Collins G. S. (2012). Post-Impact Thermal Evolution of Porous Planetesimals. Geochimica et Cosmochimica Acta, 95, 252–269.

Davison T. M., Collins, G. S., & Bland, P. A. (2014). Mesoscale Numerical Modelling of Compaction of Primitive Solar System Solids in Low-Velocity Collisions. 45th Lunar and Planetary Science Conference, Abstract #2718.

Davison T. M., Collins, G. S., & Ciesla, F. J. (2010). Numerical Modelling of Heating in Porous Planetesimal Collisions. Icarus, 208(1), 468–481.

Dodd R. T., & Jarosewich, E. (1979). Incipient Melting in and Shock Classification of L- Group Chondrites. Earth and Planetary Science Letters, 44(2), 335–340.

Dominik C., & Tielens, A. G. G. M. (1997) The Physics of Dust Coagulation and the Structure of Dust Aggregates in Space. The Astrophysical Journal, 480(2), 647.

Dyl K. A., Cleverley J. S., Bland P. A., Ryan C. G., Fisher L. & Hough R. M. (2014) Quantified, Whole Section Trace Element Mapping of Carbonaceous Chondrites by Synchrotron X-Ray Fluorescence Microscopy: 1. CV Meteorites. Geochimica et Cosmochimica Acta, 134(4), 1176-1180.

Fisher L. A., Fougerouse D., Cleverley J. S., Ryan C. G., Micklethwaite S., Halfpenny A., Hough R., Gee M., Paterson D., Howard D. L. & Spiers, K. (2014) Quantified, multi- scale X-ray fluorescence element mapping using the Maia detector array: application to mineral deposit studies, Mineralium Deposita.

Fliervoet, T. F., Drury, M. R., & Chopra, P. N. (1999). Crystallographic preferred orientations and misorientations in some olivine rocks deformed by diffusion or dislocation creep. Tectonophysics, 303 (1), 1-27.

Fujimara A., Kato M. & Kamazawa M. (1983) Preferred orientation of phyllosilicate (001) in matrix of Murchison meteorite and possible mechanisms of generating the oriented texture in chondrites. Earth & Planetary Science Letters, 66, 25-32.

Gattacceca, J., Rochette, P., Denise, M., Consolmagno, G., and Folco, L., 2005, An impact origin for the foliation of chondrites: Earth and Planetary Science Letters, v. 234, no. 3-4, p. 351–368.

Goetze, C., & Poirier, J. P. (1978). The mechanisms of creep in olivine [and discussion].Philosophical Transactions of the Royal Society of London A: Mathematical, Physicaland Engineering Sciences, 288 (1350), 99-119.

Gray, E. M. (2013) Deformation of Earth's upper mantle: insights from naturally occurring fabric types. Diss. PhD Thesis Curtin University, pp 327.

Hansen, L. N., Zimmerman, M. E. & Kohlstedt, D. L. (2012). The influence of microstructure on deformation of olivine in the grain boundary sliding regime. Journal of Geophysical Research: Solid Earth (1978–2012), 117 (B9).

Hayashi C., Nakazawa, K., & Nakagawa, Y. (1985) Formation for the Solar System, in Protostars and Planets II, eds. D.C. Black and M.S. Matthews, Univ. Arizona Press,Tuscon. Ariz. 1100-1154.

Johansen A., Oishi, J. S., Mac Low, M.-M., Klahr, H., Henning, T., & Youdin, A. (2007). Rapid Planetesimal Formation in Turbulent Circumstellar Discs. Nature, 448, 1022.

Johansen A., Youdin, A., & Mac Low, M.-M. (2009). Particle Clumping and Planetesimal Formation Depend Strongly on Metallicity. Astrophysical Journal Letters, 704(2), L75-L79.

Karato S., Haemyeong J., Katayama I. & Skemer P. (2008) Geodynamic Significance of Seismic Anisotropy of the Upper Mantle: New Insights from Laboratory Studies. Annual Review of Earth & Planetary Science, 36, 59-95.

Keil K., Stöffler, D., Love, S. G., & Scott, E. R. D. (1997). Constraints on the Role of Impact Heating and Melting in Asteroids. Meteoritics & Planetary Science, 32(3), 349–363.

Kohlstedt, D. L. & Goetze, C. (1974). Low-stress high-temperature creep in olivine single crystals. J. geophys. Res, 79 (14), 2045-2051.

McSween H. R. (1979). Are Carbonaceous Chondrites Primitive or Processed? A Review. Rev. Geophysics & Space Physics, 17 (1059), 1075.

Macke R. J., Britt, D. T., & Consolmagno, G. J. (2011). Density, Porosity, and Magnetic Susceptibility of Achondritic Meteorites. Meteoritics & Planetary Science, 46(2), 311–326.

Nakamura T., Tomeoka K. & Takeda H. (1992) Shock Effects of the Leoville CV Carbonaceous Chondrite: A Transmission Electron Microscope Study. Earth & Planetary Science Letters, 114, 159-170.

Poirier J. P. (1975) On the Slip Systems of Olivine. Journal of Geophysical Research, 80 (29), 4059-4061.

Prior, D. J., Wheeler, J., Peruzzo, L., Spiess, R., & Storey, C. (2002). Some garnet microstructures: an illustration of the potential of orientation maps and misorientation analysis in microstructural studies. Journal of Structural Geology, 24(6), 999-1011.

Rubin A. (2004) Postshock Annealing And Postannealing Shock In Equilibrated Ordinary Chondrites: Implications for the Thermal and Shock Histories of Chondritic Asteroids. Geochimica et Cosmochimica Acta, 68(3), 673-689

Scott E. R. D., Keil, K., & Stöffler, D. (1992). Shock Metamorphism of Carbonaceous Chondrites. Geochimica et Cosmochimica Acta, 56 (12), 4281–4293.

Scott E. R. D. (2002) Meteorite Evidence for the Accretion and Collisional Evolution of Asteroids. In Asteroids III eds. W. F. Bottke et al., Univ. of Arizona, Tucson,

Sharp T. G., & DeCarli, P. S. (2006). Shock Effects in Meteorites, in Meteorites and the Early Solar System II. eds Lauretta D. S., McSween H. Y. Jr., Univ. Arizona Press, 653–677.

Stacey F. D., Lovering J. F., & Parry L. G. (1961). Thermomagnetic Properties, Natural Magnetic Moments, and Magnetic Anisotropies of some Chondritic Meteorites. Journal of Geophysical Research, 66, 1523–1534.

Stöffler D., Keil, K., & Scott, E. (1991). Shock Metamorphism of Ordinary Chondrites. Geochimica et Cosmochimica Acta, 55(12), 3845–3867.

Töpel-Schadt J. & Müller W. F. (1985) The Submicroscopic Structure Of The Unequilibrated Ordinary Chondrites Chainpur, Mezo_Madaras and Tieschitz: A Transmission Electron Microscope Study. Earth & Planetary Science Letters, 74, 1-12.

Trimby, P.W., (2012) Orientation mapping of nanostructured materials using transmission Kikuchi diffraction in the scanning electron microscope. Ultramicroscopy 120, 16-24. Trimby, P.W., Cao, Y., Chen, Z., Han, S., Hemker, K.J., Lian, J., Liao, X., Rottmann, P.,

Samudrala, S., Sun, J., Wang, J.T., Wheeler, J. & Cairney, J.M. (2014) Characterizing deformed ultrafine-grained and nanocrystalline materials using transmission Kikuchi diffraction in a scanning electron microscope. Acta Materialia 62, 69-80.

Watt L., Bland P. A., Prior D. J. & Russell S. S. (2006) Fabric Analysis of Allende Matrix using EBSD. Meteoritics & Planetary Science, 41, 989-1001.

Weidenschilling S. J. (2011). Initial Sizes of Planetesimals and Accretion of the Asteroids. Icarus, 214(2), 671–684.

Weidenschilling S. J. & Cuzzi, J. (2006) Accretion Dynamics and Timescales: Relation to chondrites. In Meteorites and the Early Solar

System II, eds Lauretta D. S., McSween H. Y. Jr., Univ. Arizona Press, 473-485.

Weisberg M. K., McCoy, T. J., & Krot, A. N. (2006). Systematics and Evaluation of Meteorite Classification. in Meteorites and the Early Solar System II (Vol. 2), eds Lauretta D. S., McSween H. Y. Jr., Univ. Arizona Press, 653–677.

Wetherill G. W., & Stewart, G. R. (1989). Accumulation of a Swarm of Small Planetesimals. Icarus, 77, 350-357.

Wurm G., Krauss, O., & Paraskov, G. (2004) On the Importance of Gas Flow Through Porous Bodies for the Formation of Planetesimals. The Astrophysical Journal, 606(2), 983-987.

Zolensky M. E., Mittlefehldt D. W., Lipschutz M. E., Wang M. S., Clayton R. N., Mayeda T. K., Grady M. M., Pillinger C., and Barber D. (1997). CM Chondrites Exhibit the Complete Petrologic Range from Type 2 to 1. Geochimica et Cosmochimica Acta, 61, 5099–5115.

9. SUPPLEMENTARY MATERIAL

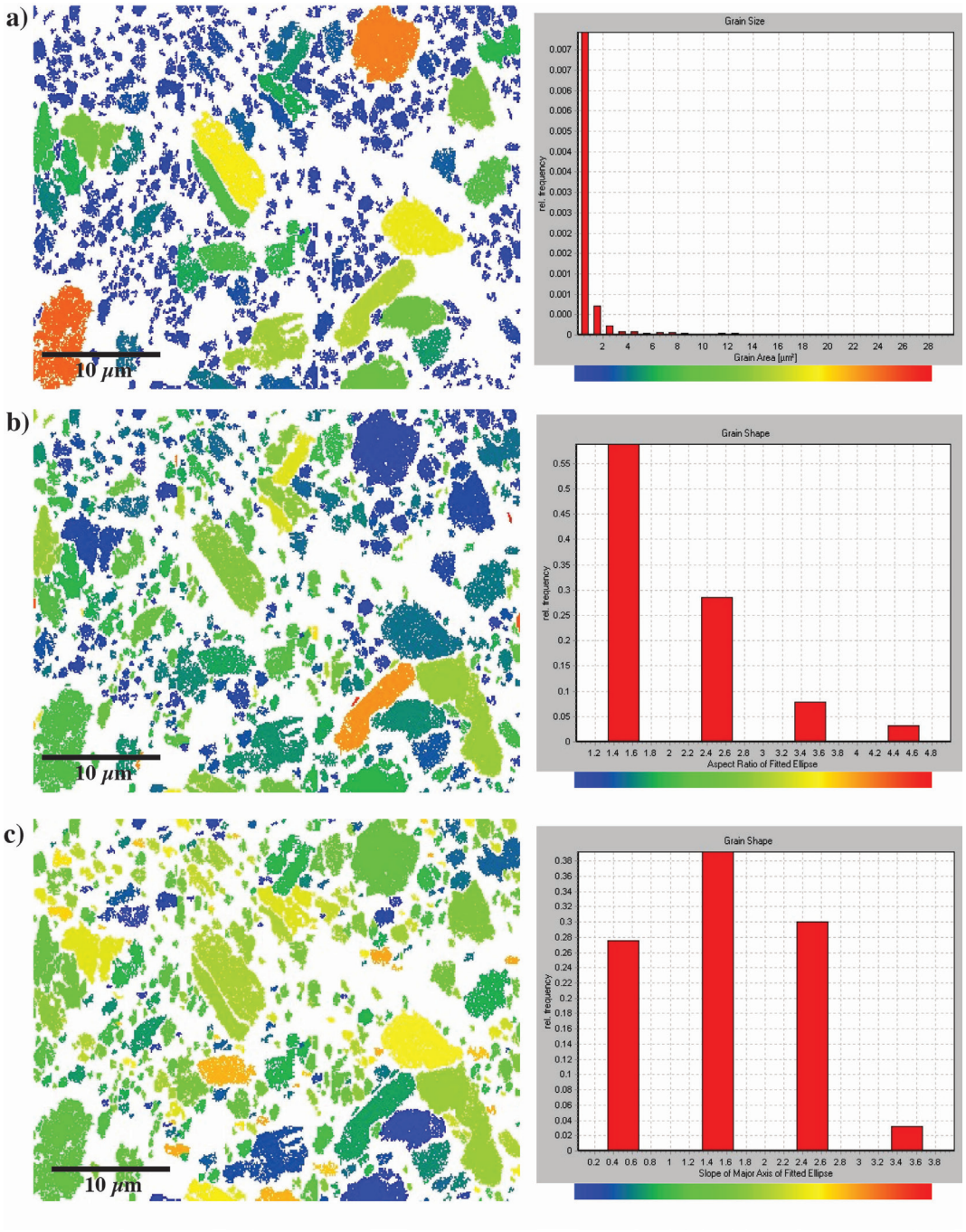

Supplementary Figure 2.1: *Maps of site M-1: a) Grain area map; b) Grain shape map (aspect ratio); c) Grain Shape map (slope).*

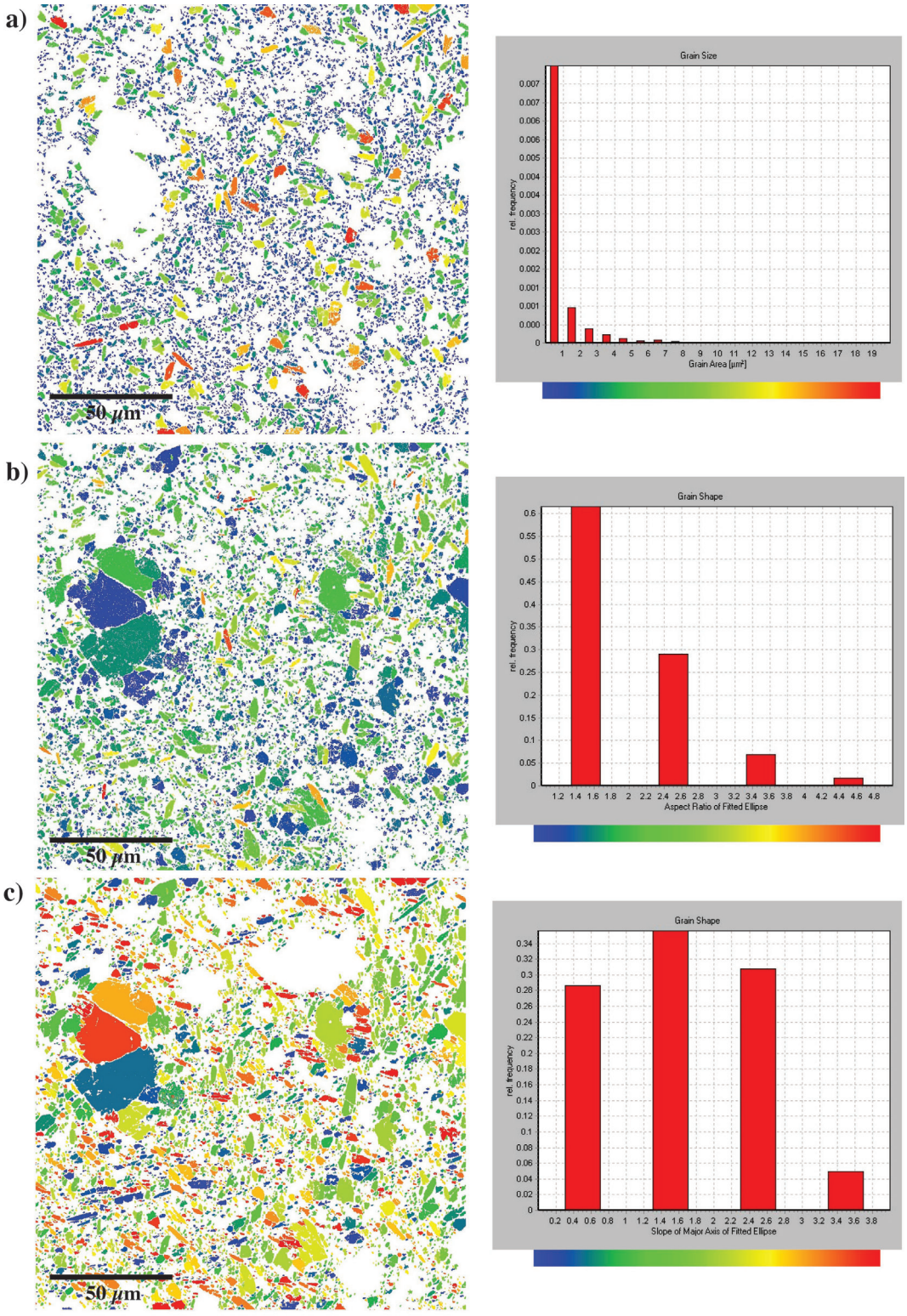

Supplementary Figure 2.2: *Maps of site M-2: a) Grain area map; b) Grain shape map (aspect ratio); c) Grain Shape map (slope).*

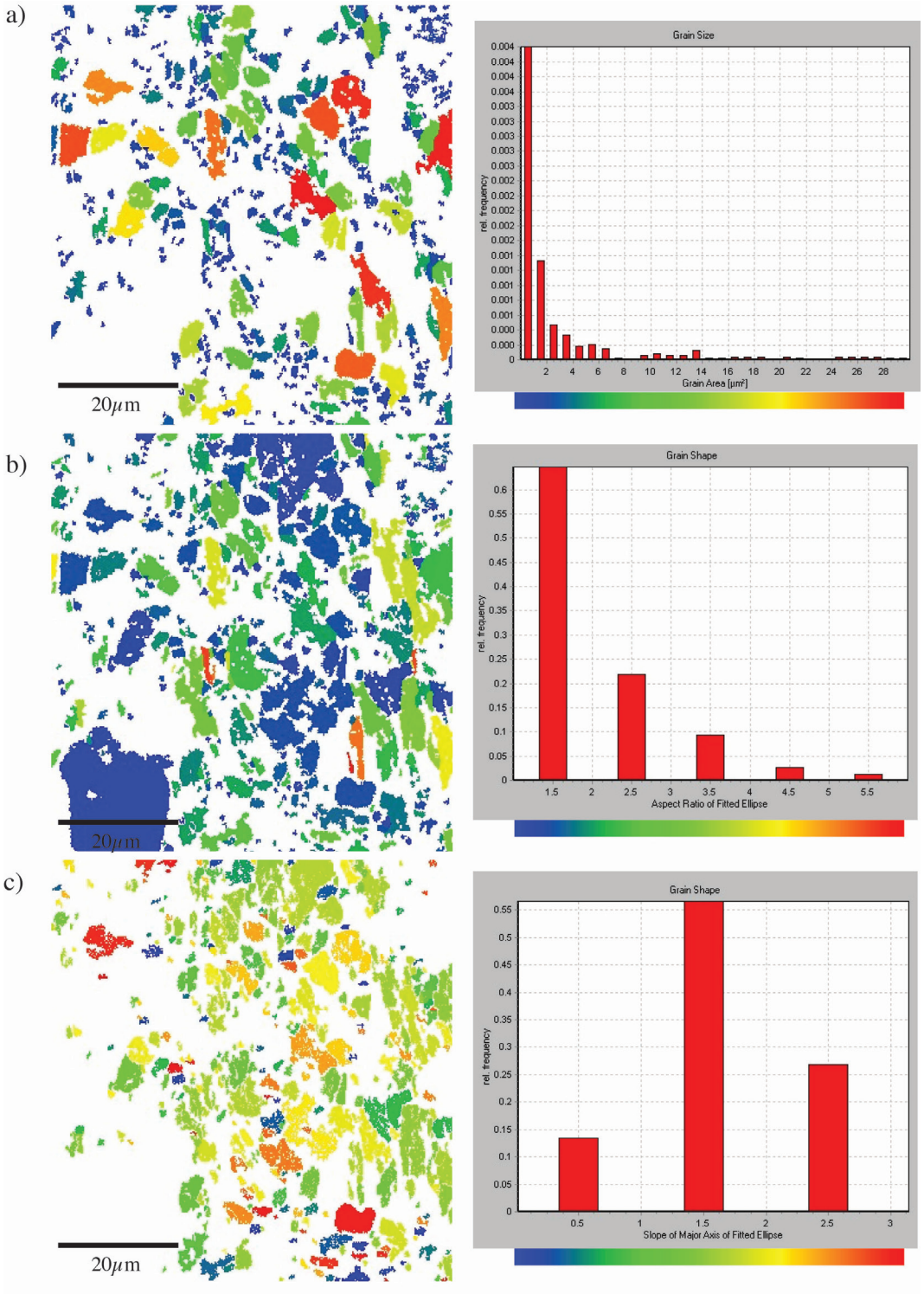

Supplementary Figure 2.3: *Maps of site M-3: a) Grain area map; b) Grain shape map (aspect ratio); c) Grain Shape map (slope).*

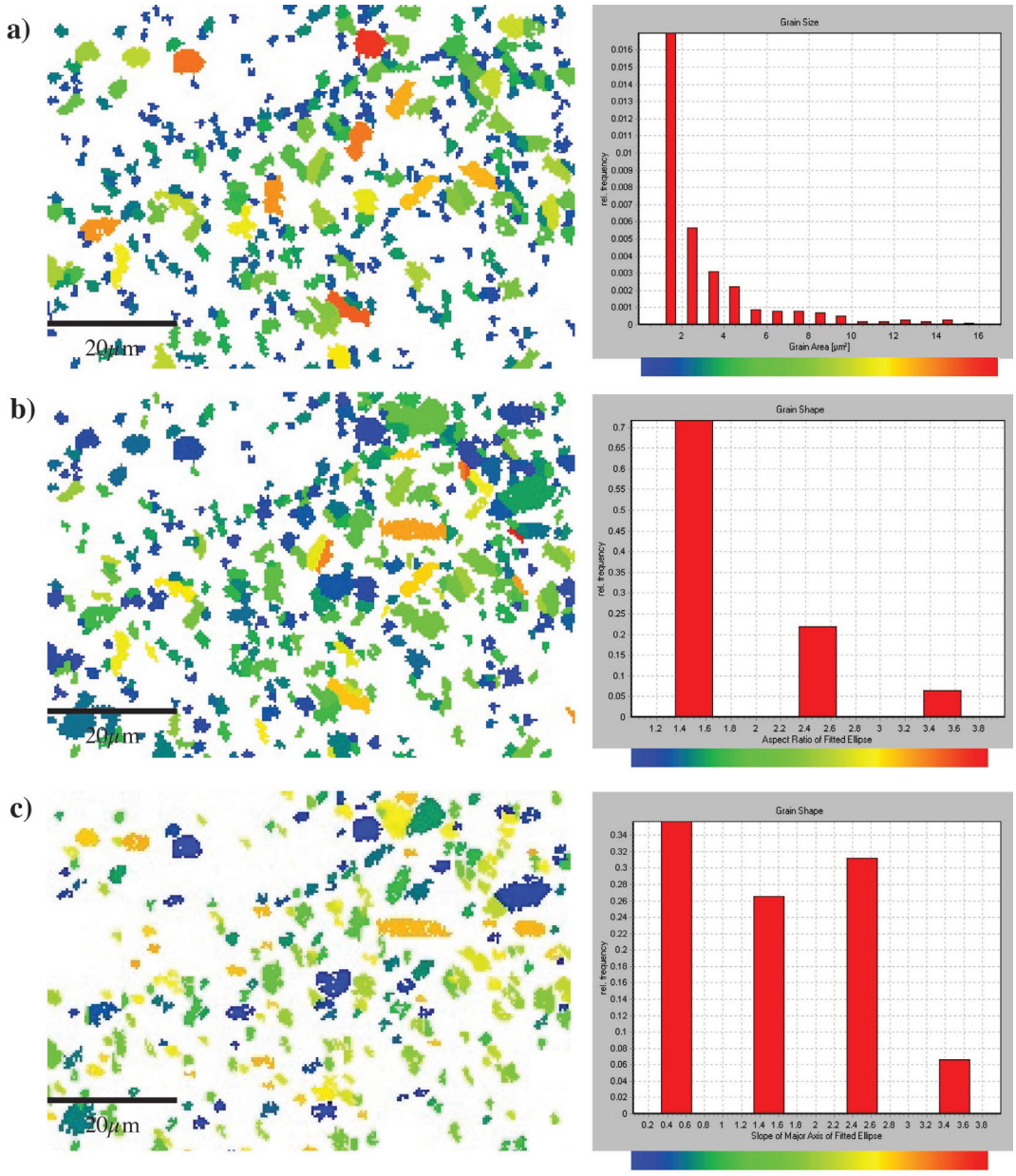

Supplementary Figure 2.4: *Maps of site M-4: a) Grain area map; b) Grain shape map (aspect ratio); c) Grain Shape map (slope).*

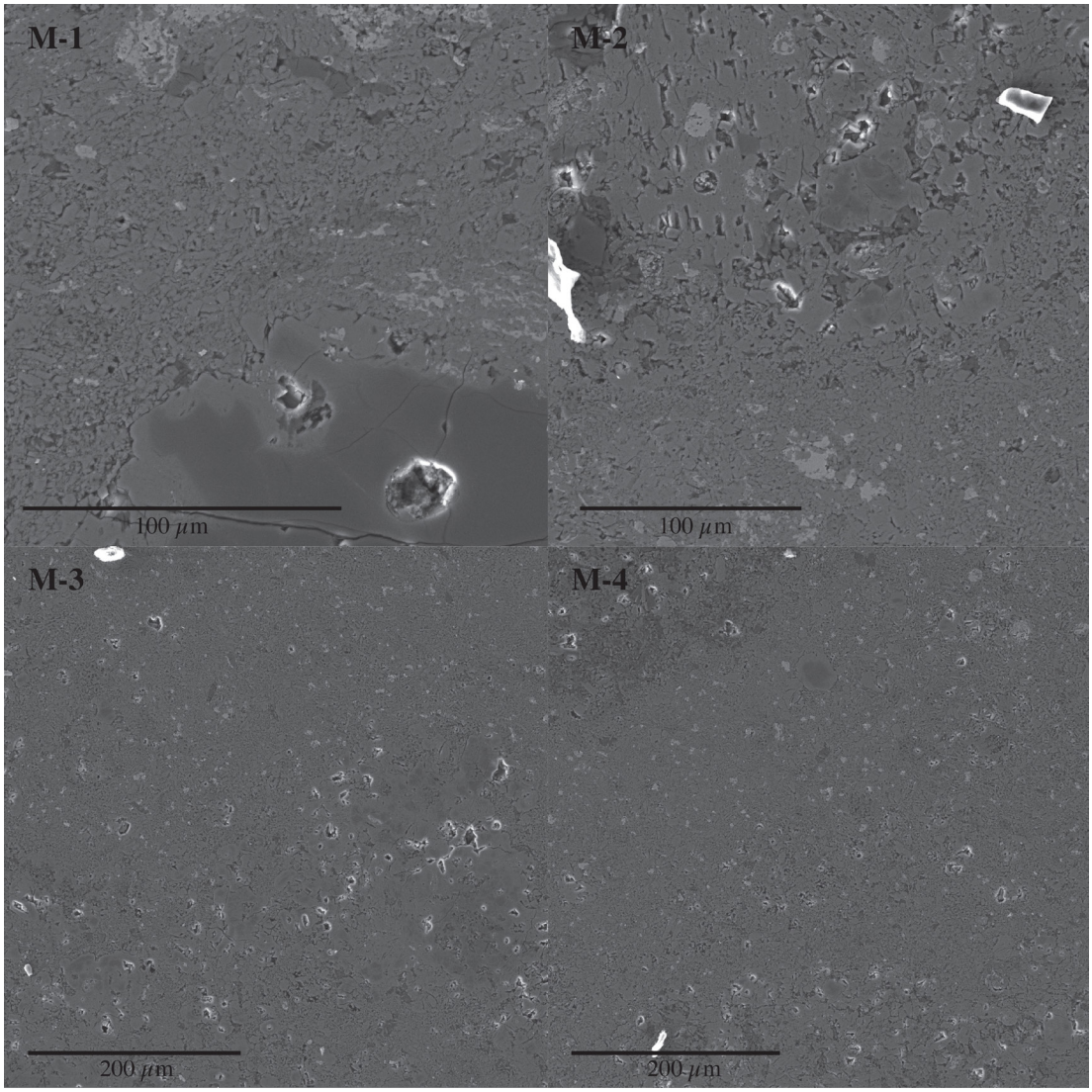

***Supplementary Figure* 2.5:** *Secondary Electron (SE) images of each matrix site (1–4). Even at different scales the porosity appears variable with localised high and low porosities present.*

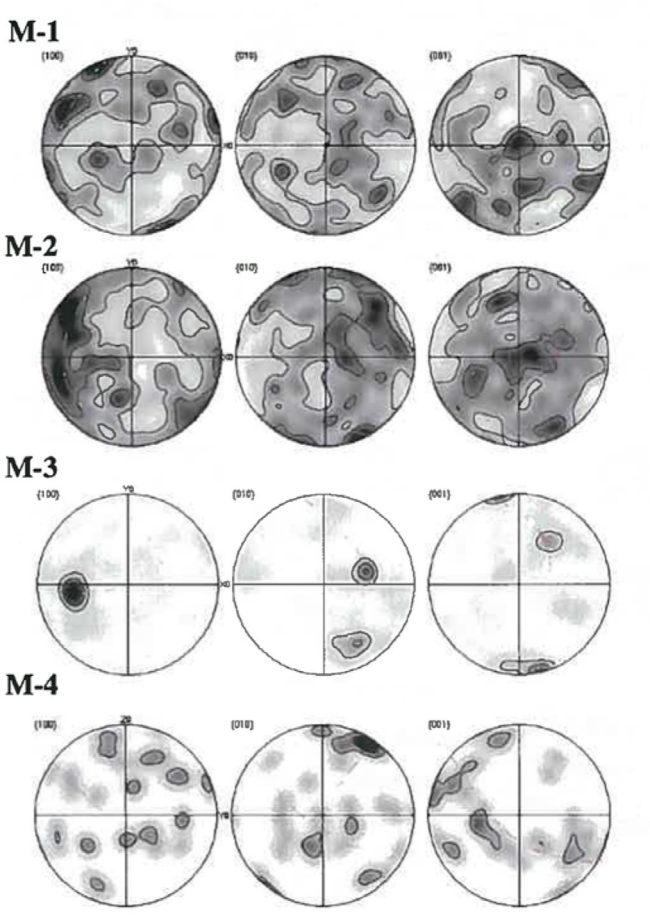

	Number of points	Max. MUD	Average grain size (μm)
M-1	281	3.34	0.835
M-2	2060	1.93	1.006
M-3	315	17.83	1.531
M-4	34	8.71	1.838

Supplementary Figure 2.6: *Crystallographic Preferred Orientation (CPO) equal area, lower hemisphere plots for each matrix site and associated grain statistics.*

Chapter 3

Defining the Mechanism for Compaction of the CV Parent Body

The following chapter has been published in GEOLOGY. The original format has been modified for the purposes of this thesis, but all content remains the same.

L. V. Forman[1], P. A. Bland[1], N. E. Timms[1], L. Daly[1], G. K. Benedix[1], P. W. Trimby[2], G. S. Collins[3] & T. M. Davison[3], 2017, Defining the Mechanism for Compaction of the CV Parent Body: Geology, v. 45, no. 6, p.559-562.

[1]Department of Applied Geology, Curtin University, GPO Box U1987, Perth, WA 6845, Australia.

[2]Australian Centre for Microscopy and Microanalysis, University of Sydney, Room 234, Madsen Building F09, NSW 2006, Australia.

[3]Impact and Astromaterials Research Centre, Department of Earth Science & Engineering, Imperial College London, Prince Consort Road, South Kensington, SW7 2BJ, United Kingdom.

1. ABSTRACT

The Allende meteorite, a relatively unaltered member of the CV carbonaceous chondrite group, contains primitive crystallographic textures that can inform our understanding of early Solar System planetary compaction. To test between models of porosity reduction on the CV parent body, complex microstructures within ~0.5-mm-diameter chondrules and ~10-μm-long matrix olivine grains were analyzed by electron backscattered diffraction (EBSD) techniques. The large area map presented is one of the most extensive EBSD maps to have been collected in application to extraterrestrial materials. Chondrule margins preferentially exhibit limited intragrain crystallographic misorientation due to localized crystal-plastic deformation. Crystallographic preferred orientations (CPOs) preserved by matrix olivine grains are strongly coupled to grain shape, most pronounced in shortest dimension <a>, yet are locally variable in orientation and strength. Lithostatic pressure within plausible chondritic model asteroids is not sufficient to drive compaction or create the observed microstructures if the aggregate was cold. Significant local variability in the orientation and intensity of compaction is also inconsistent with a global process. Detailed microstructures indicative of crystal-plastic deformation are consistent with brief heating events that were small in magnitude. When combined with a lack of sintered grains and the spatially heterogeneous CPO, ubiquitous hot isostatic pressing is unlikely to be responsible. Furthermore, Allende is the most metamorphosed CV chondrite, so if sintering occurred at all on the CV parent body it would be evident here. We conclude that the crystallographic textures observed reflect impact compaction and indicate shock-wave directionality. We therefore present some of the first significant evidence for shock compaction of the CV parent body.

2. INTRODUCTION

Meteorites in our collections sample both planets and small bodies within the inner Solar System. However, the process driving the lithification of these small bodies, specifically chondritic asteroids, is still debated. Meteorites preserve metamorphic textures that do not represent their state of accretion on the parent body, specifically their initial porosity (Consolmagno et al., 2008). It is therefore important to assess the microstructural evolution from high-porosity primordial materials to low-porosity meteorites.

Gravitational forces on chondritic asteroids have been proposed as a mechanism to compact a highly porous body into lithified rock (Fujimura et al., 1983), as well as being potentially associated with considerable planetary-scale heating (Horedt, 1980). However, lithostatic pressure is low, even in objects 100s km across (Weidenschilling and

Cuzzi, 2006). The weak effect of stress bridging between grains would likely equilibrate over long time periods. We infer that the resultant CPOs from this process would be weak but homogeneous throughout the sample, and intragrain deformation would be weak or absent. If cold compaction occurred, then brittle deformation textures may arise, and there would likely be a coupling of the CPO and shape preferred orientations (SPOs) of the grains, owing to the lack of heat to encourage grain shape modification.

As an alternative model to a pure mechanical compaction, cold compaction followed by radiogenic heating primarily by ^{26}Al is proposed to result in sintering of the primitive grains and parent body compaction (Gail et al., 2015). This is termed hot isostatic pressing (HIP), and is predicted to occur over ~1 m.y. (Gail et al., 2015). Olivine matrix grains are predicted to be sintered at 650–700 K by surface diffusion, and chondrules at >900 K by dislocation creep (Gail et al., 2015). We would therefore observe consistent and homogeneous CPOs throughout the sample reflecting the planet-wide process and predicted timeframe. If surface diffusion has modified the shape of the matrix olivine grains due to growth into available pore space (Carter & Norton, 2013), the SPOs would likely be decoupled from the CPOs.

Porosity reduction in primordial chondritic asteroids may also have occurred through impact-induced compaction (Bland et al., 2014; Hanna et al., 2015; Davison et al., 2016). The shock wave produced by an impact into a porous body propagates through the medium resulting in rapid pore collapse and localized pressure excursions over timescales of a few microseconds to seconds. Crystallographic deformation is predicted to be concentrated in initially porous regions and at the edges of chondrules, and weak, heterogeneous and localized CPOs are likely to occur (Davison et al., 2016). Similar to cold compaction, SPOs and CPOs are expected to be coupled due to the very short timescale for heating.

We examined the CV3 carbonaceous chondrite, Allende, at microscales and meso-scales to understand the microstructural deformation and CPOs generated on the CV chondrite parent body. Allende has undergone relatively little aqueous alteration, and still contains anhydrous matrix material (although it has been at relatively higher metamorphic temperatures than other CV meteorites (Krot et al., 1998; Bonal et al., 2006)). In terms of impact processing, it is classified as an unshocked S1 (Scott et al., 1992). Previous microstructural analyses of the fine-grained matrix grains of Allende (<5 μm (Scott et al., 1988)) have focused on localized CPOs around individual chondrules (Watt et al., 2006; Hanna et al., 2015) and crystal-plastic deformation microstructures of selected individual chondrules, calcium-aluminum inclusions (CAIs) and matrix grains (Forman et al., 2016). Modeling of impact-induced compaction mapped the response of the chondritic medium to impact over a much larger area (256 mm^2) (Davison

et al., 2016). Micro-scale observations from previous studies are therefore difficult to compare to modeling predictions. In this paper, crystallographic textures at meso- and micro-scales were systematically examined over a large area of 6 mm^2, incorporating numerous chondrules and matrix regions. This provided a quantitative visualization of how the parent body of Allende responded to compaction, and facilitated direct comparisons with numerical simulations of different compaction processes.

3. METHODOLOGY

An 8 mm^2 area of Allende (from sample WAM 13102) was mapped to obtain phase and crystallographic data (Supp. Fig. 3.1) at a step size of 0.5 μm over 380 h, resulting in the collection of 46 x 10^6 electron backscatter diffraction patterns, representing one of the largest EBSD data sets ever collected from a single area. (Further details are provided in the data repository.)

A 6 mm^2 area of the mapped region was subdivided into 120 ~250 × 250 μm grid squares to constrain regional and local CPOs of the fine-grained interstitial matrix olivine grains (Fig. 3.1). Multiple meteoritic components were included in this area, making this one of the most comprehensive EBSD applications to meteoritic materials. The right-most 2 mm^2 of the mapped area comprised a large, fine-grained ameboid olivine aggregate and was therefore not included in the analysis. Large chondrule olivine grains were omitted from this analysis. Crystallographic orientations were plotted onto lower hemisphere, equal area plots in the x-y-z reference frame (Fig. 3.1) and overlain onto the phase map for spatial reference (Fig. 3.2). Shape-preferred orientation (SPO) fabrics of the olivine grains were quantified and the relationships between SPO and CPO were investigated (Fig. 3.3, Supp. Fig. 3.2, Supp. Mat. Methodology). All chondrule rim grains within the mapped area were also inspected for evidence of crystal-plastic deformation to characterize the deformation of chondrule margins within spatial context of the entire sample (e.g., Fig. 3.4), following the procedures outlined by Forman et al. (2016).

4. RESULTS

We identified a total of 339,040 grains; 85.3% of the grains were indexed as

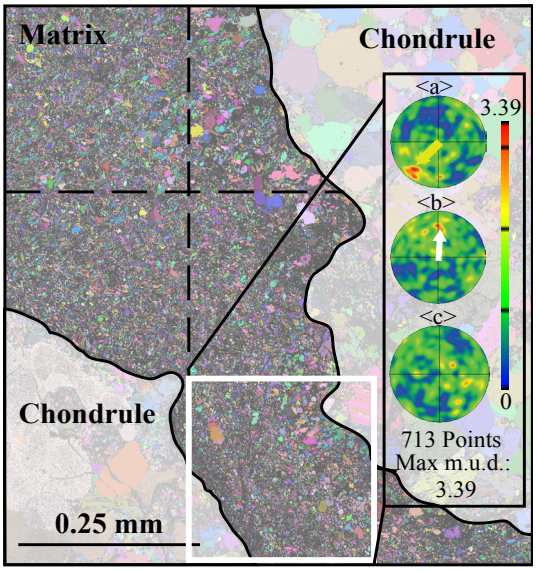

Figure 3.1: *The mapped area of meteorite Allende was divided into a grid (Euler map is background). The orientations of the crystallographic axes for each matrix grain were plotted onto lower hemisphere, equal area plots to identify CPOs. In this case, a moderate <a> axis CPO perpendicular to the chonrule edge and weak <b> axis CPO parallel to the chondrule edge are observed. Max m.u.d.= maximum mean uniform density.*

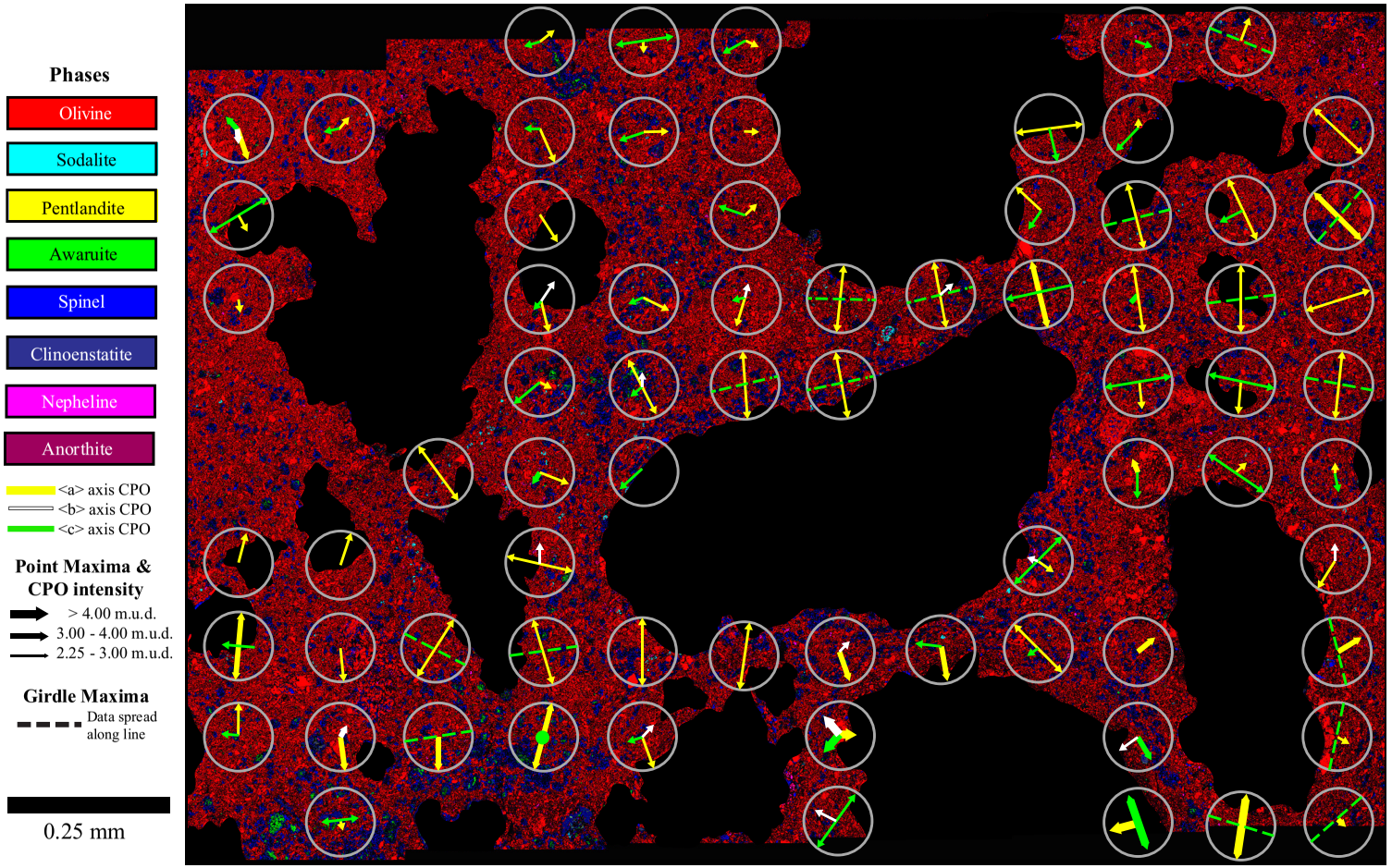

Figure 3.2: *Full CPO analysis overlaid onto the phase map. Black regions are chondrules. Colored arrows within gray circles indicate an alignment of the crystallographic axes. The thickness of each line reflects the m.u.d. of the CPO. Double ended arrows indicate the axis cluster lies on the edge of the lower hemisphere plot, indicating this axis is parallel to the plane of the sample (i.e., x-y reference plane shown here). The dominant CPO is in <a> (yellow lines) which lies predominantly parallel to the y-axis of the reference plane, but also shows localized deviations at chondrule edges.*

olivine (Fig. 3.2). Sparse coarse grains of clinoenstatite, spinel and awaruite were concentrated into loose bands between chondrules, which also contained larger, rounded olivine grains (~0.02 mm). The regions immediately adjacent to chondrules (Fig. 2) primarily comprised fine-grained, euhedral and subhedral olivine laths (<10 μm).

4.1 Chondrule Edge Measurements

Of the 30 chondrule grain sites, approximately 65% indicated as much as 5° of lattice misorientation concentrated in the outer 10–20 μm at the top or bottom of the grain (in reference frame of Fig. 3.2), and 25% indicated that deformation was concentrated on the right or left sides of the chondrules (e.g., Fig. 3.4). The remaining 10% of sites exhibited no deformation textures. Very limited lattice misorientation was detected in the chondrule interiors (< 0.5°).

4.2 Grain Morphologies

Olivine matrix grains in the plane of the sample are euhdral to subhedral and lath-shaped. Close inspection reveals the grains have sharp edges with minimal impingement (e.g., Fig 3.3). However, small grains that are close to the step size of the EBSD mapping were omitted to avoid the geometric artifacts associated with grains defined by two pixels or less.

4.3 SPO and CPO Olivine Matrix Grain Analyses

Analyses of the SPOs and CPOs of the matrix olivines throughout the sample show that the <c>, <b> and <a> and axes are the

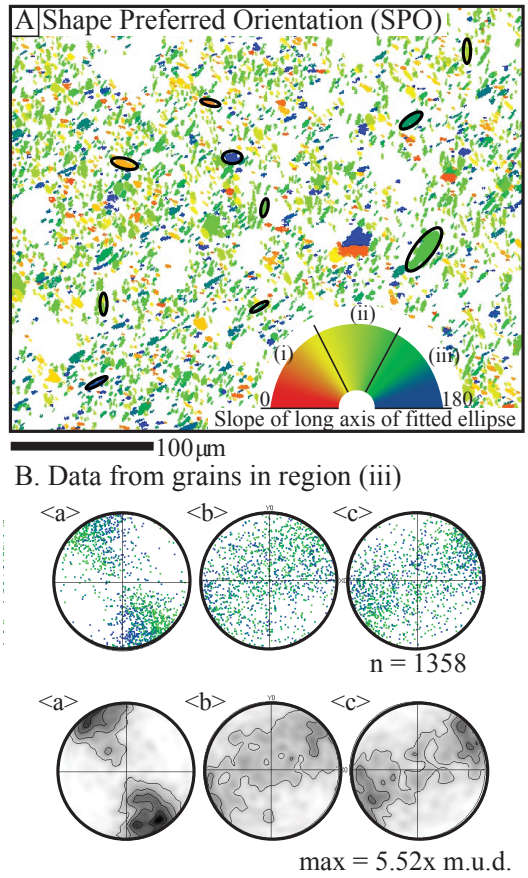

Figure 3.3: *Shape analysis of matrix olivine grains demonstrated on a small region of the total area. a) map color coded to indicate orientation of long axis of the fitted ellipse (fitted ellipses= black ovals) for each matrix olivine, b) Pole figures of subset (iii) of the total matrix olivine data set. Top shows <a>, <b> and <c> with one point per grain in map color scheme; contoured data are below. These indicate the CPO and SPO of this region are coupled; the crystallographic orientation of each grain is strongly correlated to the grain shape. Lower hemisphere equal area plots in map x-y-z reference frame. Max—maximum; m.u.d.—mean uniform density.*

long, intermediate and short dimensions of the grains, respectively (e.g. Fig. 3.3). Matrix olivine grains show significant CPOs (>2.00 mean uniform density- m.u.d.) in 72 of the 120 measured regions. Of those regions, 25% had an m.u.d. of >3.00 (moderate-strong

clustering of crystallographic axes). A strong point maxima CPO of <a> was observed in 68 regions (yellow arrows Fig. 3.2) predominantly in the y direction (vertical) of the EBSD map (Fig. 3.2). The CPOs of <c> (green arrows in Fig. 3.2) form moderate intensity girdles that aligned with the map x direction, in 51 of the 56 regions where CPOs in <c> were observed. The CPOs of <b> (white arrows in Fig. 3.2) were generally weak, spatially heterogeneous point maxima with variable orientations in 14 areas directly adjacent to chondrules. These data indicate a strong coupling between grain shape (SPO) and CPO, with a predominant flattening of the matrix olivine grains parallel to the map y direction, and elongation in the map x direction (Figs. 3.2, 3.3, Supp. Fig. 3.2). The dominant CPO is observed in <a>, consistent with previous studies (Watt et al., 2006).

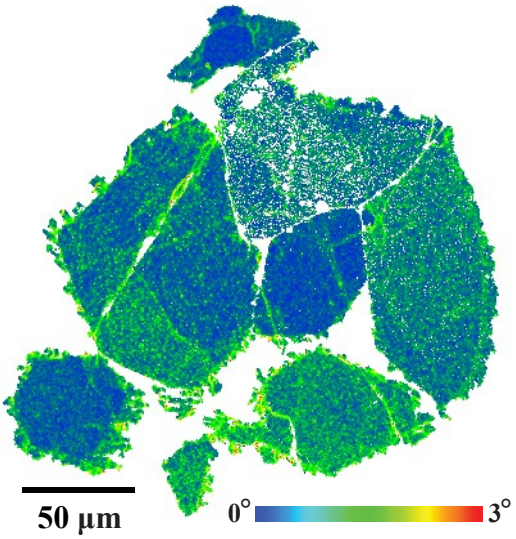

Figure 3.4: *Chondrule olivine grains showing crystallographic deformation concentrated towards the bottom of the chondrule. Local misorientation map is colour-coded to demonstrate the deviation of crystallographic orientation of each pixel with relation to the orientation of the surrounding 8 pixels (measured in degrees/1.5 µm).*

The strongest CPOs are in close proximity to chondrule margins, with many at the top or bottom of chondrules, or in between closely-spaced (<0.1 mm) chondrules (Fig. 3.2). Strong, localized variations of the overall CPOs are evident around chondrules (Fig. 3.2), where grains are flattened against the chondrule margins.

5. DISCUSSION

Matrix olivine grains in Allende have preserved euhedral-subhedral lath morphologies. They have a moderate SPO throughout the mapped region, which correlates consistently to the observed CPO, indicating a flattening fabric of variable strength has been produced. The relationship between CPO and SPO implies that sintering and surface diffusion have not occurred, therefore the CV parent body was not at the high temperatures required for HIP to occur over the required timescales. If subgrain rotation recrystallization had generated the CPOs, rotation through large angles would be required, which would act to reduce the aspect ratio of the matrix laths. Because the matrix laths are elongate, some primary porosity is still present, and crystal-plastic deformation effects are minor (Forman et al., 2016), the CPO is predominantly the result of the physical realignment of anisotropic olivine grains rather than dislocation or diffusion creep.

The minor crystal-plastic strain observed at the margins of chondrules and a lack of such strain in chondrule interiors indicate

Allende must have undergone high (but transient) stresses and temperatures during deformation (Frost and Ashby, 1982), at a local scale. Comparatively, matrix olivine grains have undergone significantly more intragrain deformation (Forman et al., 2016), which is inferred to result from brief localized temperature excursions predicted from impact-induced compaction. Allende is expected to have been at temperatures between 300 K- 800 K (e.g., Weinbruch et al., 1994; Huss et al., 2006; Cody et al., 2008), implying that sintering within Allende could only have been achieved in matrix grains, and any temperature excursion above that threshold was not sustained for a significantly long period of time, and certainly not 1 m.y..

Local variations in CPO alignment and intensity were observed over a small area of 6 mm^2 at the meso-scale, and are consistent with previous EBSD studies (Watt et al., 2006). It has been argued that stress applied by lithostatic forces within the parent asteroid were negligible (1 MPa at the center of a 200 km diameter body (Weidenschilling and Cuzzi, 2006)). In addition, uniform, planetary-scale compaction of a highly porous, low-gravity small planetary body would not generate such localized textures because stress bridging between grains would equilibrate over time, nor would it create discrepancies in deformation between chondritic components. Heating to >500 °C and compaction associated with HIP or hot gravitational compression would have been sustained over a time period of ~1 Ma (Gail et al., 2015). Rheological constraints from olivine (Karato et al., 1986) indicate that significant diffusion creep is predicted at this temperature, timeframe, and matrix grain size, that would have reduced porosity in a homogenous way via diffusion creep recrystallization and new grain growth, and resulted in a recovered and annealed microstructure. However, as this was not observed HIP is unlikely to have contributed to the textural development of Allende. Because Allende is the most thermally altered CV chondrite studied (Bonal et al., 2006; Cody et al., 2008) this argument applies to the entire suite of CV chondrites.

Impact-induced compaction would generate shockwave interactions with chondritic components, and associated localized heating and compression throughout the parent body over short timescales, which would be rapidly equilibrated following the compression event (Davison et al., 2012; Bland et al., 2014). The collapse of abundant pores adjacent to chondrule edges is predicted to generate localized temperature excursions (up to ~850 K in a 1.5 km/s impact into a mixture of 70% porous matrix and nonporous chondrules, with a bulk porosity of 50% (Bland et al., 2014)) when compared to non-porous regions, i.e., chondrule interiors (~330 K in the same scenario (Bland et al., 2014)). This brief heating discrepancy easily explains the deformational textures in chondrule and matrix grains, and would be associated with heterogeneous SPOs and CPOs that are also likely to be asymmetric around chondrules. As

heat production is the result of pore collapse due to compression, regions experiencing the highest temperatures are the same regions to undergo the most compression, and therefore form the most significant CPOs.

6. CONCLUSIONS

We examined the crystallographic textural features at both microscales and mesoscales within the CV3 chondrite Allende using one of the most comprehensive EBSD maps ever collected, to explore compaction processes on the CV chondrite parent body. Abundant but minimal chondrule edge lattice deformations that are not uniformly distributed around chondrule margins, and moderately strong yet heterogeneously oriented <a> axis CPOs and coupled SPOs were detected throughout the fine-grained matrix regions, consistent with a variably-developed flattening fabric. Allende has also been at higher temperatures than other CVs. If sintering, and therefore HIP, had occurred we would see it in this sample. These observations rule out HIP and other forms of gravity-driven compaction as viable compaction processes of the CV parent body, and by inference, any small, primitive bodies. Impact-induced compaction provides the required heterogeneous distribution of heating and compaction over a short timescale, and our findings closely replicate the small-scale spatial heterogeneities predicted by numerical modeling. The orientations of the SPOs and CPOs in association with chondrule edge lattice deformations provide directionality for shockwave propagation; compaction was parallel to the y-direction of Fig. 3.2 and occurred primarily due to impacts into the highly porous parent body.

This unique study is one of the first to identify crystallographic evidence for impact-induced compaction of the CV parent body, and therefore is a very significant application of EBSD techniques to meteorites. Although this finding is limited to formation of the CV parent body in this study, small planetary bodies would likely have undergone similar impacts, and would have small lithostatic pressures acting to compact the body. There is therefore scope to expand this approach to other chondrites and small parent bodies.

7. ACKNOWLEDGEMENTS

This work was funded by the Australian Research Council via their Australian Laureate Fellowship program (FL110100074) (PAB). We acknowledge the technical assistance and use of facilities at the University of Sydney node of the Australian Microscopy and Microanalysis Research Facility. GSC and TMD were funded by UK Science and Technology Facilities Council grant ST/J001260/1. We thank editor Prof. Bob Holdsworth, reviewer Jon Friedrich, and two anonymous reviewers.

8. REFERENCES

Bland, P.A., Collins, G.S., Davison, T.M., Abreu, N.M., Ciesla, F.J., Muxworthy, A.R., and Moore, J., 2014, Pressure–Temperature Evolution of Primordial Solar System Solids During Impact-Induced Compaction: Nature Communications, v. 5, p. 5451, doi:10.1038/

ncomms6451.

Bonal, L., Quirico, E., Bourot-Denise, M., and Montagnac, G., 2006, Determination of the petrologic type of CV3 chondrites by Raman spectroscopy of included organic matter: Geochimica et Cosmochimica Acta, v. 70, p. 1849–1863, doi:10.1016/j.gca.2005.12.004.

Carter, C.B. and Norton, M.G., 2013, Sintering and grain growth, in Carter, C.B., and Norton, G.M., Ceramic materials: Science and engineering: Springer, New York, p. 439–456, doi:10.1007/978-1-4614-3523-5_24.

Cody, G.D., Alexander, C.O.D., Yabuta, H., Kilcoyne, A.L.D., Araki, T., Ade, H., Dera, P., Fogel, M., Militzer, B., and Mysen, B.O., 2008, Organic thermometry for chondritic parent bodies: Earth and Planetary Science Letters, v. 272, p. 446–455, doi:10.1016/j.epsl.2008.05.008.

Consolmagno, G.J., Britt, D.T., and Macke, R.J., 2008, The significance of meteorite density and porosity: Chemie der Erde, v. 68, p. 1–29, doi:10.1016/j.chemer.2008.01.003.

Davison, T.M., Ciesla, F.J., and Collins, G.S., 2012, Post-impact thermal evolution of porous planetesimals: Geochimica et Cosmochimica Acta, v. 95, p. 252–269, doi:10.1016/j.gca.2012.08.001.

Davison, T.M., Collins, G.S., and Bland, P.A., 2016, Mesoscale modeling of impact compaction of primitive solar system solids: Astrophysical Journal, v. 821, p. 68.

Forman, L.V., et al., 2016, Hidden secrets of deformation: Impact-induced compaction within a CV chondrite: Earth and Planetary Science Letters, v. 452, p. 133–145, doi:10.1016/j.epsl.2016.07.050.

Frost, H.J., and Ashby, M.F., 1982, Deformation-mechanism maps: The plasticity and creep of metals and ceramics: Oxford, UK, Pergamon Press, 165 p.

Fujimura, A., Kato, M., and Kamazawa, M., 1983, Preferred orientation of phyllosilicate (001) in matrix of Murchison meteorite and possible mechanisms of generating the oriented texture in chondrites: Earth and Planetary Science Letters, v. 66, p. 25–32, doi:10.1016/0012-821X(83)90123-1.

Gail, H.P., Henke, S., and Trieloff, M., 2015, Thermal evolution and sintering of chondritic planetesimals—II. Improved treatment of the compaction process: Astronomy & Astrophysics, v. 576, A60, doi:10.1051/0004-6361/201424278.

Hanna, R.D., Ketcham, R.A., Zolensky, M., and Behr, W., 2015, Impact-induced brittle deformation, porosity loss, and aqueous alteration in the Murchison CM chondrite: Geochimica et Cosmochimica Acta, v. 171, p. 256–282, doi:10.1016/j.gca.2015.09.005.

Horedt, G.P., 1980, Gravitational heating of planets: Physics of the Earth and Planetary Interiors, v. 21, p. 22–30, doi:10.1016/0031-9201(80)90016-3.

Huss, G.R., Rubin, A.E., and Grossman, J.N., 2006, Thermal metamorphism in chondrites, in Lauretta, D.S., and McSween, H.Y., eds., Meteorites and the early Solar System II: Tuscan, University of Arizona Press, p. 567–586.

Karato, S.I., Paterson, M.S., and FitzGerald, J.D., 1986, Rheology of synthetic olivine aggregates: Influence of grain size and water: Journal of Geophysical Research, v. 91, p. 8151–8176, doi:10.1029/JB091iB08p08151.

Krot, A.N., Petaev, M.I., Scott, E.R., Choi, B.G., Zolensky, M.E., and Keil, K., 1998, Progressive alteration in CV3 chondrites: More evidence for asteroidal alteration: Meteoritics & Planetary Science, v. 33, p. 1065–1085, doi:10.1111/j.1945- 5100.1998.tb01713.x.

Scott, E.R.D., Barber, D.J., Alexander, C.M., Hutchison, R., and Peck, J.A., 1988, Primitive material surviving in chondrites: Matrix, in Kerridge, J.F., and Matthews, M. S., eds., Meteorites and

the early solar system: Tucson, Arizona, The University of Arizona Press, p. 718–745.

Scott, E.R.D., Keil, K., and Stöffler, D., 1992, Shock metamorphism of carbonaceous chondrites: Geochimica et Cosmochimica Acta, v. 56, p. 4281–4293, doi:10.1016/0016-7037(92)90268-N.

Watt, L.E., Bland, P.A., Prior, D.J., and Russell, S.S., 2006, Fabric analysis of Allende matrix using EBSD: Meteoritics & Planetary Science, v. 41, p. 989–1001, doi:10.1111/j.1945-5100.2006.tb00499.x.

Weidenschilling, S.J., and Cuzzi, J.N., 2006, Accretion dynamics and timescales: Relation to chondrites, in Lauretta, D.S., and McSween, H.Y., eds., Meteorites and the early Solar System II: Tuscon, University of Arizona Press, p. 473–485.

Weinbruch, S., Armstrong, J., and Palme, H., 1994, Constraints on the thermal history of the Allende parent body as derived from olivine-spinel thermometry and Fe/Mg interdiffusion in olivine: Geochimica et Cosmochimica Acta, v. 58, p. 1019–1030, doi:10.1016/0016-7037(94)90523-1.

GSA Data Repository item 2017178, Supplementary Figure 1: Mapped region of the CV3 meteorite Allende; Supplementary Figure 2: Detailed shape preferred orientation (SPO) analysis; Supplementary Methodology: further information regarding methods and approach., is available online at http://www.geosociety.org/datarepository/2017/ or on request from editing@geosociety.org.

9. SUPPLEMENTARY MATERIAL

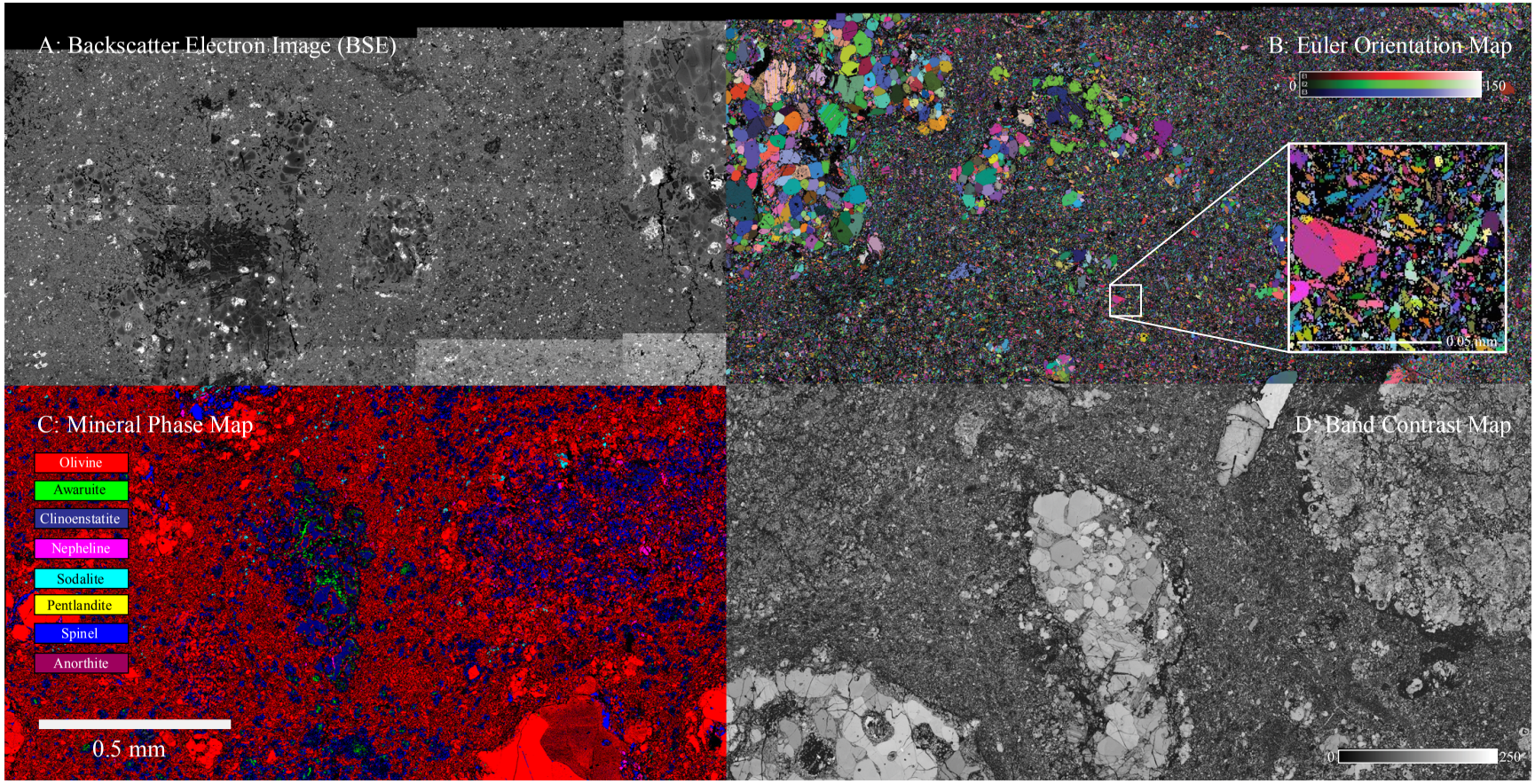

Supplementary material figure 3.1: *Map of Allende shown with four different imaging techniques- a) backscatter electron image (BSE), b) all euler orientation map, colour coded to reflect collective crystallographic orientation with respect to the three primary crystallographic axes of each grain, c) mineral phase map, and d) band contrast map, where bright regions indicate a strong diffraction pattern and dark regions indicate a weak or absent diffraction pattern.*

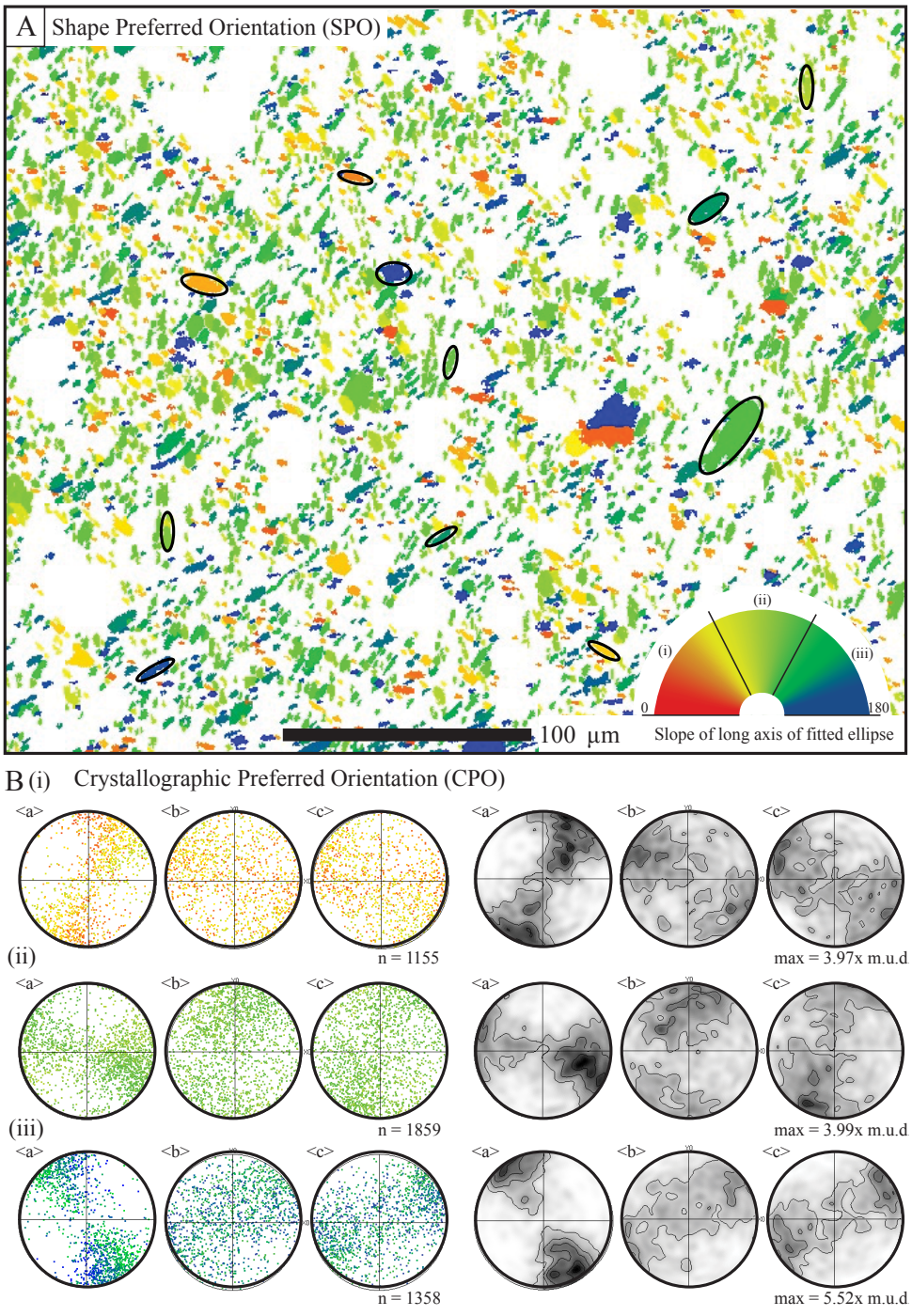

Supplementary material figure 3.2: *Shape analysis of matrix olivines- a) map colour coded to indicate orientation of long axis of the fitted ellipse for each matrix olivine, b) grains divided into subsets i, ii and iii. Lower hemisphere, equal area plots show one point per grain for each grain in the subset on the left, and the contoured data is displayed on the right.*

Supplementary material: Methodology

An 8 mm² area of Allende was mapped using a Carl Zeiss Ultra Plus field emission gun scanning electron microscope (FEG SEM) at the University of Sydney node of the Australian Microscopy & Microanalysis Research Facility. Element, phase and crystallographic data maps (Supplementary Material Fig. 3.1) were collected at a step size of 0.5 μm over 380 hours, using both the NordlysNano EBSD detector and X-Max 20 silicon drift detector (EDS), using 20 keV accelerating voltage and 10 nA current. This resulted in the detection of over 46 million diffraction patterns, and 7 billion x-rays. The EBSD patterns were indexing using Oxford Instruments AZtec software, and resulting orientation maps were processed using the Oxford Instruments CHANNEL 5.12 system. Data were noise reduced as per the procedure outlined by Watt et al. (2006), and grains smaller than 1.5 μm (3 x step size of 0.5μm) were disregarded for further analysis to conservatively account for any potential mapping artefacts.

30 chondrules or chondrule rim grains within the mapped area were inspected for evidence of crystal-plastic deformation to constrain chondrule edge deformation within spatial context. For a detailed description of the chondrule deformation measurement, we direct the reader to the procedures of Forman et al., (2016), found in Chapter 2.3.

CPO analysis required a subdivision of the mapped region into 120 grid squares to identify local and regional textures between olivine matrix grains (Fig. 3.1a). The collective crystallographic orientations within each grid square were plotted onto lower hemisphere, equal area plots (Fig. 3.1b) and overlain on the phase map for spatial reference (Figs. 3.1 & 3.2). One point per grain was plotted to avoid data bias. Both point and girdle maximas were observed. Point maximas are indicated by an arrow from the centre of the plot to the axes clusters (e.g. in Fig. 3.1b), and double-ended arrows are used where the point maxima are positioned on the edge of the plot. A dotted line is used for girdle maximas. The thickness of each line specifies the intensity of the CPO present (mean uniform density (m.u.d.)). This approach allowed for an effective visual representation of the three primary crystallographic axes from ~2000 grains in one plot within their spatial context, and allowed for cross-examination of localised and overall CPOs from a broad area. To comprehend our CPO data, a comparison with shape-preferred orientation of the olivine grains was necessary (Fig. 3.3). The full analytical process is detailed in Fig. 3.3 and supplementary material Fig. 3.2.

Chapter 4

A Morphologic & Crystallographic Comparison of CV Chondrite Matrices

The following chapter is in preparation for submission to METEORITICS & PLANETARY SCIENCE.

L. V. Forman[1], N. E. Timms[1], P. A. Bland[1], L. Daly[1], G. K. Benedix[1] & P. W. Trimby[2].

[1]Department of Applied Geology, Curtin University, GPO Box U1987, Perth, WA 6845, Australia

[2]Australian Centre for Microscopy and Microanalysis, The University of Sydney, NSW, 2006, Australia

1. ABSTRACT

The matrices of meteorites are commonly classified by their modal mineralogy, alteration and shock levels. Whereas, other 'textural' characteristics are not generally considered in classification schemes, yet could carry important information about their genesis and subsequent evolution. This paper investigates three CV chondrites- Allende ($CV3.2_{oxA}$), Kaba ($CV3.0_{oxB}$) and Vigarano ($CV3.3_{red}$)- to determine the morphological signature of olivine matrix grains in each meteorite. For each sample, the grain size and shape, crystallographic preferred orientations (CPOs) and shape preferred orientations (SPOs) are quantified via electron backscatter diffraction mapping. Kaba and Vigarano contain much smaller forsterite matrix grains than Allende, however Allende contains the most elongate grains and strongest CPO, which is strongly linked to the SPO. We infer the matrix grain morphologies and textural features are a function of aqueous and thermal alteration on the parent body, prior to asteroidal compaction. Grain aspect ratio appears to correlate to the temperature the sample has experienced, and grain size and the presence of grain facets correlate to the degree of aqueous alteration the sample has been subjected to. Higher temperatures, aqueous alteration, and therefore grain growth, are more likely to be present at depth, therefore Vigarano and Kaba would have originated from shallow depths on the parent body, whereas Allende likely originated from greater depths. The relationship between CPO intensity and relative depth of the sample on the parent body also indicates asteroid compaction via impacts and the material response to that process is highly complex and may not yet be fully constrained. Similar analysis of other CV chondrites may aid in further constraining compaction according to formation depth.

2. INTRODUCTION

Carbonaceous chondrites (CCs) encompass ~3% of all meteorites in global collections, and are split into 7 classes based upon physical and chemical characteristics (Brearley and Jones, 1998). The 'Vigarano-type' CCs, known as CVs, are some of the most primitive meteorites to have been studied. We are therefore able to gain an insight into early solar system processes by examining these rocks, that are not as simple to interpret from more chemically and texturally altered meteorites. We can also learn of their parent body origins and secondary processing history, both during the initial asteroid formation period and post-lithification (e.g. Rietmeijer and Mackinnon, 1985; Stöffler et al., 1991; Krot et al., 1998; Bonal et al., 2006; Cody et al., 2008; Consolmagno et al., 2008; Forman et al., 2016). Textural and geochemical variations within the CV chondrite group have resulted in further classification into three subclasses (oxidised types A & B, and the reduced subtype) (McSween, 1977a; Weisberg

et al., 1997), which have been interpreted to reflect varying environments or processing conditions on the same parent body (Krot et al., 1998; Krot et al., 2000; Krot et al., 2004). Chondrules, calcium-aluminium inclusions (CAIs), and amoeboid olivine aggregates (AOAs) within carbonaceous chondrites have been the focus of various studies over the last 5 decades, including optical, scanning and transmission electron microscopy (SEM and TEM, respectively) research, whereby their mineralogy and microstructure have been characterized and major, trace and isotope geochemistry analysed (e.g. McSween, 1977b; Grossman et al., 1988; Hewins, 1997; Tait et al., 2016). Conversely, the fine-grained, interstitial matrix of such meteorites has had comparatively less attention (e.g. Scott et al., 1988; Krot et al., 2004; Watt et al., 2006; Bland et al., 2011; Forman et al., 2016). Nevertheless, these few studies have highlighted the importance of characterizing the matrix mineralogies and textures of meteorites to interpret their history.

The matrices of one sample from each CV subgroup is examined in this study; Vigarano, a reduced subtype (CV_{red}), Allende, an oxidised subtype A (CV_{oxA}) and Kaba, an oxidised subtype B (CV_{oxB}) (Table 1). The petrology of each meteorite has been described previously, with Vigarano being the most thermally altered (petrologic type 3.3), followed by Allende (3.2) and then Kaba (3.0) (Krot et al., 1995). According to the classification system of Van Schmus & Wood (1967), Kaba is the most primitive of all the samples examined here (e.g. Huss et al., 2006). Vigarano contains the lowest matrix abundance (matrix: chondrule ratio of 0.55) (McSween, 1977a), and is the most shocked (S1-2) of the three samples (Scott et al., 1992). Allende contains a similar abundance of matrix (matrix: chondrule ratio of 0.66) to Vigarano (McSween, 1977a), whereas Kaba contains considerably more matrix (matrix: chondrule ratio of 1.17) than either Vigarano or Allende (McSween, 1977a). However, all CV chondrites are assumed to come from the same parent body based upon their similar textures, petrologic type and oxygen isotopes .Clasts of oxidised CV material have also been found within the reduced meteorite

	Allende	**Kaba**	**Vigarano**
Classification[1]	$CV3.2_{oxA}$	$CV3.0_{oxB}$	$CV3.3_{r}$
Shock stage[2]	S1	S1	S1-2
Olivine composition	$Fa_{45\text{-}55}$[3, 4]	$Fa_{20\text{-}40}$[5]	$Fa_{35\text{-}45}$[3, 6]
Matrix: chondrule ratio[7]	0.66	1.17	0.55
Porosity	21.9%[8]	3.0%[9]	8.3%[8]

oxA= oxidized subclass, Allende-type.
oxB= oxidized subclass, Bali-type.
r= reduced subclass.
References: 1= Krot *et al.*, 1995; 2= Scott *et al.*, 1992; 3= Peck, 1983; 4= MacPherson *et al.*, 1985; 5= Keller & Buseck, 1990; 6= Graham & Lee, 1992; 7= McSween, 1977, 8= Macke *et al.*, 2011, 9= Corrigan *et al.*, 1997.

Table 4.1*: Collated geochemical and modal properties of the matrices in the CV chondrites Allende, Kaba and Vigarano.*

Vigarano, providing further evidence that all CV chondrites have the same origin (Krot et al., 2000; Weisberg et al., 2006).

When describing fine-grained meteoritic media, a geochemical shorthand is commonly used to quote the average composition of a specific mineral, which is typically olivine in the matrices of most chondrites (Brearley and Jones, 1998). This allows for compositional variance to be constrained in one number, or a range of numbers, and reveal some aspect of the meteorite petrogenesis (e.g. Hua and Buseck, 1995; Hua et al., 2005). The composition of the matrix olivine grains is usually expressed as a percentage of one of the olivine end members, forsterite (Fo) and fayalite (Fa), which indicate the proportions of Mg and Fe respectively within each grain (Table 4.1) (Peck, 1984). Examining the morphologic properties and crystallographic orientations of the same matrix grains enables two-dimensional (2D) grain size and shape distribution, and crystallographic and shape preferred orientations to be quantified. The 2D morphology of matrix grains from in chondrites are often described qualitatively (e.g. Brearley and Jones, 1998; Scott and Krot, 2003), however our approach described here permits quantitative characterisation over the area of a petrographic thin section, which allows use of this standardized approach to determine the crystallographic and morphological fingerprint of each meteorite. In addition, shape and crystallographic preferred orientations (SPOs and CPOs, respectively) that are specific to the sample of interest can be easily characterised, which can aid in the interpretation of various processes associated with lithification, metamorphism and mechanisms of deformation (e.g. Forman et al., 2017).

In this study, we quantitatively characterise the microstructure, textures and morphologies of the olivine matrix grains of the three CV meteorites. Previous research has established the relative depths of the three meteorites examined here from deepest origin to shallowest, as Allende >> Kaba ≥ Vigarano, based on a wide range of characteristics, such as magnetic properties, aqueous alteration products and the predicted maximum temperatures the samples have experienced, using various thermometry techniques (Bonal et al., 2006; Cody et al., 2008; Elkins-Tanton et al., 2011; Weiss and Elkins-Tanton, 2013). Our results are therefore considered in the context of these prior studies to establish any links between morphology, texture, alteration, and surmised relative depth on the parent body.

3. METHODS AND APPROACH

Two regions of interstitial matrix- proximal to chondrule edges- per chondrite, were mapped to obtain crystallographic and phase data using electron backscatter diffraction techniques (EBSD) and the Oxford Instruments' Aztec acquisition system. EBSD maps were collected at a fixed step size of 0.12 μm for Kaba and Vigarano, and at 0.5 μm for Allende; this discrepancy reflects the observable matrix grain size in each sample, and allowed between 3000 and 4000 grains to be consistently sampled within each region of

interest. Using the Oxford Instruments HKL software Channel 5.12, the data were noise reduced by removal of isolated erroneous data points ('wildspike' correction) followed by a 6-point nearest neighbour zero solution extrapolation to facilitate grain definition without generating significant artefacts.

Grains were defined using the automated 'grain detect' algorithm in Channel 5, based on contiguous adjacent pixels within a 10° crystallographic misorientation threshold. The threshold is assumed to represent the transition from low-angle to high-angle boundaries, and results in generation of fewer artefacts. Several grain parameters and their statistics, such as grain size, shape (aspect ratio), were quantified using the Channel 5.12 software package, collated from all grains in each respective region, and averaged to quantify the 'typical' interstitial olivine matrix characteristics in each sample. Grain sizes from both sites in each sample were amalgamated to improve the reliability of our grain size and shape results.

Grain size can be expressed in a number of ways; grain diameter- circle equivalent, length of long axis of ellipse, length of short axis of ellipse, and grain area. This study used the circle equivalent diameter parameter, because the elongate nature of the majority of the grains meant deceptive relationships between grain size and shape arose when other parameters were displayed. Grains smaller than 3 times the step size were removed from the dataset to improve collective statistical and orientation accuracy by removing grains that were insufficiently sampled; this is a commonly-used cut-off parameter to ensure a grain is sampled at least three times leading to improved accuracy of grain detection and quantification (e.g. Watt et al., 2006). Grain size frequency distribution histograms allowed us to determine the sampling accuracy of this approach; the main limitation of the approach is that the minimum grain size is constrained by the step size of data collection, and therefore the datasets may not be fully representative of the lower range of the grain size distribution.

The crystallographic orientation data for olivine from each map were reduced to one representative point per grain, and

	Allende *(n= 8318)*			**Kaba** *(n=7678)*			**Vigarano** *(n= 7892)*		
	Average	Min.	Max	**Average**	Min.	Max.	**Average**	Min.	Max.
Grain Diameter (μm)	**2.328**	1.439	21.938	**0.793**	0.358	10.428	**0.695**	0.358	8.687
Grain Area (μm^2)	**5.238**	1.750	378.00	**0.701**	0.101	85.4	**0.550**	0.101	59.27
Aspect Ratio	**2.05**	1	7.904	**1.722**	1	5.304	**1.909**	1	8.496

Min. = minimum value recorded.
Max. = maximum value recorded.
Grain diameter is measured as circle equivalent diameter.
Aspect ratio = $\frac{grain\ length}{grain\ width}$ based on assigned ellipses.

Table 4.2: *Grain statistics for Allende, Kaba and Vigarano interstitial olivine matrix grains. Statistics sample grains above 1.5 μm for Allende, and 0.36 μm for Kaba and Vigarano.*

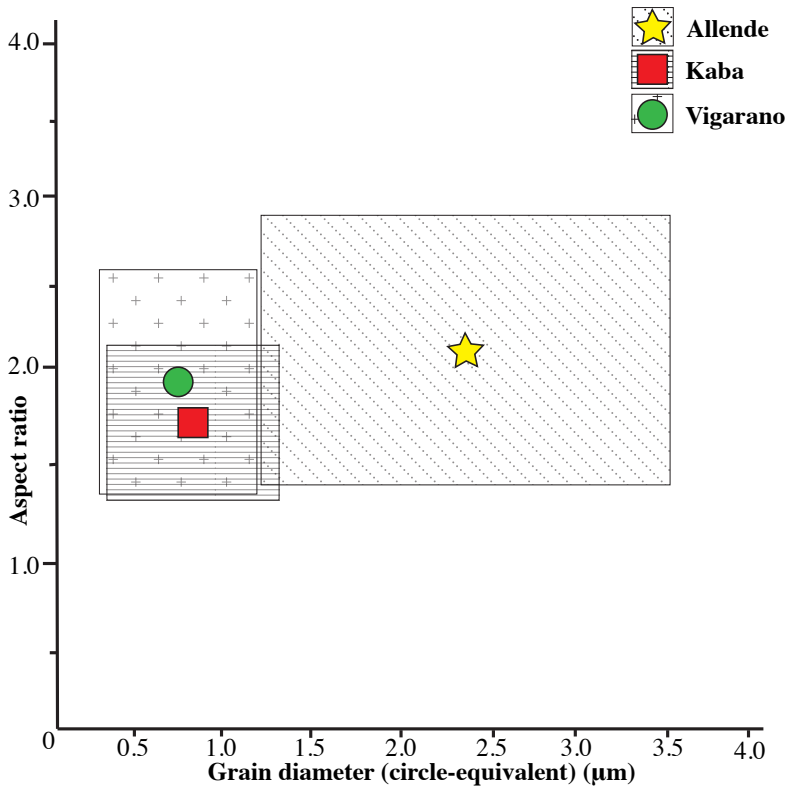

Fig. 4.1: *Collated grain statistics displayed for each meteorite. The average grain diameters and aspect ratios within each meteorite are shown by the colour symbols. The boxes contain the 68.2% of each dataset (1 standard deviation).*

used to construct crystallographic preferred orientations (CPOs) for each of the three principal crystallographic axes of olivine (<a> = <100>, <b> = <010>, and <c> = <001>) on lower hemisphere, equal area plots (pole figures) in the sample/map x-y-z reference frame. Pole figures were colour coded to reflect the orientation of each grain by ascribing Euler angles (i.e., - ϕ2, -Φ, -ϕ1) to red, blue and green channels, respectively. The pole figure data were then contoured for data density, facilitating description of the forms- and quantification of the strengths of CPOs. The strengths of CPOs are expressed as multiples of uniform density (m.u.d.).

Two-dimensional (2D) grain shapes and their long-axis azimuths were quantified as the aspect ratio and slope of the long axis of the best-fit ellipse, respectively, for each grain using the algorithm available in Channel 5 Tango. These data were used to generate thematic maps, histograms, and colour-coded pole figures, which were used to assess shape preferred orientations (SPOs), grain shape statistics, and links between SPOs and CPOs, respectively, for each sample. It is important to note that the 2D grain size and shape data were not corrected for 3D grain shapes or cut effects, because neither were the 3D grain shapes characterized, nor macroscopic fabrics relative to thin section orientations known.

4. RESULTS

4.1 Grain Statistics and Morphologies

The average grain size, grain aspect ratio and area statistics of matrix olivine grains for each region of interest in each sample are displayed in Table 4.2. Allende has a markedly higher average olivine matrix grain size

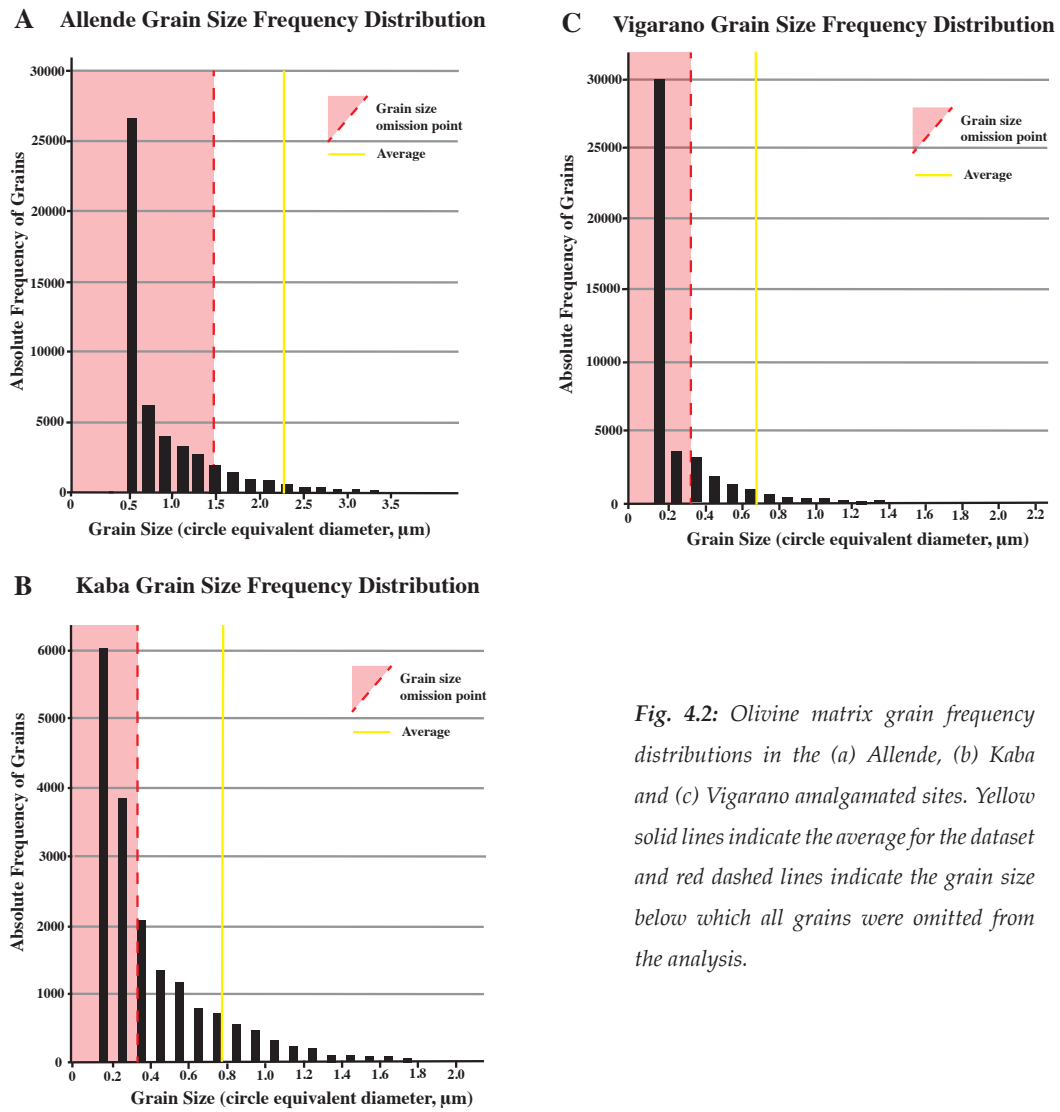

Fig. 4.2: *Olivine matrix grain frequency distributions in the (a) Allende, (b) Kaba and (c) Vigarano amalgamated sites. Yellow solid lines indicate the average for the dataset and red dashed lines indicate the grain size below which all grains were omitted from the analysis.*

(2.328 µm) compared to Kaba and Vigarano, and also has the mean highest aspect ratio of the three (2.050), meaning Allende's grains are larger and more elongate. Kaba has the stubbiest grains with an average aspect ratio of 1.722, and Vigarano has the smallest mean matrix grain size of the three samples, with an average olivine matrix grain size of 0.695 µm. Aspect ratio, grain diameter and the area within which 68.2% (1 standard deviation) of each data set plots is shown in Fig. 4.1. Smaller grains across all three meteorite samples typically have the largest aspect ratios, meaning these are the most elongate laths present, whereas larger grains are typically more rounded in shape with a lower aspect ratio (<1.5). Allende displays significantly more euhedral laths when compared with Kaba and Vigarano, which contain more subhedral and anhedral olivine grain morphologies respectively.

Grain frequency distributions (Fig. 4.2)

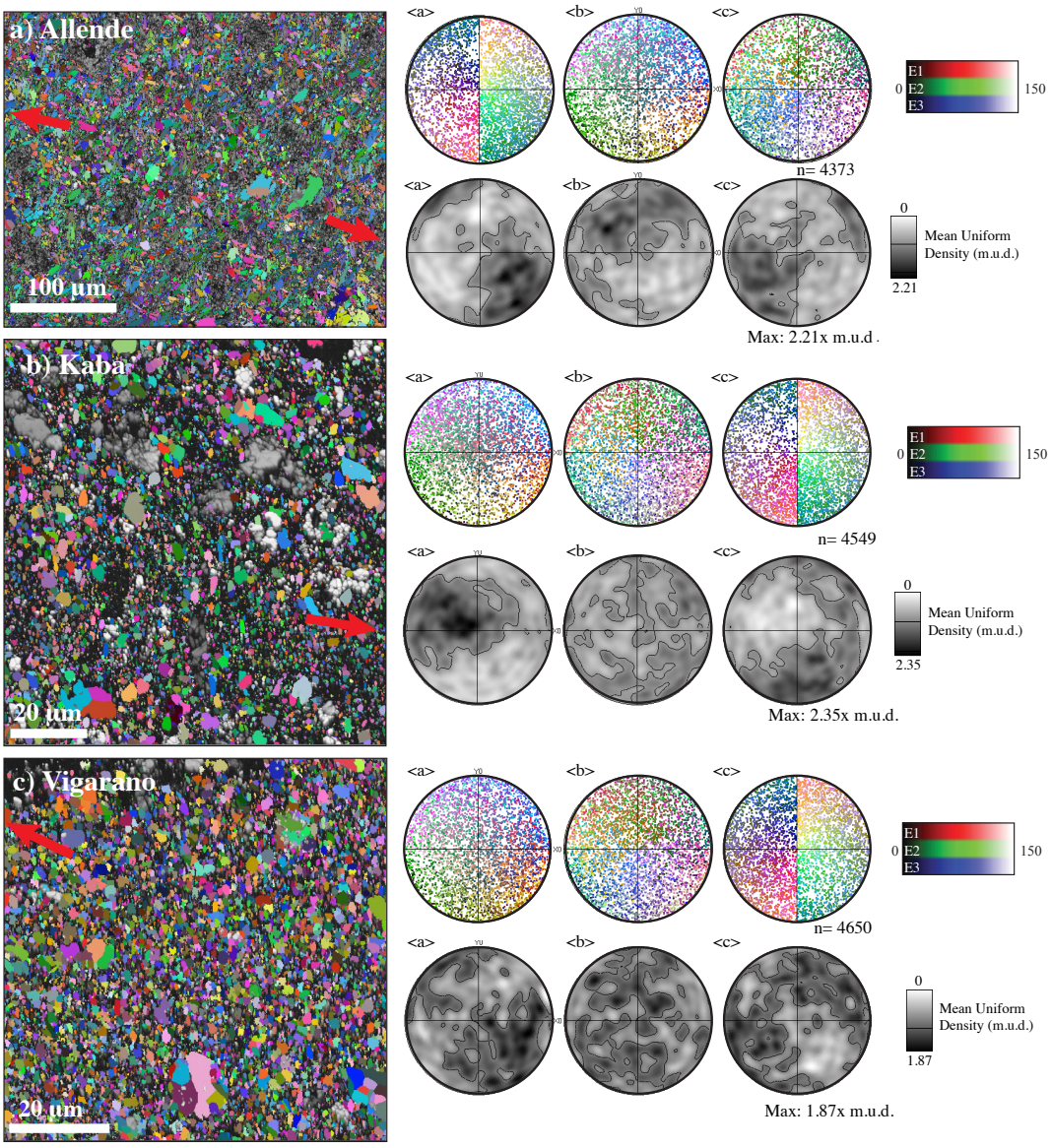

Fig. 4.3: *Euler maps for one matrix region in each of the meteorites (a) Allende, (b) Kaba and (c) Vigarano respectively. Grains are colour coded to reflect their crystallographic orientation and one point per grain is displayed on the lower hemisphere, equal area plots. These plots were then contoured in black and white to highlight any axis clustering (m.u.d. = mean uniform density, high density = dark regions).*

demonstrate that a large proportion of the detected 'grains' were omitted from our analyses. However, the omitted grains included those that were only represented by 1 pixel; even after subsequent to noise reduction these result in artefacts in the grain size distribution, and hence were not be treated as reliable data for our analysis. A region of interest in Allende was also mapped at a step size of 0.12 µm to compare statistical results and ascertain reliability of our initial fixed step size analysis. Whilst the average grain size decreased by less than 1 µm to 1.450 µm, the spread of the data was larger

(1 standard deviation ~1.20). Fewer grains overall, and fewer larger grains, were sampled given the increase in time required to sample a sufficient number of grains at a small step size in a relatively coarse-grained material, and therefore we deem the reliability of the successive analysis is lower than that of the initial analysis.

4.2 Crystallographic preferred orientations (CPOs)

One region for each of the sampled meteorites is shown in Fig. 4.3 to demonstrate the CPOs present. Each of the three meteorites has a weak-moderate alignment of <a> axes, as indicated by the point maxima clustering of the data points in the <a> pole figures. Vigarano displays the weakest point maxima (maximum mean uniform density (m.u.d.) ~1.87x) whilst Kaba shows the strongest (m.u.d. ~2.35x). Kaba displays a weak-moderate girdle maxima in <c> (m.u.d. ~2.00x), which lies perpendicular to <a> point maxima. Allende also shows a weak point maxima in both <b> and <c> (m.u.d. ~1.50-2.00). The orientations of the CPOs can't be compared because the samples were not oriented with respect to any particular reference frame and the meteorites do not have any spatial or orientation context to one another.

4.3 Shape preferred orientations (SPOs)

Shape preferred orientations were characterised in 2D to show the trend of the long axis of the fitted ellipse of each grain, and were visualised as colour-coded maps (Fig. 4.4). Colour-coding the lower-hemisphere,

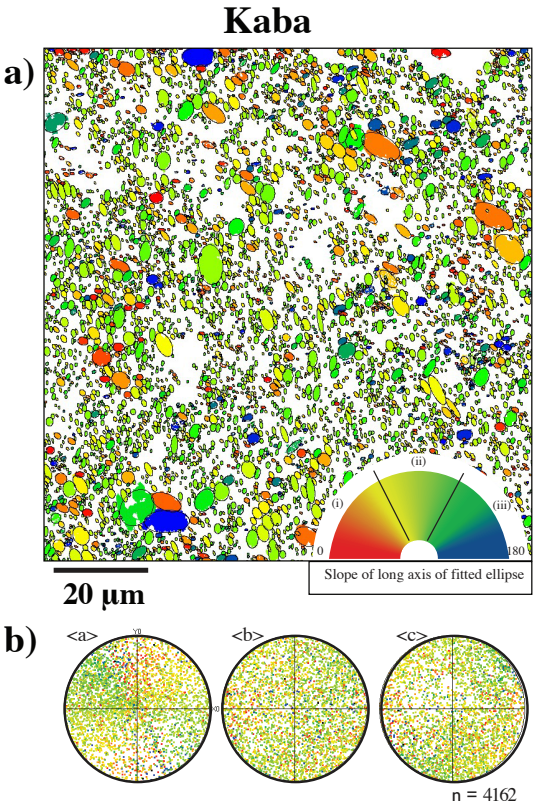

Fig. 4.4: *a) Map of interstitial matrix olivine grains in Kaba, colour coded to reflect the orientation or 'slope' of the long axis of the fitted ellipse; b) crystallographic orientation data of one point per grain displayed on lower hemisphere, equal area plots, for each of the three primary crystallographic axes of olivine (<a>, <b> & <c>) with same colour coding as map in (a).*

equal-area plots to this parameter allowed for links to be investigated between SPO (Fig. 4.5) and CPO (Fig. 4.3). However, the high density of data points on pole figures inhibits recognition of patterns between SPO and CPO, and so the data were subdivided into three subsets based on the ellipse long axis trend ranges (subsets i, ii & iii) and presented on separate pole figures (Fig. 4.5). All three case studied meteorites show a strong relationship between the orientation of crystallographic data points and grain

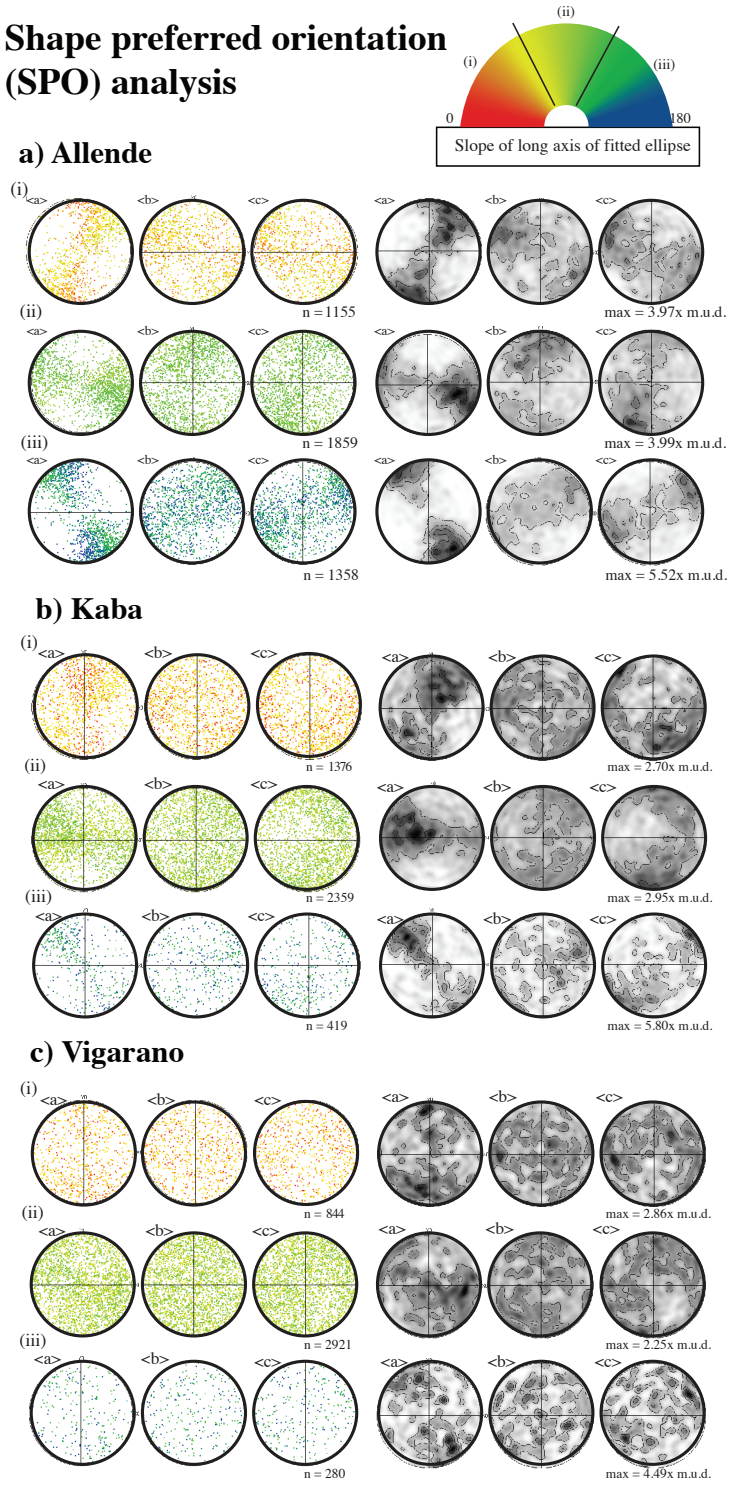

Fig. 4.5: *Shape preferred orientation (SPO) analysis lower hemisphere, equal area plots. Grains are same as those shown in Fig. 4.4, but colour coded to reflect the 'slope' or orientation of the long axis of assigned ellipse. Grains are subdivided into three subsets based on ellipse orientation; (i) (0° -60°), (ii) (60° -120°) & (iii) (120° -180°) and shown separately. The data were contoured to highlight SPO point and girdle maximas (dark regions on black and white plots).*

shape preferred orientation (Fig. 4.5). Allende displays strong yet differently oriented point maxima in <a> for each of the three subdivisions, with associated moderate girdle maxima in <c>. Kaba has a moderate <a> point maxima across the three subsets and a weak girdle maxima in <c>. Vigarano displays the weakest SPO, as only a weak point maxima can be identified in <a> within the subsets (i) and (ii).

5. DISCUSSION

Allende contains relatively large and elongate, euhedral matrix olivine laths (Fig. 4.3), which align to produce a readily identifiable CPO and closely associated SPO (Figs. 4.3 and 4.5). Kaba contains much smaller olivine grains, which are stubby and subhedral in morphology (Fig. 4.3). However, there is also a readily identifiable CPO and closely associated SPO within the mapped region of similar intensity to Allende. Conversely, Vigarano contains the smallest grains, which are subhedral-anhedral in morphology (Fig. 4.3), but still relatively elongate, and more elongate than Kaba. The SPO patterns observed in Allende demonstrate clearly that <a> and <c> correspond with the physical short and long dimensions of the matrix olivine grains, respectively. This similar pattern is observed in Kaba, although somewhat less prominently. The weak point and girdle maxima in Vigarano imply the same relationship is present, but it must be considered tentative for further interpretations.

The matrix regions mapped were situated near chondrules; the red arrows on each map of Fig. 4.3 show the locations of the chondrules with respect to the matrix area. When compared with the SPO data, <a> are oriented perpendicular to the chondrule margins, and <c> tend to be parallel to them. Given the strong crystallographic control on matrix olivine grain shape, we can, therefore, conclude the matrix grains in both Allende and Kaba are flattened against the edge of the chondrules present, and appear to weakly follow this trend in Vigarano.

The intensity and type of CPO present in an extraterrestrial sample has implications for asteroidal processing and alteration, such as impact-induced compaction, planetary-scale heating, and aqueous alteration with associated directionality (e.g. Ando et al., 2003; Forman et al., 2016; Forman et al., 2017). The three CVs examined in this study contain short <a> axis CPOs of varying intensities (Fig. 4.3) roughly perpendicular to the adjacent chondrule edges. Given that the short physical dimension of the matrix olivine laths are parallel to <a>, this distribution suggests that these grains are flattened against the larger, solid chondrules (chondrule locations shown by red arrows in Fig. 4.3), which requires compressional forces. Recent microstructural studies have concluded the flattening CPO found in Allende is the result of impact-induced compaction at the asteroidal scale, involving small but common, low-velocity surface collisions when the parent body was highly porous (Bland et al., 2014; Forman et al., 2016). Allende preserves

the most intense CPO, followed by Kaba, and Vigarano has the weakest crystallographic alignment. If considered with grain size and shape information, Kaba's grains are much smaller and stubbier (Figs. 4.1 & 4.3) than those in Allende, meaning that the CPOs may be less prominent due to grain geometry. By this logic, it could be expected that the more elongate grains of Vigarano would have produced a stronger CPO. As this is not the case (Fig. 4.3), the CPO texture may have been overprinted or controlled by another process, such as thermal alteration (Lee and Hutchison, 1996) or accumulated effects of bombardment, as evidenced by Vigarano's low porosity (Table 4.1) (Macke et al., 2011) and classification as a breccia. We therefore infer that the presence and intensity of the CPOs in these samples is, in part, controlled by grain morphology.

Vigarano does not show a strong coupling of the CPO and SPO, in contrast to those of Allende and Kaba (Figs. 4.3 & 4.5), which can be used to assess the extent and timing of parent body alteration the sample has experienced (e.g. Forman et al., 2017). Where olivine laths become less euhedral by growth into remnant pore spaces, often as a product of alteration and metamorphism, the CPO and SPO can become decoupled (Carter and Norton, 2013), which can be observed in Vigarano (Figs. 4.3 & 4.5). In contrast, olivine matrix laths in Allende have strongly coupled SPOs and CPOs and are euhedral, indicating no significant grain shape modification occurred within the Allende meteorite after asteroid compaction. This is in agreement with the extensive work of Krot et al. (2004). Conversely, decoupling of the CPO and SPO has occurred within the matrix grains of the Vigarano sample (Fig. 4.5), which contains an abundance of subhedral-anhedral olivine grains (Fig. 4.3). Based upon the inferences from Allende, the matrix olivine grains in Vigarano may have experienced shape modification or growth after porosity reduction had occurred.

The dominant control for pre-compacted grain growth must also pre-date CPO generation and asteroid compaction based on grain shape observations, which is in alignment with numerous micro-analytical studies (Rietmeijer and Mackinnon, 1985; Krot et al., 1995; Krot et al., 1998; Brenker et al., 2000; Krot et al., 2004; Hua et al., 2005). The discrepancies in grain size and aspect ratio most likely arose due to locality or depth on the parent body (Krot and Scott, 1995; Krot et al., 1995; MacPherson and Krot, 2002; Krot et al., 2004; Weiss et al., 2010; Elkins-Tanton et al., 2011). All meteorites in global collections, in addition to those examined here, are well-sorted. If the grain size and shape distributions were controlled by nebular processes, then the differences among the case study meteorites indicate that some form of sorting according to grain morphology occurred during parent body accretion. We are not aware of any disk models that have attempted to simulate this process, nor any that generate this sorting effect. We therefore concur with the studies mentioned above, and deduce the grain size

variation between the samples did not arise from nebular processing.

These samples have experienced varying extents of aqueous and thermal alteration (Krot and Scott, 1995; Krot et al., 1995; MacPherson and Krot, 2002; Krot et al., 2004), which primarily occurred prior to asteroid compaction (e.g. Krot et al., 2004). Allende has been subjected to temperatures of up to ~550 °C (Huss et al., 2006; Cody et al., 2008), which is the highest of all CV chondrites (Bonal et al., 2006), and contains olivine matrix grains with the highest iron content of the three samples (Fa_{45-55}) (Table 4.1) (Peck, 1983; MacPherson et al., 1985). Kaba and Vigarano matrices have experienced similar maximum temperatures of 415 °C and 370 °C, respectively, during thermal alteration, but differ vastly in terms of aqueous alteration, as Kaba contains a greater proportion of hydrosillicates when compared with the sparse fibrous intergrowths of hydrous minerals within the Vigarano matrices (Keller and Buseck, 1990; Hua and Buseck, 1995; Lee and Hutchison, 1996; Hua et al., 2005; Bonal et al., 2006; Cody et al., 2008). The matrix of Kaba has a large range of olivine compositions (Table 4.1), whereas the Vigarano matrix grains have a lower iron content than Allende, but of a similarly small range (Table 4.1), and hence Vigarano is interpreted to be more metamorphically equilibrated than Kaba. Aqueous alteration on the CV parent body produced secondary ferrous olivine laths by diffusion of iron into the originally Mg-rich olivines, via replacement from a low-temperature and mobile Fe-rich aqueous solution (Krot et al., 2004). Therefore, we may expect the largest and most elongate and Fe-rich grains to be present in samples that have undergone sufficient aqueous alteration. The mean grain sizes, aspect ratios, and the presence or absence of crystal facets appear to be interrelated in the three samples that were investigated (Table 4.2); from largest to smallest, average grain size is in the order Allende>Kaba>Vigarano. In terms of how euhedral the grains are, the order is the same, however in terms of aspect ratio, Vigarano has distinctly more elongate grains than Kaba. The average size and how euhedral grains are in each sample follows the same order as the predicted extent of aqueous alteration; Allende has the largest, most euhedral grains, whilst Vigarano has the smallest and most anhedral grains. The aspect ratio, or elongation of the matrix grains, follows the order of maximum temperature experienced by the sample, where Allende has the most elongate grains and has experienced >550 °C, and Kaba has the stubbiest grains, and has experienced only ~370 °C (Bonal et al., 2006; Cody et al., 2008). We therefore conclude the grain size, presence of crystal facets and potentially the Fe content of the grains, aligns with the degree of aqueous alteration, and the aspect ratio of the grains aligns with the maximum temperature experienced, that have both been established by previous studies.

The CPOs and associated grain morphologies may then be used in tandem to

predict the relative localities of each meteorite on the parent body, when considered within the context of previous observations (Krot and Scott, 1995; Krot et al., 1995; Krot et al., 1998; Krot et al., 2004). The intensity of aqueous and thermal alteration has been proposed to increase with depth (e.g. Krot et al., 1995), and so Allende would have originated from the deepest rocky part of the parent body based on the temperatures it has experienced (Bonal et al., 2006; Huss et al., 2006; Cody et al., 2008). The morphological similarities and temperatures experienced by Kaba and Vigarano imply they originated from similar depths on the CV parent body, and shallower than is inferred for Allende. Impact-induced compaction has been proposed as the porosity-reducing mechanism for Allende within the period of asteroid lithification (e.g. Bland et al., 2014; Forman et al., 2016; Forman et al., 2017). A low-intensity impact, such as that which would induce localised asteroid compaction, would be felt most severely at the surface, and the physical effects would attenuate with increased depth. Conceivably, impact-induced compaction could lead to a low-porosity 'crust' on the surface of the parent bodies. The similarly low porosities of Kaba and Vigarano can, therefore, be explained by originally shallow positions on parent bodies. However, Allende and Kaba have a substantial CPO, whereas Vigarano does not. As it is classified as a breccia, it is possible that any CPO formed from early compression has been modified beyond recognition by post-lithification reworking. It is also classed at a higher shock level of S2, and so it may have felt a more substantial impact or been closer to the impacted surface, thereby potentially creating fractures and contributing to a higher measured bulk porosity. Furthermore, higher intensity impacts would decrease porosity and cause higher temperatures due to more pores collapsing (Bland et al., 2014; Davison et al., 2016), therefore this form of thermal processing should be considered as a mechanism for creating more equilibrated and less euhedral grains at shallow depths. There is also the likelihood that these three samples were not physically close to one another; as they were probably affected by impacts of differing velocity, size and impact angle, morphological analyses of other CV chondrites would build a clearer understanding of how alteration and early compaction varied according to depth of origin and relative lateral position on the parent body.

The interplay between impacts, aqueous and thermal alteration, and the resultant characteristics of each sub-type of CV chondrite, is complex and requires further exploration. For example, it has been suggested that the differing porosities of the CV_{ox} and CV_{red} chondrites are due to the presence of primordial ice at the time of compaction (Ebel et al., 2014). Such ice within the CV_{ox} Allende may have caused rock-water reactions to take place following impact, potentially aiding matrix grain growth to create the large laths we have observed. On the contrary, CV_{red} chondrites such as

Vigarano have a much lower porosity, which may result from an initial lower abundance of primordial ice, and/or the volatilisation of much of the primordial ice prior to impact (Ebel et al., 2014), resulting in limited grain growth due to alteration. Whilst our study places tentative constraints on the timing of porosity reduction and alteration features, data from other CV chondrites is required to present a clearer and scientifically sound interpretation.

6. CONCLUSIONS

We conclude that interstitial olivine matrix grains of these CV chondrites can offer a host of morphological information directly related to the processing history of the meteorite;

- Grain sizes and how euhedral the grains are correlate to the level of aqueous alteration the sample has experienced. This means Allende has experienced the most grain growth via aqueous alteration prior to asteroidal compaction, which is confirmed by prior studies (e.g. Bonal et al., 2006; Cody et al., 2008), and Vigarano has experienced the least.

- The aspect ratio of the grains correlates to the maximum temperatures the samples have reached; Allende has again seen the highest temperatures, and has the most elongate grains, whereas Kaba is surmised to have experienced the lowest temperatures, and has the stubbiest grains of the three samples.

- CPO textures and orientations confirmed the samples were condensed by impact-induced compaction, and that these textures may be used to further explore any depth-dependency of the compaction process via impacts.

- CPO generation appears to, at least partially, be controlled by grain morphology, where the most elongate grains preserve the CPO most prominently as in the Allende and Kaba samples.

- We predict that Allende originated from the greatest depth and that Kaba and Vigarano may have been at a similar, shallow depth, but in different lateral locations on the parent body, to account for the differing shock classifications and amounts of aqueous alteration present in the two samples.

- SPO and CPO coupling gives an indication of any grain growth and recrystallization that has occurred after compaction of the parent body. Vigarano's matrix grains are anhedral and therefore may have been modified when the rock had been compacted, potentially due to impact-induced compaction heating. In contrast, Allende's grains are largely euhedral laths, indicating very little grain growth or shape modification occurred once the parent body had been compacted.

This study has emphasised the importance of assessing morphological characteristics of a meteoritic sample, and demonstrated what inferences can be drawn from such data. This approach, using EBSD datasets that can be obtained rapidly and over a wide area, may be easily implemented as a regular characteristic technique in addition to the traditional geochemical information. A large, multi-class, standardized morphological

database would allow whole classes and subclasses to be compared and contrasted to identify similarities and discrepancies, and potentially reveal new grain growth and alteration features common to a number of meteorites. We propose that an approach such as this become commonplace when characterising meteorites in future work to further our understanding of parent body processing.

7. ACKNOWLEDGEMENTS

This work was funded by the Australian Research Council via their Australian Laureate Fellowship programme (FL110100074) (PAB). We acknowledge the technical assistance and use of facilities at John de Laeter Microscopy centre, at Curtin University and the University of Sydney node of the Australian Microscopy & Microanalysis Research Facility.

8. REFERENCES

Ando, J., Tomioka, N., Petaev, M.L., Kanagawa, K., Honda, K., Shibata, Y., and Yamanaka, S., 2003, Microstructures of Olivine in the Weakly Shocked Divnoe Meteorite: AGU Fall Meeting Abstracts.

Bland, P.A., Collins, G.S., Davison, T.M., Abreu, N.M., Ciesla, F.J., Muxworthy, A.R., and Moore, J., 2014, Pressure–temperature evolution of primordial solar system solids during impact-induced compaction: Nature Communications, v. 5, p. 5451.

Bland, P.A., Howard, L.E., Prior, D.J., Wheeler, J., Hough, R.M., and Dyl, K.A., 2011, Earliest rock fabric formed in the Solar System preserved in a chondrule rim: Nature Geoscience, v. 4, no. 4, p. 244–247.

Bonal, L., Quirico, E., Bourot-Denise, M., and Montagnac, G., 2006, Determination of the petrologic type of CV3 chondrites by Raman spectroscopy of included organic matter: Geochimica et Cosmochimica Acta, v. 70, no. 7, p. 1849–1863.

Brearley, A.J., and Jones, R.H., 1998, Chondritic meteorites: Reviews in Mineralogy and Geochemistry, v. 36, no. 1, p. 3.1–3.198.

Brenker, F.E., Palme, H., and Klerner, S., 2000, Evidence for solar nebula signatures in the matrix of the Allende meteorite: Earth and Planetary Science Letters, v. 178, no. 3-4, p. 185–194.

Cody, G.D., Alexander, C.M.O., Yabuta, H., Kilcoyne, A.L.D., Araki, T., Ade, H., Dera, P., Fogel, M., Militzer, B., and Mysen, B.O., 2008, Organic thermometry for chondritic parent bodies: Earth and Planetary Science Letters, v. 272, no. 1-2, p. 446–455.

Consolmagno, G.J., Britt, D.T., and Macke, R.J., 2008, The significance of meteorite density and porosity: Chemie der Erde-Geochemistry, v. 68, no. 1, p. 1–29.

Davison, T.M., Collins, G.S., and Bland, P.A., 2016, Mesoscale modeling of impact compaction of primitive solar system solids: The Astrophysical Journal, v. 821, no. 1, p. 68.

Ebel, D. S., Weisberg, M.K., and Friedrich, J.M., 2014, Primordial Ice Abundance in CV Chondrites: Lunar and Planetary Science Conference, v. 45, p. 1207.

Elkins-Tanton, L.T., Weiss, B.P., and Zuber, M.T., 2011, Chondrites as samples of differentiated planetesimals: Earth and Planetary Science Letters, v. 305, no. 1-2, p. 1–10.

Forman, L.V., Bland, P.A., Timms, N.E., Collins, G.S., Davison, T.M., Ciesla, F.J., Benedix, G.K., Daly, L., Trimby, P.W., Yang, L., and Ringer, S.P., 2016, Hidden secrets of deformation: Impact-induced compaction within a CV chondrite: Earth and Planetary Science Letters, v. 452, p. 133–145.

Forman, L. V., Bland, P. A., Timms, N. E., Daly, L., Benedix, G. K., Trimby, P. W., Collins, G. S., & Davison, T. M., 2017, Defining the mechanism for compaction of the CV chondrite parent body: Geology, v. 45, no. 6, p.559-562.

Grossman, J.N., Rubin, A.E., Nagahara, H., and King, E.A., 1988, Properties of chondrules, in Kerridge, J.F. and Matthews, M.S. eds., Meteorites and the Early Solar System, University of Arizona Press, Tuscon, Arizona, p. 619–659.

Hewins, R.H., 1997, Chondrules: Annual Review of Earth and Planetary Sciences, v. 25, no. 1, p. 61–83, doi: 10.1146/annurev.earth.25.1.61.

Hua, X., and Buseck, P.R., 1995, Fayalite in the Kaba and Mokoia carbonaceous chondrites: Geochimica et Cosmochimica Acta, v. 59, no. 3, p. 563–578.

Hua, X., Huss, G.R., Tachibana, S., and Sharp, T.G., 2005, Oxygen, silicon, and Mn-Cr isotopes of fayalite in the Kaba oxidized CV3 chondrite: Constraints for its formation history: Geochimica et Cosmochimica Acta, v. 69, no. 5, p. 1333–1348.

Huss, G.R., Rubin, A.E., and Grossman, J.N., 2006, Thermal metamorphism in chondrites, in McSween, H.Y. and Lauretta, D.S. eds., Meteorites and the Early Solar System II, University of Arizona, Tuscon, Arizona, p. 567–586.

Keller, L.P., and Buseck, P.R., 1990, Aqueous alteration in the Kaba CV3 carbonaceous chondrite: Geochimica et Cosmochimica Acta, v. 54, no. 7, p. 2113–2120.

Krot, A.N., and Scott, E.R.D., 1995, Alteration of CV3 carbonaceous chondrites: Parent body vs. nebular processes: Lunar and Planetary Science Conference, v. 26, p. 803.

Krot, A.N., Meibom, A., and Keil, K., 2000, A clast of Bali-like oxidized CV material in the reduced CV chondrite breccia Vigarano: Meteoritics & Planetary Science, v. 35, no. 4, p. 817–825.

Krot, A.N., Petaev, M.I., and Bland, P.A., 2004, Multiple formation mechanisms of ferrous olivine in CV carbonaceous chondrites during fluid-assisted metamorphism: Antarctic Meteorite Research, v. 17, p. 153–171.

Krot, A.N., Petaev, M.I., Scott, E.R.D., Choi, B.G., Zolensky, M.E., and Keil, K., 1998, Progressive alteration in CV3 chondrites: More evidence for asteroidal alteration: Meteoritics & Planetary Science, v. 33, no. 5, p. 1065–1085.

Krot, A.N., Scott, E.R.D., and Zolensky, M.E., 1995, Alteration and dehydration in the parent asteroid of Allende: Meteoritics, v. 30, no. 5, p. 530–531.

Lee, M.R., and Hutchison, R., 1996, Aqueous alteration in the matrix of the Vigarano (CV3) carbonaceous chondrite: Meteoritics & Planetary Science, v. 31, p. 477–483.

Macke, R.J., Britt, D.T., and Consolmagno, G.J., 2011, Density, porosity, and magnetic susceptibility of achondritic meteorites: Meteoritics & Planetary Science, v. 46, no. 2, p. 311–326.

MacPherson, G.J., and Krot, A.N., 2002, Distribution of Ca-Fe-silicates in CV3 chondrites: Possible controls by parent-body compaction.: Meteoritics & Planetary Science, v. 37, no. 7, p. A91–A91.

MacPherson, G.J., Hashimoto, A., and Grossman, L., 1985, Accretionary rims on inclusions in the Allende meteorite: Geochimica et Cosmochimica Acta, v. 49, no. 11, p. 2267–2279.

McSween, H.Y., 1977a, Petrographic variations among carbonaceous chondrites of the Vigarano type: Geochimica et Cosmochimica Acta, v. 41, no. 12, p. 1777–1790.

McSween, H.Y., Jr, 1977b, Carbonaceous chondrites of the Ornans type: A metamorphic sequence: Geochimica et Cosmochimica Acta, v. 41, no. 4, p. 477–491.

Peck, J.A., 1983, An SEM petrographic study of C3 (V) meteorite matrix: Lunar and Planetary

Science Conference, v. 14, p. 598–599.

Peck, J.A., 1984, Origin of the variation in properties of CV3 meteorite matrix and matrix clasts: Lunar and Planetary Science Conference, v. 15, p. 635.

Rietmeijer, F.J.M., and Mackinnon, I.D.R., 1985, Poorly graphitized carbon as a new cosmothermometer for primitive extraterrestrial materials: Nature, v. 315, no. 6022, p. 733–736.

Scott, E.R.D., and Krot, A.N., 2003, Chondrites and their Components: Treatise on geochemistry, v. 1, p. 7.01–7.72.

Scott, E.R.D., Barber, D.J., Alexander, C.M., Hutchinson, R., and Peck, J.A., 1988, Primitive material surviving in chondrites - Matrix, in Sears, D. and Dodd, R.T. eds., Meteorites and the Early Solar System, University of Arizona Press, Tuscon, Arizona, p. 718–745.

Stöffler, D., Keil, K., and Scott, E.R.D., 1991, Shock Metamorphism of Ordinary Chondrites: Geochimica et Cosmochimica Acta, v. 55, no. 12, p. 3845–3867.

Tait, A.W., Fisher, K.R., Srinivasan, P., and Simon, J.I., 2016, Evidence for impact induced pressure gradients on the Allende CV3 parent body: Consequences for fluid and volatile transport: Earth and Planetary Science Letters, v. 454, p. 213–224.

Van Schmus, W.R., and Wood, J.A., 1967, A chemical-petrologic classification for the chondritic meteorites: Geochimica et Cosmochimica Acta, v. 31, no. 5, p. 747–765.

Watt, L.E., Bland, P.A., Prior, D.J., and Russell, S.S., 2006, Fabric analysis of Allende matrix using EBSD: Meteoritics & Planetary Science, v. 41, no. 7, p. 989–1001.

Weisberg, M.K., Prinz, M., and Clayton, R.N., 1997, CV3 chondrites: Three subgroups, not two: Meteoritics and Planetary Science, v. 32, no. 4, p. A138–A139.

Weiss, B.P., Carporzen, L., Elkins-Tanton, L.T., Shuster, D.L., Ebel, D.S., Gattacceca, J., Zuber, M.T., Chen, J.H., Papanastassiou, D.A., Binzel, R.P., Rumble, D., and Irving, A.J., 2010, A Partially Differentiated Body for CV Chondrites?: Lunar and Planetary Science Conference, v. 41, p. 1688.

Chapter 5

Relicts of an impactor: searching for the iridium carrier within the distal K-Pg Boundary Clays

The following chapter is in preparation for submission to GEOCHIMICA ET COSMOCHIMICA ACTA.

L.V. Forman[1], L. Daly[1], P. A. Bland[1], N. Evans[1], K. Merigot[2], C. G. Ryan[3] N. E. Timms[1], G. K. Benedix[1], M. Saunders[4].

[1]Department of Applied Geology, Curtin University, GPO Box U1987, Perth, WA 6845, Australia

[2]John de Laeter Centre of Excellence, Curtin University, Bentley, WA 6102, Australia.

[3]CSIRO Mineral Resources, Clayton, VIC 3168, Australia

[4]Centre for Microscopy, Characterisation and Analysis, The University of Western Australia, WA 6009, Australia.

1. ABSTRACT

The K-Pg boundary sites are enriched in iridium, amongst other PGEs, above terrestrial values. This enrichment is somewhat uniform across all locations originally distal (<4000 km) to the Chicxulub impact crater. This study identified the carrier phase of Ir as FeO and amphibole within the Woodside Creek K-Pg sample, from New Zealand, which was at a paleo-distance of 14,000 km from the impact site. X-ray fluorescence (XRF) analysis, liberation analysis using the Tescan Integrated Mineral Analyser (TIMA), laser ablation inductively-coupled plasma mass spectrometry (LA-ICP-MS), feature mapping and transmission electron microscopy (TEM) techniques were employed to identify and explore this relationship. Association with these two dissimilar phases implies Ir is unlikely to be in native meteoritic form, and has condensed from a cooling vapour cloud of bulk intermediate composition.

TEM of the FeO spherule inclusion revealed no nano-nuggets of Ir are present within the sampled region. There is a small possibility that sampling effects resulted in a TEM lamella devoid of nuggets, however the probability is sufficiently low that we may conclude Ir is not present as nuggets at all within the FeO, and is possibly disseminated throughout the oxide phase. This may therefore imply that the oxygen fugacity of the vapour plume and atmosphere was sufficiently high that Ir did not exsolve out of the phase upon melting. Further TEM investigations of this phase and all other phases associated with Ir are recommended to fully constrain the form of Ir present, and to advance our understanding of ejecta cloud processes for the K-Pg impact event.

2. INTRODUCTION

The Cretaceous-Paleogene (K-Pg) boundary clays worldwide record varied bulk-analysis enrichments of Ir and other platinum group elements (PGEs), at numerous well-documented marine, shallow marine and terrestrial locations, that were proximal (<2000 km), intermediate (2000-4000 km) and distal (>4000 km) paleo-distances from the impact site (e.g. Fig. 5.1) (Smit and Hertogen, 1980; Smit and Kyte, 1984; Smit, 1999; Schulte et al., 2010). This kind of enrichment in a highly siderophile element within terrestrial materials did not originate on Earth; refractory elements only exist in such abundances on asteroids, or within meteorites. These clays were formed during one of the most extreme mass extinctions in Earth's history at 66.043 Ma (Gartner and McGuirk, 1979; Alvarez et al., 1980; Alvarez et al., 1982), which is believed to have at least partially resulted from a catastrophic impact at the Chicxulub crater impact site on the Yucatán peninsula in Mexico (red dot in Fig. 5.1) (Hildebrand et al., 1991; Pope et al., 1991; Alvarez et al., 1995). The boundary layers are

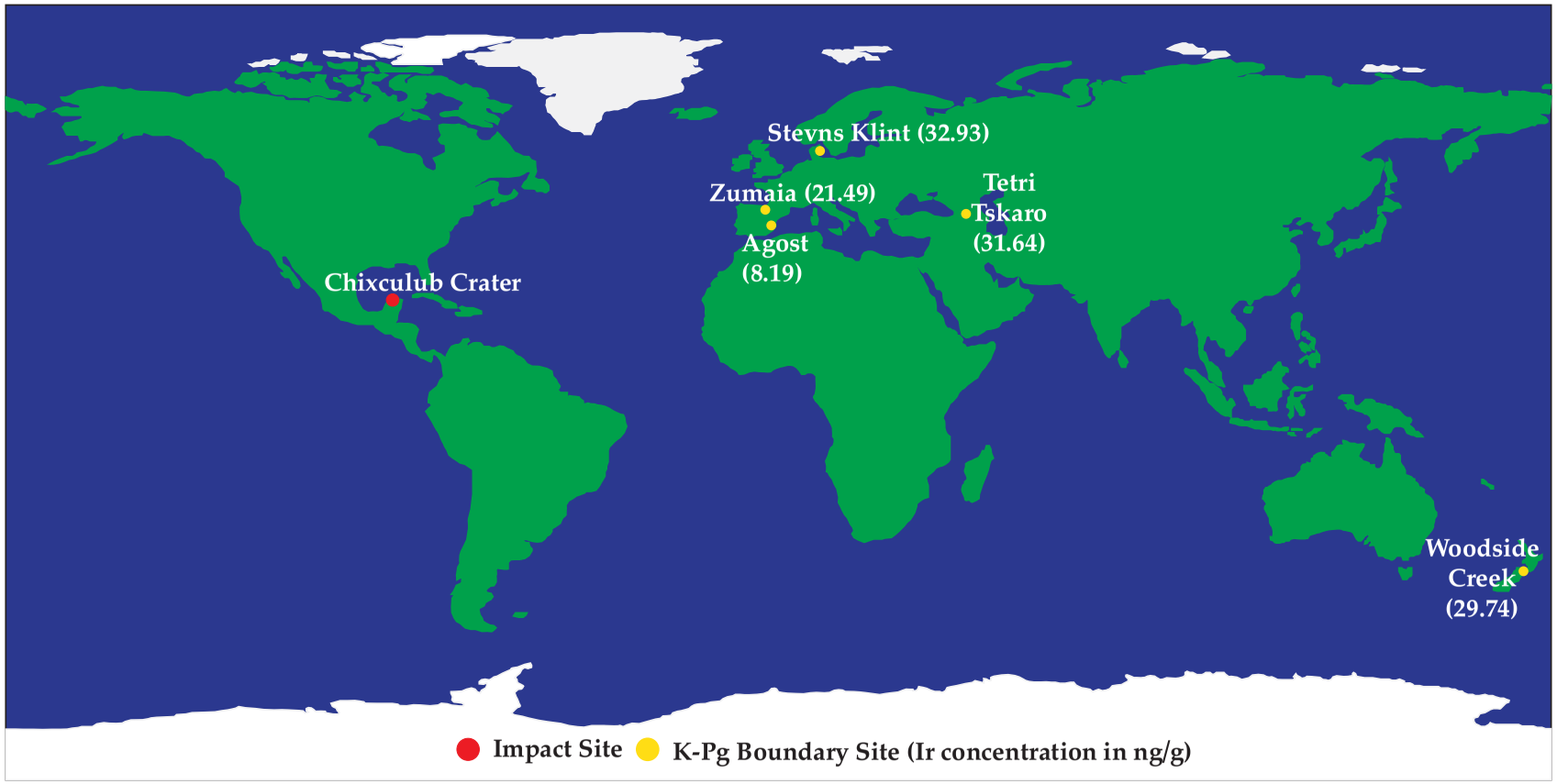

Figure 5.1: *World map of Cretaceous- Paleogene boundary samples examined in this study. Quoted Ir concentrations are in ng/g (Goderis et al., 2013). Yellow dots indicate the location of a distal ejecta site, and the red dot represents the location of the impact.*

confirmed to contain material that originated from the projectile (Alvarez et al., 1980; Kyte, 1998; Shukolyukov and Lugmair, 1998a; Shukolyukov and Lugmair, 1998b; Trinquier et al., 2006; Quitte et al., 2007; Schulte et al., 2010; Goderis et al., 2012) which identified the impactor as a carbonaceous chondrite (CM) based on the geochemical fingerprint present in the ejecta (Smit, 1999; Goderis et al., 2012). Therefore, further examination of the distribution of PGEs within this layer, specifically the Ir, will enhance our understanding of impact ejecta transport as well as the environmental conditions within the expanding impact plume, where most distal ejecta is thought to have been processed (e.g. Smit and Klaver, 1981).

Numerical models have been constructed to constrain the nature of the impact scenario based upon global ejecta distributions. Artemieva & Morgan (2009) concluded the most probable scenario involved a 10-14.4 km diameter (Morgan, 2008) projectile impacting on a 45 degree incidence angle, although the velocity it was travelling at remains unclear (Artemieva and Morgan, 2009). Complimentary impact cloud numerical simulations (Artemieva and Morgan, 2007; Pierazzo and Artemieva, 2012) predicted temperatures at different locations within the impact plume and ejecta curtain, as well as plume size and shape. In addition, Artemieva and Morgan (2009) discussed the possibility that the global ejecta distribution, specifically at distal sites, may be the result of debris re-entry (Artemieva and Morgan, 2009). Their simulations which considered only ballistic debris transport and vapour cloud fallout did not accurately replicate the relatively consistent thickness of distal ejecta that has been observed in the field. Therefore, additional transport mechanisms are required. Upon debris re-entry, the atmosphere would heat and expand (Artemieva and Morgan, 2009) and may have been the driver for debris transport to the paleo-distal K-Pg sites. Preliminary simulation results (Artemieva and Morgan, 2009) imply rapid and efficient dispersion of the re-entry debris. This form of debris transport resolves the shortfalls of previous models, such as too much material being predicted at the North American sites, and insufficient and variable debris deposited at distal sites (Artemieva and Morgan, 2009). We therefore consider this process in the context of our investigation.

Archaean PGE micro-nuggets (3.2 Ga) have been identified within a similar impact spherule layer situated in the Barberton Greenstone Belt, South Africa (Goderis et al., 2013a; Mohr-Westheide et al., 2015; Mohr-Westheide et al., 2016). These nuggets were enclosed in Ni-Cr spinel, but lacked a chemical or structural relationship with the host phase, indicating the nuggets formed independently of the surrounding phase (Mohr-Westheide et al., 2016). One of the micro-nuggets investigated by Mohr-Westheide et al. (2016) presented with a hexagonal close-packed (hcp) crystal structure, which is a stable form of PGE alloys at high-temperature (Harries et al., 2012; Mohr-Westheide et al.,

2016), potentially reflecting the conditions such nuggets were exposed to or formed in following impact. Another impact spherule layer, also Archaean in age (2.57 Ga), contains PGE micro- and nano-nuggets with a depletion in Os relative to Ir, that the authors attribute to temperature-dependant impact plume fractionation processes given that Os will oxidise more readily than Ir (Goderis et al., 2013a). This has also been proposed to have occurred following the K-Pg impact within the impact plume (Evans et al., 1994). The PGEs within the Archaean impact layers were concentrated within spherules and as nano-nuggets at spherule rims, indicating the formation of the PGE nuggets preceded the spherules but both resulted from primary condensation and recrystallisation within the ejecta cloud (Goderis et al., 2013a).

Iridium located at the K-Pg boundary has predominantly been identified and examined via bulk geochemical analysis (e.g. Alvarez et al., 1980; Smit and Hertogen, 1980; Ganapathy et al., 1981; Alvarez et al., 1982; Smit and Kyte, 1984; Kyte et al., 1985; Alvarez et al., 1990; Elliot et al., 1994; Evans et al., 1994; Alvarez et al., 1995; Kyte, 1998; Shukolyukov and Lugmair, 1998a; Shukolyukov and Lugmair, 1998b; Smit, 1999; Claeys et al., 2002; Quitte et al., 2007; Osawa et al., 2009; Schulte et al., 2010). Our study is one of the first to address the in situ form of the Ir within the K-Pg boundary lithologies (e.g. Goderis et al., 2013a). Iridium and other PGEs are highly refractory, and as such they have high melting points (2719 K) (Harvey and Day, 2016) and high 50% condensation temperatures (1408-1821 K) (Lodders, 2003; Harvey and Day, 2016). Therefore, the phase the Ir is associated with, and the form (nugget- micro or nano- or disseminated as an oxide) the Ir currently takes may constrain the temperature and

Table 5.1: *Characteristics of the five distal K-Pg sites examined in this study. All sites have similar thickness and Ir concentrations, despite the difference in paleo-distance from the Chicxulub impact crater in Mexico.*

Boundary Site	Paleo-distance to Chicxulub Crater (km)	Thickness of unit (cm)	Ir Concentration (ng/g)
Agost[1,2]	5600	0.3	8.19
Zumaya[2,3]	5500	0.3	21.49
Stevns Klint[2,4]	6400	0.3	32.93
Tetri Tskaro[2,5,6]	9000	0.3	31.64
Woodside Creek[2,7]	14,000	0.2	29.74

1= Molina et al., 2005; 2= Goderis et al., 2013b; 3= Doehne and Margolis, 1990; 4= Drits et al., 2004; 5= Heymann et al., 1996; 6= Smit et al., 1999; 7= Brooks et al., 1985.

oxidation conditions during ejecta debris transport from the impact site (Goderis et al., 2013a; Goderis et al., 2013b).

3. SAMPLES AND METHODS

Samples from five, well-established K-Pg boundary sites were examined in this study (Fig. 5.1, Table 5.1):

1. Agost, Southern Spain
2. Zumaya, Northern Spain
3. Stevns Klint, Denmark
4. Tetri Tskaro, Georgia
5. Woodside Creek, South Island, New Zealand

The primary aim of this study was to identify the host phase of Ir within the distal (>4000 km) K-Pg boundary layers. We utilised five samples (Fig. 5.1, Table 5.1), from various paleo-distances from the impact site, to help constrain post-impact processing conditions during ejecta dispersion using an extensive range of analytical techniques.

3.1 Synchrotron X-Ray Fluorescence Microscopy (XRF) Imaging

X-ray fluorescence microscopy (XRF) images were collected for Zumaya, Tetritskaro, Stevns Klint and Woodside Creek at the Australian Synchrotron facility in Melbourne, Australia. One thin section of each sample site was prepared for this analysis; sections across the boundary were impregnated with epoxy resin into 2.5 cm round slides. Using the XRF beamline, the Maia 384 detector array and integrated real-time processor were employed to obtain 25 element maps of each boundary sample (Ryan et al., 1990; Cleverley et al., 2012). We used a focussed spot size of 2 μm, which produced XRF maps with 2 μm spatial resolution. A beam energy of 18.5 keV was used throughout. The instrument collected diagnostic X-rays between the 3.3-19.9 keV energy range, and an energy resolution of 300-400 eV, which produce quantitative abundances for a number of major and minor elements (including As, Au, Bi, Br, Ca, Co, Cr, Cu, Fe, Ga, Ge, Hg, Ir, Mn, Ni, Os, Pb, Pt, Rb, Re, Sc, Se, Sr, Ti, Tl, V, W, Y, Zn and Zr) (Ryan et al., 1990; Ryan et al., 2010; Cleverley et al., 2012; Dyl et al., 2014). Furthermore, this instrument can detect elemental abundances to the 10-100 ppm level, which is an improvement on typical imaging techniques (Fisher et al., 2014). XRF is particularly sensitive to the PGEs and has previously been used to identify PGE-bearing nuggets in primitive meteorites (Daly et al., in press) making particularly useful for the purpose required here.

Data reduction was done using the software package GeoPIXE (Ryan et al., 1990). This allowed us to deconvolve the elemental spectra and obtain accurate element maps (Ryan et al., 2005). Further details of this process may be found in the methods section of Dyl et al. (2014). Three elements were combined into composite RGB maps using the GeoPIXE software to highlight the location of Ir enrichments and their associations with lithological components and major elements.

All further sample preparations and analyses detailed hereafter were conducted at the John de Laeter Centre for Excellence at Curtin University, Perth, unless otherwise

stated.

3.2 TIMA Imaging

Mineral liberation analysis was carried out on four of the samples (Agost, Stevns Klint, Woodside Creek & Zumaya) using the Tescan Integrated Mineral Analyser (TIMA)- a Field Emission Scanning Electron Microscope with four silicon drift Energy Dispersive X-ray Spectrometers (EDS). The TIMA system is designed to identify mineral phases in thin sections or resin mounted samples. This technique uses a combination of Backscattered Electron (BSE) imaging and EDS measurements to identify variations between pixels to define grain boundaries. When a grain is identified, the EDS spectra from each pixel in the grains is summed to produce a characteristic spectrum from which the grains composition can be determined. The characteristic spectrum is then matched against sets of rules used to define minerals until a match is found, and a mineral assigned. If the spectrum does not match any minerals within the classification scheme, it must be correctly identified and used to create a new mineral definition file. When a sufficient area of the sample has been correctly classified, the TIMA software can provide liberation characteristics such as mineral abundance, elemental abundance, grain size, mineral associations, porosity and much more.

To carry out this analysis, the 4 boundary samples were laid flat and coated with 10nm of carbon to be made conductive. The TIMA was operated at a voltage of 25 KeV, with a spot size of 52 nm and 15 mm working distance. The EDS was collected with a 2 μm step size.

3.3 LA-ICP-MS Analyses

After TIMA analysis, two samples were selected for laser ablation ICPMS analysis to produce elemental maps over a selected area of the Woodside Creek (Fig. 5.9) and Zumaya samples using an Australian Scientific Instruments RESOlution M-50A-LR incorporating a Compex 102 excimer laser, coupled to an Agilent 7700s quadrupole ICP-MS. These two samples were selected based on their similar Ir bulk concentrations and their dissimilar paleo-distances to the impact crater. Mapping was undertaken using a 28 μm beam with a frequency of 10 Hz, energy at sample surface of 2.5 Jcm^{-2}, and 12 μm/s scan speed with a 50% path cleaning overlap. Total mapping time was 15 hours for the 6 mm^2 mapped area and a duplicate series of trace element standards (GSD-1G, NIST 610, Po726) was analysed at the start and end of the sample map lines. Oxide polyatomic interferences were minimized by tuning gas flow rates for a ThO/Th of < 0.5%. The sample cell was flushed with ultrahigh purity He (350 ml min-1) and N2 (3.8 ml min-1) and high purity Ar was employed as the plasma carrier gas. The mass spectra were reduced using Iolite (Paton et al., 2011 and references therein). Data were collected on a total of 39 isotopes (^{24}Mg, ^{27}Al, ^{28}Si , ^{29}Si, ^{31}P, ^{43}Ca, ^{44}Ca, ^{47}Ti, ^{49}Ti, ^{51}V, ^{52}Cr, ^{56}Fe, ^{57}Fe, ^{58}Ni, ^{59}Co, ^{60}Ni, ^{63}Cu, ^{66}Zn, ^{71}Ga, ^{72}Ge, ^{75}As, ^{77}Se, ^{82}Se, ^{90}Zr, ^{101}Ru, ^{103}Rh, ^{105}Pd, ^{107}Ag, ^{125}Te, ^{178}Hf, ^{182}W, ^{185}Re, ^{189}Os, ^{193}Ir, ^{195}Pt, ^{197}Au, ^{201}Hg, ^{208}Pb, ^{238}U). Initially, a

background subtracted counts per second (cps) map of Ir was obtained. Areas of high counts were correlated with the TIMA maps in order to determine a reasonable estimation of host composition for internal isotopic referencing. The highest cps Ir regions corresponded to FeO (57.4% Fe, 37.6% O) allowing us to determine quantitative Ir abundance maps for this phase. We used international glass standard GSD-1G as the primary reference material (assuming 57.4% ^{57}Fe as the internal standard element) in order to produce a quantitative elemental map and to correct for instrument drift on all elements.

3.3.1 Data Reduction

The LA-ICP-MS Ir counts per second (cps) maps must be reduced according to the mineralogy of the sample. Given that the samples dealt with here are polymineralic, separate maps were generated to reflect different mineralogies in various parts of the sample, and the regions with that respective mineralogy were indicated in each case. Composite maps could not be created at this time, therefore the Ir concentrations are accurate only where the mineralogy used to reduce the data is located.

3.4 Feature Mapping Analyses

The identification of small (~100 nm) particles of high density within a large area can be performed using the Oxford Instruments INCA feature mapping software, whereby BSE images are taken of areas of interest and all regions or 'hotspots' of the sample within a defined contrast band are analysed. This can also be done in conjunction with EDS to identify if a specific element is present. We used the Zeiss EVO50 Scanning Electron microscope with a LaB6 filament at the Australian Centre for Microscopy and Microanalysis (ACMM) in Sydney at 25 keV, to rapidly detect grains with a high comparative density to the rest of the sample, such as PGE nuggets (e.g. Daly et al., 2016). This allowed all grains containing Ir and similar heavy elements above 100 nm in diameter to be identified for further analysis. The entire sections of the Zumaya, Stevns Klint and Woodside Creek samples were analysed using this technique.

3.5 FIB & TEM Imaging

A sample of the iron-bearing spherule/Ir-enriched inclusion from the Woodside Creek sample (Fig. 5.9 & 5.11) identified using LA-ICP-MS was prepared for TEM analysis using focussed ion beam techniques (see Li et al., 2006 and references therein). A TEM lamellae was extracted using the FEI Helios Nanolab G3 CX DualBeam FIB/SEM, at the Centre for Microscopy, Characterisation and Analysis, University of Western Australia. An initial protective layer of Pt was deposited over the sample using the gas injection system (GIS). The first layer was deposited using an electron beam and a further, thicker layer was deposited using a Ga ion beam. The sample was then milled using the Ga beam to produce a series of trenches around the protective layer. The lamella was then attached to a Kleindiek micromanipulator with a Pt weld, and cut free from the sample and lifted out. It was attached to a pre-prepared Cu TEM

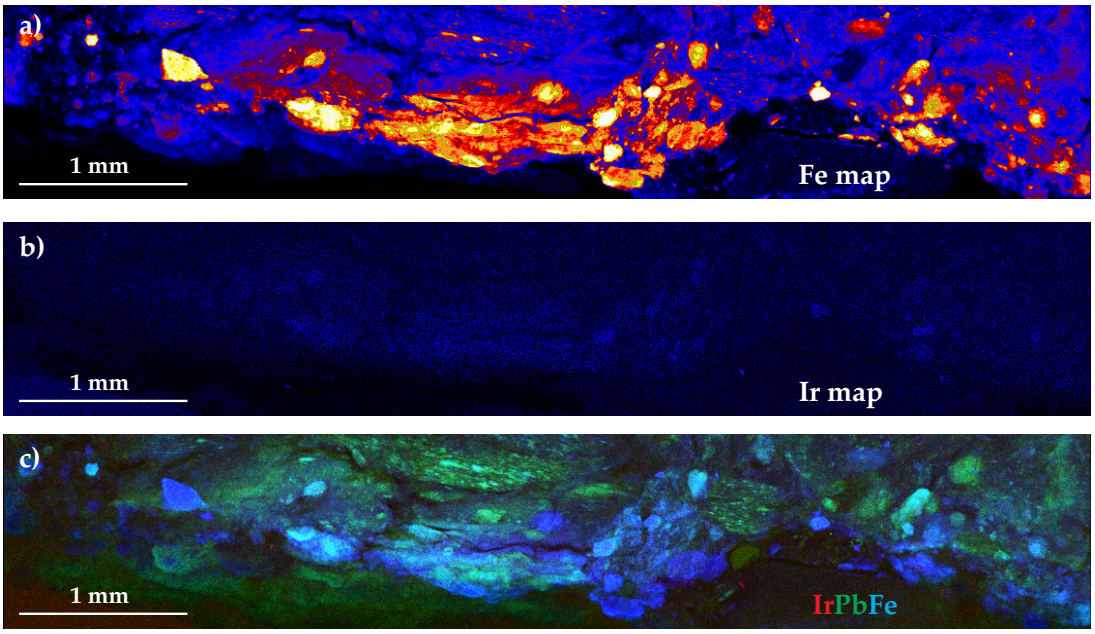

Figure 5.2: *XRF Synchrotron image of the Woodside Creek boundary section. A) Fe distribution map, b) Ir distribution map c) RGB composite map of Ir, Pb and Fe, respectively. Fe-rich spherules here have some correlation to the Ir-hotspots (b).*

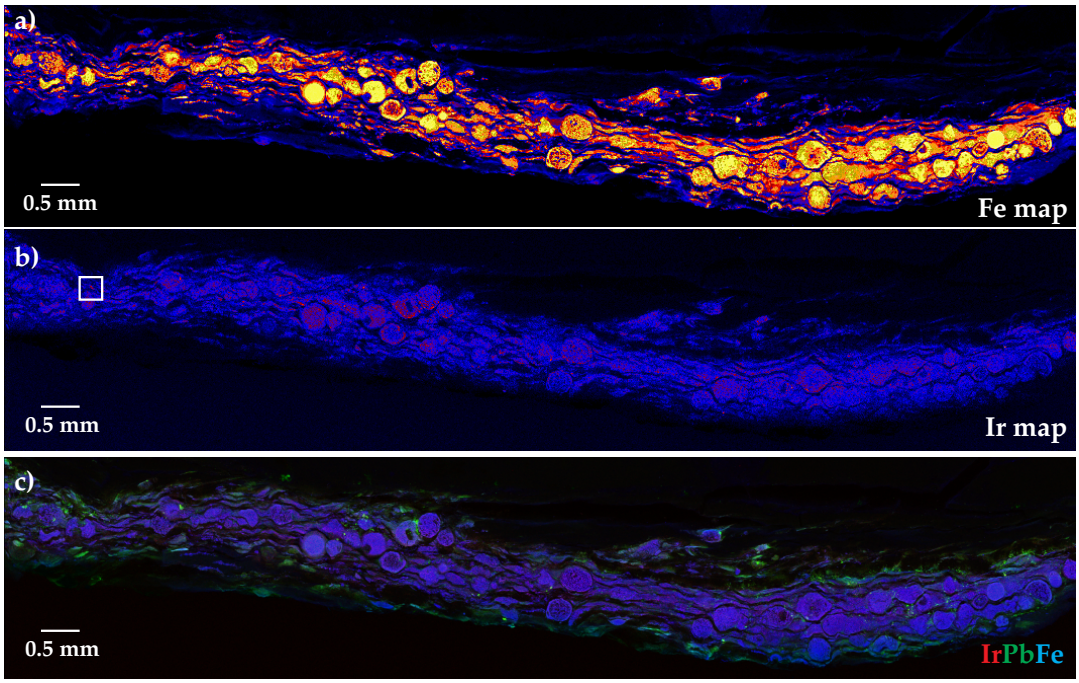

Figure 5.3: *XRF Synchrotron image of the Zumaya boundary section. A) Fe distribution map, b) Ir distribution map c) RGB composite map of Ir, Pb and Fe respectively. Abundant Fe-rich spherules correlate well to a significant Ir enrichment (b), but this also appears to coincide, with high Pb areas (c). White box marks region analysed in spectra in Fig. 5.4.*

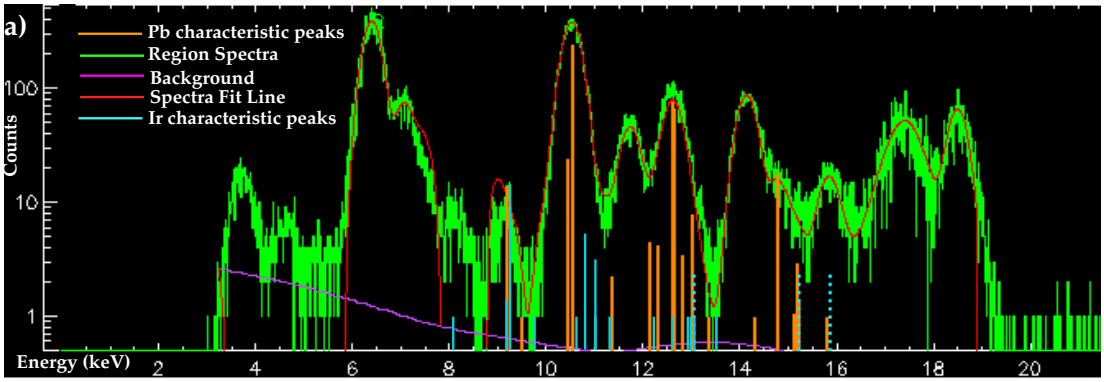

***Figure 5.4**: Energy spectra for hotspot identified in Fig. 5.3. Ir and Pb can be identified on this spectra by their characteristic energy peaks; Pb characteristic peaks shown in orange, Ir characteristic peaks in blue, spectral measurement shown in green. The hotspot identified as Ir-enriched in Fig. 5.3 may therefore be a Pb hotspot, as there is a significant overlap in the characteristic energies of the spectral measurement.*

sample holder by means of two further Pt welds. The sample was then thinned using a fine Ga beam until the lamellae was electron transparent (~100 nm). The resulting sample was 6.16 μm x 5.68 μm and 100 nm thick. The sample was then placed in the FEI Titan G2 80-200 TEM/STEM with ChemiSTEM Technology, at the Centre for Microscopy, Characterisation and Analysis, University of Western Australia. The sample was analysed at 200 keV. EDS was acquired using the Super-X 4-SDD, windowless EDS detector system.

4. RESULTS

4.1 XRF Synchrotron Imaging

The XRF synchrotron maps presented for two of the five samples show that Ir appears to be heterogeneously disseminated throughout the clays (e.g. Figs. 5.2 & 5.3). Each figure shows the Fe distribution map (top), the Ir distribution map (middle) and an RGB composite map of Ir, Pb and Fe (bottom). A small number of Ir-rich hotspots were identified for separate analysis (e.g. region outlined in Fig. 5.3), however examination of the associated spectra for the hotspot regions revealed there is a significant overlap between the characteristic energy peaks of Ir and Pb at 10.5 keV and 12.5 keV (Fig. 5.4). This was the case for all PGE hotspots identified for further investigation using the XRF beamline. There is therefore significant uncertainty as to whether the Ir identified by the GeoPIXE software package is real or an artefact from Pb overlaps, and subsequently the Ir host phase could not be identified using this technique.

4.2 TIMA Imaging

TIMA phase maps provided full spatial context of the Agost, Zumaya, Stevns Klint and Woodside Creek sections of the K-Pg boundary (Figs. 5.5-5.8). The predominant phases within the Stevns Klint and Zumaya sections are identified as both feldspars and carbonates (Figs. 5.5 & 5.6), whilst Agost and Woodside Creek are dominated by just

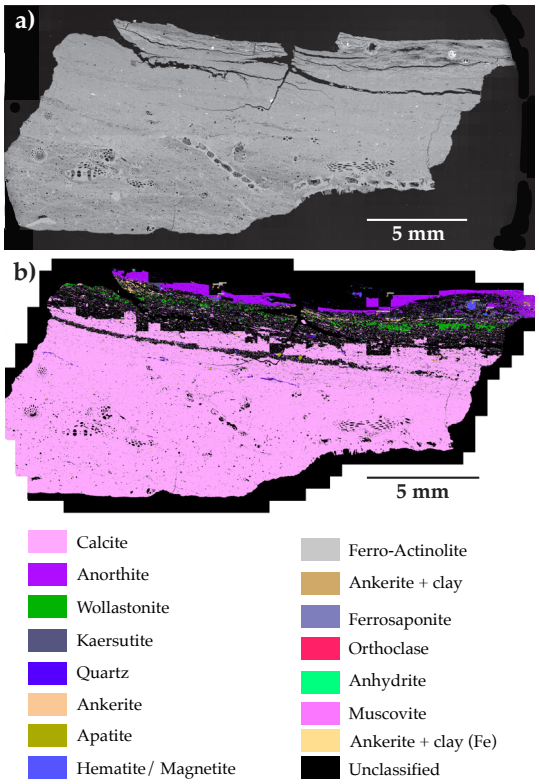

◂ ***Figure 5.5:*** *TIMA Analysis of the Stevns Klint section; a) BSE image, b) TIMA mineral phase map.*

feldspars (Figs. 5.7 & 5.8). The Agost section contained very few Fe-rich phases, whereas Woodside Creek and Stevns Klint contained a few Fe-rich spherules and inclusions. Zumaya contains abundant sulphide and sulphate-rich spherules, surrounded by calcic amphiboles and feldspars (Fig. 5.9). There is an abrupt change in mineralogy observed at the Stevns Klint and Zumaya boundary sections (Figs. 5.5 & 5.6), with prominent sulphides, sulphates and calcic amphiboles in the spherule layer of Zumaya, and calcium silicates and carbonates in the spherule layer in Stevns Klint. The mineralogy does

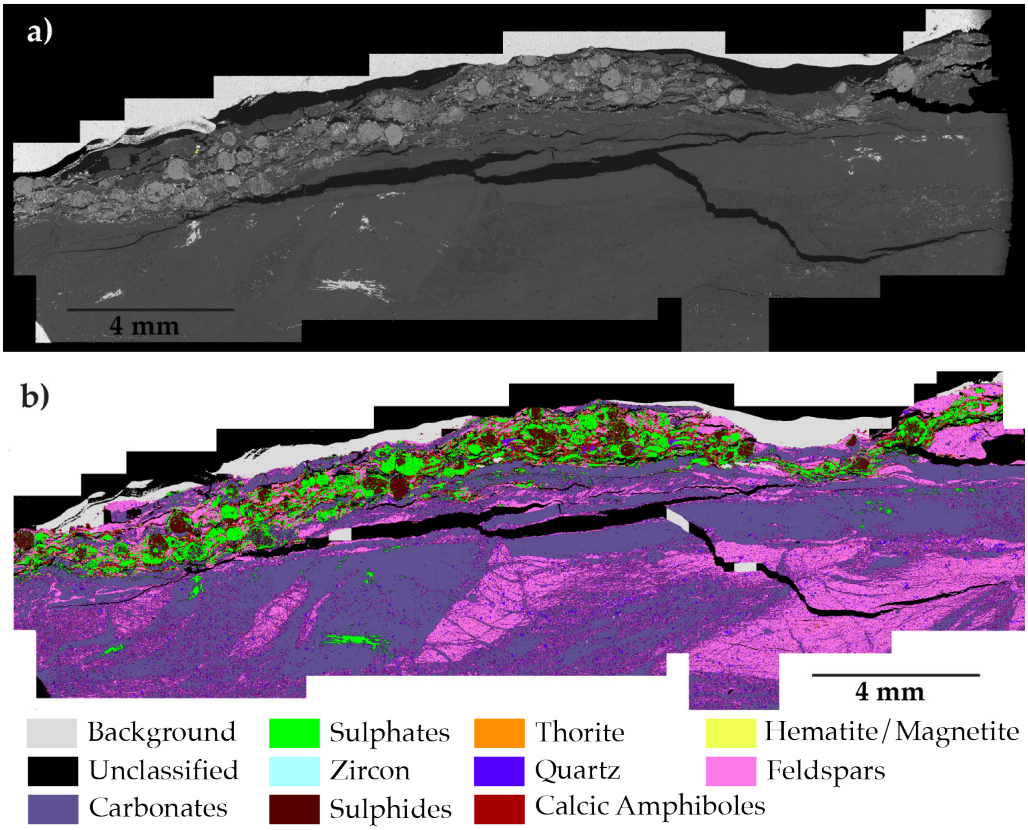

Figure 5.6: *TIMA Analysis of the Zumaya section; a) BSE image, b) TIMA mineral phase map.*

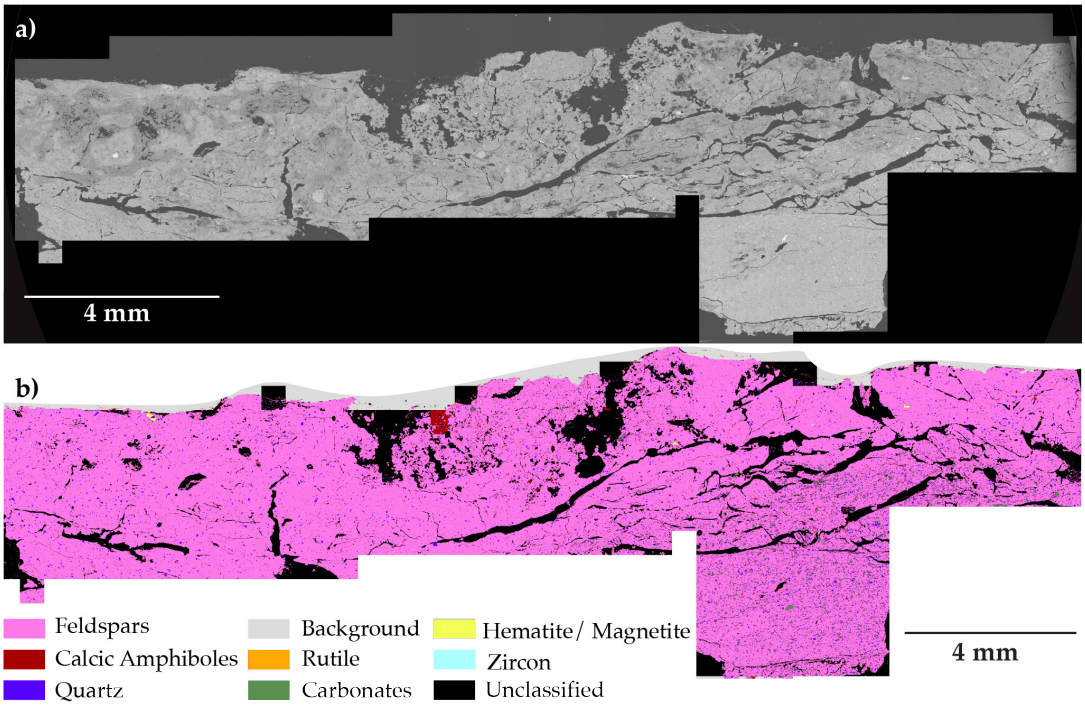

Figure 5.7: *TIMA Analysis of the Agost section; a) BSE image, b) TIMA mineral phase map.*

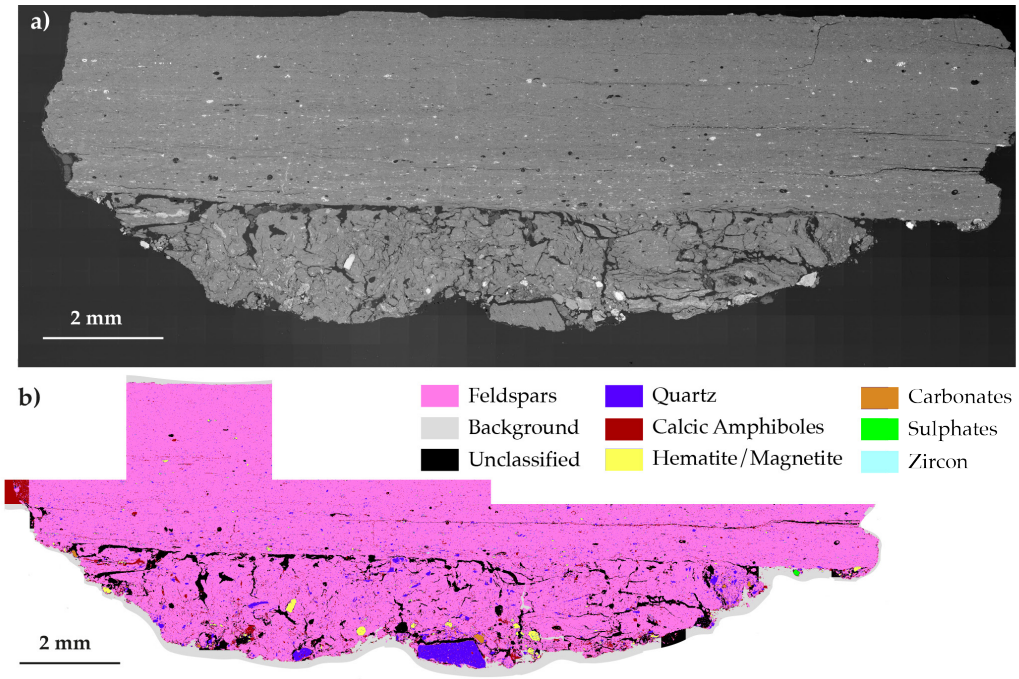

Figure 5.8: *TIMA Analysis of the Woodside Creek section; a) BSE image, b) TIMA mineral phase map.*

not change significantly across the K-Pg boundary in the Agost or Woodside Creek sections (Figs. 5.7 & 5.8).

4.3 LA-ICP-MS Mapping

Fig. 5.9 shows the background subtracted Ir counts per second (cps) (Fig. 5.9a) and parts per million (ppm) laser maps for

Woodside Creek. Iridium background subtracted cps maps imply that Ir is weakly concentrated in calcic amphiboles and some FeO spherules. The data were then reduced based upon mineralogical data from the TIMA map (Figure 5.8 & 5.9b); assuming a host phase of FeO for spherules (Fig. 5.9c) and plagioclase (Fig 5.9d) for the matrix respectively, quantitative Ir abundance maps were produced (Fig. 5.9). No Ir enrichment was observed in the feldspar, but up to 4 ppm Ir was observed in some FeO spherules (Fig. 5.9c), and between 2-6 ppm Ir was observed within amphibole (Fig. 5.10). A further enrichment was also observed in spherules that were not characterised successfully by the TIMA technique (black on TIMA image; Fig. 5.9a & b). Only the white boxes in these LA-ICP-MS maps reflect the true concentration of Ir, as processing is reliant on the mineral phase.

4.4 Feature Mapping

If Ir is hosted in micro-nugget alloys of the size range observed in other impact layers (Goderis et al., 2013a; Mohr-Westheide et al., 2015; Mohr-Westheide et al., 2016) they should be identifiable in our feature mapping which can identify features >100

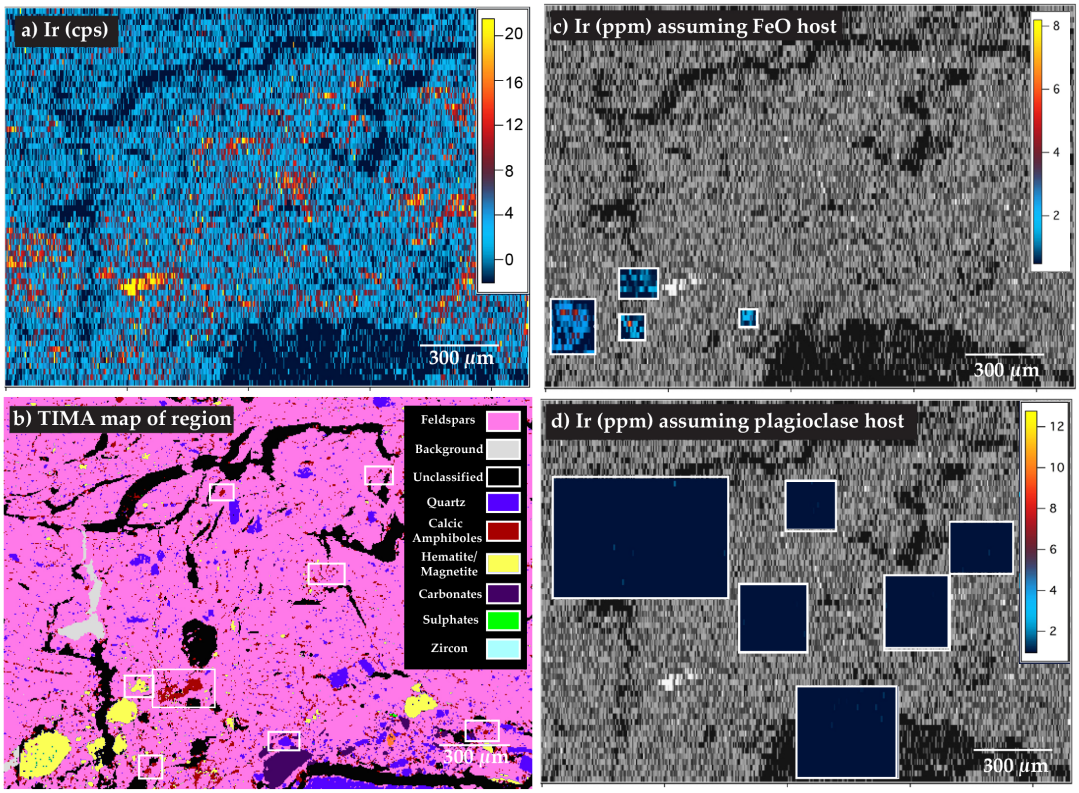

Figure 5.9*: LA-ICP-MS images of a section of the Woodside Creek boundary layer. Ir (cps) map highlights the location of the Ir, which was then correlated to a phase from the TIMA mineral identification maps. The LA-ICP-MS data was then reduced based upon the likely host mineral of the Ir; this was conducted for both the FeO spherules, and the assumed plagioclase-rich clays, but the respective maps are only accurate where those minerals are presetn (white boxes). Some FeO spherules contain 2-4 ppm Ir, however no Ir was observed within the matrix clays.*

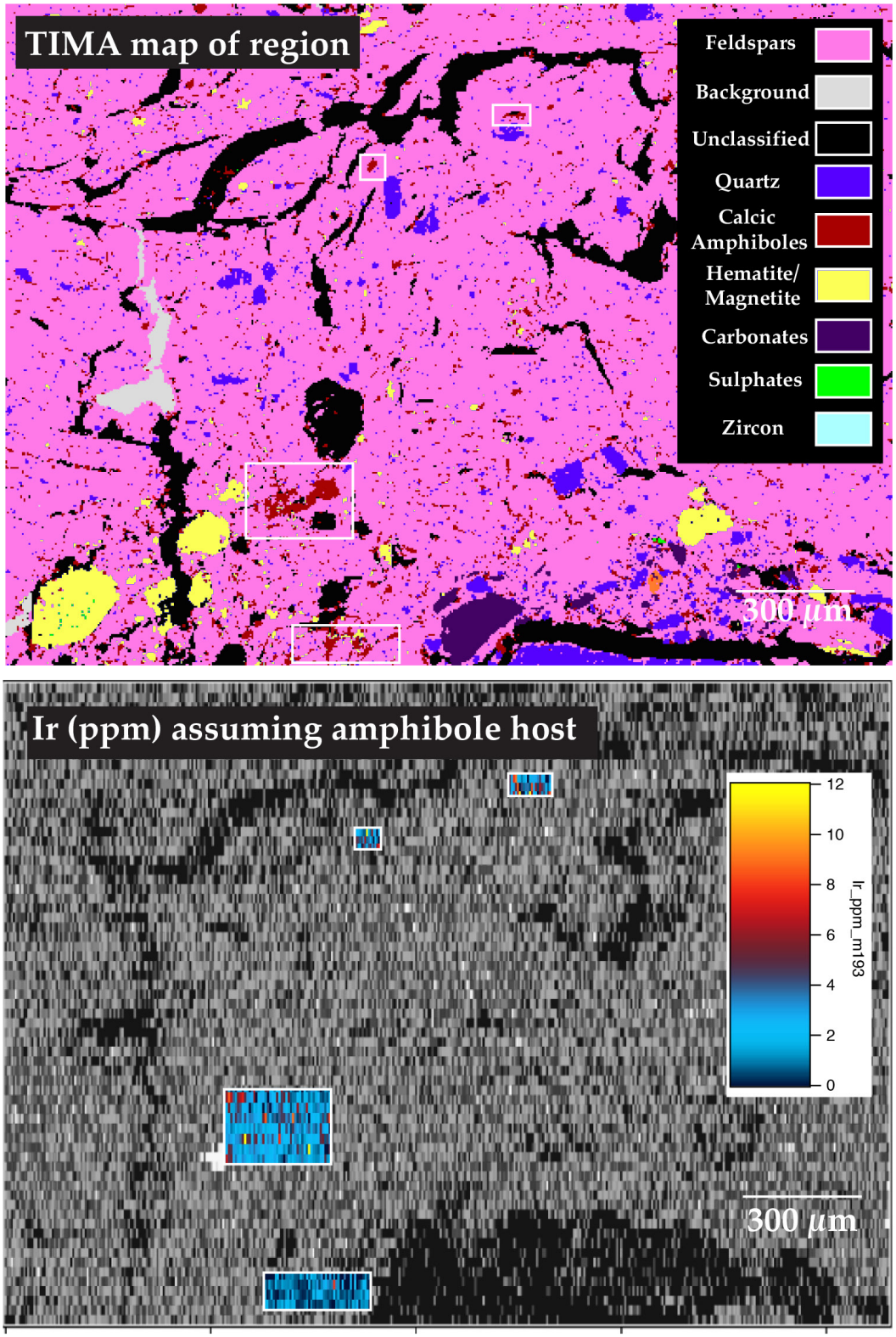

Figure 5.10: *TIMA map of a small section of Woodside Creek, and LA-ICP-MS data processed for an assumed amphibole host. Regions of high Ir counts were identified to be amphiboles from Fig. 5.9. The processed map is only accurate for the regions where amphibole is present, which are shown in colour and within white boxes.*

nm in size (e.g. Daly et al., 2016). Within the Woodside Creek sample for example, a bulk Ir concentration of 29.74 ppb (Goderis et al., 2013b) would require a single 1 micrometre particle of Ir to be present within a 16 x 16 mm region of host rock, assuming the layer is one particle thick. We would expect to locate 0.5-1 ~1 μm micro-nuggets, or >50 ~100 nm nuggets across the Woodside Creek sample based on this calculation (and assuming an Ir to rock density ratio of 7.5). However, no high-density hotspots containing Ir were identified using the INCA feature mapping software, in any of the analysed samples.

4.5 TEM Imaging

An Fe-rich nodule from the Woodside Creek sample was inspected using TEM (Fig. 5.13) because recent studies (e.g. Goderis et al., 2013b), and our LA-ICP-MS maps indicated Ir may be enriched within Fe-rich spherules. The original location of the region prepared for TEM is shown in Fig. 5.11a and b. No bright (e.g. high-density) spots were observed within the FeO spherule. TEM has the required resolution to detect nanometre sized high-density grains of Ir (e.g. Stroud et al., 2016) such as would be expected here. However, none were observed in this section, implying that the Ir enrichment does not present as nanometre sized alloys within the FeO spherule.

5. DISCUSSION

Based on LA-ICP-MS maps of the Woodside Creek sample, Ir enrichments were observed in very specific phases (i.e. FeO and amphibole). There are enrichments also found in some unclassified inclusions in the Woodside Creek sample. Reduction of the cps maps implied a bulk Ir concentration of ~4 ppm was present within the FeO inclusions, and up to ~6 ppm in the amphibole phases. When the LA-ICP-MS data were reduced to examine the clay matrix of the boundary samples, no Ir was identified, in contrast to the possible inference from the XRF analyses.

The association of the Ir with the FeO phase is as expected, given that Ir is a highly siderophile element it will readily partition into metal phases. However, the presence of Ir within the amphibole phase, and at a comparable concentration to the FeO, is somewhat perplexing. This identification is based on LA-ICP-MS maps of ^{193}Ir, an isotope of Ir which is not affected by interferences from other isotopes expected to be present in this sample. Therefore, these data are reliable and Ir is a real component of the amphibole. Ir is more likely to be present in the FeO, therefore we focussed on this phase in further analyses.

We can then consider the form of the Ir within the FeO phase, based upon the data presented here and constraints from the impact event. Iridium is highly siderophile and so

► ***Figure 5.11:*** *TIMA map of Woodside Creek, BSE locality maps of the imaged spherule, and TEM image of a lamella taken from an Fe-rich spherule. No nuggets >1 nm were observed within this phase, and therefore if Ir is present it is possibly dissmeinated throughout the phase.*

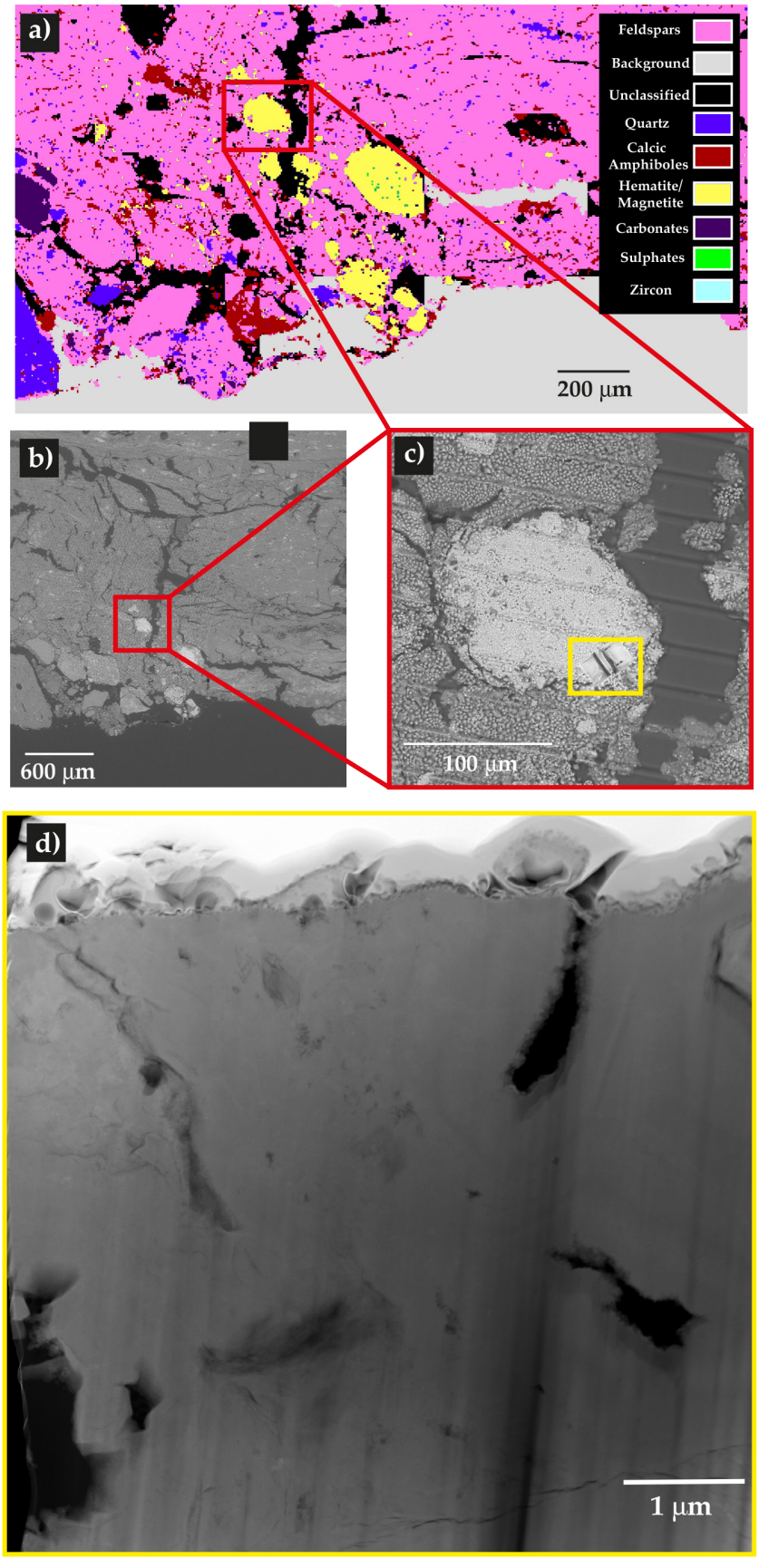
a)
Feldspars
Background
Unclassified
Quartz
Calcic Amphiboles
Hematite/ Magnetite
Carbonates
Sulphates
Zircon
200 µm
b)
600 µm
c)
100 µm
d)
1 µm

partitions strongly into metallic phases, and is observed as sub-micrometre HSE-alloys in meteorites (Palme and Wlotzka, 1976) and, interestingly, also in Archean impact layers (Goderis et al., 2013a; Mohr-Westheide et al., 2015; Mohr-Westheide et al., 2016). Feature mapping can identify high-density phases, such as Ir-alloys, that are > 100 nm, however, no high-density features were detected with this approach in any phase of all samples analysed. Therefore, if present as a metallic alloy in nugget form, similar to the Archaean impact spherule layer, then the Ir-hosting metallic nuggets must be <100 nm in size. Subsequent TEM, with a resolution of ~1 nm, of the FeO phase also did not identify any high-density hotspots. If in nugget form, at a concentration of 4 ppm within the FeO phase in Woodside Creek, we might have expected to identify 2000 ~1 nm metallic nuggets, or 20 ~10 nm metallic nuggets. As neither were observed, it is unlikely that the Ir is in metallic nugget form in this sample. TEM analyses of the amphibole phase would constrain if this is an isolated situation, however this is beyond the scope of this study.

There are consequently two possibilities to consider based on this finding: (1) Ir-rich metallic nuggets are present but not homogeneously distributed throughout the inclusion, and our TEM lamella sampled a region devoid of these nuggets; or (2) the Ir within the FeO inclusion has not hosted a metallic alloy and is disseminated throughout the oxide phase as part of the crystal lattice.

5.1 Inhomogeneously distributed nuggets in FeO spherules

Within the FeO phase, based on the bulk Ir composition and the lack of nuggets >100nm in diameter, we predict that over 2000 ~1 nm nuggets should have been observed, and if the nuggets were larger than ~10 nm, fewer than 20 would be observed. However, once the predicted nugget size exceeds ~45 nm in diameter, the likelihood of encountering an Ir-rich nugget in a single TEM lamella is sufficiently low that no nuggets may have been sampled in this case. As a nugget of this size is still below the detection limit of feature mapping, we can't completely rule out the presence of Ir-bearing nano-nuggets between 45 nm- 99 nm in size.

The Archaean impact spherule layer, in which the Ir is hosted in PGE nugget form within Ni-Cr spinels (Goderis et al., 2013a; Mohr-Westheide et al., 2015; Mohr-Westheide et al., 2016), has a strikingly higher concentration of Ir when compared to the K-Pg boundary. The Barberton Greenstone Belt in South Africa has a bulk Ir concentration of 357 ppb (Goderis et al., 2013a), in contrast to the much lower bulk Ir concentration of ~30 ppb for the K-Pg boundary at Woodside Creek (Goderis et al., 2013a; Goderis et al., 2013b; Mohr-Westheide et al., 2015). Both are attributed to a carbonaceous chondrite projectile based upon geochemical fingerprints of the ejecta material and rare earth element abundances relative to terrestrial values (Glikson and Allen, 2004; Glikson, 2011; Goderis et al., 2012; Goderis

et al., 2013b). The high concentration in these older impact layers is attributed to the 'micro-nugget effect' (Mohr-Westheide et al., 2015; Mohr-Westheide et al., 2016), however this higher concentration means PGEs are more likely to form nuggets during condensation due to the higher density of Ir atoms in the ejecta cloud (e.g. Berg et al., 2009), whilst the bulk concentration within the K-Pg boundary indicate the formation of nuggets may not have been possible here.

5.2 Ir disseminated throughout the FeO as part of the crystal lattice

Ir originating from the projectile would have travelled from the impact site via the ejecta cloud to locations worldwide (Artemieva and Morgan, 2007; Artemieva and Morgan, 2009; Artemieva and Morgan, 2011). The FeO inclusions are largely spherical (Figs. 5.9-5.11), suggesting that this phase melted during atmospheric re-entry forming melt droplets. In this case, melting of the FeO may have been sufficient to disseminate the Ir into the crystal lattice; the high partition coefficient of the Ir (Harvey and Day, 2016) but low concentration implies the size of the FeO inclusion would have been more than sufficient to incorporate the Ir into the crystal lattice. Ir is highly siderophile (Lodders, 2003; Harvey and Day, 2016) and therefore partitions strongly towards metal (Brenan et al., 2005; Brenan et al., 2016). However, the fact that it was not observed as an alloy in the FeO implies that the oxygen fugacity (Hüppauff and Lengeler, 1993; Kim et al., 2008; Palme, 2008) and the redistribution of Ir during melting may have been sufficient to retain the Ir within the oxide so that it was not exsolved in nugget form during melting (Harvey and Day, 2016). Furthermore, the oxidised 3+ valence state of Ir would be moderately compatible in the FeO crystal structure, as the ionic radii of Fe^{2+} and Ir^{3+} are comparable (Shannon, 1976; Hüppauff and Lengeler, 1993), therefore it is possible that Ir is disseminated throughout the FeO phase.

5.3 Transportation within the ejecta plume

Regardless of the which phase hosts the Ir, we can infer Ir was not transported ballistically in native form from the impact site. This is because Ir resides in PGE nuggets within meteorites (Palme and Wlotzka, 1976; Wark and Lovering, 1976; Berg et al., 2009; Daly et al., 2016), and these have not been observed in the K-Pg boundary thus far. The distance of the samples from the impact also imply this is an unlikely scenario. Predictions from numerical modelling simulations suggest material located at distal sites was transported via atmospheric dispersion following ejecta re-entry (e.g. Artemieva and Morgan, 2009). Future TEM analyses of all phases should therefore aim to constrain the form of Ir present, to gain a clearer understanding of the processes that have occurred during ejecta transportation.

6. CONCLUSIONS

This study examined five different K-Pg Boundary samples to identify the host phase of the Ir, which originated from the projectile and was subsequently dispersed around

the world. We used a variety of different techniques, which utilised a range of magnification from micrometre to nanometre, and mapped or detected elements and phases using both photon energies and particle masses. Ir was primarily identified within FeO and amphibole phases, at bulk concentrations of 4 ppm and 6 ppm, respectively.

The relationship of Ir with FeO and amphibole imply that the Ir associated with components of the target rocks that were vapourised upon impact, and subsequently condensed from the vapour cloud. The presence of Ir within the FeO and amphibole phases also suggests the vapour cloud was of intermediate bulk composition, so that Fe-metal and amphibole were the first phases to condense and thus were enriched in Ir. These inferences are in agreement with numerical modelling predictions based on the composition of the target ejecta.

Feature mapping and TEM analysis of the FeO phase revealed Ir is likely not present as metallic nuggets >100nm or <45 nm, however there is a small chance that sampling effects resulted in examination of a TEM lamella devoid of nano-nuggets, and that they are present elsewhere in the inclusion or that the nugget sizes may fall between 45 and 100nm. Furthermore, the relatively low concentration of Ir at the K-Pg sites implies the density of Ir atoms in the vapour cloud may not have been sufficient to allow nuggets to form. Conversely, Ir may be disseminated within the FeO phase as part of the crystal lattice; the high oxygen fugacity of the vapour plume and the Earth's atmosphere may have been sufficient to oxidise Ir evenly, distributing it within the FeO spherule upon melting, and hence the Ir may not exsolve into nugget form. Further TEM analyses of all phases associated with Ir are recommended for future research to definitively constrain the host phase of the PGE.

7. ACKNOWLEDGEMENTS

The Tescan Integrated Mineral Analysis (TIMA) instrument was funded by a grant from the Australian Research Council (LE140100150) and is operated by the John de Laeter Centre at Curtin University with the support of the Geological Survey of Western Australia, University of Western Australia and Murdoch University.

8. REFERENCES

Alvarez, F., Alvarez, W., Asaro, H.V., and Michel, L.W., 1980, Extraterrestrial cause for the Cretaceous-Tertiary extinction: Science, v. 208, no. 4448, p. 1095–1108.

Alvarez, W., Alvarez, F., Asaro, H.V., and Michel, L.W., 1982, Iridium Anomaly Approximately Synchronous with Terminal Eocene Extinctions: Science, v. 216, no. 4548, p. 886–888.

Alvarez, W., Asaro, H.V., and Montanari, A., 1990, Iridium profile for 10 million years across the Cretaceous-Tertiary boundary at Gubbio (Italy): Science, v. 250, no. 4988, p. 1700–1702.

Alvarez, W., Claeys, P., and Kieffer, S.W., 1995, Emplacement of Cretaceous-Tertiary Boundary Shocked Quartz from Chicxulub Crater: Science, v. 269, no. 5226, p. 930–935.

Artemieva, N., and Morgan, J., 2007, Distal Ejecta from the Chicxulub-Numerical Model: Lunar

and Planetary Science Conference, v. 38, no. 1338, p. 1543.

Artemieva, N., and Morgan, J., 2011, Global Ejecta from Chicxulub: Spherules, Shocked Quartz and More: Lunar and Planetary Science Conference, v. 42, p. 1180–1181.

Artemieva, N., and Morgan, J., 2009, Modeling the formation of the K--Pg boundary layer: Icarus, v. 201, no. 2, p. 768–780.

Berg, T., Maul, J., Schönhense, G., Marosits, E., Hoppe, P., Ott, U., and Palme, H., 2009, Direct evidence for condensation in the early solar system and implications for nebular cooling rates: The Astrophysical Journal Letters, v. 702, no. 2, p. L172–L176.

Brenan, J.M., Bennett, N.R., and Zajacz, Z., 2016, Experimental Results on Fractionation of the Highly Siderophile Elements (HSE) at Variable Pressures and Temperatures during Planetary and Magmatic Differentiation: Reviews in Mineralogy and Geochemistry, v. 81, no. 1, p. 1–87.

Brenan, J.M., McDonough, W.F., and Ash, R., 2005, An experimental study of the solubility and partitioning of iridium, osmium and gold between olivine and silicate melt: Earth and Planetary Science Letters, v. 237, no. 3-4, p. 855–872.

Brooks, R.R., Hoek, P.L., Reeves, R.D., Wallace, R.C., Johnston, J.H., Ryan, D.E., Holzbecher, J., and Collen, J.D., 1985, Weathered spheroids in a Cretaceous/Tertiary boundary shale at Woodside Creek, New Zealand: Geology, v. 13, no. 10, p. 738–740.

Claeys, P., Kiessling, W., and Alvarez, W., 2002, Distribution of Chicxulub ejecta at the Cretaceous-Tertiary boundary, in Koeberl, C. and MacLeod, K.G. eds., Catastrophic Events and Mass Extinctions: Impacts and Beyond, Geological Society of America, Boulder, Colorado, p. 55–68.

Cleverley, J.S., Ryan, C.G., Hough, R.M., Bland, P.A., Fisher, L.A., and Dyl, K.A., 2012, Quantified, Whole Section, Maia XRF Mapping of Trace Elements in Allende: Meteoritics and Planetary Science Supplement, v. 75, p. 5175.

Daly, L., Bland, P.A., Dyl, K.A., Forman, L.V., Evans, K.A., Trimby, P.W., Moody, S., Yang, L., Liu, H., Ringer, S.P., Ryan, C.G., and Saunders, M., 2016, In situ analysis of Refractory Metal Nuggets in carbonaceous chondrites: Geochimica et Cosmochimica Acta.

Doehne, E., and Margolis, S.V., 1990, Trace-element geochemistry and mineralogy of the Cretaceous/Tertiary boundary; Identification of extraterrestrial components: Geological Society of America Special Papers, v. 247, p. 367–382.

Drits, V.A., Lindgreen, H., Sakharov, B.A., Jakobsen, H.J., and Zviagina, B.B., 2004, The detailed structure and origin of clay minerals at the cretaceous/tertiary boundary, Stevns Klint (Denmark): Clay Minerals, v. 39, no. 4, p. 367–390.

Dyl, K.A., Cleverley, J.S., Bland, P.A., Ryan, C.G., Fisher, L.A., and Hough, R.M., 2014, Quantified, whole section trace element mapping of carbonaceous chondrites by Synchrotron X-ray Fluorescence Microscopy: 1. CV meteorites: Geochimica et Cosmochimica Acta, v. 134, p. 100–119.

Elliot, D.H., Askin, R.A., Kyte, F.T., and Zinsmeister, W.J., 1994, Iridium and dinocysts at the Cretaceous-Tertiary boundary on Seymour Island, Antarctica: Implications for the K-T event: Geology, v. 22, no. 8, p. 675–678.

Evans, N.J., Ahrens, T.J., McInnes, B., and Gregoire, D.C., 1994, New evidence for primary fractionation of ruthenium and iridium in the Chicxulub ejecta cloud: New Developments Regarding the KT Event and Other Catastrophes in Earth History, v. 825, p. 34–36.

Fisher, L.A., Fougerouse, D., Cleverley, J.S., Ryan, C.G., Micklethwaite, S., Halfpenny, A.,

Hough, R.M., Gee, M., Paterson, D., Howard, D.L., and Spiers, K., 2014, Quantified, multi-scale X-ray fluorescence element mapping using the Maia detector array: application to mineral deposit studies: Mineralium Deposita, v. 50, no. 6, p. 665–674.

Ganapathy, R., Gartner, S., and Jiang, M., 1981, Iridium anomaly at the Cretaceous-Tertiary boundary in Texas: Earth and Planetary Science Letters, v. 54, no. 3, p. 393–396.

Gartner, S., and McGuirk, J.P., 1979, Terminal Cretaceous extinction scenario for a catastrophe: Science, v. 206, p. 1272–1276.

Glikson, A., and Allen, C., 2004, Iridium anomalies and fractionated siderophile element patterns in impact ejecta, Brockman Iron Formation, Hamersley Basin, Western Australia: evidence for a major asteroid impact in simatic crustal regions of the early Proterozoic earth: Earth and Planetary Science Letters, v. 220, no. 3-4, p. 247–264.

Glikson, A.Y., 2011, Geochemical and isotopic signatures of Archaean to Palaeoproterozoic extraterrestrial impact ejecta/fallout units: Australian Journal of Earth Sciences, v. 52, no. 4-5, p. 785–798.

Goderis, S., Paquay, F., and Claeys, P., 2012, Projectile Identification in Terrestrial Impact Structures and Ejecta Material, in Osinski, G.R. and Pierazzo, E. eds., The Contact and Compression Stage of Impact Cratering, Processes and Products, Blackwell Publishing Ltd., Chichester, UK, p. 223–239.

Goderis, S., Simonson, B.M., McDonald, I., Hassler, S.W., Izmer, A., Belza, J., Terryn, H., Vanhaecke, F., and Claeys, P., 2013a, Ni-rich spinels and platinum group element nuggets condensed from a Late Archaean impact vapour cloud: Earth and Planetary Science Letters, v. 376, no. 1, p. 87–98.

Goderis, S., Tagle, R., Belza, J., Smit, J., Montanari, A., Vanhaecke, F., Erzinger, J., and Claeys, P., 2013b, Reevaluation of siderophile element abundances and ratios across the Cretaceous–Paleogene (K–Pg) boundary: Implications for the nature of the projectile: Geochimica et Cosmochimica Acta, v. 120, p. 417–446.

Harvey, J., and Day, J., 2016, Introduction to Highly Siderophile and Strongly Chalcophile Elements in High Temperature Geochemistry and Cosmochemistry, in Harvey, J., Day, J., and Swainson, I. eds., Highly Siderophile and Strongly Chalcophile Elements in High- Temperature Geochemistry and Cosmochemistry, Chantilly, Virginia, p. 1–12.

Heymann, D., Korochantsev, A., Nazarov, M.A., and Smit, J., 1996, Search for fullerenes C60and C70in Cretaceous–Tertiary boundary sediments from Turkmenistan, Kazakhstan, Georgia, Austria, and Denmark: Cretaceous Research, v. 17, no. 3, p. 367–380.

Hildebrand, A.R., Penfield, G.T., Kring, D.A., Pilkington, M., Camargo Z, A., Jacobsen, S.B., and Boynton, W.V., 1991, Chicxulub Crater: A possible Cretaceous/Tertiary boundary impact crater on the Yucatán Peninsula, Mexico: Geology, v. 19, no. 9, p. 867–871.

Hüppauff, M., and Lengeler, B., 1993, Valency and Structure of Iridium in Anodic Iridium Oxide Films: Journal of the Electrochemical Society, v. 140, no. 3, p. 598–602.

Kim, S.-W., Kwon, S.-H., Kwak, D.-K., and Kang, S.-W., 2008, Phase control of iridium and iridium oxide thin films in atomic layer deposition: Journal of Applied Physics, v. 103, no. 2, p. 23517.

Kyte, F.T., 1998, A meteorite from the Cretaceous/Tertiary boundary: Nature, v. 396, p. 237–239.

Kyte, F.T., Smit, J., and Wasson, J.T., 1985, Siderophile interelement variations in the Cretaceous-Tertiary boundary sediments from Caravaca, Spain: Earth and Planetary Science Letters, v. 73, no. 2-4, p. 183–195.

Li, J., Malis, T., and Dionne, S., 2006, Recent advances

in FIB–TEM specimen preparation techniques: Materials characterization, v. 57, no. 1, p. 64–70.

Lodders, K., 2003, Solar System Abundances and Condensation Temperatures of the Elements: The Astrophysical Journal, v. 591, no. 2, p. 1220–1247.

Mohr-Westheide, T., Greshake, A., Wirth, R., Reimold, W.U., and Fritz, J., 2016, Transmission Electron Microscope Study of Platinum Group Element-Rich Micronuggets from Two Spherule Layer Intersections, Barberton Greenstone Belt, South Africa: LPI Contributions, v. 1921.

Mohr-Westheide, T., Reimold, W.U., Fritz, J., Koeberl, C., Salge, T., Hofmann, A., and Schmitt, R.T., 2015, Discovery of extraterrestrial component carrier phases in Archean spherule layers: Implications for estimation of Archean bolide sizes: Geology, v. 43, no. 4, p. 299–302.

Molina, E., Alegret, L., and Arenillas, I., 2005, The Cretaceous/Paleogene boundary at the Agost section revisited: paleoenvironmental reconstruction and mass extinction pattern: Journal of Iberian Geology, v. 31, p. 137–150.

Morgan, J.V., 2008, Comment on "Determining Chondritic Impactor Size from the Marine Osmium Isotope Record": Science, v. 321, no. 5893, p. 1158a.

Osawa, T., Hatsukawa, Y., Keisuke, N., Koizumi, M., Oshima, M., Toh, Y., Kimura, A., and Furutaka, K., 2009, Iridium concentration and noble gas composition of Cretaceous-Tertiary boundary clay from Stevns Klint, Denmark: Geochemical Journal, v. 43, no. 6, p. 415–422.

Palme, H., 2008, Platinum-Group Elements in Cosmochemistry: Elements, v. 4, no. 4, p. 233–238.

Palme, H., and Wlotzka, F., 1976, A metal particle from a Ca,Al-rich inclusion from the meteorite Allende, and the condensation of refractory siderophile elements: Earth and Planetary Science Letters, v. 33, no. 1, p. 45–60.

Paton, C., Hellstrom, J., Paul, B., Woodhead, J., and Hergt, J., 2011, Iolite: Freeware for the visualisation and processing of mass spectrometric data: Journal of Analytical Atomic Spectrometry, v. 26, no. 12, p. 2508–2518.

Pierazzo, E., and Artemieva, N., 2012, Local and Global Environmental Effects of Impacts on Earth: Elements, v. 8, no. 1, p. 55–60.

Pope, K.O., Ocampo, A.C., and Duller, C.E., 1991, Mexican site for K/T impact crater?: Nature, v. 351, no. 6322, p. 105.

Quitte, G., Robin, E., Levasseur, S., Capmas, F., Rocchia, R., Birck, J.-L., and AlleGre, C.J., 2007, Osmium, tungsten, and chromium isotopes in sediments and in Ni-rich spinel at the K-T boundary: Signature of a chondritic impactor: Meteoritics & Planetary Science, v. 42, no. 9, p. 1567–1580.

Ryan, C.G., Cousens, D.R., Sie, S.H., Griffin, W.L., Suter, G.F., and Clayton, E., 1990, Quantitative pixe microanalysis of geological matemal using the CSIRO proton microprobe: Nuclear Instruments and Methods in Physics Research Section B: Beam Interactions with Materials and Atoms, v. 47, no. 1, p. 55–71.

Ryan, C.G., Etschmann, B.E., Vogt, S., Maser, J., Harland, C.L., van Achterbergh, E., and Legnini, D., 2005, Nuclear microprobe – synchrotron synergy: Towards integrated quantitative real-time elemental imaging using PIXE and SXRF: Nuclear Instruments and Methods in Physics Research Section B: Beam Interactions with Materials and Atoms, v. 231, no. 1-4, p. 183–188.

Ryan, C.G., Siddons, D.P., Kirkham, R., and Dunn, P.A., 2010, The new Maia detector system: methods for high definition trace element imaging of natural material: AIP Conference Proceedings, v. 1221, no. 9, p. 10–17.

Schulte P., Alegret L., Arenillas I., Arz J. A., Barton P. J., Bown P. R., Bralower T. J., Christeson

G. L., Claeys P., Cockell C. S., Collins G. S., Deutsch A., Goldin T. J., Goto K., Grajales-Nishimura J. M., Grieve R. A. F., Gulick S. P. S., Johnson K. R., Kiessling W., Koeberl C., Kring D. A., MacLeod K. G., Matsui T., Melosh J., Montanari A., Morgan J. V., Neal C. R., Nichols D. J., Norris R. D., Pierazzo E., Ravizza G., Rebolledo Vieyra M., Reimold W. U., Robin E., Salge T., Speijer R. P., Sweet A. R., Urrutia-Fucugauchi J., Vajda V., Whalen M. T. and Willumsen P. S., 2010, The Chicxulub Asteroid Impact and Mass Extinction at the Cretaceous-Paleogene Boundary: Science, v. 327, no. 5970, p. 1214–1218.

Shannon, R.D., 1976, Revised Effective Ionic-Radii and Systematic Studies of Interatomic Distances in Halides and Chalcogenides: Acta Crystallographica, v. 32, p. 751–767.

Shukolyukov, A., and Lugmair, G.W., 1998a, Chromium in the Cretaceous-Tertiary boundary layer: first isotopic evidence for an impactor and its type: Meteoritics and Planetary Science, v. 33, no. 4, p. A144.

Shukolyukov, A., and Lugmair, G.W., 1998b, Isotopic Evidence for the Cretaceous-Tertiary Impactor and Its Type: Science, v. 282, no. 5390, p. 927–930.

Smit, J., 1999, The global stratigraphy of the Cretaceous-Tertiary boundary impact ejecta: Annual Review of Earth and Planetary Sciences, v. 27, no. 1, p. 75–113.

Smit, J., and Hertogen, J., 1980, An extraterrestrial event at the Cretaceous-Tertiary boundary: Nature, v. 285, no. 5762, p. 198–200.

Smit, J., and Kyte, F.T., 1984, Siderophile-rich magnetic spheroids from the Cretaceous|[ndash]|Tertiary Boundary in Umbria, Italy: Nature, v. 310, no. 5976, p. 403–405.

Stroud, R.M., Pravdivtseva, O.V., Meshik, A.P., and Shatoff, E.A., 2016, Aberration-Corrected STEM Analysis of Electrophoresis Separates of Allende Nanodiamond: Lunar and Planetary Science Conference, v. 47, p. 2311.

Trinquier, A., Birck, J.-L., and Jean Allègre, C., 2006, The nature of the KT impactor. A 54Cr reappraisal: Earth and Planetary Science Letters, v. 241, no. 3-4, p. 780–788.

Wark, D.A., and Lovering, J.F., 1976, Refractory/platinum metal grains in Allende calcium-aluminium-rich clasts (CARC's): Possible exotic presolar material?: Lunar and Planetary Science Conference, v. 7, p. 912.

Chapter 6

Thesis Conclusions

L.V. Forman

Department of Applied Geology, Curtin University, GPO Box U1987, Perth, WA 6845, Australia

The work contained within this thesis has expanded our knowledge of how impact processes have led to the evolution of our Solar System over time through the examination of primitive meteorites and impact relicts.

1. EARLY COMPACTION OF THE CV PARENT BODY

This work observed textural and morphological characteristics of CV3 chondrites which provided some of the most substantial evidence for impact-induced asteroidal compaction. Broad-scale microstructural investigations (Chapters 2 & 3), and comparative matrix grain morphological analyses (Chapter 4), indicate that impact-induced compaction remains the most plausible theory for the compaction of early planetary bodies.

Chondrules and matrix grains experience impacts differently as predicted by impact-induced compaction numerical modelling simulations; pore collapse is the dominant heat generation mechanism in an impact scenario, which creates heterogeneous heating according to the distribution of pores within the sample (Davison et al., 2010; Bland et al., 2014; Davison et al., 2016). Consequently, chondrules are predicted to experience lower temperature excursions as they are non-porous, whereas matrix grains are much smaller and in regions with initially plentiful pore space. The investigation in Chapter 2 demonstrates abundant crystal-plastic deformation textures are observed within mechanically weak matrix grains, whereas deformation of the large and mechanically strong chondrules is limited to the outer margins of the grains, and is typically much less pronounced. This is inferred to be a direct result of the heating discrepancies between the different meteoritic components, which is a function of the amount of pore space that has collapsed upon impact. These deformational textures imply impact-induced compaction is the likely driver for asteroid compaction, as other models of porosity reduction of the parent body do not have the strength to overcome the internal pressure of the asteroid, or could not produce the deformation textures observed in Allende.

Examination of textural features within the matrix of the Allende CV meteorite revealed heterogeneous crystallographic preferred orientations (CPOs) throughout, with high intensity CPOs next to chondrule margins, and low to absent CPOs away from the chondrule margins. This was interpreted as the result of high compressive forces adjacent to the chondrules, resulting in the flattening of matrix olivines against the margins. In regions furthest from the solid chondrules, much of the force would likely have been absorbed by abundant pore space reduction and therefore less reorientation would have occurred. This correlates well to the heat

distribution of the mesoscale numerical simulations of Davison et al. (2016) and Bland et al. (2014), where the largest increase in heat was predicted in matrix regions at chondrule margins perpendicular to the direction of the propagating shockwave. Furthermore, chondrules in the mapped region also show limited deformation, which is concentrated at the edges. When considered collectively, the directionality of the impact shockwave can be inferred in the context of this thin section, the first study to show this (Chapter 3).

2. GRAIN GROWTH AND MODIFICATION, AND CPO GENERATION AS A FUNCTION OF DEPTH ON THE CV PARENT BODY

Through a comparison of three CV meteorites (Allende, Kaba and Vigarano) this work inferred that more intense CPOs are observed in CVs originating from greater depths on the parent body. This implies impact processing may be more effective at generating CPOs at greater depths, or in samples with more elongate grains (Chapter 4). The CV meteorites examined in this work have different average matrix grain sizes and morphologies. Allende contains larger and more elongate matrix olivine grains, and impact-induced compaction on the parent body would have resulted in such elongate grains preserving a better CPO. These grains would readily re-orient to reduce the space occupied by the grains in the plane of the compression shockwave. More equant grains may not re-orient to the same degree, as we observe in Kaba and Vigarano.

We conclude average grain size and how euhedral the matrix grains are, relates to the degree of aqueous alteration the sample has experienced, therefore pre-compaction grain growth was primarily controlled by aqueous alteration. Additionally, the aspect ratio of the matrix grains correlates well to the temperatures the samples have experienced, indicating thermal metamorphism may be a control for grain growth in terms of elongation.

Allende is surmised to originate from deepest within the parent body based on the conclusions of previous studies (e.g. Weiss et al., 2010; Elkins-Tanton et al., 2011; Macke et al., 2011; Weiss and Elkins-Tanton, 2013), which is also in agreement with our observations here. Vigarano and Kaba experienced lower temperatures of ~370-415 ℃, and have comparably low porosities, however Kaba contains abundant hydrosillicates, indicative of aqueous alteration, whereas Vigarano does not (Krot et al., 2004; Huss et al., 2006). These two samples likely originated from a similar shallow depth on the parent body, but at different lateral locations to account for the variance in aqueous alteration.

There is still much to learn from crystallographic and grain morphology comparisons between meteorites from the same parent asteroid. Chapters 2 and 3 demonstrate that the primary driver for asteroidal compaction was likely impacts, but the findings of Chapter 4 also suggest there was an interplay between compacting forces and the products of aqueous and thermal

alteration, which should be explored further.

3. IMPACT CLOUD PROCESSES

The ejecta layer from a large impact event ~65 Ma ago contains a large proportion of material from a carbonaceous chondrite projectile of CM composition (Smit, 1999; Goderis et al., 2013b). The work in Chapter 5 describes the techniques and methodology used to identify the host phase of the highly siderophile element, Ir, in situ. Ir is abundant at the K-Pg boundary relative to terrestrial values (Smit, 1999), and so we can assume all Ir originated from the projectile. Due to the large distance of the distal sites from the impact crater (>4000 km), we also infer the material was transported by, and recondensed from, the impact ejecta cloud prior to deposition.

The mineral host of the Ir was identified through LA-ICP-MS analyses of the Woodside Creek boundary sample. FeO and amphibole phases both contained ~4 ppm and ~6 ppm Ir respectively. Further analyses of the FeO phase using TEM revealed Ir is not present in nano-nugget or micro-nugget form below 10 nm or above 100 nm in size, in contrast to the Ir-rich PGE alloy nuggets identified at Archaean impact layers (Goderis et al., 2013a; Mohr-Westheide et al., 2015; Mohr-Westheide et al., 2016). There is a small chance that Ir nano-nuggets are present but were not sampled in this lamella; the low Ir concentration relative to the Archaean impact layers may indicate that insufficient Ir particles were present upon condensation within the ejecta vapour cloud to form nuggets. Iridium may also be disseminated throughout the phase, which would imply the oxygen fugacity of the vapour plume and atmosphere were substantially high for Ir to remain in oxide form (Palme, 2008). This implication is in agreement with numerical simulation results regarding the surmised composition of the vapour plume (e.g. Ebel and Grossman, 2005).

4. IMPACTS THROUGHOUT THE HISTORY OF THE SOLAR SYSTEM

Over course of the history of our Solar System, projectiles and target bodies have experienced increased cumulative processing with time; at the beginning of planetary accretion, highly porous bodies grew through dust assimilation and impacts between such bodies. Impacts were frequent and acted to compact, lithify and to some extent, heat the small planetary bodies, creating the low porosity asteroids that are interpreted through analogous meteorites today. Where evolved planetary bodies with active plate tectonics are considered, such as the Earth, the evidence for collisional events are slowly removed with time, as impact craters are subducted into the Earth's mantle or eroded away. In this case, we must look to projectile relicts, such as impact spherule layers, to identify past impact events and the effects these may have had on a planetary scale.

Projectile relicts have changed over time; there are likely remnants on the Earth's surface that originate from planetary bodies that are no longer present in our solar system. Most target bodies are also typically of

low-porosity, so this alters the compaction, shock and ejecta distribution we are likely to observe following the impact event. Impacts on Earth generate breccias and regolith, but projectiles are not generally incorporated into the planetary body as may have occurred in earlier collisional events between highly porous bodies. Instead, projectile relicts are dispersed globally. Examination of such relicts, as in Chapter 5, enables interpretation of projectile types over time when dating techniques are employed in tandem. We can also interpret atmospheric conditions on target bodies with an atmosphere, such as the Earth (Chapter 5). In context, the Earth is one of the most evolved impacted bodies in our Solar System, as it has an atmosphere, gravity, and is of low-porosity, and impacts are very different to those which occurred on early, porous planetesimals. Each of the studies in this work therefore examines planetary bodies in different states to further the understanding of impact evolution in our Solar System.

5. RECOMMENDATIONS FOR FUTURE WORK

As Chapters 2 and 3 of this work present seldom-before observed impact-induced compaction textures and microstructures, more primitive meteorites should be examined in search of similar features. Expanding the analyses to less primitive meteorites may help to discern between compaction-related textures and structures, and other secondary processing that occurred on the parent body, or weathering that has occurred on Earth.

Building upon the study in Chapter 4, other CV chondrites should be examined in context to ascertain the likely depth of origin on the parent body based upon grain size, shape and alteration. This will identify any trends within the meteorite class, and highlight any anomalous samples which do not correlate well to the depth of origin, grain size, or grain shape predictions made in Chapter 4.

Finally, additional TEM analyses of multiple phases within the Woodside Creek sample will help constrain the form of the Ir, and may result in further evidence for the mode of dispersion and transportation of the Ir within the ejecta cloud following impact. Further comparisons of Ir distributions between distal, intermediate and proximal ejecta may hold the key to identifying the form of Ir as a function of distance from the impact site at Chicxulub.

6. REFERENCES

Berg, T., Maul, J., Schönhense, G., Marosits, E., Hoppe, P., Ott, U., and Palme, H., 2009, Direct evidence for condensation in the early solar system and implications for nebular cooling rates: The Astrophysical Journal Letters, v. 702, no. 2, p. L172–L176.

Bland, P.A., Collins, G.S., Davison, T.M., Abreu, N.M., Ciesla, F.J., Muxworthy, A.R., and Moore, J., 2014, Pressure–temperature evolution of primordial solar system solids during impact-induced compaction: Nature

Communications, v. 5, p. 5451.

Campbell, A.J., Humayun, M., Meibom, A., Krot, A.N., and Keil, K., 2001, Origin of zoned metal grains in the QUE94411 chondrite: Geochimica et Cosmochimica Acta, v. 65, no. 1, p. 163–180.

Davison, T.M., Collins, G.S., and Bland, P.A., 2016, Mesoscale modeling of impact compaction of primitive solar system solids: The Astrophysical Journal, v. 821, no. 1, p. 68.

Davison, T.M., Collins, G.S., and Ciesla, F.J., 2010, Numerical modelling of heating in porous planetesimal collisions: Icarus, v. 208, no. 1, p. 468–481.

Ebel, D.S., and Grossman, L., 2005, Spinel-bearing spherules condensed from the Chicxulub impact-vapor plume: Geology, v. 33, no. 4, p. 293–296.

Elkins-Tanton, L.T., Weiss, B.P., and Zuber, M.T., 2011, Chondrites as samples of differentiated planetesimals: Earth and Planetary Science Letters, v. 305, no. 1-2, p. 1–10.

Goderis, S., Simonson, B.M., McDonald, I., Hassler, S.W., Izmer, A., Belza, J., Terryn, H., Vanhaecke, F., and Claeys, P., 2013a, Ni-rich spinels and platinum group element nuggets condensed from a Late Archaean impact vapour cloud: Earth and Planetary Science Letters, v. 376, no. 1, p. 87–98.

Goderis, S., Tagle, R., Belza, J., Smit, J., Montanari, A., Vanhaecke, F., Erzinger, J., and Claeys, P., 2013b, Reevaluation of siderophile element abundances and ratios across the Cretaceous–Paleogene (K–Pg) boundary: Implications for the nature of the projectile: Geochimica et Cosmochimica Acta, v. 120, p. 417–446.

Harvey, J., and Day, J., 2016, Introduction to Highly Siderophile and Strongly Chalcophile Elements in High Temperature Geochemistry and Cosmochemistry, in Harvey, J., Day, J., and Swainson, I. eds., Highly Siderophile and Strongly Chalcophile Elements in High Temperature Geochemistry and Cosmochemistry, Chantilly, Virginia, p. 1–12.

Huss, G.R., Rubin, A.E., and Grossman, J.N., 2006, Thermal metamorphism in chondrites, in McSween, H.Y. and Lauretta, D.S. eds., Meteorites and the Early Solar System II, University of Arizona, Tuscon, Arizona, p. 567–586.

Krot, A.N., Petaev, M.I., and Bland, P.A., 2004, Multiple formation mechanisms of ferrous olivine in CV carbonaceous chondrites during fluid-assisted metamorphism: Antarctic Meteorite Research, v. 17, p. 153–171.

Lyons, T.W., Reinhard, C.T., and Planavsky, N.J., 2014, The rise of oxygen in Earth/'s early ocean and atmosphere: Nature, v. 506, no. 7488, p. 307–315.

Macke, R.J., Britt, D.T., and Consolmagno, G.J., 2011, Density, porosity, and magnetic susceptibility of achondritic meteorites: Meteoritics & Planetary Science, v. 46, no. 2, p. 311–326.

Mohr-Westheide, T., Greshake, A., Wirth, R., Reimold, W.U., and Fritz, J., 2016, Transmission Electron Microscope Study of Platinum Group Element-Rich Micronuggets from Two Spherule Layer Intersections, Barberton Greenstone Belt, South Africa: LPI Contributions, v. 1921.

Mohr-Westheide, T., Reimold, W.U., Fritz, J., Koeberl, C., Salge, T., Hofmann, A., and Schmitt, R.T., 2015, Discovery of extraterrestrial component carrier phases in Archean spherule layers: Implications for estimation of Archean bolide sizes: Geology, v. 43, no. 4, p. 299–302.

Palme, H., 2008, Platinum-Group Elements in Cosmochemistry: Elements, v. 4, no. 4, p. 233–238.

Smit, J., 1999, The global stratigraphy of the Cretaceous-Tertiary boundary impact ejecta: Annual Review of Earth and Planetary Sciences, v. 27, no. 1, p. 75–113.

Weiss, B.P., and Elkins-Tanton, L.T., 2013, Differentiated Planetesimals and the Parent Bodies of Chondrites: Annual Review of Earth and Planetary Sciences, v. 41, p. 529–560.

Weiss, B.P., Carporzen, L., Elkins-Tanton, L.T., Shuster, D.L., Ebel, D.S., Gattacceca, J., Zuber, M.T., Chen, J.H., Papanastassiou, D.A., Binzel, R.P., Rumble, D., and Irving, A.J., 2010, A Partially Differentiated Body for CV Chondrites?: Lunar and Planetary Science Conference, v. 41, p. 1688.

Chapter 6

Bibliography

Abramov, O., and Kring, D.A., 2007, Numerical modeling of impact-induced hydrothermal activity at the Chicxulub crater: Meteoritics & Planetary Science, v. 42, no. 1, p. 93–112.

Agee, C.B., Li, J., Shannon, M.C., and Circone, S., 1995, Pressure-temperature phase diagram for the Allende meteorite: Journal of Geophysical Research: Solid Earth, v. 100, no. B9, p. 17725–17740.

Alvarez, F., Alvarez, W., Asaro, H.V., and Michel, L.W., 1980, Extraterrestrial cause for the Cretaceous-Tertiary extinction: Science, v. 208, no. 4448, p. 1095–1108.

Alvarez, W., Alvarez, F., Asaro, H.V., and Michel, L.W., 1982, Iridium Anomaly Approximately Synchronous with Terminal Eocene Extinctions: Science, v. 216, no. 4548, p. 886–888.

Alvarez, W., Asaro, H.V., and Montanari, A., 1990, Iridium profile for 10 million years across the Cretaceous-Tertiary boundary at Gubbio (Italy): Science, v. 250, no. 4988, p. 1700–1702.

Alvarez, W., Claeys, P., and Kieffer, S.W., 1995, Emplacement of Cretaceous-Tertiary Boundary Shocked Quartz from Chicxulub Crater: Science, v. 269, no. 5226, p. 930–935.

Amelin, Y., Krot, A.N., Hutcheon, I.D., and Ulyanov, A.A., 2002, Lead Isotopic Ages of Chondrules and Calcium-Aluminum-Rich Inclusions: Science, v. 297, no. 5587, p. 1678–1683.

Ames, D.E., Watkinson, D.H., and Parrish, R.R., 1998, Dating of a regional hydrothermal system induced by the 1850 Ma Sudbury impact event: Geology, v. 26, no. 5, p. 447–450.

Anders, E., and Grevesse, N., 1989, Abundances of the elements: Meteoritic and solar: Geochimica et Cosmochimica Acta, v. 53, p. 197–214.

Ando, J., Tomioka, N., Petaev, M.L., Kanagawa, K., Honda, K., Shibata, Y., and Yamanaka, S., 2003, Microstructures of Olivine in the Weakly Shocked Divnoe Meteorite: AGU Fall Meeting Abstracts.

Arenillas, I., Arz, J.A., Grajales-Nishimura, J.M., Murillo-Muñetón, G., Alvarez, W., Camargo-Zanoguera, A., Molina, E., and Rosales-Domínguez, C., 2006, Chicxulub impact event is Cretaceous/Paleogene boundary in age: New micropaleontological evidence: Earth and Planetary Science Letters, v. 249, no. 3-4, p. 241–257.

Arrowsmith, P., 1987, Laser ablation of solids for elemental analysis by inductively coupled plasma mass spectrometry: Analytical Chemistry, v. 59, p. 1437–1444.

Artemieva, N., and Morgan, J., 2007, Distal Ejecta from the Chicxulub-Numerical Model: Lunar and Planetary Science Conference, v. 38, no. 1338, p. 1543.

Artemieva, N., and Morgan, J., 2011, Global Ejecta from Chicxulub: Spherules, Shocked Quartz and More: Lunar and Planetary Science Conference, v. 42, p. 1180–1181.

Artemieva, N., and Morgan, J., 2009, Modeling the formation of the K--Pg boundary layer: Icarus, v. 201, no. 2, p. 768–780.

Artemieva, N.A., and Shuvalov, V.V., 2008, Numerical simulation of high-velocity impact ejecta

following falls of comets and asteroids onto the Moon: Solar System Research, v. 42, no. 4, p. 351–356.

Ashby, M.F., and Verrall, R.A., 1977, Deformation Maps for Olivine: American Geophysical Union, v. 58, no. 6, p. 512–512.

Ashworth, J.R., and Barber, D.J., 1975, Electron petrography of shock-deformed olivine in stony meteorites: Earth and Planetary Science Letters, v. 27, no. 1, p. 43–50.

Asphaug, E., Agnor, C.B., and Williams, Q., 2006, Hit-and-run planetary collisions: Nature, v. 439, no. 7073, p. 155–160.

Beitz, E., Güttler, C., Nakamura, A.M., Tsuchiyama, A., and Blum, J., 2013, Experiments on the consolidation of chondrites and the formation of dense rims around chondrules: Icarus, v. 225, no. 1, p. 558–569.

Bell, J.F., 1988, A probable asteroidal parent body for the CO or CV chondrites: Meteoritics, v. 23, p. 256–257.

Berg, T., Maul, J., Schönhense, G., Marosits, E., Hoppe, P., Ott, U., and Palme, H., 2009, Direct evidence for condensation in the early solar system and implications for nebular cooling rates: The Astrophysical Journal Letters, v. 702, no. 2, p. L172–L176.

Bischoff, A., and Stöffler, D., 1992, Shock metamorphism as a fundamental process in the evolution of planetary bodies: information from meteorites: European Journal of Mineralogy, v. 4, no. 4, p. 707–755.

Bland, P.A., Collins, G.S., Davison, T.M., Abreu, N.M., Ciesla, F.J., Muxworthy, A.R., and Moore, J., 2014, Pressure–temperature evolution of primordial solar system solids during impact-induced compaction: Nature Communications, v. 5, p. 5451.

Bland, P.A., Howard, L.E., Prior, D.J., Wheeler, J., Hough, R.M., and Dyl, K.A., 2011, Earliest rock fabric formed in the Solar System preserved in a chondrule rim: Nature Geoscience, v. 4, no. 4, p. 244–247.

Bleiner, D., Macrì, M., Gasser, P., Sautter, V., and Maras, A., 2006, FIB, TEM and LA–ICPMS investigations on melt inclusions in Martian meteorites—Analytical capabilities and geochemical insights: Talanta, v. 68, no. 5, p. 1623–1631.

Blum, J., 2004, Grain growth and coagulation: ASP Conference Series, v. 309, p. 369–391.

Blum, J., 2003, The Structure of Planetesimals in the Solar Nebula: Meteoritics and Planetary Science Supplement, v. 38, p. 5152.

Bonal, L., Quirico, E., Bourot-Denise, M., and Montagnac, G., 2006, Determination of the petrologic type of CV3 chondrites by Raman spectroscopy of included organic matter: Geochimica et Cosmochimica Acta, v. 70, no. 7, p. 1849–1863.

Brearley, A.J., and Jones, R.H., 1998, Chondritic meteorites: Reviews in Mineralogy and Geochemistry, v. 36, no. 1, p. 3.1–3.198.

Brenan, J.M., Bennett, N.R., and Zajacz, Z., 2016, Experimental Results on Fractionation of the Highly Siderophile Elements (HSE) at Variable Pressures and Temperatures during Planetary and Magmatic Differentiation: Reviews in Mineralogy and Geochemistry, v. 81, no. 1, p. 1–87.

Brenan, J.M., McDonough, W.F., and Ash, R., 2005, An experimental study of the solubility and partitioning of iridium, osmium and gold between olivine and silicate melt: Earth and Planetary Science Letters, v. 237, no. 3-4, p. 855–872.

Brenker, F.E., Palme, H., and Klerner, S., 2000, Evidence for solar nebula signatures in the matrix of the Allende meteorite: Earth and Planetary Science Letters, v. 178, no. 3-4, p. 185–194.

Britt, D.T., Yeomans, D., Housen, K., and Consolmagno, G., 2002, Asteroid density, porosity, and structure, in Bottke, W.F., Jr, Cellino, A., Paolicchi, P., and Binzel, R.P.B. eds., University of Arizona Press, p. 485–500.

Brooks, R.R., Hoek, P.L., Reeves, R.D., Wallace, R.C., Johnston, J.H., Ryan, D.E., Holzbecher, J., and Collen, J.D., 1985, Weathered spheroids in a Cretaceous/Tertiary boundary shale at Woodside Creek, New Zealand: Geology, v. 13, no. 10, p. 738–740.

Cain, P.M., McSween, H.Y., and Woodward, N.B., 1986, Structural deformation of the Leoville chondrite: Earth and Planetary Science Letters, v. 77, no. 2, p. 165–175.

Campbell, A.J., Humayun, M., Meibom, A., Krot, A.N., and Keil, K., 2001, Origin of zoned metal grains in the QUE94411 chondrite: Geochimica et Cosmochimica Acta, v. 65, no. 1, p. 163–180.

Carter, N.L., and Ave'Lallemant, H.G., 1970, High Temperature Flow of Dunite and Peridotite: Geological Society of America Bulletin, v. 81, no. 8, p. 2181–2202.

Chambers, J.E., 2013, Late-stage planetary accretion including hit-and-run collisions and fragmentation: Icarus, v. 224, no. 1, p. 43–56.

Chambers, J.E., 2004, Planetary accretion in the inner Solar System: Earth and Planetary Science Letters, v. 223, no. 3-4, p. 241–252.

Cheng, A.F., and Barnouin-Jha, O.S., 1999, Giant Craters on Mathilde: Icarus, v. 140, no. 1, p. 34–48.

Chyba, C.F., 1990, Impact Delivery and Erosion of Planetary Oceans in the Early Inner Solar-System: Nature, v. 343, no. 6254, p. 129–133.

Cintala, M.J., 1992, Impact-induced thermal effects in the lunar and Mercurian regoliths: Journal of Geophysical Research: Solid Earth, v. 97, no. E1, p. 947–973.

Claeys, P., Kiessling, W., and Alvarez, W., 2002, Distribution of Chicxulub ejecta at the Cretaceous-Tertiary boundary, in Koeberl, C. and MacLeod, K.G. eds., Catastrophic Events and Mass Extinctions: Impacts and Beyond, Geological Society of America, Boulder, Colorado, p. 55–68.

Clayton, R.N., and Mayeda, T.K., 1983, Oxygen isotopes in eucrites, shergottites, nakhlites, and chassignites: Earth and Planetary Science Letters, v. 62, no. 1, p. 1–6.

Cleverley, J.S., Ryan, C.G., Hough, R.M., Bland, P.A., Fisher, L.A., and Dyl, K.A., 2012, Quantified, Whole Section, Maia XRF Mapping of Trace Elements in Allende: Meteoritics and Planetary Science Supplement, v. 75, p. 5175.

Cody, G.D., Alexander, C.M.O., Yabuta, H., Kilcoyne, A.L.D., Araki, T., Ade, H., Dera, P., Fogel, M., Militzer, B., and Mysen, B.O., 2008, Organic thermometry for chondritic parent bodies: Earth and Planetary Science Letters, v. 272, no. 1-2, p. 446–455.

Collins, G.S., Melosh, H.J., and Osinski, G.R., 2012, The Impact-Cratering Process: v. 8, no. 1, p. 25–30.

Collins, G.S., Wünnemann, K., Artemieva, N., and Pierazzo, E., 2013, Numerical Modelling of Impact Processes, in Osinski, G.R. and Pierazzo, E. eds., The Contact and Compression Stage of Impact Cratering, Blackwell Publishing Ltd., Chichester, UK, p. 254–270.

Consolmagno, G.J., Britt, D.T., and Macke, R.J., 2008, The significance of meteorite density and porosity: Chemie der Erde-Geochemistry, v. 68, no. 1, p. 1–29.

Consolmagno, G.J., Britt, D.T., and Stoll, C.P., 1998, The porosities of ordinary chondrites: Models and interpretation: Meteoritics & Planetary Science, v. 33, no. 6, p. 1221–1229.

Cooper, R.F., and Kohlstedt, D.L., 1984, Sintering of olivine and olivine-basalt aggregates: Physics and Chemistry of Minerals, v. 11, no. 1, p. 5–16.

Corrigan, C.M., Zolensky, M.E., Dahl, J., Long, M., Weir, J., Sapp, C., and Burkett, P.J., 1997, The porosity and permeability of chondritic meteorites and interplanetary dust particles: Meteoritics & Planetary Science, v. 32, no. 4, p. 509–515.

Cuzzi, J.N., and Weidenschilling, S.J., 2006, Particle-gas dynamics and primary accretion, in McSween, H.Y. and Lauretta, D.S. eds., Meteorites and the Early Solar System II, University of Arizona Press, University of Arizona, Tuscon, p. 353–381.

Cuzzi, J.N., Ciesla, F.J., Petaev, M.I., and Krot, A.N., 2005, Nebula evolution of thermally processed solids: Reconciling models and meteorites: Chondrites and the Protoplanetary Disk, v. 341, p. 732–773.

Cuzzi, J.N., Hogan, R.C., and Shariff, K., 2008, Toward Planetesimals: Dense Chondrule Clumps in the Protoplanetary Nebula: The Astrophysical Journal, v. 687, no. 2, p. 1432–1447.

Daly, L., Bland, P.A., Dyl, K.A., Forman, L.V., Evans, K.A., Trimby, P.W., Moody, S., Yang, L., Liu, H., Ringer, S.P., Ryan, C.G., and Saunders, M., 2016, In situ analysis of Refractory Metal Nuggets in carbonaceous chondrites: Geochimica et Cosmochimica Acta.

Davison, T.M., Ciesla, F.J., and Collins, G.S., 2012, Post-impact thermal evolution of porous planetesimals: Geochimica et Cosmochimica Acta, v. 95, p. 252–269.

Davison, T.M., Collins, G.S., and Bland, P.A., 2016, Mesoscale modeling of impact compaction of primitive solar system solids: The Astrophysical Journal, v. 821, no. 1, p. 68.

Davison, T.M., Collins, G.S., and Bland, P.A., 2014, Mesoscale Numerical Modeling of Compaction of Primitive Solar System Solids in Low-Velocity Collisions: Lunar and Planetary Science Conference, v. 45, p. 2718.

Davison, T.M., Collins, G.S., and Ciesla, F.J., 2010, Numerical modelling of heating in porous planetesimal collisions: Icarus, v. 208, no. 1, p. 468–481.

Davison, T.M., O'Brien, D.P., Ciesla, F.J., and Collins, G.S., 2013, The early impact histories of meteorite parent bodies: Meteoritics & Planetary Science, v. 48, no. 10, p. 1894–1918.

Dodd, R.T., and Jarosewich, E., 1979, Incipient Melting in and Shock Classification of L-Group Chondrites: Earth and Planetary Science Letters, v. 44, no. 2, p. 335–340.

Dodd, R.T., Grover, J.E., and Brown, G.E., 1975, Pyroxenes in the Shaw (L-7) chondrite: Geochimica et Cosmochimica Acta, v. 39, no. 12, p. 1585–1594.

Doehne, E., and Margolis, S.V., 1990, Trace-element geochemistry and mineralogy of the Cretaceous/Tertiary boundary; Identification of extraterrestrial components: Geological Society of America Special Papers, v. 247, p. 367–382.

Doyle, P.M., Jogo, K., Nagashima, K., Krot, A.N., Wakita, S., Ciesla, F.J., and Hutcheon, I.D., 2015, Early aqueous activity on the ordinary and carbonaceous chondrite parent bodies recorded by fayalite: Nature Communications, v. 6, p. 7444.

Drits, V.A., Lindgreen, H., Sakharov, B.A., Jakobsen, H.J., and Zviagina, B.B., 2004, The detailed structure and origin of clay minerals at the cretaceous/tertiary boundary, Stevns Klint (Denmark): Clay Minerals, v. 39, no. 4, p. 367–390.

Dyl, K.A., Cleverley, J.S., Bland, P.A., Ryan, C.G., Fisher, L.A., and Hough, R.M., 2014, Quantified, whole section trace element mapping of carbonaceous chondrites by Synchrotron X-ray Fluorescence Microscopy: 1. CV meteorites: Geochimica et Cosmochimica Acta, v. 134, p. 100–119.

Ebel, D. S., Weisberg, M.K., and Friedrich, J.M., 2014, Primordial Ice Abundance in CV Chondrites: Lunar and Planetary Science Conference, v. 45, p. 1207.

Ebel, D.S., and Grossman, L., 2005, Spinel-bearing spherules condensed from the Chicxulub impact-vapor plume: Geology, v. 33, no. 4, p. 293–296.

Elkins-Tanton, L.T., Weiss, B.P., and Zuber, M.T., 2011, Chondrites as samples of differentiated planetesimals: Earth and Planetary Science Letters, v. 305, no. 1-2, p. 1–10.

Elliot, D.H., Askin, R.A., Kyte, F.T., and Zinsmeister, W.J., 1994, Iridium and dinocysts at the Cretaceous-Tertiary boundary on Seymour Island, Antarctica: Implications for the K-T event: Geology, v. 22, no. 8, p. 675–678.

Endress, M., Zinner, E., and Bischoff, A., 1996, Early aqueous activity on primitive meteorite parent bodies: Nature, v. 379, no. 6567, p. 701–703.

Evans, N.J., Ahrens, T.J., McInnes, B., and Gregoire, D.C., 1994, New evidence for primary fractionation of ruthenium and iridium in the Chicxulub ejecta cloud: New Developments Regarding the KT Event and Other Catastrophes in Earth History, v. 825, p. 34–36.

Ferrière, L., and Osinski, G.R., 2013, Shock Metamorphism: John Wiley & Sons, Ltd, Chichester, UK.

Fisher, L.A., Fougerouse, D., Cleverley, J.S., Ryan, C.G., Micklethwaite, S., Halfpenny, A., Hough, R.M., Gee, M., Paterson, D., Howard, D.L., and Spiers, K., 2014, Quantified, multi-scale X-ray fluorescence element mapping using the Maia detector array: application to mineral deposit studies: Mineralium Deposita, v. 50, no. 6, p. 665–674.

Fitzgerald, R., Keil, K., and Heinrich, K.F.J., 1968, Solid-State Energy-Dispersion Spectrometer for Electron-Microprobe X-ray Analysis: Science, v. 159, no. 3814, p. 528–530.

Fliervoet, T.F., Drury, M.R., and Chopra, P.N., 1999, Crystallographic preferred orientations and misorientations in some olivine rocks deformed by diffusion or dislocation creep: Tectonophysics, v. 303, no. 1-4, p. 1–27.

Forman, L.V., Bland, P.A., Timms, N.E., Collins, G.S., Davison, T.M., Ciesla, F.J., Benedix, G.K., Daly, L., Trimby, P.W., Yang, L., and Ringer, S.P., 2016, Hidden secrets of deformation: Impact-induced compaction within a CV chondrite: Earth and Planetary Science Letters, v. 452, p. 133–145.

Forman, L.V., Bland, P.A., Timms, N.E., Daly, L., Benedix, G. K., Trimby, P. W., Collins, G. S., and Davison, T. M., 2017, Defining the Mechanism for Compaction of the CV Parent Body: Geology, v. 45, no. 6, p.559-562.

Franchi, I.A., Wright, I.P., Sexton, A.S., and Pillinger, C.T., 1999, The oxygen-isotopic composition of Earth and Mars: Meteoritics & Planetary Science, v. 34, no. 4, p. 657–661.

Friedrich, J.M., Rubin, A.E., Beard, S.P., Swindle, T.D., Isachsen, C.E., Rivers, M.L., and Macke, R.J., 2014, Ancient porosity preserved in ordinary chondrites: Examining shock and compaction on young asteroids: Meteoritics & Planetary Science, v. 49, no. 7, p. 1214–1231.

Frost, H.J., and Ashby, M.F., 1982, Deformation mechanism maps: the plasticity and creep of metals and ceramics: Pergamon Press, Oxford, UK.

Fujimura, A., Kato, M., and Kumazawa, M., 1983, Preferred orientation of phyllosilicate [001] in matrix of Murchison meteorite and possible mechanisms of generating the oriented texture in chondrites: Earth and Planetary Science Letters, v. 66, p. 25–32.

Gail, H.-P., Henke, S., and Trieloff, M., 2015, Thermal evolution and sintering of chondritic planetesimals - II. Improved treatment of the compaction process: Astronomy & Astrophysics, v. 576, p. A60.

Ganapathy, R., Gartner, S., and Jiang, M., 1981, Iridium anomaly at the Cretaceous-Tertiary boundary

in Texas: Earth and Planetary Science Letters, v. 54, no. 3, p. 393–396.

Gartner, S., and McGuirk, J.P., 1979, Terminal Cretaceous extinction scenario for a catastrophe: Science, v. 206, p. 1272–1276.

Garvie, L.A.J., and Buseck, P.R., 2004, Nanosized carbon-rich grains in carbonaceous chondrite meteorites: Earth and Planetary Science Letters, v. 224, no. 3-4, p. 431–439.

Gattacceca, J., Rochette, P., Denise, M., Consolmagno, G., and Folco, L., 2005, An impact origin for the foliation of chondrites: Earth and Planetary Science Letters, v. 234, no. 3-4, p. 351–368.

Gillet, P., and Goresy, El, A., 2013, Shock Events in the Solar System: The Message from Minerals in Terrestrial Planets and Asteroids: Annual Review of Earth and Planetary Sciences, v. 41, no. 1, p. 257–285.

Glikson, A., and Allen, C., 2004, Iridium anomalies and fractionated siderophile element patterns in impact ejecta, Brockman Iron Formation, Hamersley Basin, Western Australia: evidence for a major asteroid impact in simatic crustal regions of the early Proterozoic earth: Earth and Planetary Science Letters, v. 220, no. 3-4, p. 247–264.

Glikson, A.Y., 2011, Geochemical and isotopic signatures of Archaean to Palaeoproterozoic extraterrestrial impact ejecta/fallout units: Australian Journal of Earth Sciences, v. 52, no. 4-5, p. 785–798.

Goderis, S., Paquay, F., and Claeys, P., 2012, Projectile Identification in Terrestrial Impact Structures and Ejecta Material, in Osinski, G.R. and Pierazzo, E. eds., The Contact and Compression Stage of Impact Cratering, Processes and Products, Blackwell Publishing Ltd., Chichester, UK, p. 223–239.

Goderis, S., Simonson, B.M., McDonald, I., Hassler, S.W., Izmer, A., Belza, J., Terryn, H., Vanhaecke, F., and Claeys, P., 2013a, Ni-rich spinels and platinum group element nuggets condensed from a Late Archaean impact vapour cloud: Earth and Planetary Science Letters, v. 376, no. 1, p. 87–98.

Goderis, S., Tagle, R., Belza, J., Smit, J., Montanari, A., Vanhaecke, F., Erzinger, J., and Claeys, P., 2013b, Reevaluation of siderophile element abundances and ratios across the Cretaceous–Paleogene (K–Pg) boundary: Implications for the nature of the projectile: Geochimica et Cosmochimica Acta, v. 120, p. 417–446.

Goetze, C., and Poirier, J.P., 1978, The Mechanisms of Creep in Olivine [and Discussion]: Philosophical Transactions of the Royal Society of London A: Mathematical, Physical and Engineering Sciences, v. 288, no. 1350, p. 99–119.

Goldin, T.J., and Melosh, H.J., 2007, Interactions Between Chicxulub Ejecta and the Atmosphere: The Deposition of the K/T Double Layer: Lunar and Planetary Institute Science Conference Abstracts, v. 38, p. 2114–2115.

Goldstein, J., Newbury, D.E., and Williams, D.B., 2012a, X-Ray Spectrometry in Electron Beam Instruments: Springer Science & Business Media.

Goldstein, J., Newbury, D.E., Joy, D.C., Lyman, C.E., Echlin, P., Lifshin, E., Sawyer, L., and Michael, J.R., 2012b, Scanning Electron Microscopy and X-ray Microanalysis: Springer Science & Business Media.

Göpel, C., Manhès, G., and Allègre, C.J., 1994, U-Pb systematics of phosphates from equilibrated ordinary chondrites: Earth and Planetary Science Letters, v. 121, no. 1-2, p. 153–171.

Gradstein, F.M., Ogg, J.G., and Smith, A.G., 2004, A geologic time scale: Newsletters on Stratigraphy, v. 45, no. 2, p. 171–188.

Graham, A.L., and Lee, M., 1992, The Matrix Minerology of the Vigarano (CV3) Chondrite: Lunar and Planetary Science Conference, v. 23, p. 435.

Gray, E.M., 2013, Deformation of Earth's upper mantle: insights from naturally occurring fabric types: Curtin University.

Grieve, R., Rupert, J., Smith, J., and Therriault, A., 1995, The record of terrestrial impact cratering: GSA Today, v. 5, no. 10, p. 189.

Grieve, R.A.F., and Pesonen, L.J., 1992, The terrestrial impact cratering record: Tectonophysics, v. 216, no. 1-2, p. 1–30.

Groeber, M.A., Rowenhorst, D.J., and Uchic, M.D., 2009, Collection, Processing, and Analysis of Three-Dimensional EBSD Data Sets, in Schwartz, A.J., Kumar, M., Adams, B.L., and Field, D.P. eds., Electron Backscatter Diffraction in Materials Science, Springer Science & Business Media, Boston, MA, p. 123–137.

Grossman, J.N., Rubin, A.E., Nagahara, H., and King, E.A., 1988, Properties of chondrules, in Kerridge, J.F. and Matthews, M.S. eds., Meteorites and the Early Solar System, University of Arizona Press, Tuscon, Arizona, p. 619–659.

Grossman, L., and Larimer, J.W., 1974, Early chemical history of the solar system: Reviews of Geophysics, v. 12, no. 1, p. 71–101.

Guimon, R.K., Symes, S.J.K., Sears, D.W.G., and Benoit, P.H., 1995, Chemical and physical studies of type 3 chondrites XII: The metamorphic history of CV chondrites and their components: Meteoritics & Planetary Science, v. 30, no. 6, p. 704–714.

Gulick, S.P.S., Christeson, G.L., Barton, P.J., Grieve, R.A.F., Morgan, J.V., and Urrutia Fucugauchi, J., 2013, Geophysical characterization of the Chicxulub impact crater: Reviews of Geophysics, v. 51, no. 1, p. 31–52.

Hanna, R.D., Ketcham, R.A., Zolensky, M., and Behr, W.M., 2015, Impact-induced brittle deformation, porosity loss, and aqueous alteration in the Murchison CM chondrite: Geochimica et Cosmochimica Acta, v. 171, p. 256–282.

Harvey, J., and Day, J., 2016, Introduction to Highly Siderophile and Strongly Chalcophile Elements in High Temperature Geochemistry and Cosmochemistry, in Harvey, J., Day, J., and Swainson, I.

eds., Highly Siderophile and Strongly Chalcophile Elements in High- Temperature Geochemistry and Cosmochemistry, Chantilly, Virginia, p. 1–12.

Henke, S., Gail, H.P., Trieloff, M., Schwarz, W.H., and Kleine, T., 2012, Thermal evolution and sintering of chondritic planetesimals: Astronomy & Astrophysics, v. 537, p. A45.

Hewins, R.H., 1997, Chondrules: Annual Review of Earth and Planetary Sciences, v. 25, no. 1, p. 61–83.

Heymann, D., Korochantsev, A., Nazarov, M.A., and Smit, J., 1996, Search for fullerenes C60and C70in Cretaceous–Tertiary boundary sediments from Turkmenistan, Kazakhstan, Georgia, Austria, and Denmark: Cretaceous Research, v. 17, no. 3, p. 367–380.

Hildebrand, A.R., and Stansberry, J.A., 1992, K/T boundary ejecta distribution predicts size and location of Chicxulub crater: Lunar and Planetary Science Conference, v. 23, p. 537.

Hildebrand, A.R., Penfield, G.T., Kring, D.A., Pilkington, M., Camargo Z, A., Jacobsen, S.B., and Boynton, W.V., 1991, Chicxulub Crater: A possible Cretaceous/Tertiary boundary impact crater on the Yucatán Peninsula, Mexico: Geology, v. 19, no. 9, p. 867–871.

Horedt, G.P., 1980, Gravitational heating of planets: Physics of the Earth and Planetary Interiors, v. 21, no. 1, p. 22–30.

Housen, K.R., and Holsapple, K.A., 2011, Ejecta from impact craters: Icarus, v. 211, no. 1, p. 856–875.

Housen, K.R., and Holsapple, K.A., 2003, Impact cratering on porous asteroids: Icarus, v. 163, no. 1, p. 102–119.

Housen, K.R., Holsapple, K.A., and Voss, M.E., 1999, Compaction as the origin of the unusual craters on the asteroid Mathilde: Nature, v. 402, no. 6758, p. 155–157.

Hua, X., and Buseck, P.R., 1995, Fayalite in the Kaba and Mokoia carbonaceous chondrites: Geochimica et Cosmochimica Acta, v. 59, no. 3, p. 563–578.

Hua, X., Huss, G.R., Tachibana, S., and Sharp, T.G., 2005, Oxygen, silicon, and Mn-Cr isotopes of fayalite in the Kaba oxidized CV3 chondrite: Constraints for its formation history: Geochimica et Cosmochimica Acta, v. 69, no. 5, p. 1333–1348.

Humphreys, F.J., 2004, Characterisation of fine-scale microstructures by electron backscatter diffraction (EBSD): Scripta materialia, v. 51, no. 8, p. 771–776.

Huss, G.R., Rubin, A.E., and Grossman, J.N., 2006, Thermal metamorphism in chondrites, in McSween, H.Y. and Lauretta, D.S. eds., Meteorites and the Early Solar System II, University of Arizona, Tuscon, Arizona, p. 567–586.

Hutchison, R., 2004, Meteorites: Cambridge University Press, Cambridge.

Hüppauff, M., and Lengeler, B., 1993, Valency and Structure of Iridium in Anodic Iridium Oxide Films: Journal of the Electrochemical Society, v. 140, no. 3, p. 598–602.

Jarvis, K.E., and Williams, J.G., 1993, Laser ablation inductively coupled plasma mass spectrometry (LA-ICP-MS): a rapid technique for the direct, quantitative determination of major, trace and rare-earth elements in geological samples: Chemical Geology, v. 106, no. 3-4, p. 251–262.

Johansen A., Oishi, J. S., Mac Low, M.-M., Klahr, H., Henning, T., & Youdin, A. (2007). Rapid Planetesimal Formation in Turbulent Circumstellar Discs. Nature, 448, 1022.

Johansen, A., Youdin, A., and Mac Low, M.-M., 2009, Particle clumping and planetesimal formation depend strongly on metallicity: The Astrophysical Journal Letters, v. 704, no. 2, p. L75–L79.

Kallemeyn, G.W., and Wasson, J.T., 1981, The compositional classification of chondrites—I. The carbonaceous chondrite groups: Geochimica et Cosmochimica Acta, v. 45, no. 7, p. 1217–1230.

Karato, S.-I., Jung, H., Katayama, I., and Skemer, P., 2008, Geodynamic Significance of Seismic Anisotropy of the Upper Mantle: New Insights from Laboratory Studies: Annual Review of Earth and Planetary Sciences, v. 36, no. 1, p. 59–95.

Karato, S.-I., Paterson, M.S., and FitzGerald, J.D., 1986, Rheology of synthetic olivine aggregates: Influence of grain size and water: Journal of Geophysical Research: Solid Earth, v. 91, no. B8, p. 8151–8176.

Katayama, I., 2009, Thin anisotropic layer in the mantle wedge beneath northeast Japan: Geology, v. 37, no. 3, p. 211–214.

Keil, K., Haack, H., and Scott, E.R.D., 1994, Catastrophic fragmentation of asteroids: evidence from meteorites: Planetary and Space Science, v. 42, no. 12, p. 1109–1122.

Keil, K., Stöffler, D., Love, S.G., and Scott, E.R.D., 1997, Constraints on the role of impact heating and melting in asteroids: Meteoritics & Planetary Science, v. 32, no. 3, p. 349–363.

Keller, L.P., and Buseck, P.R., 1990, Aqueous alteration in the Kaba CV3 carbonaceous chondrite: Geochimica et Cosmochimica Acta, v. 54, no. 7, p. 2113–2120.

Kim, S.-W., Kwon, S.-H., Kwak, D.-K., and Kang, S.-W., 2008, Phase control of iridium and iridium oxide thin films in atomic layer deposition: Journal of Applied Physics, v. 103, no. 2, p. 23517.

Kirsimäe, K., and Osinski, G.R., 2013, Impact-Induced Hydrothermal Activity, in The Contact and Compression Stage of Impact Cratering, Blackwell Publishing Ltd., Chichester, UK, p. 76–89.

Kohlstedt, D.L., and Goetze, C., 1974, Low-stress high-temperature creep in olivine single crystals: Journal of Geophysical Research: Solid Earth, v. 79, no. 14, p. 2045–2051.

Kring, D.A., 2002, Cataclysmic bombardment throughout the inner solar system 3.9–4.0 Ga: Journal of Geophysical Research, v. 107, no. E2, p. 4.1–4.6.

Krot, A.N., and Scott, E.R.D., 1995, Alteration of CV3 carbonaceous chondrites: Parent body vs. nebular processes: Lunar and Planetary Science Conference, v. 26, p. 803.

Krot, A.N., Meibom, A., and Keil, K., 2000, A clast of Bali-like oxidized CV material in the reduced CV

chondrite breccia Vigarano: Meteoritics & Planetary Science, v. 35, no. 4, p. 817–825.

Krot, A.N., Petaev, M.I., and Bland, P.A., 2004, Multiple formation mechanisms of ferrous olivine in CV carbonaceous chondrites during fluid-assisted metamorphism: Antarctic Meteorite Research, v. 17, p. 153–171.

Krot, A.N., Petaev, M.I., Scott, E.R.D., Choi, B.G., Zolensky, M.E., and Keil, K., 1998, Progressive alteration in CV3 chondrites: More evidence for asteroidal alteration: Meteoritics & Planetary Science, v. 33, no. 5, p. 1065–1085.

Krot, A.N., Scott, E.R.D., and Zolensky, M.E., 1995a, Alteration and dehydration in the parent asteroid of Allende: Meteoritics, v. 30, no. 5, p. 530–531.

Krot, A.N., Scott, E.R.D., and Zolensky, M.E., 1995b, Mineralogical and chemical modification of components in CV3 chondrites: Nebular or asteroidal processing?: Meteoritics & Planetary Science, v. 30, no. 6, p. 748–775.

Krot, A.N., Yurimoto, H., Hutcheon, I.D., and MacPherson, G.J., 2005, Chronology of the early Solar System from chondrule-bearing calcium-aluminium-rich inclusions: Nature, v. 434, no. 7036, p. 998–1001.

Kyte, F.T., 1998, A meteorite from the Cretaceous/Tertiary boundary: Nature, v. 396, p. 237–239.

Kyte, F.T., Smit, J., and Wasson, J.T., 1985, Siderophile interelement variations in the Cretaceous-Tertiary boundary sediments from Caravaca, Spain: Earth and Planetary Science Letters, v. 73, no. 2-4, p. 183–195.

Langenhorst, F., 2002, Shock metamorphism of some minerals: Basic introduction and microstructural observations: Bulletin of the Czech Geological Survey, v. 77, no. 4, p. 265–282.

Lee, M.R., and Hutchison, R., 1996, Aqueous alteration in the matrix of the Vigarano (CV3) carbonaceous chondrite: Meteoritics & Planetary Science, v. 31, p. 477–483.

Lee, M.R., Bland, P.A., and Graham, G., 2003, Preparation of TEM samples by focused ion beam (FIB) techniques: applications to the study of clays and phyllosilicates in meteorites: Mineralogical Magazine, v. 67, no. 3, p. 581–592.

Li, J., Malis, T., and Dionne, S., 2006, Recent advances in FIB–TEM specimen preparation techniques: Materials characterization, v. 57, no. 1, p. 64–70.

Liu, Y., Hu, Z., Gao, S., Günther, D., Xu, J., Gao, C., and Chen, H., 2008, In situ analysis of major and trace elements of anhydrous minerals by LA-ICP-MS without applying an internal standard: Chemical Geology, v. 257, no. 1-2, p. 34–43.

Liu, Y., Hu, Z., Li, M., and Gao, S., 2013, Applications of LA-ICP-MS in the elemental analyses of geological samples: Chinese Science Bulletin, v. 58, no. 32, p. 3863–3878.

Lodders, K., 1997, An Oxygen Isotope Model for the Composition of Mars: Icarus, v. 126, no. 2, p.

373–394.

Lodders, K., 2003, Solar System Abundances and Condensation Temperatures of the Elements: The Astrophysical Journal, v. 591, no. 2, p. 1220–1247.

Lyman, C.E., Goldstein, J.I., Romig, A.D., Jr, Echlin, P., Joy, D.C., Newbury, D.E., Williams, D.B., Armstrong, J.T., Fiori, C.E., Lifshin, E., and Peters, K.-R., 1990, Backscattered Electron Imaging, in Scanning Electron Microscopy, X-Ray Microanalysis, and Analytical Electron Microscopy, Springer US, New York, USA, p. 51–54.

Lyons, T.W., Reinhard, C.T., and Planavsky, N.J., 2014, The rise of oxygen in Earth/'s early ocean and atmosphere: Nature, v. 506, no. 7488, p. 307–315.

Macdougall, J.D., Lugmair, G.W., and Kerridge, J.F., 1984, Early Solar System aqueous activity: Sr isotope evidence from the Orgueil CI meteorite: Nature, v. 307, no. 5948, p. 249–251.

Macke, R.J., Britt, D.T., and Consolmagno, G.J., 2011, Density, porosity, and magnetic susceptibility of achondritic meteorites: Meteoritics & Planetary Science, v. 46, no. 2, p. 311–326.

MacPherson, G.J., and Krot, A.N., 2002, Distribution of Ca-Fe-silicates in CV3 chondrites: Possible controls by parent-body compaction.: Meteoritics & Planetary Science, v. 37, no. 7, p. A91–A91.

MacPherson, G.J., Hashimoto, A., and Grossman, L., 1985, Accretionary rims on inclusions in the Allende meteorite: Geochimica et Cosmochimica Acta, v. 49, no. 11, p. 2267–2279.

Marzo, G.A., Davila, A.F., Tornabene, L.L., Dohm, J.M., Fairén, A.G., Gross, C., Kneissl, T., Bishop, J.L., Roush, T.L., and McKay, C.P., 2010, Evidence for Hesperian impact-induced hydrothermalism on Mars: Icarus, v. 208, no. 2, p. 667–683.

Matsui, T., 1986, Evolution of an impact-induced atmosphere and magma ocean on the accreting Earth: Nature, v. 319, p. 303–305.

Matsui, T., and Abe, Y., 1986, Impact-induced atmospheres and oceans on Earth and Venus: Nature, v. 322, no. 6079, p. 526–528.

McSween, H.Y., 1979, Are carbonaceous chondrites primitive or processed? A review: Reviews of Geophysics, v. 17, no. 5, p. 1059–1078.

McSween, H.Y., 1977a, Petrographic variations among carbonaceous chondrites of the Vigarano type: Geochimica et Cosmochimica Acta, v. 41, no. 12, p. 1777–1790.

McSween, H.Y., and Patchen, A.D., 1989, Pyroxene thermobarometry in LL-group chondrites and implications for parent body metamorphism: Meteoritics & Planetary Science, v. 24, no. 4, p. 219–226.

McSween, H.Y., Jr, 1977b, Carbonaceous chondrites of the Ornans type: A metamorphic sequence: Geochimica et Cosmochimica Acta, v. 41, no. 4, p. 477–491.

McSween, H.Y., Sears, D., and Dodd, R., 1988, Thermal Metamorphism, in Kerridge, J.F. and Matthews,

M.S. eds., Meteorites and the Early Solar System, Tucson, p. 102–113.

Melosh, H.J., 2012, The Contact and Compression Stage of Impact Cratering, in Osinski, G.R. and Pierazzo, E. eds., The Contact and Compression Stage of Impact Cratering, Blackwell Publishing Ltd., Chichester, UK, p. 32–42.

Metzler, K., Bobe, K.D., Palme, H., Spettel, B., and Stöffler, D., 1995, Thermal and impact metamorphism on the HED parent asteroid: Planetary and Space Science, v. 43, no. 3-4, p. 499–525.

Michel, P., and Morbidelli, A., 2013, Population of Impactors and the Impact Cratering Rate in the Inner Solar System, in Osinski, G.R. and Pierazzo, E. eds., The Contact and Compression Stage of Impact Cratering, John Wiley & Sons, Ltd, Chichester, UK, p. 21–31.

Mohr-Westheide, T., Greshake, A., Wirth, R., Reimold, W.U., and Fritz, J., 2016, Transmission Electron Microscope Study of Platinum Group Element-Rich Micronuggets from Two Spherule Layer Intersections, Barberton Greenstone Belt, South Africa: LPI Contributions, v. 1921.

Mohr-Westheide, T., Reimold, W.U., Fritz, J., Koeberl, C., Salge, T., Hofmann, A., and Schmitt, R.T., 2015, Discovery of extraterrestrial component carrier phases in Archean spherule layers: Implications for estimation of Archean bolide sizes: Geology, v. 43, no. 4, p. 299–302.

Molina, E., Alegret, L., and Arenillas, I., 2005, The Cretaceous/Paleogene boundary at the Agost section revisited: paleoenvironmental reconstruction and mass extinction pattern: Journal of Iberian Geology, v. 31, p. 137–150.

Morgan, J.V., 2008, Comment on "Determining Chondritic Impactor Size from the Marine Osmium Isotope Record": Science, v. 321, no. 5893, p. 1158a.

Morgan, W., Ganapathy, R., Higuchi, H., and Anders, E., 1974, Lunar basins: characterization of projectiles, from meteorite trace elements in highland samples.: Moon, v. 11, p. 424–425.

Nakamura, T., Tomeoka, K., and Takeda, H., 1992, Shock effects of the Leoville CV carbonaceous chondrite: a transmission electron microscope study: Earth and Planetary Science Letters, v. 114, no. 1, p. 159–170.

Naumov, M.V., 2002, Impact-Generated Hydrothermal Systems: Data from Popigai, Kara, and Puchezh-Katunki Impact Structures, in Plado, J. and Pesonen, L.J. eds., Impacts in Precambrian Shields, Impact Studies, Springer Berlin Heidelberg, Berlin, Heidelberg, p. 117–171.

Newbury, D.E., 2002, Energy-Dispersive Spectrometry: John Wiley & Sons, Inc., Hoboken, NJ, USA.

Nicolas, A., and Poirier, J.P., 1976, Crystalline Plasticity and Solid State Flow in Metamorphic Rocks: John Wiley & Sons, London & New York.

Nicolas, A., Boudier, F., and Boullier, A.M., 1973, Mechanisms of flow in naturally and experimentally deformed peridotites: American Journal of Science, v. 273, p. 853–876.

Noronha, B.A., and Friedrich, J.M., 2014, Chemical compositions and classification of five thermally

altered carbonaceous chondrites: Meteoritics & Planetary Science, v. 49, no. 8, p. 1494–150.

O'Keefe, J.D., and Ahrens, T.J., 1977, Impact-induced energy partitioning, melting, and vaporization on terrestrial planets: Lunar and Planetary Science Conference, v. 8, p. 3357–3374.

O'Neill, C., Marchi, S., Zhang, S., and Bottke, B., 2016, Impact-driven tectonism in the Hadean: Lunar and Planetary Science Conference, v. 47, p. 2733.

Ormel, C.W., Cuzzi, J.N., and Tielens, A.G.G.M., 2008, Co-Accretion of Chondrules and Dust in the Solar Nebula: The Astrophysical Journal, v. 679, no. 2, p. 1588–1610.

Osawa, T., Hatsukawa, Y., Keisuke, N., Koizumi, M., Oshima, M., Toh, Y., Kimura, A., and Furutaka, K., 2009, Iridium concentration and noble gas composition of Cretaceous-Tertiary boundary clay from Stevns Klint, Denmark: Geochemical Journal, v. 43, no. 6, p. 415–422.

Osinski, G.R., and Pierazzo, E., 2012, Impact Cratering Processes and Products: John Wiley & Sons.

Osinski, G.R., Lee, P., Parnell, J., Spray, J.G., and Baron, M., 2005, A case study of impact-induced hydrothermal activity: The Haughton impact structure, Devon Island, Canadian High Arctic: Meteoritics & Planetary Science, v. 40, no. 12, p. 1859–1877.

Osinski, G.R., Tornabene, L.L., Banerjee, N.R., Cockell, C.S., Flemming, R., Izawa, M.R.M., McCutcheon, J., Parnell, J., Preston, L.J., Pickersgill, A.E., Pontefract, A., Sapers, H.M., and Southam, G., 2013, Impact-generated hydrothermal systems on Earth and Mars: Icarus, v. 224, no. 2, p. 347–363.

Palme, H., 2008, Platinum-Group Elements in Cosmochemistry: Elements, v. 4, no. 4, p. 233–238.

Palme, H., and Wlotzka, F., 1976, A metal particle from a Ca,Al-rich inclusion from the meteorite Allende, and the condensation of refractory siderophile elements: Earth and Planetary Science Letters, v. 33, no. 1, p. 45–60.

Papike, J.J., 1998, Comparative planetary mineralogy; chemistry of melt-derived pyroxene, feldspar, and olivine: Reviews in Mineralogy and Geochemistry, v. 36, p. 7.1–7.11.

Paton, C., Hellstrom, J., Paul, B., Woodhead, J., and Hergt, J., 2011, Iolite: Freeware for the visualisation and processing of mass spectrometric data: Journal of Analytical Atomic Spectrometry, v. 26, no. 12, p. 2508–2518.

Peck, J.A., 1983, An SEM petrographic study of C3 (V) meteorite matrix: Lunar and Planetary Science Conference, v. 14, p. 598–599.

Peck, J.A., 1984, Origin of the variation in properties of CV3 meteorite matrix and matrix clasts: Lunar and Planetary Science Conference, v. 15, p. 635.

Perkins, W.T., Pearce, N.J.G., and Jeffries, T.E., 1993, Laser ablation inductively coupled plasma mass spectrometry: A new technique for the determination of trace and ultra-trace elements in silicates: Geochimica et Cosmochimica Acta, v. 57, no. 2, p. 475–482.

Pierazzo, E., and Artemieva, N., 2012, Local and Global Environmental Effects of Impacts on Earth: Elements, v. 8, no. 1, p. 55–60.

Pierazzo, E., and Melosh, H.J., 2000, Hydrocode modeling of oblique impacts: The fate of the projectile: Meteoritics & Planetary Science, v. 35, no. 1, p. 117–130.

Pierazzo, E., Kring, D.A., and Melosh, H.J., 1998, Hydrocode simulation of the Chicxulub impact event and the production of climatically active gases: Journal of Geophysical Research: Solid Earth, v. 103, no. E12, p. 28607–28625.

Pirajno, F., 2009, Hydrothermal Processes Associated with Meteorite Impacts, in Hydrothermal Processes and Mineral Systems, Springer Netherlands, Dordrecht, p. 1097–1130.

Podosek, F.A., and Swindle, T.D., 1988, Extinct radionuclides, in Kerridge, J.F. and Matthews, M.S. eds., Meteorites and the Early Solar System, University of Arizona Press, Tuscon, Arizona, p. 1093–1113.

Pope, K.O., Ocampo, A.C., and Duller, C.E., 1991, Mexican site for K/T impact crater?: Nature, v. 351, no. 6322, p. 105.

Prior, D.J., Trimby, P.W., Weber, U.D., and Dingley, D.J., 1996, Orientation contrast imaging of microstructures in rocks using forescatter detectors in the scanning electron microscope: Mineralogical Magazine, v. 60, no. 403, p. 859–869.

Quitte, G., Robin, E., Levasseur, S., Capmas, F., Rocchia, R., Birck, J.-L., and AlleGre, C.J., 2007, Osmium, tungsten, and chromium isotopes in sediments and in Ni-rich spinel at the K-T boundary: Signature of a chondritic impactor: Meteoritics & Planetary Science, v. 42, no. 9, p. 1567–1580.

Renne, P.R., Deino, A.L., Hilgen, F.J., Kuiper, K.F., Mark, D.F., Mitchell, W.S.I., Morgan, L.E., Mundil, R., and Smit, J., 2013, Time Scales of Critical Events Around the Cretaceous-Paleogene Boundary: Science, v. 339, no. 6120, p. 684–687.

Richardson, J., Melosh, H., Greenberg, R., and O'Brien, D., 2005, The global effects of impact-induced seismic activity on fractured asteroid surface morphology: Icarus, v. 179, no. 2, p. 325–349.

Rietmeijer, F.J.M., and Mackinnon, I.D.R., 1985, Poorly graphitized carbon as a new cosmothermometer for primitive extraterrestrial materials: Nature, v. 315, no. 6022, p. 733–736.

Rubin, A.E., 1997, Mineralogy of meteorite groups: Meteoritics & Planetary Science, v. 32, no. 2, p. 231–247.

Rubin, A.E., 2004, Postshock annealing and postannealing shock in equilibrated ordinary chondrites: Implications for the thermal and shock histories of chondritic asteroids: Geochimica et Cosmochimica Acta, v. 68, no. 3, p. 673–689.

Rubin, A.E., Trigo-Rodríguez, J.M., Huber, H., and Wasson, J.T., 2007, Progressive aqueous alteration of CM carbonaceous chondrites: Geochimica et Cosmochimica Acta, v. 71, no. 9, p. 2361–2382.

Russell, S.S., Hartmann, L., Cuzzi, J., and Krot, A.N., 2006, Timescales of the solar protoplanetary disk, in Lauretta, D.S. and McSween, H.Y. eds., Meteorites and the Early Solar System II, University of Arizona Press, p. 233–251.

Ryan, C.G., Cousens, D.R., Sie, S.H., Griffin, W.L., Suter, G.F., and Clayton, E., 1990, Quantitative pixe microanalysis of geological matemal using the CSIRO proton microprobe: Nuclear Instruments and Methods in Physics Research Section B: Beam Interactions with Materials and Atoms, v. 47, no. 1, p. 55–71.

Ryan, C.G., Etschmann, B.E., Vogt, S., Maser, J., Harland, C.L., van Achterbergh, E., and Legnini, D., 2005, Nuclear microprobe – synchrotron synergy: Towards integrated quantitative real-time elemental imaging using PIXE and SXRF: Nuclear Instruments and Methods in Physics Research Section B: Beam Interactions with Materials and Atoms, v. 231, no. 1-4, p. 183–188.

Ryan, C.G., Siddons, D.P., Kirkham, R., and Dunn, P.A., 2010, The new Maia detector system: methods for high definition trace element imaging of natural material: AIP Conference Proceedings, v. 1221, no. 9, p. 10–17.

Ryder, G., 1990, Lunar samples, lunar accretion and the early bombardment of the Moon: Eos, Transactions American Geophysical Union, v. 71, no. 10, p. 313–323.

Schmitz, B., Andersson, P., and Dahl, J., 1988, Iridium, sulfur isotopes and rare earth elements in the Cretaceous-Tertiary boundary clay at Stevns Klint, Denmark: Geochimica et Cosmochimica Acta, v. 52, no. 1, p. 229–236.

Schulte P., Alegret L., Arenillas I., Arz J. A., Barton P. J., Bown P. R., Bralower T. J., Christeson G. L., Claeys P., Cockell C. S., Collins G. S., Deutsch A., Goldin T. J., Goto K., Grajales-Nishimura J. M., Grieve R. A. F., Gulick S. P. S., Johnson K. R., Kiessling W., Koeberl C., Kring D. A., MacLeod K. G., Matsui T., Melosh J., Montanari A., Morgan J. V., Neal C. R., Nichols D. J., Norris R. D., Pierazzo E., Ravizza G., Rebolledo Vieyra M., Reimold W. U., Robin E., Salge T., Speijer R. P., Sweet A. R., Urrutia-Fucugauchi J., Vajda V., Whalen M. T. and Willumsen P. S., 2010, The Chicxulub Asteroid Impact and Mass Extinction at the Cretaceous-Paleogene Boundary: Science, v. 327, no. 5970, p. 1214–1218.

Schwenn, M.B., and Goetze, C., 1978, Creep of olivine during hot-pressing: Tectonophysics, v. 48, no. 1-2, p. 41–60.

Schwenzer, S.P., and Kring, D.A., 2009, Impact-generated hydrothermal systems capable of forming phyllosilicates on Noachian Mars: Geology, v. 37, no. 12, p. 1091–1094.

Scott, E.R.D., 2002, Meteorite evidence for the accretion and collisional evolution of asteroids: Asteroids, v. 3, p. 697–709.

Scott, E.R.D., and Krot, A.N., 2003, Chondrites and their Components: Treatise on geochemistry, v. 1, p. 7.01–7.72.

Scott, E.R.D., Barber, D.J., Alexander, C.M., Hutchinson, R., and Peck, J.A., 1988, Primitive material

surviving in chondrites - Matrix, in Sears, D. and Dodd, R.T. eds., Meteorites and the Early Solar System, University of Arizona Press, Tuscon, Arizona, p. 718–745.

Scott, E.R.D., Keil, K., and Stöffler, D., 1992, Shock Metamorphism of Carbonaceous Chondrites: Geochimica et Cosmochimica Acta, v. 56, no. 12, p. 4281–4293.

Scott, E.R.D., Taylor, G.J., Newsom, H.E., Herbert, F., and Zolensky, M., 1989, Chemical, thermal and impact processing of asteroids, in Binzel, R.P.B., Gehrels, T., and Matthews, M.S. eds., Asteroids II, Asteroids II, Tuscon, Arizona, p. 701–739.

Sears, D., and Dodd, R.T., 1988, Overview and Classification of Meteorites, in Kerridge, J.F. and Matthews, M.S. eds., Meteorites and the Early Solar System, University of Arizona Press, Tuscon, Arizona, p. 3–31.

Shannon, R.D., 1976, Revised Effective Ionic-Radii and Systematic Studies of Interatomic Distances in Halides and Chalcogenides: Acta Crystallographica, v. 32, p. 751–767.

Sharp, T.G., and DeCarli, P.S., 2006, Shock effects in meteorites, in Meteorites and the Early Solar System II, University of Arizona Press, Tuscon, Arizona, p. 653–677.

Shoemaker, E.M., 1972, Cratering history and early evolution of the moon: Lunar and Planetary Science Conference Proceedings, v. 3, p. 696–698.

Shukolyukov, A., and Lugmair, G.W., 1998a, Chromium in the Cretaceous-Tertiary boundary layer: first isotopic evidence for an impactor and its type: Meteoritics and Planetary Science, v. 33, no. 4, p. A144.

Shukolyukov, A., and Lugmair, G.W., 1998b, Isotopic Evidence for the Cretaceous-Tertiary Impactor and Its Type: Science, v. 282, no. 5390, p. 927–930.

Smit, J., 1999, The global stratigraphy of the Cretaceous-Tertiary boundary impact ejecta: Annual Review of Earth and Planetary Sciences, v. 27, no. 1, p. 75–113.

Smit, J., and Hertogen, J., 1980, An extraterrestrial event at the Cretaceous-Tertiary boundary: Nature, v. 285, no. 5762, p. 198–200.

Smit, J., and Kyte, F.T., 1984, Siderophile-rich magnetic spheroids from the Cretaceous | [ndash] | Tertiary Boundary in Umbria, Italy: Nature, v. 310, no. 5976, p. 403–405.

Spicuzza, M.J., Day, J.M.D., Taylor, L.A., and Valley, J.W., 2007, Oxygen isotope constraints on the origin and differentiation of the Moon: Earth and Planetary Science Letters, v. 253, no. 1-2, p. 254–265.

Stacey, F.D., Lovering, J.F., and Parry, L.G., 1961, Thermomagnetic properties, natural magnetic moments, and magnetic anisotropies of some chondritic meteorites: Journal of Geophysical Research: Solid Earth, v. 66, no. 5, p. 1523–1534.

Stöffler, D., Bischoff, A., Buchwald, V., and Rubin, A.E., 1988, Shock effects in meteorites, in Kerridge,

J.F. and Matthews, M.S. eds., Meteorites and the Early Solar System, University of Arizona Press, p. 165–202.

Stöffler, D., Keil, K., and Scott, E.R.D., 1991, Shock Metamorphism of Ordinary Chondrites: Geochimica et Cosmochimica Acta, v. 55, no. 12, p. 3845–3867.

Strom, R.G., Malhotra, R., Ito, T., Yoshida, F., and Kring, D.A., 2005, The origin of planetary impactors in the inner solar system: Science, v. 309, p. 1847–1850.

Stroud, R.M., Pravdivtseva, O.V., Meshik, A.P., and Shatoff, E.A., 2016, Aberration-Corrected STEM Analysis of Electrophoresis Separates of Allende Nanodiamond: Lunar and Planetary Science Conference, v. 47, p. 2311.

Svetsov, V.V., Nemtchinov, I.V., and Teterev, A.V., 1995, Disintegration of Large Meteoroids in Earth's Atmosphere: Theoretical Models: Icarus, v. 116, no. 1, p. 131–153.

Swindle, T.D., Caffee, M.W., Hohenberg, C.M., Lindstrom, M.M., and Taylor, G.J., 1991, Iodine-xenon studies of petrographically and chemically characterized Chainpur chondrules: Geochimica et Cosmochimica Acta, v. 55, no. 3, p. 861–880.

Tait, A.W., Fisher, K.R., Srinivasan, P., and Simon, J.I., 2016, Evidence for impact induced pressure gradients on the Allende CV3 parent body: Consequences for fluid and volatile transport: Earth and Planetary Science Letters, v. 454, p. 213–224.

Tait, A.W., Tomkins, A.G., Godel, B.M., Wilson, S.A., and Hasalova, P., 2014, Investigation of the H7 ordinary chondrite, Watson 012: Implications for recognition and classification of Type 7 meteorites: Geochimica et Cosmochimica Acta, v. 134, p. 175–196.

Trimby, P., Day, A., Mehnert, K., and Schmidt, N.H., 2002, Is fast mapping good mapping? A review of the benefits of high-speed orientation mapping using electron backscatter diffraction: Journal of Microscopy, v. 205, no. 3, p. 259–269.

Trimby, P.W., 2012, Orientation mapping of nanostructured materials using transmission Kikuchi diffraction in the scanning electron microscope: Ultramicroscopy, v. 120, p. 16–24.

Trimby, P.W., and Prior, D.J., 1999, Microstructural imaging techniques: a comparison between light and scanning electron microscopy: Tectonophysics, v. 303, no. 1-4, p. 71–81.

Trimby, P.W., Cao, Y., Chen, Z., Han, S., Hemker, K.J., Lian, J., Liao, X., Rottmann, P., Samudrala, S., Sun, J., Wang, J.T., Wheeler, J., and Cairney, J.M., 2014, Characterizing deformed ultrafine-grained and nanocrystalline materials using transmission Kikuchi diffraction in a scanning electron microscope: Acta Materialia, v. 62, p. 69–80.

Trinquier, A., Birck, J.-L., and Jean Allègre, C., 2006, The nature of the KT impactor. A 54Cr reappraisal: Earth and Planetary Science Letters, v. 241, no. 3-4, p. 780–788.

Turner, G., 1988, Dating of secondary events, in Kerridge, J.F. and Matthews, M.S. eds., Meteorites and the Early Solar System, University of Arizona Press, Tuscon, Arizona, p. 276–288.

Twiss, R.J., and Moores, E.M., 2006, Structural Geology: W. H. Freeman.

Van Schmus, W.R., and Wood, J.A., 1967, A chemical-petrologic classification for the chondritic meteorites: Geochimica et Cosmochimica Acta, v. 31, no. 5, p. 747–765.

Wark, D.A., and Lovering, J.F., 1976, Refractory/platinum metal grains in Allende calcium-aluminium-rich clasts (CARC's): Possible exotic presolar material?: Lunar and Planetary Science Conference, v. 7, p. 912.

Warner M., Morgan J., the Chicxulub Working Group, Brittan J., Buffler R., Camargo A., Christeson G., Denton P., Hildebrand A., Hobbs R., Macintyre H., Mackenzie G., Maguire P., Marin L., Nakamura Y., Pilkington M., Sharpton V., Snyder D., Suarez G. and Trejo A., 1997, Size and morphology of the Chicxulub impact crater: Nature, v. 390, no. 6659, p. 472–476.

Wasson, J.T., and Kallemeyn, G.W., 1988, Compositions of chondrites: Philosophical Transactions of the Royal Society of London, v. 325, no. 325, p. 535–544.

Wasson, J.T., Boynton, W.V., Chou, C.-L., and Baedecker, P.A., 1975, Compositional evidence regarding the influx of interplanetary materials onto the lunar surface: The Moon, v. 13, no. 1-3, p. 121–141.

Watt, L.E., Bland, P.A., Prior, D.J., and Russell, S.S., 2006, Fabric analysis of Allende matrix using EBSD: Meteoritics & Planetary Science, v. 41, no. 7, p. 989–1001.

Weidenschilling, S.J., 2011, Initial sizes of planetesimals and accretion of the asteroids: Icarus, v. 214, no. 2, p. 671–684.

Weidenschilling, S.J., and Cuzzi, J.N., 2006, Accretion dynamics and timescales: Relation to chondrites, in Lauretta, D.S. and McSween, H.Y. eds., Meteorites and the Early Solar System II, University of Arizona, Tuscon, Arizona, p. 473–485.

Weinbruch, S., Armstrong, J., and Palme, H., 1994, Constraints on the thermal history of the Allende parent body as derived from olivine-spinel thermometry and Fe/Mg interdiffusion in olivine: Geochimica et Cosmochimica Acta, v. 58, no. 2, p. 1019–1030.

Weisberg, M.K., McCoy, T.J., and Krot, A.N., 2006, Systematics and Evaluation of Meteorite Classification, in Lauretta, D.S. and McSween, H.Y. eds., Meteorites and the Early Solar System II, Tuscon, Arizona, p. 19–52.

Weisberg, M.K., Prinz, M., and Clayton, R.N., 1997, CV3 chondrites: Three subgroups, not two: Meteoritics and Planetary Science, v. 32, no. 4, p. A138–A139.

Weiss, B.P., Carporzen, L., Elkins-Tanton, L.T., Shuster, D.L., Ebel, D.S., Gattacceca, J., Zuber, M.T., Chen, J.H., Papanastassiou, D.A., Binzel, R.P., Rumble, D., and Irving, A.J., 2010, A Partially Differentiated Body for CV Chondrites?: Lunar and Planetary Science Conference, v. 41, p. 1688.

Wheeler, J., Reddy, S.M., and Cliff, R.A., 2001, Kinematic linkage between internal zone extension and

shortening in more external units in the NW Alps: Journal of the Geological Society, v. 158, no. 3, p. 439–443.

Wittmann, A., Kenkmann, T., Hecht, L., and Stöffler, D., 2007, Reconstruction of the Chicxulub ejecta plume from its deposits in drill core Yaxcopoil-1: Geological Society of America Bulletin, v. 119, no. 9-10, p. 1151–1167.

Zinner, E., and Gopel, C., 1992, Evidence for 26Al in feldspars from the H4 chondrite Ste. Marguerite: Meteoritics, v. 27, no. 3, p. 311.

Zinner, E., and Göpel, C., 2002, Aluminum-26 in H4 chondrites: Implications for its production and its usefulness as a fine-scale chronometer for early solar system events: Meteoritics & Planetary Science, v. 37, no. 7, p. 1001–1013.

Zolensky, M.E., 1997, Structural water in the Bench Crater chondrite returned from the Moon: Meteoritics & Planetary Science, v. 32, no. 1, p. 15–18.

Appendix A

First Author Journal Publications & Author Contributions to Thesis

Appendix A1

Hidden Secrets of Deformation: Impact-Induced Compaction within a CV Chondrite

Forman L. V., Bland P. A., Timms N. E., Collins G. S., Davison T. M., Ciesla F. J., Benedix G. K., Daly L., Trimby P. W., Yang L. and Ringer S. P., 2016, Hidden secrets of deformation: Impact-induced compaction within a CV chondrite: Earth and Planetary Science Letters v. 452, p. 133–145.

STATEMENT OF AUTHORSHIP

I hereby confirm the primary author, Miss L. V. Forman, conducted the majority of this study and give my permission for this to be included in the candidate's PhD thesis.

MISS LUCY. V. FORMAN

- Lead on planning, data collection and analysis
- Drafted & formatted manuscript

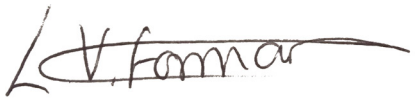

Contribution: *70%* ***Date:*** *22.2.17*

PROF. PHIL BLAND

- Assisted with initial concept and planning
- Manuscript editing and planning

Contribution: *10%* ***Date:*** *23.2.17*

DR. NICK TIMMS

- Assisted with initial concept and planning
- Assisted with data interpretation
- Manuscript editing

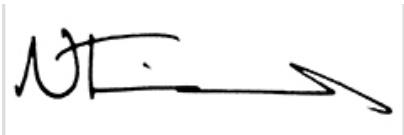

Contribution: *7%* ***Date:*** *23.2.17*

DR. GARETH COLLINS

- Offered insight from modelling simulations
- Manuscript editing

Contribution: *2%* ***Date:*** *28.2.17*

DR. THOMAS DAVISON

- Offered insight from modelling simulations
- Manuscript editing

Contribution: *2%* ***Date:*** *28.2.17*

DR. FRED CIESLA

- Offered insight from modelling simulations

Contribution: *1%* ***Date:*** *28.2.17*

DR. GRETCHEN BENEDIX

- Manuscript editing

Contribution: *1%* ***Date:*** *28.2.17*

MR LUKE DALY

- Conducted FIB and TKD work
- Manuscript editing

Contribution: *3%* *Date:* *22.2.17*

DR. PATRICK TRIMBY

- Assisted with TKD work
- Manuscript editing

Contribution: *2%* *Date:* *24.2.17*

DR. LIMEI YANG

- Assisted with TKD work

Contribution: *1%* *Date:* *25.2.17*

PROF. SIMON RINGER

- Assisted with TKD work

Contribution: *1%* *Date:* *1.3.17*

Earth and Planetary Science Letters 452 (2016) 133–145

Contents lists available at ScienceDirect

Earth and Planetary Science Letters

www.elsevier.com/locate/epsl

Hidden secrets of deformation: Impact-induced compaction within a CV chondrite

L.V. Forman [a,*], P.A. Bland [a], N.E. Timms [a], G.S. Collins [b], T.M. Davison [b], F.J. Ciesla [c], G.K. Benedix [a], L. Daly [a], P.W. Trimby [d], L. Yang [d], S.P. Ringer [e]

[a] Department of Applied Geology, Curtin University, GPO Box U1987, Perth, WA 6845, Australia
[b] Royal School of Mines, Department of Earth Science & Engineering, Imperial College London, Prince Consort Road, South Kensington, SW7 2BJ, United Kingdom
[c] Department of the Geophysical Sciences, The University of Chicago, 5734 South Ellis Avenue, Chicago, IL 60637, USA
[d] Australian Centre for Microscopy and Microanalysis, The University of Sydney, NSW, 2006, Australia
[e] Australian Institute for Nanoscale Science and Technology, and School of Aerospace, Mechanical and Mechatronic Engineering, The University of Sydney, NSW, 2006, Australia

ARTICLE INFO

Article history:
Received 1 October 2015
Received in revised form 27 July 2016
Accepted 27 July 2016
Available online 12 August 2016
Editor: C. Sotin

Keywords:
Allende
impact
compaction
meteorite
deformation
crystallography

ABSTRACT

The CV3 Allende is one of the most extensively studied meteorites in worldwide collections. It is currently classified as S1—essentially unshocked—using the classification scheme of Stöffler et al. (1991), however recent modelling suggests the low porosity observed in Allende indicates the body should have undergone compaction-related deformation. In this study, we detail previously undetected evidence of impact through use of Electron Backscatter Diffraction mapping to identify deformation microstructures in chondrules, AOAs and matrix grains. Our results demonstrate that forsterite-rich chondrules commonly preserve crystal-plastic microstructures (particularly at their margins); that low-angle boundaries in deformed matrix grains of olivine have a preferred orientation; and that disparities in deformation occur between chondrules, surrounding and non-adjacent matrix grains. We find heterogeneous compaction effects present throughout the matrix, consistent with a highly porous initial material. Given the spatial distribution of these crystal-plastic deformation microstructures, we suggest that this is evidence that Allende has undergone impact-induced compaction from an initially heterogeneous and porous parent body. We suggest that current shock classifications (Stöffler et al., 1991) relying upon data from chondrule interiors do not constrain the complete shock history of a sample.

1. Introduction

Planetary systems evolve from a molecular cloud comprised of dust (condensed minerals and presolar grains) and gas, to a protoplanetary disk, where most of the mass is concentrated in the 'mid-plane' of that disk. Turbulence allows for gas and particle clumping and accretion of the dust into centimetre- to metre-sized bodies (Cuzzi and Weidenschilling, 2006). Interactions with the gas and collisions lead these solids to grow and accumulate into planetesimals measuring 10 s to 100 s of kilometers in diameter. As this accumulation must be relatively gentle to ensure sticking and adhesion among the components, primordial planetesimals formed in this way would preserve large pore spaces in between each component, resulting in very high porosities (>65%) (Blum, 2003; Weidenschilling and Cuzzi, 2006).

Planetary evolution from these primordial objects to the asteroids that we see today requires that porosity be greatly reduced, as evidenced by the worldwide collection of meteorites that comprises comparatively low-porosity rocks. A number of mechanisms for porosity reduction and weak fabric development have been suggested, including metamorphism and expansion/contraction cycles (Stacey et al., 1961; Zolensky et al., 1997), accretional compaction (Cain et al., 1986), gravitational compaction (Fujimara et al., 1983) and sedimentation; perhaps the two most plausible mechanisms being compaction from lithostatic overburden (Cain et al., 1986) and impacts (Scott, 2002; Sharp and DeCarli, 2006; Davison et al., 2010; Beitz et al., 2013; Bland et al., 2014). It is apparent that the gravity field of even relatively large planetesimals would be insufficient and to generate the required lithostatic pressure to cause sufficient compaction that could adequately explain the low porosities of meteorites (Weidenschilling and Cuzzi, 2006; Friedrich et al., 2014). The anisotropy of magnetic susceptibility (AMS) studies done by Gattacceca et al. (2005) conclude that dynamic compaction via impacts is the most likely mechanism for

* Corresponding author.
E-mail address: lucy.forman@curtin.edu.au (L.V. Forman).

http://dx.doi.org/10.1016/j.epsl.2016.07.050

fabric development and therefore porosity reduction, which is also supported by a wide number of findings within meteorite collections; low (but variable) porosities throughout a given sample; heterogeneous porosities within the same chondrite group; subtle mineral deformation microstructures; widespread planar fabrics; and localised melt pockets within matrix (Nakamura et al., 1992; Consolmagno et al., 1998; Brenker et al., 2000; Cuzzi et al., 2008; Johansen et al., 2009). Such evidence is not unique to carbonaceous chondrites; it is also present in ordinary chondrites, in the form of high-pressure polymorphism, vitrification of silicate minerals and deformation of olivine grains (Rubin, 2004). Recent work on the CM meteorite Murchison has also revealed porosity loss was induced by impact and predicted a pre-compaction bulk porosity of up to ∼50% (Hanna et al., 2015). Further support for the occurrence of impacts on early highly porous bodies is found in Housen et al.'s work (1999) regarding impact-cratering on the asteroid Mathilde; an unusual lack of blanket ejecta around prominent craters indicate the impacts that produced them occurred when the body was highly porous. Other studies also argue that impacts on such a large scale may destroy the target body if the porosity was not sufficiently high and the impact direct; the pores allow the target to sustain the impacts without being disrupted and oblique impacts lead to less ejecta and the crater morphologies present on Mathilde (Housen et al., 1999; Cheng and Barnouin-Jha, 1999; Housen and Holsapple, 2011). Impact-induced compaction is therefore discussed in depth with relation to the research outlined in this paper.

Evidence of impact shock is routinely observed in current meteorite collections and a shock level is assigned to each meteorite (Stöffler et al., 1991; Scott et al., 1992; Sharp and DeCarli, 2006). The approach taken by Stöffler et al. (1991) uses published data from impact experiments on low-porosity and homogeneous terrestrial rocks, lunar rocks and single crystals, taking these materials as analogues for low-porosity, H, L and LL ordinary chondrites. A set of shock metamorphic features seen in analogue materials are used to calibrate the peak pressure experienced for that meteorite, and determine a shock level. This classification is based upon the largest of grains in any sample (Stöffler et al., 1991; Scott et al., 1992), meaning only a few larger grains are considered. Allende, the sample of study in this paper, is identified as an S1-virtually unshocked- and is expected to have experienced no more than 5 GPa in peak shock pressure (Scott et al., 1992). The samples and procedures used in the early study may not be ideal for several reasons: meteorites are not homogeneous materials, and grain size plays an important role in determining the shock reaction of a grain, especially when pore space is considered (Davison et al., 2010). Most importantly, the experimental impact studies that underpin the Stöffler et al. (1991) and Scott et al. (1992) approach are concerned with impacts into low- or zero-porosity targets and, by extension, impacts into compacted planetesimals. Therefore, this approach may not be suitable for approximating impacts into highly porous primordial objects.

Recent numerical models consider more complex scenarios, concerned with impacts into uncompacted porous planetesimals, bimodal material and mixed compositions of the target body. Davison et al. (2010) model shock propagation through homogeneous, porous planetesimals and find high porosity to be positively related to higher impact-generated temperatures on an asteroidal scale. Similar numerical simulations have highlighted the importance of pore collapse in the target body upon impact, which generates large amounts of heat, allowing the whole medium to experience elevated temperatures and potential melting (Consolmagno et al., 1998; Davison et al., 2010; 2014). Further improvements were made to these models to acknowledge the small-scale and complex material properties of primitive bodies: chondrites are essentially bimodal mixtures of porous, fine-grained matrix and large chondrules without intercrystalline porosity (Bland et al., 2011; 2014; Davison et al., 2014). In an impact compaction simulation with a bulk shock pressure of only ∼1 GPa, the bulk post-shock temperature was ≈ 425 K, but the matrix was heated to ≈ 530 K from an initial temperature of 300 K, whereas chondrules were heated by only a few degrees (Bland et al., 2014). Heating occurs at chondrule edges adjacent to initially porous areas of matrix, and at the edges of closely spaced chondrules, and pressure distribution within chondrules is also not uniform; chondrule edges are predicted to experience higher pressures than chondrule interiors. Porosity in matrix also varies, with high-porosity regions observed in the lee of chondrules. Petrologic evidence of these features has yet to be identified, but the models give an indication of how a bimodal heterogeneous material may react upon impact.

In light of the models described above (Davison et al., 2010; Bland et al., 2014), the shock pressure aspect of Allende's impact history may simply be absent from large, resilient chondrules. Allende is a well-studied sample that contains approximately 40% matrix (Macke et al., 2011), and has a measured bulk porosity of 22%. Recent fabric analysis has inferred that ∼50% pore volume reduction has occurred in Allende via impact (Bland et al., 2011; Hanna et al., 2015), but this is unlikely to be homogeneous throughout any sample. Assuming initial matrix porosity in the >65% range, this implies a pre-compaction matrix:chondrule volume ratio of $> 2:1$. Numerical simulations that exposed such a chondrule–matrix mixture to a ∼1 GPa shock wave reproduced the observed bulk and matrix porosity in Allende, and suggest that localised heating by heterogeneous pore collapse may have been a significant process.

In this study we explore the possibility that matrix grains and chondrules responded differently to planetary compaction. We establish how the microanalytical and textural study of this meteorite holds interesting implications about the evolution of the parent body of Allende.

2. Approach & methods

In this study we analysed a thin section of Allende. The initial imaging of this sample was conducted at the X-Ray Fluorescence Beamline (XRF) at the Australian Synchrotron facilities in Melbourne. Here, 25 element maps were collected for the entire sample in under 10 h (Fig. 1). These were compared with the collected Energy Dispersive Spectroscopy (EDS) data for accuracy of elemental distribution throughout the sample, in addition to monitoring any instrumental drift. The Maia detector on this beamline had an energy sensitivity in the range of 3.3–19.9 keV, encompassed a number of major elements with an energy resolution of 300–400 eV, and in this case, produced maps with a spatial resolution of 2 µm per pixel. Elements were detected in the spectra processing stage and so were not required beforehand for the imaging to occur. In addition, the Maia detector was able to detect elements at the 10–100 ppm scale – commonly lower than other traditional imaging techniques (Fisher et al., 2014). Owing to the high-energy beam in use (18.5 keV), this technique sampled a larger depth than other traditional imaging techniques, and so data collected represented an average of the volume sampled (Dyl et al., 2014). Further information regarding this imaging technique can be found in the Analytical Methods section of Dyl et al. (2014). This map was used as a means of identifying areas of interest for further Secondary Electron (SE), Backscatter Electron (BSE), EDS and Electron Backscatter Diffraction (EBSD) analyses.

Ten regions encompassing chondrules, Amoeboid Olivine Aggregates (AOAs) and matrix grains were mapped using a variety of imaging techniques, utilising the Tescan Mira3 FESEM, at the John de Laeter centre at Curtin University, Western Australia. It is important to note that all maps were taken in the same physical

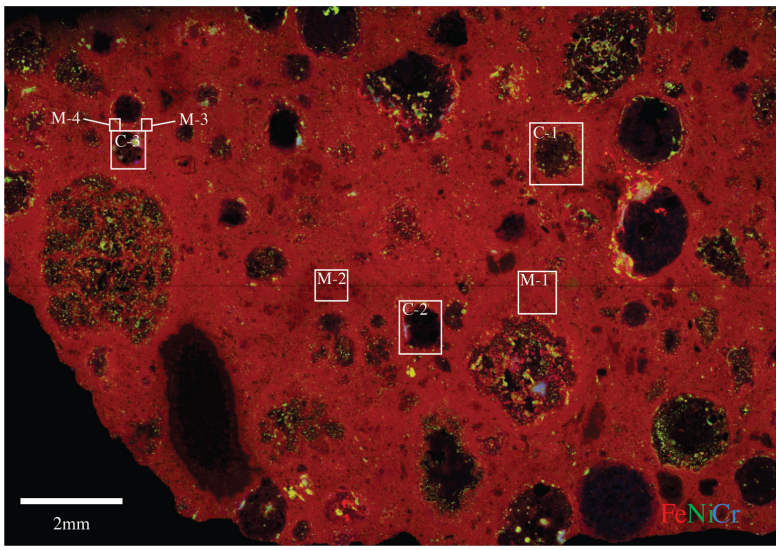

Fig. 1. X-Ray Flourescence Synchrotron map of a thin section of the Allende meteorite. Chondrule and matrix sites to be discussed are shown (C = chondrule/AOA, M = matrix). Note that M-1, M-3 and M-4 are proximal to a chondrule or AOA, and M-2 is in an area devoid of chondrules, AOAs and CAIs.

Table 1
EBSD and SEM imaging parameters used for imaging at each of the chondrule, AOA and matrix sites in this sample of Allende.

Site	Type	Step size (μm)	Imaging threshold (μm)	Number of points	Mean Angular Deviation (MAD) (°)	Acc. voltage (keV)	Forsterite indexed (%)	Not indexed (%)
C-1	Chondrule	0.5	2	77284	0.38	20	82.5	16.0
C-2	Chondrule	2	8	172125	0.60		45.8	49.8
C-3	AOA	0.81	3.6	2403310	0.53		36.3	63.2
M-1	Matrix	0.1	0.4	130732	0.68		48.9	49.0
M-2	Matrix	0.12	0.48	2314956	0.67		37.2	59.3
M-3	Matrix	0.2	0.8	122760	0.67		36.55	52.87
M-4	Matrix	0.35	1.4	35708	0.80		37.9	57.1

orientation in the SEM, allowing for direct and accurate comparisons of crystallographic features between sites.

Standard Secondary Electron (SE) and Back-Scattered Electron (BSE) images were collected at a voltage of 20 keV, a beam intensity of 17, an aperture size of 30 μm and a working distance between 10 and 15 mm. These images were used to define regions of interest for further analysis and image collection.

Electron Backscatter Diffraction (EBSD) was the primary technique used in the study. EBSD enabled mapping of the crystallographic orientation of grains in a thin section, both in relation to crystallographic axes and neighbouring grains. Automated and simultaneous EBSD and EDS maps were generated using Oxford Instruments' Aztec acquisition system, using a fixed *x* and *y* step size for each site in a user-defined grid, varying between 0.1 μm and 8 μm, dependant upon the grain size distribution at each particular site. This approach generated a dataset with high spatial resolution whilst also being time-efficient. Table 1 shows the conditions under which the maps were collected at each site. SE images were obtained to confirm that topographic features present in or around chondrules did not bias the EBSD data and interpretation.

Allende was found to contain abundant matrix grains at the sub-micrometre scale, and so greater spatial resolution was required for accurate analysis of the smaller grains. The Transmission Kikuchi Diffraction (TKD) technique utilised electron transparent samples in the SEM, coupled with conventional EBSD instrumentation, resulting in an order of magnitude improvement in spatial resolution compared to EBSD (sub 10 nm – Trimby et al., 2014). A transmission electron microscope (TEM) foil was extracted containing a sectional view of a chondrule rim and adjacent matrix material. The sample was created using a focused ion beam (FIB) SEM (Carl Zeiss Auriga) at the Australian Centre for Microscopy & Microanalysis (ACMM), Sydney. To protect the sample from gallium beam damage a platinum layer was deposited and the sample lifted out using a Kleindiek micromanipulator. The section was mounted on a molybdenum grid using platinum welds and the sample was further thinned to 100 nm. The TEM foil was analysed using TKD and EDS on a Carl Zeiss Ultra Plus FEG SEM at the ACMM, Sydney. TKD and EDS data were acquired using an Oxford Instruments AZtec system with a Nordlys-Nano EBSD detector and an X-Max 20 mm^2 SDD EDS detector and with an accelerating voltage of 30 kV.

EBSD data were processed using the Oxford Instruments HKL software package Channel 5.12, generating crystallographic orientation maps, phase maps and pole figure plots that were compared across each site. In this process, noise reduction and data processing were done in a very similar manner to that described in Watt et al. (2006); isolated misindexed data points were removed using a wildspike correction, and all non-indexed points infilled to a six nearest-neighbour extrapolation. Grains were detected in each map based upon crystallographic orientation, and using a misori-

entation angle of at least 10° between two adjacent pixels to identify grain boundaries. Grains with diameters less than four times the step size were removed to allow for reliable data interpretation, which also removed misindexed points. Grain orientation data from the entirety of each map were plotted on to lower hemisphere, equal area projections as one point per grain to avoid grain size related bias during contouring. In this study, we focused on olivine grains to enable a direct comparison with shock-level studies. Although compositions across the olivine solid-solution can be found in Allende, there was little variation in their crystal structure: EBSD does not discriminate between olivine sub-types, and so all EBSD patterns from olivine were successfully indexed using the 'forsterite' match unit in the HKL database (indexing statistics are given for each region of interest in Table 1).

Low-angle boundaries (LABs) can form due to a number of mechanisms. Both orientation selective dissolution and grain growth in a vein setting may result in grains of similar orientation forming apparent low-angle sub-grain boundaries where their edges meet. Neither of these mechanisms are likely given the primitive nature of Allende. LABs can also be a geometric consequence of grain impingement between two similarly-orientated grains (Wheeler et al., 2001). Where grains preserve crystallographic variations that cannot be attributed to fractures, it was assumed that they were deformed crystal-plastically (via dislocation creep and recovery). Dislocation slip systems were then inferred assuming pure tilt boundary geometry, whereby an orthogonal relationship exists between the rotation axis of low-angle boundaries, pole to the dominant dislocation slip plane and slip direction (e.g. Prior et al.) combined with cumulative dispersion of crystallographic poles in each grain. As the rotation axes did not lie in the plane perpendicular to the LAB trace, we can infer these boundaries formed due to tilt and did not show evidence of twist-boundary formation. Further information regarding this test can be found in the methods section of Gray (2013). LAB planes were inferred from traces in map view and contain misorientation axes. Axes of misorientation were identified based upon axes of pole dispersions in lower hemisphere plots. The related slip systems were then inferred using geometric criteria: a slip-system is composed of both a slip plane and direction; the pole to the slip plane is contained within the low-angle boundary with the misorientation axis, and the slip direction is perpendicular to that plane.

The numerical simulations described by Bland et al. (2014) provided peak and post-shock stress (pressure), temperature and porosity distributions for numerous impactor velocity and initial matrix/chondrule abundance scenarios. To compare more directly the data from our study with the simulation predictions, shear strain distribution maps were produced from the simulation outputs. The tracer particle positions in the simulations were used to derive the second invariant of the total strain tensor using the method described by Bowling (2015). This invariant measure of shear deformation includes the net elastic plus plastic strain at the end of the simulations (i.e., the finite strains). As the elastic–plastic rheological model used in the numerical simulations to represent the chondrules and matrix incorporates a yield strength that is pressure, strain and temperature dependent, it can describe (very approximately) both brittle (low pressure) and ductile (high pressure) deformation. In reality, olivine rheology is more complex in detail, and involves anisotropic elastic and plastic properties. Furthermore, as the matrix of fine grains and interstitial pore space is treated as a uniform continuum in the simulations, we note that the strain in the matrix is the bulk strain of the grains and the pore spaces, which will be largely accommodated by grain rearrangement and pore collapse, rather than permanent deformation of individual matrix grains: i.e., 'details' of the strain in individual matrix grains is not resolved. Despite these limitations we expect the qualitative distribution of shear strain observed in the numerical simulations to provide an informative comparison with permanent strain derived from our crystallographic orientation analysis.

3. Results & analysis

Olivine in the chondrules in Allende was commonly Mg-rich, i.e., forsteritic, whereas matrix olivine was more Fe-rich, i.e., fayalitic (Fig. 1). Prior studies calculate proportions of chondrule and matrix to be approximately 60% and 40% respectively (McSween, 1979; Macke et al., 2011). The chondrules, AOAs and Calcium–Aluminium Inclusions (CAIs) were also weakly elongate as is shown in Fig. 1. Within the 1.28 cm^2 sample area of our sample, we observed a large variation in matrix grain size (Supplementary Figs. 1–4). EBSD analyses resolved forsterite, diopside, and enstatite, which have been recorded previously (Stöffler et al., 1991). As expected, this sample was highly texturally heterogeneous, containing different chondrule types and a wide range of matrix grain shapes and sizes. We found no evidence of high-pressure polymorphs, such as ringwoodite, that would indicate high shock pressures.

3.1. Chondrules and AOAs

Three chondrule and AOA sites were examined (Fig. 2), and are collectively referred to as 'chondrule sites' from this point forward. For each site, a 'cumulative misorientation map' was generated such that each datapoint was coloured for the minimum mismatch in crystallographic orientation (minimum misorientation) from a user-specified point within the grain (all sites, Fig. 2c). These maps resolved misorientations to a precision based upon the fit quality of the indexing solutions (mean angular deviation (MAD), Table 1) in each map, which were typically reliable down to approximately 0.5° in this study. Each of the chondrules showed very little or no internal deformation in their interior: up to a maximum of 1° in the central parts of the grains. However, the outer 10–30 μm of the chondrule and outermost AOA grains commonly preserved up to 6° of progressive, cumulative misorientation that did not relate to brittle fractures (all sites, Fig. 2c and Fig. 3). This relationship is visible in the local misorientation maps, where each pixel was coloured to reflect mean misorientation with the eight nearest neighbour data points (Fig. 4). Figs. 3 and 4 show that progressive crystallographic misorientations at the edges of the grains are accommodated by many relatively planar LABs, parallel to the grain edge. Fig. 3 demonstrates the deformation at C-1 is cumulative and begins in the outer 30 μm of the grain, reaching maximum deformation at the edge (7–8°). Not only were the highest degrees of strain at the grain edges at each site, but LABs were also generally concentrated at the top and bottom, and to the right of the chondrules and AOA, as indicated by the continuous, cumulative strain at the margins of chondrule C-1, for example (Figs. 2b, 2c, 3 and 4).

3.2. Matrix grains

Maps of crystallographic orientation for olivine at the four matrix sites are shown in Fig. 5. Grain size and shape maps and distribution histograms are presented in Supplementary Figs. 1–4, and matrix grains measured in the TKD section are shown in Fig. 6. It is clear a variety of grain sizes are present; between 0.1 μm and 50 μm. The grains were chiefly subhedral and lath-shaped, characterised as having an aspect ratio greater than 2:1 in 2D. A wide range of intragrain misorientation characteristics were observed at a very fine scale in matrix grains; up to 20° of internal deformation across a 20 μm grain was recorded at site M-2, with as little

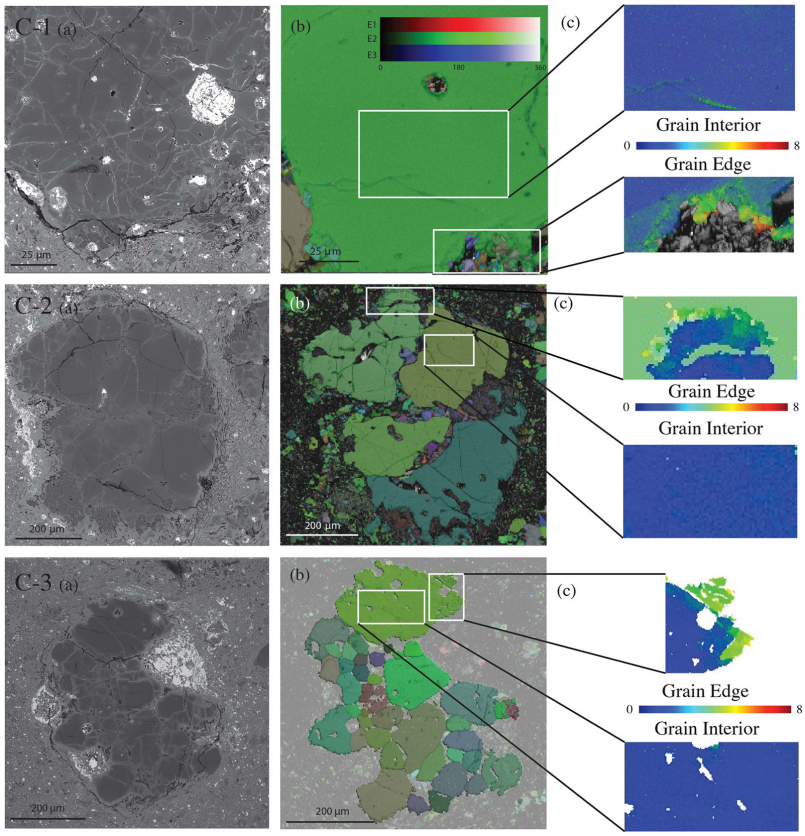

Fig. 2. Chondrule/AOA sites C-1, C-2 and C-3 respectively. (a) Backscatter Electron (BSE) images, (b) Euler maps of each site, showing the orientation of each grain in terms of the three Euler angles, and (c) texture component maps showing a vast increase in deformation at grain edges when compared to grain interiors (scale bar is shown in degrees °).

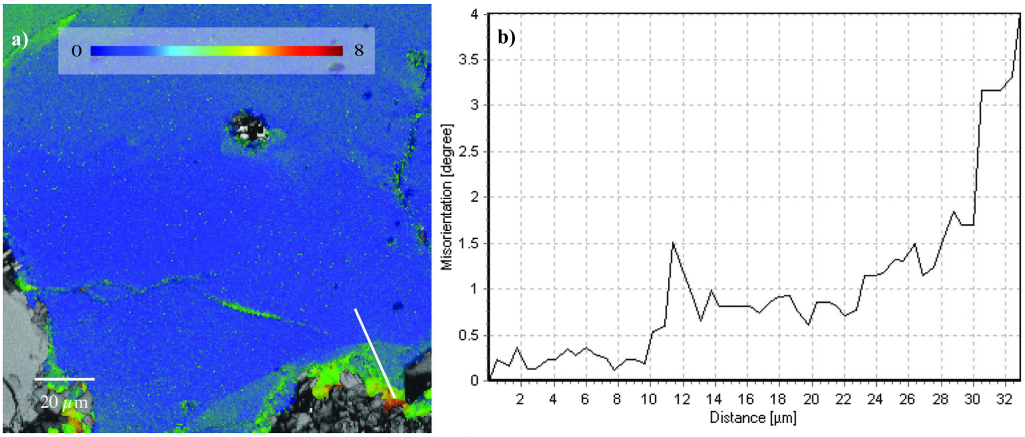

Fig. 3. (a) Map of texture component for chondrule at C-1. White transect line is shown through lower outer edge of the chondrule. (b) Misorientation profile for the white transect line in (a) demonstrates the gradual increase in orientation deviation in an outwards direction from the innermost point of the transect. This confirms the outer edges of chondrules deform gradually and cumulatively from the inner to outer points along the transect.

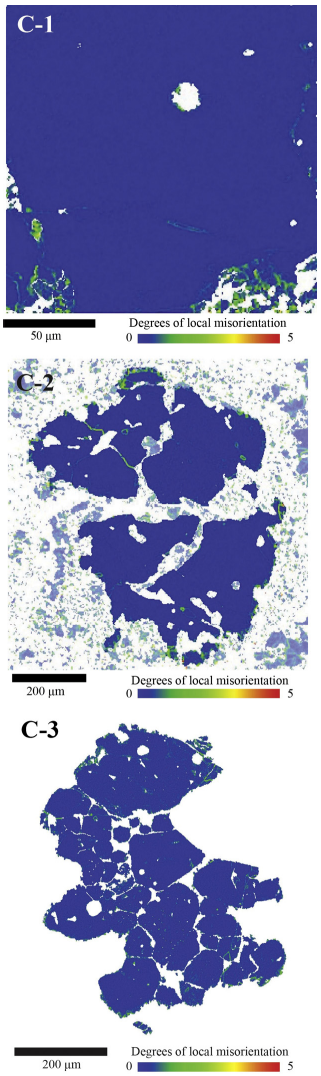

Fig. 4. Local misorientation maps of the chondrule/AOA sites. Each pixel is colour coded to reflect its degree of misorientation from the surrounding 8 pixels.

as 2° internal deformation across a selection of grains at site M-1 (Figs. 5 and 6). Whilst a wide range of values were recorded, average internal deformation was high, with the majority of values in the 8–15° range. It is important to note that in contrast to chondrules, intragrain deformation was observed throughout the full length of the matrix grains, and the magnitude of deformation is consistently greater in all cases.

At sites M-1 and M-3, the trace of planar LAB orientations were measured relative to the map x–y reference frame plotted onto rose diagrams (Fig. 7). The rose plots reveal a dominant trend of the LABs, preferentially aligned with map y direction (i.e., circa 0° and 180° in Fig. 7). This is significant because aligned LABs indicate a relatively consistent applied stress field at the scale of the observations, such as those produced in controlled olivine deformation experiments by Kohlstedt and Goetze (1974). The spatial density of low-angle boundaries was more consistent throughout the matrix grains when compared with chondrule sites; where chondrules and AOAs have a higher density of LABs at their edges, those found in matrix grains were not confined to the grain edges and were present throughout the grain area (Figs. 5 and 6). This is consistent with findings of experimentally stressed olivine crystals; undulose extinction along the grains indicates multiple, similarly oriented low-angle boundaries are present, accommodating changes in crystallographic orientation (Kohlstedt and Goetze, 1974; Fliervoet et al., 1999).

The matrix sites also presented a range of porosities. In some locations, grains appeared very compact with an extremely low porosity (e.g. M-2), whereas areas of M-1 and M-4 appeared more porous with lower indexing rates over the whole region-quantification of this porosity is currently a work in progress. It is important to recall that images at each site were collected at different image resolutions, allowing for maximum efficiency and coverage whilst maintaining the high indexing ratios (Table 1). As some grains were smaller than the specified step-size for imaging each site, this may have resulted in non-indexing of those grains, making the EBSD-inferred porosity of the region incorrect. In light of this, secondary electron images were obtained (Supplementary Fig. 5) for each matrix site, and these confirmed and qualified the porosity variations implied in the EBSD maps.

3.3. Slip systems

Based upon the misorientation axes observed from the EBSD maps we have inferred the likely slip-systems that have contributed to the LABs in chondrules, AOA grains and matrix grains including those within the TKD data. C-1 and C-3 had a misorientation axis of the [100] (a-axis), while C-2 had misorientation along the [010] (b-axis) (Fig. 8). Matrix grains largely had misorientation axes of [010] (b-axis) whilst one examined grain at M-3 had a misorientation axis of [100] (a-axis). EBSD, BSE and SE images indicated that the LABs occur within grains and so it was assumed they result from intragrain plasticity, which would have required high stresses. Chondrule site C-3 (Fig. 7c) displayed evidence of two different slip systems; the misorientation axis was [100] in both cases, but one slip system comprised slip in the [001] direction along the (010) plane, and the other involved slip in the [010] direction along the (001) plane. A variety of slip systems were inferred across each of the sites; of the 9 examples found, matrix slip systems were most commonly (001)[100] (slip in the (001) direction along the [100] plane), with occurrences of other common systems at each site. Chondrule grain slip systems were more widely varied and include (001)[010], (001)[100] and (010)[100] throughout the sites.

3.4. Strain distribution observations

The qualitative distribution of strain observed in chondrules and matrix is consistent with numerical simulations results (Fig. 9). In the simulated chondrules, the predicted mean strain is low, but localised near their margins for 1.0 and 1.5 km/s cases (Figs. 9a and b), whereas strain is higher and distributed throughout the chondrules for the 2 km/s case (Fig. 9c). In all simulated impactor velocity scenarios, the matrix strain is always higher than within the chondrules, with an increase in mean strain with impactor velocity (Fig. 9). Strain in the matrix is typically more intensely developed immediately adjacent to the chondrules, most commonly with an eccentric distribution and asymmetric strain shadows (Fig. 9). All of the simulations predict strong gradients in matrix strain over the micrometre scale (Fig. 9).

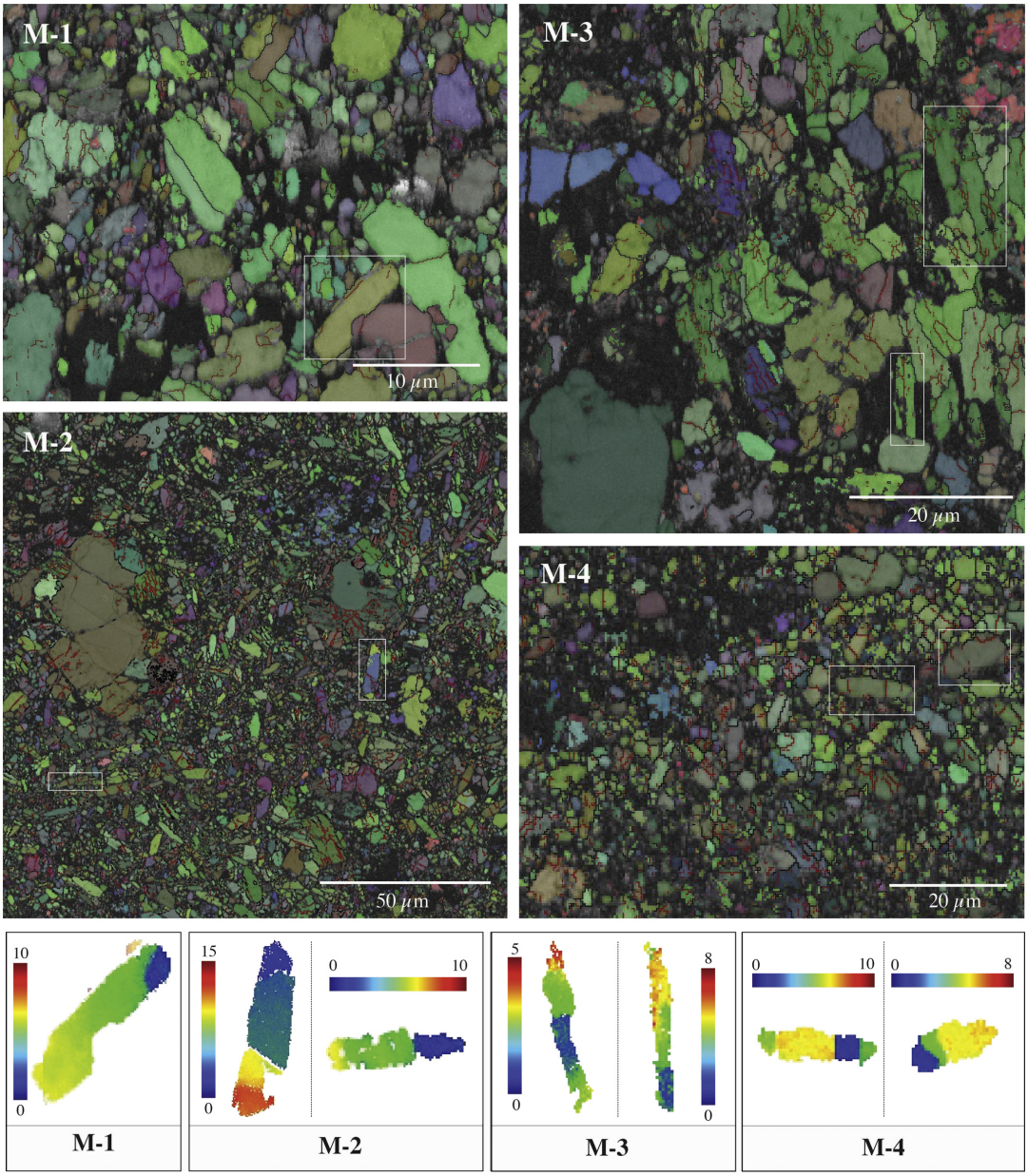

Fig. 5. Four matrix sites (M-1–4) shown using Euler maps. White boxes in each image refer to laths displayed in lower panel; texture maps of individual grains demonstrate the extent of deformation that has occurred throughout the full length of the grain. Scale bar shows degrees (°) of deformation from pre-defined unstrained point of grain (blue region).

4. Discussion

Previous work has shown that Allende has a weak but prominent fabric throughout, with an alignment of the short < 100 > axis of fayalitic olivine grains (Watt et al., 2006). Our study confirmed the weak fabric, albeit with varying alignments (Supplementary Figs. 1–4 and 6). Chondrules, AOAs, CAIs and larger grains are elongate in the vertical orientation, indicative of a horizontal compaction orientation in the plane of the images (Fig. 1). However, we also observed a significant difference in spatial distri-

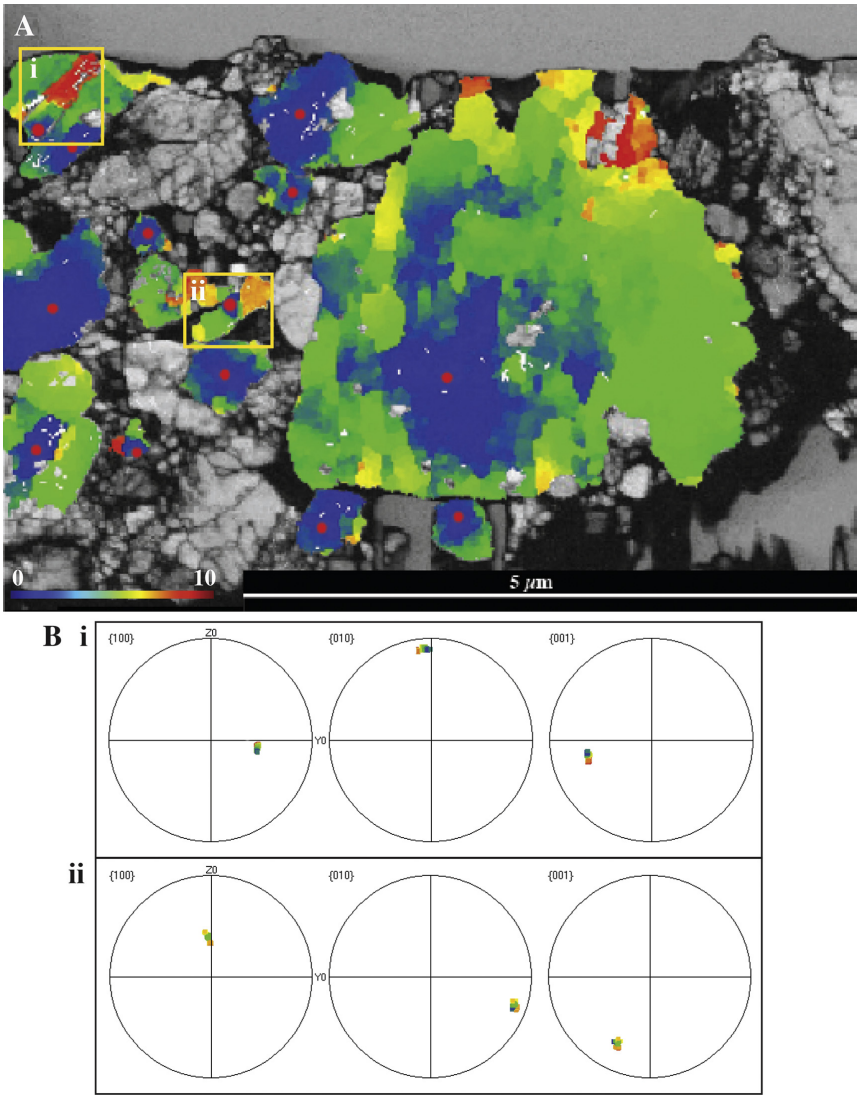

Fig. 6. EBSD image of a TKD section of Allende (A). Greyscale image is the band contrast map, indicating the quality of the patterns obtained in imaging by the brightness of the colours (i.e. white/light greys = good band contrast and pattern quality). Colour overlay demonstrates the amount of crystallographic orientation deviation in degrees from user-defined reference points (red dots) in selected grains. Lower-hemisphere, equal area plots show dispersion of each crystallographic axis within the grain (B).

bution and density of deformation between chondrule and matrix olivines: an absence of deformation of chondrule interiors, minor crystal-plastic deformation at the edges of chondrule grains (up to 6° misorientation ductile strain in the outer 20 μm of these grain edges), and moderate yet heterogeneous crystal-plastic deformation throughout matrix grains (e.g., 20° misorientation along the length of a 20 μm grain). The low-angle boundaries in the matrix grains also have a preferential alignment (their traces are vertical in the plane of the images) whereas those in the chondrules rims are generally parallel to the edge of the grains (Fig. 7).

A large portion of the deformation of chondrule grain edges is concentrated at the top, bottom and to the right of the chondrules. Further to this, deformation is absent on the left and less prominent on the right of these grains when compared with the top and bottom areas. Coupled with an absence of matrix grain deformation to the left of such grains, a compressional 'shadow' has been generated. It is possible that compaction of pores against the boundary of the grain normal to the compacting direction generated enough heat such that these areas of the grains were compressed but show no evidence of strain. The top and bottom of the

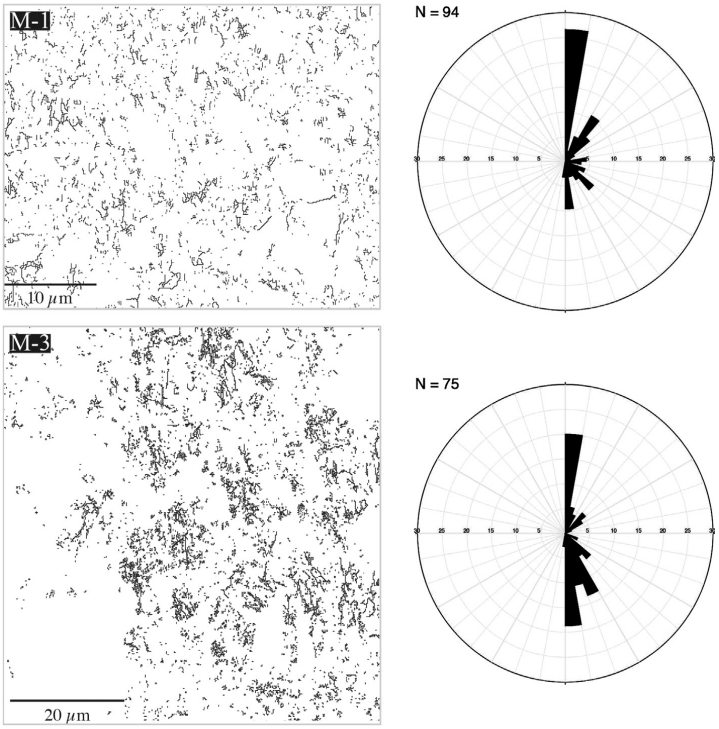

Fig. 7. Low-angle boundaries (1°–10°) are presented for matrix sites M-1 and M-3 on the left. The orientations of these boundaries are plotted onto rose diagrams on the right, demonstrating the preferential orientation for both sites is roughly N–S, or at 0° and 180°.

chondrules may not have experienced the same degree of compaction and, therefore, less pore collapse and subsequent heating would have occurred (Davison et al., 2010). Here, there may not have been sufficient heat to deform these regions without strain being evident. However, the lack of evidence for melting observed at this scale indicates this may not be the case, and therefore other possibilities, such as shear heating, should be considered. Given that the presence of strain 'shadows' on the left side of the larger grains, it is probable that a similar shadow would be evident in the matrix as a higher porosity relative to surrounding matrix areas. Whilst the sample has lost a large portion of it's initial porosity (∼50%), the compaction process is very unlikely to generate uniformly low porosities throughout the matrix due to the bimodal grain size distribution of the material, and therefore porosity heterogeneities are to be expected.

The microstructural analysis clearly shows that deformation was spatially heterogeneous, and indicative that Allende experienced locally heterogeneous (stress, temperature) conditions. Olivine deforms crystal-plastically in response to stress at high temperatures. This is achieved by the activity of several possible dislocation slip systems, and it is well established that distinct slip systems operate in different environmental conditions (e.g. stress, temperature, H_2O activity) for terrestrially deformed olivine (Karato et al., 2008). Operation of different slip systems produces different types of crystallographic fabric, which can be identified by trends in clustering in lower-hemisphere, equal-area plots of the EBSD data (Karato et al., 2008). Therefore, quantification of fabrics may be used to infer temperature and pressure conditions at the time of fabric generation. Using this approach, we can deduce that the variable slip-systems identified within the chondrules and AOA probably reflected heterogeneous stress and temperature conditions throughout the sample. Most slip systems within matrix grains are indicative of deformation under dry and low-moderate stress conditions, with some variation to higher-stress slip systems (Karato et al., 2008). M-1 and M-2 presented a weak A-type fabric when compared with Karato et al.'s (2008) classification system, where M-3 displayed a D-type fabric. The fabric types indicated high temperatures (>1470 K) and low stresses (0–350 MPa) at sites M-1 and M-2, and moderate temperature (1200–1470 K) and stress (>350 MPa) conditions at M-3 (Karato et al., 2008). Sites M-1 and M-2 were situated away from chondrules, whereas M-3 was very close to and between two chondrules and so higher stresses may be expected. However, the lack of high-pressure phases and mosaicism of LABs in the sample limit the shock pressures at time of deformation to below 10 GPa (Langenhorst, 2002). There has been some speculation that the presence of pores prior to compaction allows for higher-temperature slip-systems to activate in olivine when compared with zero-porosity samples (Goetze and Poirier, 1978). Therefore, it is possible that higher-temperature slip-systems may have activated in highly porous regions of the sample.

The microstructures observed in this sample of Allende and other evidence can be used to evaluate several different models for the compaction of Allende. An early theory highlighted a static force, such as burial compaction due to gravity, as a possible source of compression (Fujimara et al., 1983). The microstructural features we have observed in this study do not indicate that this is the compaction mechanism; the asymmetry in large grain deformation

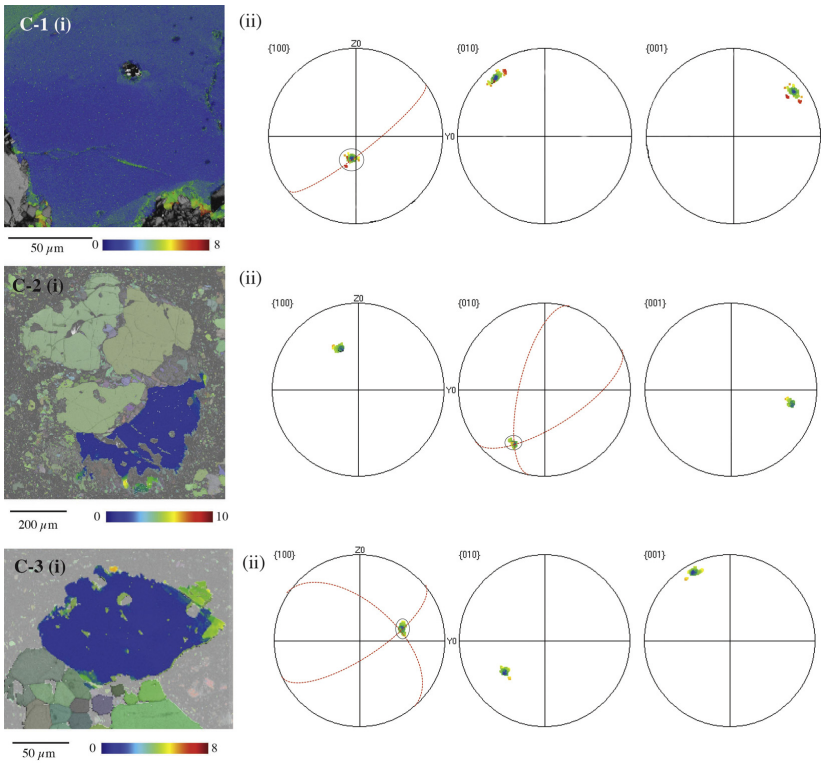

Fig. 8. Texture component maps of Chondrule/AOA site C-1, C-2 and C-3 (i). This demonstrates the degrees of rotation in Euler angles from a central, unstrained point within the presented grain. This data is plotted on lower hemisphere, equal area, stereographic projections (ii). At each site the orientation of the low-angle boundaries is shown on the equal area plots as red lines for each highlighted grain in the maps. At site C-1 and C-3, the misorientation axis is the [100] axis, and at C-2 the misorientation axis is [010]. At sites C-2 and C-3 two sets of low-angle boundaries are observed and cause a two-way dispersion in the data.

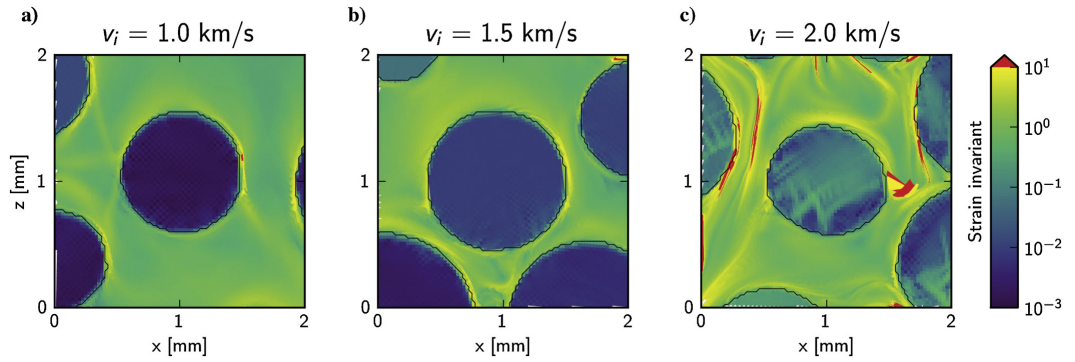

Fig. 9. Finite invariant shear strain distribution maps derived from numerical simulations for three impact speeds: a) $v = 1.0$ km/s; b) 1.5 km/s; c) 2.0 km/s, which generate bulk shock pressures of approximately 1, 1.7 and 3 GPa, respectively. In these simulations chondrules are treated as single grains and the matrix of fine grains and pore space is treated as a continuum. Hence, while simulated strains in the chondrules are expected to be comparable to those observed inside chondrule grains, the strain distribution within the matrix is the bulk strain of both matrix grains and pore space combined and is not directly comparable to strain observed in individual matrix grains.

indicates localised compaction from one direction, not multiple directions. The slip systems that activated within the grains are widely varied, but some require heating beyond 1450 °C; in the case of lithostatic compaction, heating is expected to be continuous for the duration of the slow compaction process as pores are continuously destroyed. If temperatures of 1450 °C were achieved for any length of time, widespread melting would have occurred, which has not been observed. A lack of overprinting in the mi-

crostructures also implies all structural features were generated at the same time; compaction due to lithostatic forces would result in microstructures forming over longer time periods, and therefore we might expect to see cross-cutting deformation relationships. At a larger scale, Allende's tensile strength is approximately 28 MPa in its currently compressed form (Svetsov et al., 1995). This strength may be surpassed in the centre of a planetary body with a radius greater than approximately 300 km and, therefore, lithostatic pressure may result in the compaction observed if Allende sampled the centre of a planetary body. However, this mechanism is unable to explain the asymmetry of deformation in the chondrules and distribution of porosity and crystal-plasticity in the matrix grains. Porosity reduction under these conditions should have orthorhombic symmetry. Overburden-related stresses in small planetary bodies are unlikely to be high enough to activate slip systems responsible for the observed fabrics in the matrix olivine in Allende. Furthermore, Allende is a primitive meteorite of petrologic type 3, and if it originates from the centre of a planetary body, it would not remain in a primitive state. A number of CO, CR and CM meteorites have lower porosities than Allende (Macke et al., 2011), and so if the same principle applies to their deep origin on their respective parent bodies, many asteroids would have been completely destroyed to create a number of meteorites in our collections. The oxidised CV subclass (e.g. Allende) is significantly less compacted than the reduced CV subclass (20% porosity compared with ∼5% porosity) (Macke et al., 2011), but the oxidised samples present significantly higher metamorphism. We would expect the inverse relationship to be evident where lithostatic overburden forces are dominant. There are currently asteroids in our solar system that appear to be of low bulk density when compared with their likely meteorite equivalents (Britt et al., 2002); this suggests that these bodies are still highly porous, and so a planet-wide compaction process is further unlikely. Gravitational compressional forces generate gradual and continuous heating and were likely involved in the early heating of the body and initial stages of lithification. Therefore, we believe that it is improbable that lithostatic overburden could have generated the compressional microstructures, but possibly contributed to overall lithification.

Consequently, we consider the case of dynamic and rapid compressional forces during impact events in the creation of the aforementioned microstructures. The asymmetric distribution of strain (i.e., crystal-plastic deformation and porosity reduction) around chondrules and AOA grains, and highly heterogeneous stresses and temperatures inferred from operative slip systems are consistent with numerical simulations of impacts at these scales (Davison et al., 2010; 2014; Bland et al., 2014). We observed a varied yet generally greater intensity of deformation in small matrix grains when compared with large chondrule and AOA grains; given a rapid loss of pore space upon compaction generates a temperature increase, the matrix would likely experience more heat than chondrules, and consequently would be more deformed relative to the large low-porosity grains. The preferential orientation of LAB planes and crystallographic preferred orientation in the matrix grains can be readily explained by differential heating between chondrules and matrix during a single moderate-strong impact event, which would consequently reduce bulk porosity. Microstructural evidence also indicates an instantaneous and rapid compressional force is responsible.

Allende has a lack of macrostructure shock features that previously suggested it was unaffected by impact, however as a result of porosity loss, any further impacts post-compaction are unlikely to cause substantial compression or generate compaction-related shock features (Sharp and DeCarli, 2006; Davison et al., 2010; Bland et al., 2014). Compaction via impact is a much simpler scenario when compared with lithostatic overburden; it is unlikely that a large number of asteroids were completely destroyed to produce the samples in our vast meteorite collections, and low-velocity collisions into small planetary bodies are much more common and easier to achieve (Housen and Holsapple, 2011; Beitz et al., 2013). At a planetary scale, samples originating closer to the asteroid surface would show more evidence of metamorphism when compared with samples at depth on the parent body following impact processing; this is reflected in the properties of oxidised and reduced CV class meteorites, where higher porosities and significant metamorphism are observed in oxidised samples compared with reduced samples. *In situ* evidence of impacts into highly porous bodies has been found on C-type asteroid Mathilde; whilst CV meteorites may not originate from C-type asteroids (Bell, 1988), the principal of impacts into early, highly porous bodies is well supported by this prior research (Housen et al., 1999; Cheng and Barnouin-Jha, 1999; Housen and Holsapple, 2011). Furthermore, conclusions from impact compaction studies that correlate compaction pressures with overall shock stages for each carbonaceous chondrite class support our findings (Weidenschilling and Cuzzi, 2006; Beitz et al., 2013).

Shock wave attenuation into a polymineralic and porous media has been shown to induce shear heating at grain boundary contacts (Gillet and Goresy, 2013). We predict Allende to have experienced no more than 10 GPa based on the absence of high-pressure polymorphs and mosaicism in the olivine grains. At this pressure, we expect that Allende would have begun to melt at 1600 °C, but at lower pressures heating to 1150 °C could have induced melting (Agee et al., 1995). The microstructural features presented indicate that these grains did not experience such temperatures, but shear heating may have been more pronounced at the grain boundaries, resulting in grain sintering, lithification and strengthening of Allende. The geometry of deformation seen in the matrix does show potential evidence of shear processing (Fig. 5), whereby LABs parallel to the direction of compression have formed. Additionally, the lower edges of C-1 and C-3 (Fig. 2) appear fragmented from the rest of the surrounding material, which could indicate that shear-induced disaggregation has occurred. Experiments examining the sintering behaviour of olivine have found that it is favoured where a fine-grained (micrometre-scale) aggregate is rapidly heated to high T: an analogous scenario to that encountered by a high porosity matrix during impact-induced compaction (Cooper and Kohlstedt, 1984). Weak evidence of this can be found in Allende (Fig. 6), where grains have a higher amount of deformation at their contact margin. However, understanding the intricacies of lithification in this sample is beyond the scope of this paper and should be examined at higher resolution in future work.

The local and regional pressure and temperature anomalies over distances of 10–100 μm can be attributed to interactions of shock waves in the bimodal, porous medium, resulting in heterogeneous deformation. The simulations described by Bland et al. (2014) reveal that low-velocity impacts of 2 km/s in a material of 70% matrix, 30% chondrule result in peak pressures in chondrules of ≈6.5 GPa, but with predicted post-shock heating temperatures of 370 K in chondrules, and 1100 K in the matrix. These models also yield large disparities in peak pressure between matrix and chondrules; chondrule interiors realistically experience 4–5 GPa, chondrule edges approximately up to 8 GPa, and over only 100 μm within the matrix, a pressure range of 7–18 GPa may arise (Bland et al., 2014). Whilst peak pressures cannot be directly compared with our data, comparisons with the modelled first order approximations of corresponding strain distribution are more analogous. Acknowledging the limitations of the simulations to be able to capture the complexity of olivine rheology exactly, the strain in the modelled 1.0 km/s and 1.5 km/s scenarios (<2 GPa bulk shock pressure) show the strongest similarity to the observed chondrule deformation from EBSD mapping (Figs. 2, 3 and 4). First-order predictions of the higher intensity strain in the matrix are also

consistent with observations from EBSD mapping (Figs. 5 and 6). These outcomes suggest the modelling accurately predicts the response of a bimodal sample to compression and we infer impacts are responsible for the petrographic features described.

5. Conclusions

EBSD analysis in this study of Allende has revealed the following:

1. Crystal-plastic deformation at the margins of chondrule grains, commonly with an asymmetric distribution (in the context of all figures shown).
2. A lack of crystal-plastic deformation within chondrule interiors ($<1°$).
3. High degrees of crystal-plastic deformation throughout matrix olivine grains (up to 20° of misorientation). This deformation was spatially heterogeneous, with asymmetric zones of intense deformation close to chondrules.
4. A dominance of LABs in matrix olivine grains with strongly preferred boundary plane orientations in the reference frame of the sample surface.

We conclude Allende has been compacted via impact processing. Planar shock modelling shows a low impact velocity of a few km/s into a 50% bulk porosity target material is sufficient to produce the features present. The effect of the temperature difference between the two components following impact is large and significant; however, such expected low pressures (1–1.3 GPa, Bland et al., 2014) are unlikely to have produced petrographic shock evidence traditionally observed in chondrules. Matrix grains are the key to understanding the magnitude of the compaction-inducing impact, as they show preservation of compaction-related deformation and provide a more accurate representation of peak temperatures and stresses.

Acknowledgements

This work was funded by the Australian Research Council via their Australian Laureate Fellowship programme (FL110100074) (PAB). This research was supported by the Curtin International Postgraduate Research Scholarship awarded to LF and LD, and GKB acknowledges support from Curtin University via their Research Fellowship scheme. GSC and TMD acknowledge funding from the UK Science and Technology Facilities Council STFC grant ST/J001260/1. The authors would also like to acknowledge the technical assistance and use of facilities at John de Laeter Microscopy centre, at Curtin University; the Australian Synchrotron XFM beamline, and the University of Sydney node of the Australian Microscopy & Microanalysis Research Facility: Sydney Microscopy & Microanalysis. The authors would like to thank the handling editor and anonymous reviewer for their constructive comments in the review process.

Appendix A. Supplementary material

Supplementary material related to this article can be found online at http://dx.doi.org/10.1016/j.epsl.2016.07.050.

References

Agee, C.B., Li, J., Shannon, M.C., Circone, S., 1995. Pressure-temperature phase diagram for the Allende meteorite. J. Geophys. Res., Solid Earth (1978–2012) 100 (B9), 17725–17740.

Bland, P.A., Howard, L.E., Prior, D.J., Wheeler, J., Hough, R.M., Dyl, K.A., 2011. Earliest rock fabric formed in the solar system preserved in a chondrule rim. Nat. Geosci. 4 (4), 244–247.

Bland, P.A., Collins, G.S., Davison, T.M., Abreu, N.M., Ciesla, F.J., Muxworthy, A.R., Moore, J., 2014. Pressure–temperature evolution of primordial solar system solids during impact-induced compaction. Nat. Commun. 5, 5451.

Beitz, E., Guettler, C., Nakamura, A.M., Tsuchiyama, A., Blum, J., 2013. Experiments on the consolidation of chondrites and the formation of dense rims around chondrules. Icarus 225 (1), 558–569.

Bell, J.F., 1988. A probable asteroidal parent body for the CO or CV chondrites. Meteoritics 23, 256–257.

Blum, J., 2003. The structure of planetesimals in the solar nebula (abstract #5152). Meteorit. Planet. Sci. 38 (Suppl.), A83.

Bowling, T.J., 2015. Global surface modification of asteroid 4 Vesta following the Rheasilvia impact. PhD thesis. Purdue University.

Brenker, F.E., Palme, H., Klerner, S., 2000. Evidence for solar nebula signatures in the matrix of the Allende meteorite. Earth Planet. Sci. Lett. 178, 185–194.

Britt, D.T., Yeomans, D., Housen, K., Consolmagno, G., 2002. Asteroid density, porosity, and structure. In: Asteroids III.

Cain, P.M., McSween, H.Y., Woodward, N.B., 1986. Structural deformation of the Leoville chondrite. Earth Planet. Sci. Lett. 77, 165–175.

Cheng, A.F., Barnouin-Jha, O.S., 1999. Giant craters on Mathilde. Icarus 140 (1), 34–48.

Consolmagno, G.J., Britt, D.T., Stoll, C.P., 1998. The porosities of ordinary chondrites: models and interpretation. Meteorit. Planet. Sci. 33 (6), 1221–1229.

Cooper, R.F., Kohlstedt, D.L., 1984. Sintering of olivine and olivine-basalt aggregates. Phys. Chem. Miner. 11 (1), 5–16.

Cuzzi, J.N., Weidenschilling, S.J., 2006. Particle-gas dynamics and primary accretion. In: Lauretta, D.S., McSween Jr., H.Y. (Eds.), Meteorites and the Early Solar System II. Univ. of Arizona, Tucson, pp. 353–381.

Cuzzi, J.N., Hogan, R.C., Shariff, K., 2008. Toward planetesimals: dense chondrule clumps in the protoplanetary nebula. Astrophys. J. 687, 1432.

Davison, T.M., Collins, G.S., Ciesla, F.J., 2010. Numerical modelling of heating in porous planetesimal collisions. Icarus 208 (1), 468–481.

Davison, T.M., Collins, G.S., Bland, P.A., 2014. Mesoscale numerical modelling of compaction of primitive solar system solids in low-velocity collisions. In: 45th Lunar and Planetary Science Conference. Abstract #2718.

Dyl, K.A., Cleverley, J.S., Bland, P.A., Ryan, C.G., Fisher, L., Hough, R.M., 2014. Quantified, whole section trace element mapping of carbonaceous chondrites by synchrotron X-ray fluorescence microscopy: 1. CV meteorites. Geochim. Cosmochim. Acta 134 (4), 1176–1180.

Fisher, L.A., Fougerouse, D., Cleverley, J.S., Ryan, C.G., Micklethwaite, S., Halfpenny, A., Hough, R., Gee, M., Paterson, D., Howard, D.L., Spiers, K., 2014. Quantified, multi-scale X-ray fluorescence element mapping using the Maia detector array: application to mineral deposit studies. Miner. Depos. 50 (6), 665–674.

Fliervoet, T.F., Drury, M.R., Chopra, P.N., 1999. Crystallographic preferred orientations and misorientations in some olivine rocks deformed by diffusion or dislocation creep. Tectonophysics 303 (1), 1–27.

Friedrich, J.M., Rubin, A.E., Beard, S.P., Swindle, T.D., Isachsen, C.E., Rivers, M.L., Macke, R.J., 2014. Ancient porosity preserved in ordinary chondrites: examining shock and compaction on young asteroids. Meteorit. Planet. Sci. 49 (7), 1214–1231.

Fujimara, A., Kato, M., Kamazawa, M., 1983. Preferred orientation of phyllosilicate (001) in matrix of Murchison meteorite and possible mechanisms of generating the oriented texture in chondrites. Earth Planet. Sci. Lett. 66, 25–32.

Gattacceca, J., Rochette, P., Denise, M., Consolmagno, G., Folco, L., 2005. An impact origin for the foliation of chondrites. Earth Planet. Sci. Lett. 234 (3), 351–368.

Gillet, P., Goresy, A.E., 2013. Shock events in the solar system: the message from minerals in terrestrial planets and asteroids. Annu. Rev. Earth Planet. Sci. 41, 257–285.

Goetze, C., Poirier, J.P., 1978. The mechanisms of creep in olivine [and discussion]. Philos. Trans. R. Soc., Math. Phys. Eng. Sci. 288 (1350), 99–119.

Gray, E.M., 2013. Deformation of Earth's upper mantle: insights from naturally occurring fabric types. Diss. PhD thesis. Curtin University, 327 pp.

Hanna, R.D., Ketcham, R.A., Zolensky, M., Behr, W.M., 2015. Impact-induced brittle deformation, porosity loss, and aqueous alteration in the Murchison CM chondrite. Geochim. Cosmochim. Acta 171, 256–282.

Housen, K.R., Holsapple, K.A., Voss, M.E., 1999. Compaction as the origin of the unusual craters on the asteroid Mathilde. Nature 402 (6758), 155–157.

Housen, K.R., Holsapple, K.A., 2011. Ejecta from impact craters. Icarus 211 (1), 856–875.

Johansen, A., Youdin, A., Mac Low, M.-M., 2009. Particle clumping and planetesimal formation depend strongly on metallicity. Astrophys. J. Lett. 704 (2), L75–L79.

Karato, S., Haemyeong, J., Katayama, I., Skemer, P., 2008. Geodynamic significance of seismic anisotropy of the upper mantle: new insights from laboratory studies. Annu. Rev. Earth Planet. Sci. 36, 59–95.

Kohlstedt, D.L., Goetze, C., 1974. Low-stress high-temperature creep in olivine single crystals. J. Geophys. Res. 79 (14), 2045–2051.

Langenhorst, F., 2002. Shock metamorphism of some minerals: basic introduction and microstructural observations. Bull. Czech Geol. Surv. 77 (4), 265–282.

Macke, R.J., Britt, D.T., Consolmagno, G.J., 2011. Density, porosity, and magnetic susceptibility of achondritic meteorites. Meteorit. Planet. Sci. 46 (2), 311–326.

McSween Jr., H.Y., 1979. Are carbonaceous chondrites primitive or processed? A review. Rev. Geophys. Space Phys. 17 (1059), 1075.

Nakamura, T., Tomeoka, K., Takeda, H., 1992. Shock effects of the Leoville CV carbonaceous chondrite: a transmission electron microscope study. Earth Planet. Sci. Lett. 114, 159–170.
Rubin, A., 2004. Postshock annealing and postannealing shock in equilibrated ordinary chondrites: implications for the thermal and shock histories of chondritic asteroids. Geochim. Cosmochim. Acta 68 (3), 673–689.
Scott, E.R.D., Keil, K., Stöffler, D., 1992. Shock metamorphism of carbonaceous chondrites. Geochim. Cosmochim. Acta 56 (12), 4281–4293.
Scott, E.R.D., 2002. Meteorite evidence for the accretion and collisional evolution of asteroids. In: Bottke, W.F., et al. (Eds.), Asteroids III. Univ. of Arizona, Tucson, pp. 697–709.
Sharp, T.G., DeCarli, P.S., 2006. Shock effects in meteorites. In: Lauretta, D.S., McSween Jr., H.Y. (Eds.), Meteorites and the Early Solar System II. Univ. Arizona Press, pp. 653–677.
Stacey, F.D., Lovering, J.F., Parry, L.G., 1961. Thermomagnetic properties, natural magnetic moments, and magnetic anisotropies of some chondritic meteorites. J. Geophys. Res. 66, 1523–1534.
Stöffler, D., Keil, K., Scott, E., 1991. Shock metamorphism of ordinary chondrites. Geochim. Cosmochim. Acta 55 (12), 3845–3867.
Svetsov, V.V., Nemtchinov, I.V., Teterev, A.V., 1995. Disintegration of large meteoroids in Earth's atmosphere: theoretical models. Icarus 116 (1), 131–153.
Trimby, P.W., Cao, Y., Chen, Z., Han, S., Hemker, K.J., Lian, J., Liao, X., Rottmann, P., Samudrala, S., Sun, J., Wang, J.T., Wheeler, J., Cairney, J.M., 2014. Characterizing deformed ultrafine-grained and nanocrystalline materials using transmission Kikuchi diffraction in a scanning electron microscope. Acta Mater. 62, 69–80.
Watt, L., Bland, P.A., Prior, D.J., Russell, S.S., 2006. Fabric analysis of Allende matrix using EBSD. Meteorit. Planet. Sci. 41, 989–1001.
Weidenschilling, S.J., Cuzzi, J., 2006. Accretion dynamics and timescales: relation to chondrites. In: Lauretta, D.S., McSween Jr., H.Y. (Eds.), Meteorites and the Early Solar System II. Univ. Arizona Press, pp. 473–485.
Wheeler, J., Reddy, S.M., Cliff, R.A., 2001. Kinematic linkage between internal zone extension and shortening in more external units in the NW Alps. J. Geol. Soc. 158 (3), 439–443.
Zolensky, M.E., Mittlefehldt, D.W., Lipschutz, M.E., Wang, M.S., Clayton, R.N., Mayeda, T.K., Grady, M.M., Pillinger, C., Barber, D., 1997. CM chondrites exhibit the complete petrologic range from type 2 to 1. Geochim. Cosmochim. Acta 61, 5099–5115.

Appendix A2

Author Contributions, Chapter 3:

Defining the Mechanism for Compaction of the CV Parent Body

L.V. Forman[1], P.A. Bland[1], N.E. Timms[1], L. Daly[1], G.K. Benedix[1], P.W. Trimby[2], G.S. Collins[3], and T.M. Davison[3], 2017, Defining the Mechanism for Compaction of the CV Parent Body: Geology, v. 45, no. 6, p.559-562.

[1]Department of Applied Geology, Curtin University, GPO Box U1987, Perth, WA 6845, Australia

[2]Australian Centre for Microscopy and Microanalysis, University of Sydney, Room 234, Madsen Building F09, NSW 2006, Australia

Impact and Astromaterials Research Centre, Department of Earth Science & Engineering, Imperial College London, Prince Consort Road, South Kensington SW7 2BJ, UK

STATEMENT OF AUTHORSHIP

I hereby confirm the primary author, Miss L. V. Forman, conducted the majority of this study and give my permission for this to be included in the candidate's PhD thesis.

MISS LUCY. V. FORMAN

- Lead on planning, data collection and analysis
- Drafted & formatted manuscript

Contribution: *75%* ***Date:*** *22.2.17*

PROF. PHIL BLAND

- Assisted with initial concept
- Manuscript editing

Contribution: *8%* ***Date:*** *23.2.17*

DR. NICK TIMMS

- Assisted with data interpretation
- Manuscript editing

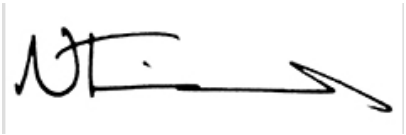

Contribution: *10%* ***Date:*** *23.2.17*

MR LUKE DALY

- Conducted EBSD data collection
- Manuscript editing

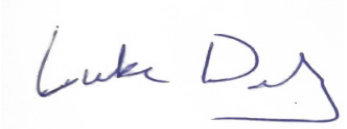

Contribution: *3%* ***Date:*** *22.2.17*

DR. GRETCHEN BENEDIX

- Manuscript editing

Contribution: *1%* ***Date:*** *28.2.17*

DR. PATRICK TRIMBY

- Assisted with EBSD data collection

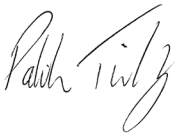

Contribution: *1%* ***Date:*** *24.2.17*

DR. GARETH COLLINS

- Offered insight from modelling simulations
- Manuscript editing

Contribution: *1%* ***Date:*** *28.2.17*

DR. THOMAS DAVISON

- Offered insight from modelling simulations
- Manuscript editing

Contribution: *1%* ***Date:*** *28.2.17*

THE GEOLOGICAL SOCIETY OF AMERICA®

Defining the mechanism for compaction of the CV chondrite parent body

L.V. Forman[1]*, P.A. Bland[1], N.E. Timms[1], L. Daly[1], G.K. Benedix[1], P.W. Trimby[2], G.S. Collins[3], and T.M. Davison[3]
[1]Department of Applied Geology, Curtin University, GPO Box U1987, Perth, WA 6845, Australia
[2]Australian Centre for Microscopy and Microanalysis, University of Sydney, Room 234, Madsen Building F09, NSW 2006, Australia
[3]Impact and Astromaterials Research Centre, Department of Earth Science & Engineering, Imperial College London, Prince Consort Road, South Kensington SW7 2BJ, UK

ABSTRACT

The Allende meteorite, a relatively unaltered member of the CV carbonaceous chondrite group, contains primitive crystallographic textures that can inform our understanding of early Solar System planetary compaction. To test between models of porosity reduction on the CV parent body, complex microstructures within ~0.5-mm-diameter chondrules and ~10-µm-long matrix olivine grains were analyzed by electron backscatter diffraction (EBSD) techniques. The large area map presented is one of the most extensive EBSD maps to have been collected in application to extraterrestrial materials. Chondrule margins preferentially exhibit limited intragrain crystallographic misorientation due to localized crystal-plastic deformation. Crystallographic preferred orientations (CPOs) preserved by matrix olivine grains are strongly coupled to grain shape, most pronounced in shortest dimension <a>, yet are locally variable in orientation and strength. Lithostatic pressure within plausible chondritic model asteroids is not sufficient to drive compaction or create the observed microstructures if the aggregate was cold. Significant local variability in the orientation and intensity of compaction is also inconsistent with a global process. Detailed microstructures indicative of crystal-plastic deformation are consistent with brief heating events that were small in magnitude. When combined with a lack of sintered grains and the spatially heterogeneous CPO, ubiquitous hot isostatic pressing is unlikely to be responsible. Furthermore, Allende is the most metamorphosed CV chondrite, so if sintering occurred at all on the CV parent body it would be evident here. We conclude that the crystallographic textures observed reflect impact compaction and indicate shock-wave directionality. We therefore present some of the first significant evidence for shock compaction of the CV parent body.

INTRODUCTION

Meteorites in our collections sample both planets and small bodies within the inner Solar System. However, the process driving the lithification of these small bodies, specifically chondritic asteroids, is still debated. Meteorites preserve metamorphic textures that do not represent their state of accretion on the parent body, specifically their initial porosity (Consolmagno et al., 2008). It is therefore important to assess the microstructural evolution from high-porosity primordial materials to low-porosity meteorites.

Gravitational forces on chondritic asteroids have been proposed as a mechanism to compact a highly porous body into lithified rock (Fujimura et al., 1983), as well as being potentially associated with considerable planetary-scale heating (Horedt, 1980). However, lithostatic pressure is low, even in objects hundreds of kilometers across (Weidenschilling and Cuzzi, 2006). The weak effect of stress bridging between grains would likely equilibrate over long time periods. We infer that the resultant crystallographic preferred orientations (CPOs) from this process would be weak but homogeneous throughout the sample, and intragrain deformation would be weak or absent. If cold compaction occurred, then brittle deformation textures may arise, and there would likely be a coupling of the CPO and shape preferred orientations (SPOs) of the grains, owing to the lack of heat to encourage grain shape modification.

As an alternative model to a pure mechanical compaction, cold compaction followed by radiogenic heating primarily by ^{26}Al is proposed to result in sintering of the primitive grains and parent body compaction (Gail et al., 2015). This is termed hot isostatic pressing (HIP), and is predicted to occur over ~1 m.y. (Gail et al., 2015). Olivine matrix grains are predicted to be sintered at 650–700 K by surface diffusion, and chondrules at >900 K by dislocation creep (Gail et al., 2015). We would therefore observe consistent and homogeneous CPOs throughout the sample reflecting the planet-wide process and predicted time frame. If surface diffusion has modified the shape of the matrix olivine grains due to growth into available pore space (Carter and Norton, 2013), the SPOs would likely be decoupled from the CPOs.

Porosity reduction in primordial chondritic asteroids may also have occurred through impact-induced compaction (Bland et al., 2014; Hanna et al., 2015; Davison et al., 2016). The shock wave produced by an impact into a porous body propagates through the medium, resulting in rapid pore collapse and localized pressure excursions over time scales of a few microseconds to seconds. Crystallographic deformation is predicted to be concentrated in initially porous regions and at the edges of chondrules, and weak, heterogeneous, and localized CPOs are likely to occur (Davison et al., 2016). Similar to cold compaction, SPOs and CPOs are expected to be coupled due to the very short time scale for heating resulting in limited modification of primary grain shapes yet alignment of grains by physical rotation.

We examined the CV3 (carbonaceous chondrite) meteorite, Allende, at microscales and mesoscales to understand the microstructural deformation and CPOs generated on the CV chondrite parent body. Allende has undergone relatively little aqueous alteration, and still contains anhydrous matrix material (although it has been at relatively higher metamorphic temperatures than other CV meteorites; Krot et al., 1998; Bonal et al., 2006). In terms of impact processing, it is classified as an unshocked S1 (Scott et al., 1992). Previous microstructural analyses of the fine-grained matrix grains of Allende (<5 µm; Scott et al., 1988) have focused on localized CPOs around individual chondrules (Watt et al., 2006; Hanna et al., 2015) and crystal-plastic deformation microstructures of selected individual chondrules, calcium-aluminum inclusions (CAIs), and matrix grains (Forman et al., 2016). Modeling of impact-induced compaction mapped the response of the chondritic medium to impact over a much larger area (256 mm^2) (Davison et al., 2016). Microscale observations from previous studies are therefore difficult to compare to modeling predictions. In this paper, crystallographic textures at mesoscales and microscales were systematically examined over a large area of 6 mm^2, incorporating numerous

*E-mail: lucy.forman@postgrad.curtin.edu.au

GEOLOGY, June 2017; v. 45; no. 6; p. 559–562 | Data Repository item 2017178 | doi:10.1130/G38864.1 | Published online 4 April 2017

chondrules and matrix regions. This provided a quantitative visualization of how the parent body of Allende responded to compaction, and facilitated direct comparisons with numerical simulations of different compaction processes.

METHODOLOGY

An 8 mm² area of Allende (from sample WAM 13102) was mapped to obtain phase and crystallographic data (Fig. DR1 in the GSA Data Repository[1]) at a step size of 0.5 µm over 380 h, resulting in the collection of 46 × 10⁶ electron backscattered diffraction (EBSD) patterns, representing one of the largest EBSD data sets ever collected from a single area. (Further details are provided in the Data Repository.)

A 6 mm² area of the mapped region was subdivided into 120 ~250 × 250 µm grid squares to constrain regional and local CPOs of the fine-grained interstitial matrix olivine grains (Fig. 1). Multiple meteoritic components were included in this area, making this one of the most comprehensive EBSD applications to meteoritic materials. The right-most 2 mm² of the mapped area comprised a large, fine-grained amoeboid olivine aggregate and was therefore not included in the analysis. Large chondrule olivine grains were omitted from this analysis. Crystallographic orientations were plotted onto lower hemisphere, equal-area plots in the map x-y-z reference frame (Fig. 1) and overlain onto the phase map for spatial reference (Fig. 2). SPO fabrics of the olivine grains were quantified and the relationships between SPO and CPO were investigated (Fig. 3; Fig. DR2; see the Data Repository for methodology). All chondrule rim grains within the mapped area were also inspected for evidence of crystal-plastic deformation to characterize the deformation of chondrule margins within spatial context of the entire sample (e.g., Fig. 4), following the procedures outlined in Forman et al. (2016).

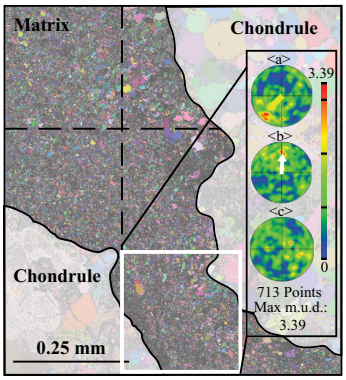

Figure 1. The mapped area of meteorite Allende was divided into a grid (Euler map is background). The orientations of the crystallographic axes for each matrix grain were plotted onto lower hemisphere, equal-area plots to identify crystallographic preferred orientations (CPOs). In this case, a moderate <a> CPO perpendicular to the chondrule edge and weak <b> CPO parallel to the chondrule edge are observed. Max m.u.d.—maximum mean uniform density.

[1]GSA Data Repository item 2017178, supplemental information regarding methods and approach, Figure DR1 (mapped region of the CV3 meteorite Allende), and Figure DR2 (detailed shape preferred orientation [SPO] analysis), is available online at http://www.geosociety.org/datarepository/2017/ or on request from editing@geosociety.org.

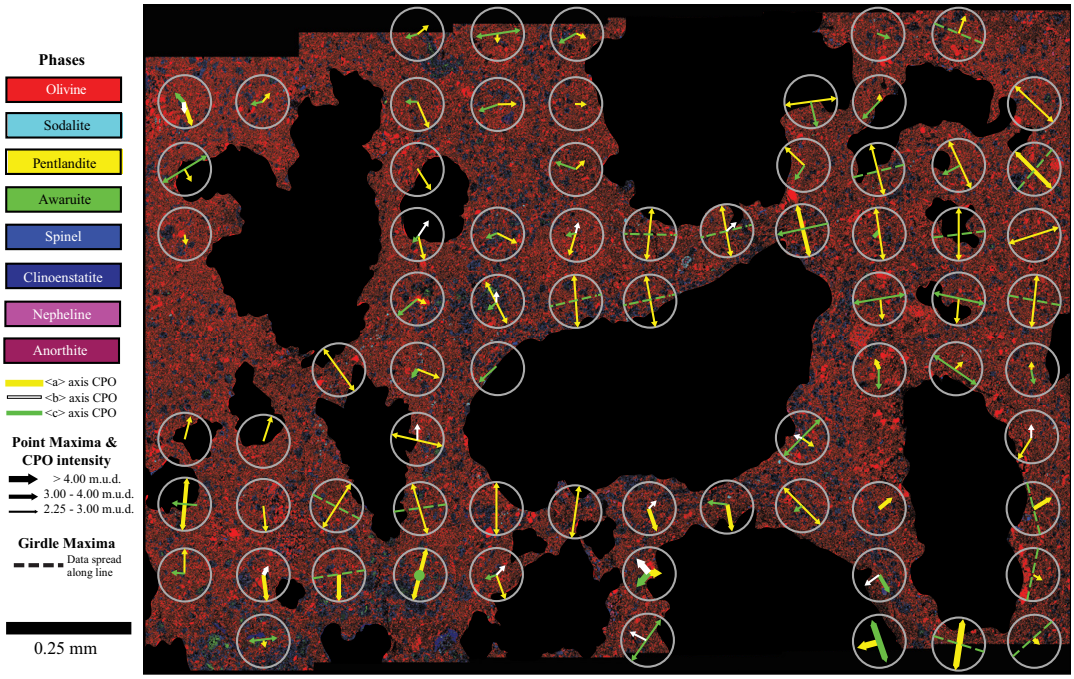

Figure 2. Full crystallographic preferred orientation (CPO) analysis overlaid onto the phase map. Black regions are chondrules. Colored arrows within gray circles indicate an alignment of the crystallographic axes. The thickness of each line reflects the mean uniform density (m.u.d.) of the CPO. Double-ended arrows indicate that the axis cluster is on the edge of the lower hemisphere plot, indicating that this axis is parallel to the plane of the sample (i.e., x-y reference plane shown here). The dominant CPO is in <a> (yellow lines), which is predominantly parallel to the y axis of the reference plane, but also shows localized deviations at chondrule edges.

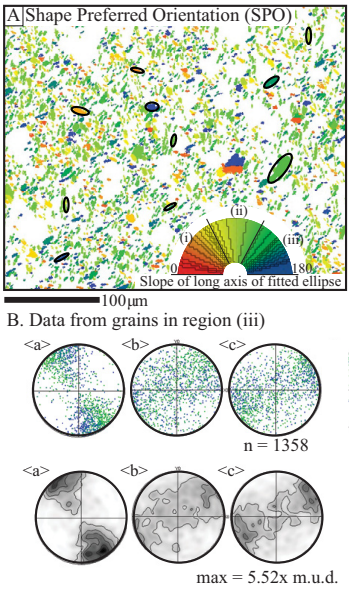

Figure 3. Shape analysis of matrix olivine grains demonstrated on a small region of the total area. A: Map color coded to indicate orientation of long axis of the fitted ellipse (black ovals) for each matrix olivine. B: Pole figures of subset (iii) of the total matrix olivine data set. Top shows <a>, <b>, and <c> with one point per grain in map color scheme; contoured data are below. These indicate that the crystallographic preferred orientation (CPO) and shape preferred orientation (SPO) of this region are coupled; the crystallographic orientation of each grain is strongly correlated to the grain shape. Lower hemisphere equal-area plots in map x-y-z reference frame. Max—maximum; m.u.d.— mean uniform density.

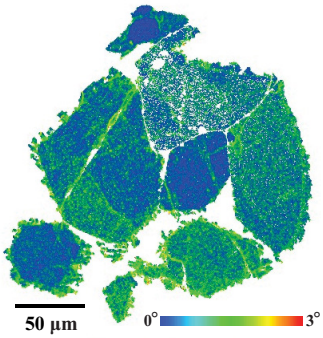

Figure 4. Chondrule olivine grains showing crystallographic deformation concentrated toward the bottom of the chondrule. Local misorientation map is color coded to demonstrate the deviation of crystallographic orientation of each pixel with relation to the orientation of the surrounding 8 pixels (measured in degrees/1.5 µm).

RESULTS

We identified a total of 339,040 grains; 85.3% of the grains were indexed as olivine (Fig. 2). Sparse coarse grains of clinoenstatite, spinel, and awaruite were concentrated into loose bands between chondrules, which also contained larger, rounded olivine grains (~0.02 mm). The regions immediately adjacent to chondrules (Fig. 2) primarily comprised fine-grained euhedral and subhedral olivine laths (<10 µm).

Chondrule Edge Measurements

Of the 30 chondrule grain sites, ~65% indicated as much as 5° of lattice misorientation concentrated in the outer 10–20 µm at the top or bottom of the grain (in reference frame of Fig. 2), and 25% indicated deformation that was concentrated on the right or left sides of the chondrules (e.g., Fig. 4). The remaining 10% of sites exhibited no deformation textures. Very limited lattice misorientation was detected in the chondrule interiors (<0.5°).

Grain Morphologies

Olivine matrix grains in the plane of the sample are euhdral to subhedral and lath shaped. Close inspection reveals the grains have sharp edges with minimal impingement (e.g., Fig. 3). However, small grains that are close to the step size of the EBSD mapping were omitted to avoid the geometric artifacts associated with grains defined by two pixels or less.

SPO and CPO Olivine Matrix Grain Analyses

Analyses of the SPOs and CPOs of the matrix olivines throughout the sample show that <c>, <b>, and <a> are the long, intermediate, and short dimensions of the grains, respectively (e.g., Fig. 3). Matrix olivine grains show significant CPOs (>2.00 mean uniform density, m.u.d.) in 72 of the 120 measured regions. Of those regions, 25% had a m.u.d. of ≥3.00 (moderate to strong clustering of crystallographic axes). A strong point maxima CPO of <a> was observed in 68 regions (yellow arrows in Fig. 2) predominantly in the y direction (vertical) of the EBSD map (Fig. 2). The CPOs of <c> (green arrows in Fig. 2) form moderate intensity girdles that aligned with the map x direction, in 51 of the 56 regions where CPOs in <c> were observed. The CPOs of <b> (white arrows in Fig. 2) were generally weak, spatially heterogeneous point maxima with variable orientations in 14 areas directly adjacent to chondrules. These data indicate a strong coupling between grain shape (SPO) and CPO, with a predominant flattening of the matrix olivine grains parallel to the map y direction, and elongation in the map x direction (Figs. 2 and 3; Fig. DR2). The dominant CPO is observed in <a>, consistent with previous studies (Watt et al., 2006).

The strongest CPOs are in close proximity to chondrule margins, with many at the top or bottom of chondrules, or in between closely spaced (<0.1 mm) chondrules (Fig. 2). Strong, localized variations of the overall CPOs are evident around chondrules (Fig. 2), where grains are flattened against the chondrule margins.

DISCUSSION

Matrix olivine grains in Allende have preserved euhedral-subhedral lath morphologies. They have a moderate SPO throughout the mapped region, which correlates consistently to the observed CPO, indicating that a flattening fabric of variable strength has been produced. The relationship between CPO and SPO implies that sintering and surface diffusion have not occurred, therefore the CV parent body was not at the high temperatures required for HIP to occur over the required time scales. If subgrain rotation recrystallization had generated the CPOs, rotation through large angles would be required, which would act to reduce the aspect ratio of the matrix laths. Because the matrix laths are elongate, some primary porosity is still present, and crystal-plastic deformation effects are minor (Forman et al., 2016), the CPO is predominantly the result of the physical realignment of anisotropic olivine grains rather than dislocation or diffusion creep.

The minor crystal-plastic strain observed at the margins of chondrules and a lack of such strain in chondrule interiors indicate Allende must have undergone high (but transient) stresses and temperatures during deformation (Frost and Ashby, 1982), at a local scale. Comparatively, matrix olivine grains have undergone significantly more intragrain deformation (Forman et al., 2016), which is inferred to result from brief localized temperature excursions predicted from impact-induced compaction. Allende is expected to have been at temperatures between 300 and 800 K (e.g., Weinbruch et al., 1994; Huss et al., 2006; Cody et al., 2008), implying that sintering within Allende could only have been achieved in matrix grains, and any temperature excursion above that threshold was not sustained for a significantly long period of time, and certainly not for durations on the order of 1 m.y.

Local variations in CPO alignment and intensity were observed over a small area of 6 mm^2 at the mesoscale, and are consistent with previous EBSD studies (Watt et al., 2006). It has been argued that stress applied by lithostatic forces within the parent asteroid were negligible (1 MPa at the center of a 200-km-diameter body; Weidenschilling and Cuzzi, 2006). In addition, uniform, planetary-scale compaction of a highly porous, low-gravity small planetary body would not generate such localized textures because stress bridging between grains would have equilibrated over time, nor would it have created discrepancies in deformation between chondritic components. Heating to >500 °C and compaction associated with HIP or hot

gravitational compression would have been sustained over a time period of ~1 m.y. (Gail et al., 2015). Rheological constraints from olivine (Karato et al., 1986) indicate that significant diffusion creep is predicted, at this temperature, time frame, and matrix grain size, that would have reduced porosity in a homogeneous way via diffusion creep recrystallization and new grain growth, and resulted in a recovered and annealed microstructure. However, as this was not observed HIP is unlikely to have contributed to the textural development of Allende. Because Allende is the most thermally altered CV chondrite studied (Bonal et al., 2006; Cody et al., 2008) this argument applies to the entire suite of CV chondrites.

Impact-induced compaction would generate shock-wave interactions with chondritic components, and associated localized heating and compression throughout the parent body over short time scales that would be rapidly equilibrated following the compression event (Davison et al., 2012; Bland et al., 2014). The collapse of abundant pores adjacent to chondrule edges is predicted to generate localized temperature excursions (to ~850 K in a 1.5 km/s impact into a mixture of 70% porous matrix and nonporous chondrules, with a bulk porosity of 50%; Bland et al., 2014) when compared to nonporous regions, i.e., chondrule interiors (~330 K in the same scenario; Bland et al., 2014). This brief heating discrepancy easily explains the deformational textures in chondrule and matrix grains, and would be associated with heterogeneous SPOs and CPOs that are also likely to be asymmetric around chondrules. As heat production is the result of pore collapse due to compression, regions that experienced the highest temperatures are the same regions that underwent the most compression, and therefore formed the most significant CPOs.

CONCLUSIONS

We examined the crystallographic textural features at both the microscales and mesoscales within the CV3 chondrite Allende using one of the most comprehensive EBSD maps ever collected, to explore compaction processes on the CV chondrite parent body. Abundant but minimal chondrule edge lattice deformations that are not uniformly distributed around chondrule margins and moderately strong yet heterogeneously oriented <a> axis CPOs and coupled SPOs were detected throughout the fine-grained matrix regions, consistent with a variably developed flattening fabric. Allende has also been at higher temperatures than other CVs. If sintering, and therefore HIP, had occurred we would see microstructural evidence of it in this sample. Our observations rule out HIP and other forms of gravity-driven compaction as viable compaction processes of the CV parent body, and by inference any small primitive bodies. Impact-induced compaction provides the required heterogeneous distribution of heating and compaction over a short time scale, and our findings closely replicate the small-scale spatial heterogeneities predicted by numerical modeling. The orientations of the SPOs and CPOs in association with chondrule edge lattice deformations provide directionality for shock-wave propagation; compaction was parallel to the y direction of Figure 2 and occurred primarily due to impacts into the highly porous parent body.

This unique study is one of the first to identify crystallographic evidence for impact-induced compaction of the CV parent body, and therefore is a very significant application of EBSD techniques to meteorites. Although this finding is limited to formation of the CV parent body in this study, small planetary bodies would likely have undergone similar impacts, and would have small lithostatic pressures acting to compact the body. There is therefore scope to expand this approach to other chondrites and small parent bodies.

ACKNOWLEDGMENTS

This work was funded by the Australian Research Council via the Australian Laureate Fellowship program (FL110100074 to Bland). We acknowledge the technical assistance and use of facilities at the University of Sydney node of the Australian Microscopy and Microanalysis Research Facility. Collins and Davison were funded by UK Science and Technology Facilities Council grant ST/N000803/1. We thank editor Bob Holdsworth, reviewer Jon Friedrich, and two anonymous reviewers for constructive comments.

REFERENCES CITED

Bland, P.A., Collins, G.S., Davison, T.M., Abreu, N.M., Ciesla, F.J., Muxworthy, A.R., and Moore, J., 2014, Pressure-temperature evolution of primordial solar system solids during impact-induced compaction: Nature Communications, v. 5, 5451, doi:10.1038/ncomms6451.

Bonal, L., Quirico, E., Bourot-Denise, M., and Montagnac, G., 2006, Determination of the petrologic type of CV3 chondrites by Raman spectroscopy of included organic matter: Geochimica et Cosmochimica Acta, v. 70, p. 1849–1863, doi:10.1016/j.gca.2005.12.004.

Carter, C.B., and Norton, M.G., 2013, Sintering and grain growth, *in* Carter, C.B., and Norton, G.M., Ceramic materials: Science and engineering: Springer, New York, p. 439–456, doi:10.1007/978-1-4614-3523-5_24.

Cody, G.D., Alexander, C.O.D., Yabuta, H., Kilcoyne, A.L.D., Araki, T., Ade, H., Dera, P., Fogel, M., Militzer, B., and Mysen, B.O., 2008, Organic thermometry for chondritic parent bodies: Earth and Planetary Science Letters, v. 272, p. 446–455, doi:10.1016/j.epsl.2008.05.008.

Consolmagno, G.J., Britt, D.T., and Macke, R.J., 2008, The significance of meteorite density and porosity: Chemie der Erde, v. 68, p. 1–29, doi:10.1016/j.chemer.2008.01.003.

Davison, T.M., Ciesla, F.J., and Collins, G.S., 2012, Post-impact thermal evolution of porous planetesimals: Geochimica et Cosmochimica Acta, v. 95, p. 252–269, doi:10.1016/j.gca.2012.08.001.

Davison, T.M., Collins, G.S., and Bland, P.A., 2016, Mesoscale modeling of impact compaction of primitive solar system solids: Astrophysical Journal, v. 821, p. 68.

Forman, L.V., et al., 2016, Hidden secrets of deformation: Impact-induced compaction within a CV chondrite: Earth and Planetary Science Letters, v. 452, p. 133–145, doi:10.1016/j.epsl.2016.07.050.

Frost, H.J., and Ashby, M.F., 1982, Deformation-mechanism maps: The plasticity and creep of metals and ceramics: Oxford, UK, Pergamon Press, 165 p.

Fujimura, A., Kato, M., and Kamazawa, M., 1983, Preferred orientation of phyllosilicate (001) in matrix of Murchison meteorite and possible mechanisms of generating the oriented texture in chondrites: Earth and Planetary Science Letters, v. 66, p. 25–32, doi:10.1016/0012-821X(83)90123-1.

Gail, H.P., Henke, S., and Trieloff, M., 2015, Thermal evolution and sintering of chondritic planetesimals—II. Improved treatment of the compaction process: Astronomy & Astrophysics, v. 576, A60, doi:10.1051/0004-6361/201424278.

Hanna, R.D., Ketcham, R.A., Zolensky, M., and Behr, W., 2015, Impact-induced brittle deformation, porosity loss, and aqueous alteration in the Murchison CM chondrite: Geochimica et Cosmochimica Acta, v. 171, p. 256–282, doi:10.1016/j.gca.2015.09.005.

Horedt, G.P., 1980, Gravitational heating of planets: Physics of the Earth and Planetary Interiors, v. 21, p. 22–30, doi:10.1016/0031-9201(80)90016-3.

Huss, G.R., Rubin, A.E., and Grossman, J.N., 2006, Thermal metamorphism in chondrites, *in* Lauretta, D.S., and McSween, H.Y., eds., Meteorites and the early Solar System II: Tuscan, University of Arizona Press, p. 567–586.

Karato, S.I., Paterson, M.S., and FitzGerald, J.D., 1986, Rheology of synthetic olivine aggregates: Influence of grain size and water: Journal of Geophysical Research, v. 91, p. 8151–8176, doi:10.1029/JB091iB08p08151.

Krot, A.N., Petaev, M.I., Scott, E.R., Choi, B.G., Zolensky, M.E., and Keil, K., 1998, Progressive alteration in CV3 chondrites: More evidence for asteroidal alteration: Meteoritics & Planetary Science, v. 33, p. 1065–1085, doi:10.1111/j.1945-5100.1998.tb01713.x.

Scott, E.R.D., Barber, D.J., Alexander, C.M., Hutchison, R., and Peck, J.A., 1988, Primitive material surviving in chondrites: Matrix, *in* Kerridge, J.F., and Matthews, M.S., eds., Meteorites and the early Solar System: Tucson, University of Arizona Press, p. 718–745.

Scott, E.R.D., Keil, K., and Stöffler, D., 1992, Shock metamorphism of carbonaceous chondrites: Geochimica et Cosmochimica Acta, v. 56, p. 4281–4293, doi:10.1016/0016-7037(92)90268-N.

Watt, L.E., Bland, P.A., Prior, D.J., and Russell, S.S., 2006, Fabric analysis of Allende matrix using EBSD: Meteoritics & Planetary Science, v. 41, p. 989–1001, doi:10.1111/j.1945-5100.2006.tb00499.x.

Weidenschilling, S.J., and Cuzzi, J.N., 2006, Accretion dynamics and timescales: Relation to chondrites, *in* Lauretta, D.S., and McSween, H.Y., eds., Meteorites and the early Solar System II: Tuscon, University of Arizona Press, p. 473–485.

Weinbruch, S., Armstrong, J., and Palme, H., 1994, Constraints on the thermal history of the Allende parent body as derived from olivine-spinel thermometry and Fe/Mg interdiffusion in olivine: Geochimica et Cosmochimica Acta, v. 58, p. 1019–1030, doi:10.1016/0016-7037(94)90523-1.

Manuscript received 5 December 2016
Revised manuscript received 15 February 2017
Manuscript accepted 7 March 2017

Printed in USA

Appendix A3

Author Contributions, Chapter 4:

A Morphologic & Crystallographic Comparison of CV Chondrite Matrices

L. V. Forman[1], N. E. Timms[1], P. A. Bland[1], L. Daly[1], G. K. Benedix[1] & P. W. Trimby[2].

[1]Department of Applied Geology, Curtin University, GPO Box U1987, Perth, WA 6845, Australia

[2]Australian Centre for Microscopy and Microanalysis, The University of Sydney, NSW, 2006, Australia.

STATEMENT OF AUTHORSHIP

I hereby confirm the primary author, Miss L. V. Forman, conducted the majority of this study and give my permission for this to be included in the candidate's PhD thesis.

MISS LUCY. V. FORMAN

- Lead on planning, data collection and analysis
- Drafted & formatted manuscript

Contribution: *80%* ***Date:*** *22.2.17*

DR. NICK TIMMS

- Assisted with data interpretation
- Manuscript editing

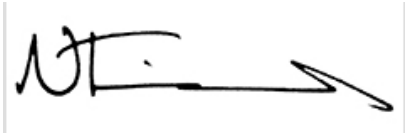

Contribution: *10%* ***Date:*** *23.2.17*

PROF. PHIL BLAND

- Assisted with initial concept
- Manuscript editing

Contribution: *5%* ***Date:*** *23.2.17*

MR LUKE DALY

- Conducted some EBSD data collection
- Manuscript editing

Contribution: *3%* ***Date:*** *22.2.17*

DR. GRETCHEN BENEDIX

- Manuscript editing

Contribution: *1%* ***Date:*** *28.2.17*

DR. PATRICK TRIMBY

- Assisted with some EBSD data collection

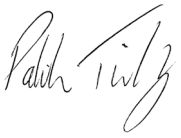

Contribution: *1%* ***Date:*** *24.2.17*

Appendix A4

Author Contributions, Chapter 5:

Relicts of an Impactor: Locating Iridium within the Distal K-Pg Boundary Clays

L.V. Forman[1], L. Daly[1], P. A. Bland[1], N. Evans[1], K. Merigot[2], C. G. Ryan[3] N. E. Timms[1], G. K. Benedix[1], M. Saunders[4].

[1] Department of Applied Geology, Curtin University, Bentley, WA 6102, Australia.

[2] John de Laeter Centre of Excellence, Curtin University, Bentley, WA 6102, Australia.

[3] CSIRO Mineral Resources, Clayton, VIC 3168, Australia

[4] Centre for Microscopy, Characterisation and Analysis, The University of Western Australia, WA 6009, Australia

STATEMENT OF AUTHORSHIP

I hereby confirm the primary author, Miss L. V. Forman, conducted the majority of this study and give my permission for this to be included in the candidate's PhD thesis.

MISS LUCY. V. FORMAN

- Lead on planning, data collection and analysis
- Drafted & formatted manuscript

Contribution: *70%* ***Date:*** *22.2.17*

MR LUKE DALY

- Conducted FIB, TEM and assisted with data analysis
- Manuscript editing

Contribution: *18%* ***Date:*** *22.2.17*

PROF. PHIL BLAND

- Assisted with initial concept
- Manuscript editing

Contribution: *5%* ***Date:*** *23.2.17*

PROF. NOREEN EVANS

- Conducted LA-ICP-MS data collection

Contribution: *2%* ***Date:*** *23.2.17*

MISS KELLY MERIGOT

- Conducted TIMA data collection

Contribution: *1%* ***Date:*** *23.2.17*

DR CHRIS RYAN

- Assisted with XRF Synchrotron data collection

Contribution: *1%* ***Date:*** *23.2.17*

DR. NICK TIMMS

- Manuscript editing

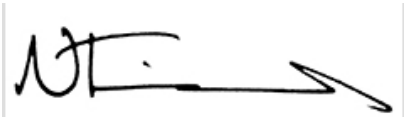

Contribution: *1%* ***Date:*** *23.2.17*

DR. GRETCHEN BENEDIX

- Manuscript editing

Contribution: *1%* ***Date:*** *28.2.17*

DR MARTIN SAUNDERS

- Conducted TEM imaging

Contribution: *1%* ***Date:*** *4.3.17*

Appendix B

Additional First Author Publications

Appendix B1

Defining the Crystallographic Fingerprint of Extraterrestrial Treasures

Conference Abstract from the 79th Annual Meeting of the Meteoritical Society (2016), relevant to Chapter 4.

Forman, L. V., Bland, P. A., Timms, N. E., Daly, L., Benedix, G. K., & Trimby, P. W., 2016, Defining the Crystallographic Fingerprint of Extraterrestrial Treasures: LPI Contributions, p. 6264.

STATEMENT OF AUTHORSHIP

I hereby confirm the primary author, Miss L. V. Forman, conducted the majority of this study and give my permission for this to be included in the candidate's PhD thesis.

MISS LUCY. V. FORMAN

- Lead on planning, data collection and analysis
- Drafted & formatted manuscript

Contribution: *70%* ***Date:*** *22.2.17*

PROF. PHIL BLAND

- Assisted with initial concept
- Manuscript editing

Contribution: *5%* ***Date:*** *23.2.17*

DR. NICK TIMMS

- Assisted with data interpretation
- Manuscript editing

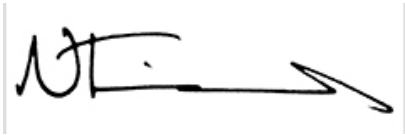

Contribution: *10%* ***Date:*** *23.2.17*

MR LUKE DALY

- Conducted some EBSD data collection
- Manuscript editing

Contribution: *10%* ***Date:*** *22.2.17*

DR. GRETCHEN BENEDIX

- Manuscript editing

Contribution: *2%* ***Date:*** *28.2.17*

DR. PATRICK TRIMBY

- Assisted with some EBSD data collection
- Manuscript editing

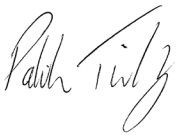

Contribution: *3%* ***Date:*** *24.2.17*

79th Annual Meeting of the Meteoritical Society (2016) **6264.pdf**

DEFINING THE CRYSTALLOGRAPHIC FINGERPRINT OF EXTRATERRESTRIAL TREASURES.

L. V. Forman[1], P. A. Bland[1], N. E. Timms[1], L. Daly[1], G. K. Benedix[1] & P. W. Trimby[2]. [1]Dept. Applied Geology, Curtin University, GPO Box U1987, Perth, WA 6845, Australia. [2]Australian Centre for Microscopy and Microanalysis, The University of Sydney, NSW 2006, Australia.

Introduction: In describing fine grained extraterrestrial materials it is common practice to employ a geochemical shorthand, e.g. quoting the average composition of a particular mineral (frequently olivine in matrices), to constrain chemical variance and reveal some aspect of the petrogenesis of the sample. Typically, this geochemical fingerprint in olivines is expressed as a percentage of one of the olivine end members, fayalite (Fa) and forsterite (Fo), which indicate the proportions of Fe and Mg within each grain (e.g. [1]).

Determining the crystallographic characteristics of the same matrix grains would enable any relationship between grain shape, size and crystal axis coordination to be identified. Whilst grain morphologies of matrix grains in chondrites are often quoted (e.g. [2, 3]), an accumulation of crystallographic data over a large area would allow for a *standardised* crystallographic fingerprint to be developed for the entire matrix of the meteorite. An understanding of the connection between crystallographic preferred orientation (CPO) and shape preferred orientation (SPO), specific to a sample of interest, allows for quick fabric interpretation and an indication of the growth and formational history of the sample. Furthermore, as the information required can be obtained using a relatively inexpensive but sensitive imaging technique, such quantification could be easily reproduced for a range of samples at a variety of scales.

Methods: In this study, we used electron backscatter diffraction (EBSD) mapping to identify phases and quantify their grain shapes, sizes, and crystallographic orientations in the CV3 meteorite Allende over a large area (4 mm^2, ~55800 data points). The analysed data are presented as maps, which can display various crystallographic parameters; grain size, grain shape, and primary crystal axis orientations for example. For each grain, the orientations of the major crystallographic axes are quantified, and then displayed collectively on lower-hemisphere equal-area plots to characterize the 'shape' and strength of CPOs. Each grain was assigned an ellipse oriented to reflect the physical longest axis of that grain and colour coded to reflect the ellipse orientation (Fig. 1A &B). Contouring of the crystallographic data (Fig. 1C) allowed for a comparison between SPO and CPO.

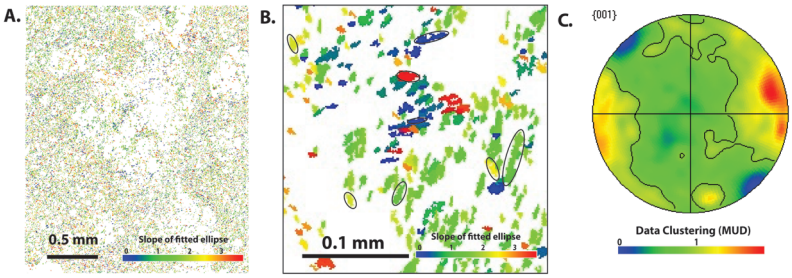

Figure 1 EBSD data of case-study application: a) large area map of ellipse orientation, b) expanded map of ellipse orientation, c) contoured CPO data.

Preliminary results: The {001} poles of many of the olivine matrix grains clustered to produce a weak fabric (Fig. 1C). When compared with the SPO maps (Fig. 1A & B), we found grain shape to be closely related to the {001} pole fabric therefore implying the two parameters may be co-dependent during grain formation. Further investigation in this study will fully determine the *signature* Allende matrix grain crystallography, complementary to the geochemical signature ($Fa_{45\text{-}56}$ [1]). This approach will enable us to examine shape and shape orientation changes around large and prominent meteoritic features, such as chondrules, and compare such results to CPO data for the same grains. We could also investigate how grain shape might impact fabric formation. By determining the average crystal shape, size and crystallographic axis coordination, we can define the crystallographic fingerprint of a chondritic sample mapped with EBSD. We suggest that identification of key crystallographic features; SPO, CPO, and their relationship should routinely form part of a comprehensive description of meteorite samples. We believe this to be important and complimentary to the geochemical data that is commonly determined for meteoritic matrix grains.

References: [1] Peck J. A. 1984. 15th Lunar and Planetary Science Conference pp. 635-636. [2] Scott E. R. D. and Krot A. N. 2003. In *Meteorites, comets, and planets*. Elsevier Press. pp. 143–200. [3] Brearley A. J. and Jones R. H. 1998. In *Planetary materials*. Mineralogical Society of America. pp. 3-1–3-307.

Appendix B2

Recovering the Primordial History of Chondrites in Unprecedented Detail using Massive EBSD Datasets

Conference Abstract from the 78th Annual Meeting of the Meteoritical Society (2015), relevant to Chapter 3.

Forman, L.V., Bland, P.A., Timms, N.E., Daly, L., Collins, G.S., Davison, T.M., Trimby, P.W. and Ringer, S.P., 2015, Recovering the Primordial Impact History of Chondrites in Unprecedented Detail Using Massive EBSD Datasets: In 78th Annual Meeting of the Meteoritical Society, v. 1856, p. 5086.

STATEMENT OF AUTHORSHIP

I hereby confirm the primary author, Miss L. V. Forman, conducted the majority of this study and give my permission for this to be included in the candidate's PhD thesis.

MISS LUCY. V. FORMAN

- Lead on planning, data collection and analysis
- Drafted & formatted manuscript

Contribution: *70%* ***Date:*** *22.2.17*

PROF. PHIL BLAND

- Assisted with initial concept
- Manuscript editing

Contribution: *5%* ***Date:*** *23.2.17*

DR. NICK TIMMS

- Assisted with initial concept
- Assisted with data interpretation
- Manuscript editing

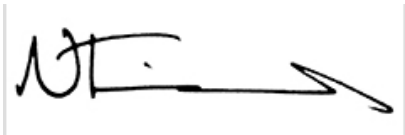

Contribution: *10%* ***Date:*** *23.2.17*

MR LUKE DALY

- Conducted EBSD data collection
- Manuscript editing

Contribution: *7%* ***Date:*** *22.2.17*

DR. GARETH COLLINS

- Offered insight from modelling simulations

Contribution: *2%* ***Date:*** *28.2.17*

DR. THOMAS DAVISON

- Offered insight from modelling simulations

Contribution: *2%* ***Date:*** *28.2.17*

DR. PATRICK TRIMBY

- Assisted with EBSD data collection

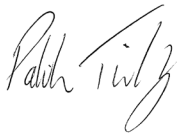

Contribution: *2%* ***Date:*** *24.2.17*

PROF. SIMON RINGER

- Assisted with TKD work

Contribution: *2%* ***Date:*** *1.3.17*

78th Annual Meeting of the Meteoritical Society (2015) **5086.pdf**

RECOVERING THE PRIMORDIAL IMPACT HISTORY OF CHONDRITES IN UNPRECEDENTED DETAIL USING MASSIVE EBSD DATASETS

L. V. Forman[1], P. A. Bland[1], N. E. Timms[1], L. Daly[1], G. S. Collins[2], T. M. Davison[2], P. W. Trimby[3] & S. P. Ringer[3]. [1]Dept of Applied Geology, Curtin University, GPO Box U1987, Perth, WA 6845, AU. E-mail: lucy.forman@curtin.edu.au [2]Earth Science & Engineering Department, Imperial College London, Exhibition Road, London SW7 2BP, UK [3]Australian Centre for Microscopy and Microanalysis & ARC Centre of Excellence for Design in Light Metals, University of Sydney, NSW 2006, AU.

Introduction: Chondrites are routinely classified in terms of shock level based on principles outlined by and modified from shock calibration studies of Stöffler *et al.* (1991). These studies characterise shock assuming parent bodies had material properties similar to extant meteorites [1], but primordial parent bodies accreted with significantly more porosity. Recent modelling has sought to understand the effects of shock and compaction of porous targets during early planetary evolution [2, 3]. Unique textures at the meso- and micro-scale are predicted, which predate the traditionally-characterised 'shock level' features described in meteorites. In this study we investigate compaction in the Allende CV3 chondrite using Electron Backscatter Diffraction (EBSD) mapping at unparalleled scale and resolution.

Methods & Materials: An 11.51 mm^2 area of Allende was mapped using EBSD with a step-size of 0.5 μm resulting in 46 million data points. The scale of this map enables the use of a novel approach– subdividing the map into 150 x 150 μm grid squares, we analysed fabrics in each area individually, allowing visualisation of shock wave interaction with the primordial aggregate. Here we consider a 0.972 mm^2 region of interest (5,426,808 data points) where fine-grained matrix encompasses a chondrule. The crystallographic preferred orientation of poles to <100>, <010> and <001> in matrix olivines were visualised for each grid square using equal-area, lower-hemisphere plots.

Results: A strong point maxima alignment of <001> (the shortest axis) normal to the chondrule margin is seen to the right of the chondrule. This is due to a grain 'flattening' with elongate grains aligning in the shortest dimension against the chondrule, and no preferential alignment of <100> and <010>, generating a moderate fabric. To the left, this fabric is absent.

Discussion & Conclusions: Allende is assigned shock level S1 due to the absence of 'traditional' shock features [4]. However, the asymmetric pattern of flattened matrix grains is consistent with model predictions of mechanical strain during earlier impact events, which cause compaction of the parent body from a bimodal mixture of initially highly-porous matrix and zero porosity chondrules. Furthermore, modelling shows that the asymmetric development of the fabric can be used as a 'way up' indicator with respect to the impact: the impact direction was oblique to the sample plane, and the shock wave propagated from the lower-right of the chondrule [2, 3]. The absence of a fabric to the left is due to chondrule 'shielding'. This approach should allow us to recover the early impact histories of chondrites in great detail, by using extant fabrics to model the response of primordial aggregates to the earliest compressive impacts.

References: [1] Stöffler D. *et al.* 1991. *Geochimica et Cosmochimica Acta*, 55(12):3845–3867 [2] Davison T. M. *et al.* 2010. *Icarus*, 208(1):468–481 [3] Bland P. A. *et al*. 2014. *Nature Communications*, 5:5451 [4] Scott. E. R. D. *et al*. 1992. *Geochimica et Cosmochimica Acta*, 56(12):4281–4293.

Appendix B3

Impact-Induced Compaction in CV Chondrites: Exploring a Hidden Record with EBSD

(MetSoc Abstract)

Conference Abstract from the 77th Annual Meeting of the Meteoritical Society (2014), relevant to Chapter 2.

Forman, L.V., Bland, P.A., Timms, N.E. and Benedix, G.K., 2014, Impact-Induced Compaction in CV Chondrites: Exploring a Hidden Record with EBSD: In 77th Annual Meeting of the Meteoritical Society, v. 1800, p. 5303.

STATEMENT OF AUTHORSHIP

I hereby confirm the primary author, Miss L. V. Forman, conducted the majority of this study and give my permission for this to be included in the candidate's PhD thesis.

MISS LUCY. V. FORMAN

- Lead on planning, data collection and analysis
- Drafted & formatted manuscript

Contribution: *80%* ***Date:*** *22.2.17*

PROF. PHIL BLAND

- Assisted with initial concept and planning
- Manuscript editing

Contribution: *5%* ***Date:*** *23.2.17*

DR. NICK TIMMS

- Assisted with initial concept
- Assisted with data interpretation
- Manuscript editing

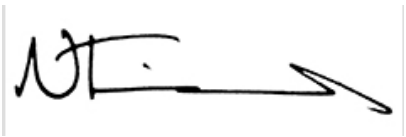

Contribution: *10%* ***Date:*** *23.2.17*

DR. GRETCHEN BENEDIX

- Manuscript editing

Contribution: *5%* ***Date:*** *28.2.17*

77th Annual Meteoritical Society Meeting (2014) **5303.pdf**

IMPACT-INDUCED COMPACTION IN CV CHONDRITES: EXPLORING A HIDDEN RECORD WITH EBSD. L. V. Forman[1], P. A. Bland[1], N. E. Timms[1] & G. K. Benedix[1]. [1]Department of Applied Geology, Curtin University, GPO Box U1987, Western Australia, 6845, Australia. E-mail: lucy.forman@curtin.edu.au

Introduction: Until recent studies such as [1] and [2], research into shock metamorphism in chondrites has focussed upon the record in chondrule grains and other large olivines visible with optical microscopy [3, 4]. The CV Allende has previously been classified as S1 - essentially unshocked [5] – using this approach. However, it is important to consider the record in matrix. Models of impact-induced compaction make a number of predictions [1, 2] e.g., a heterogeneous distribution of shock and deformation over small distances of ~100s micrometers [1, 2, 6]. Work by [2] established a spatial relationship between impact wave propagation, chondrules and matrix configuration, e.g., the lee side of the chondrule shows limited deformation, exhibiting a deformation 'shadow' effect. The matrix will likely experience a much higher temperature during impact than adjacent chondrules, and localised melting may be possible [1, 2, 6]. Furthermore, variations across and within chondrule interiors and edges are observed in these models. These types of shock metamorphic textures have not been considered until these recent studies. Here we use electron backscatter diffraction (EBSD) to search for the characteristic signatures of impact-induced compaction in Allende. We find abundant evidence for it, and our results indicate that a simple S1 classification does not adequately describe the complexity of the shock record in this meteorite.

Methods: Scanning electron microscopy techniques (including backscatter and secondary electron imaging) were used to identify matrix textures, fabric patterns and irregularities. We also used EBSD techniques to investigate the crystallographic arrangement of fabrics within the matrix, and textural relationships between the matrix and chondrules, which in essence, maps the degree of deformation.

Results: Sizeable (100 μm) olivine chondrules show little deformation in their interiors, but an intragrain strain of up to 8° at the edges. However, we observe up to 20° intragrain strain across matrix grains. The misorientation axes correspond to low-index directions in olivine, and are consistent with known dislocation slip systems. Low-angle (<10°) boundaries in individual matrix grains tend to align relative to each other, parallel to the elongation axis of elliptical chondrules. Therefore, these may be used as independent criteria for interpreting the dominant compaction direction within Allende.

Conclusions: Allende probably experienced shock deformation. Chondrule interiors show little deformation whereas the matrix shows a high amount, consistent with modelling predictions that the matrix absorbs the vast majority of the shock on impact, and deforms accordingly, preserving low-angle boundaries in alignment with one another.

References: [1] Bland P. A. et al. 2013. Abstract #5159. 76th Annual Meteoritical Society Meeting [2] Davison T. M. et al. 2014. Abstract #2718. 45th Lunar & Planetary Science Conference [3] Scott E. R. D. et al. 1991 *Geochimica et Cosmochimica Acta* 55: 3845-3867 [4] Bischoff A. & Stoffler D. 1992. *European Journal of Mineralogy* 4:707-755 [5] Scott E. R. D. et al. 1992. *Geochimica et Cosmochimica Acta* 56:4281–4293 [6] Leroux H. 2001. *European Journal of Mineralogy* 13:253-272

Appendix B4

Constraining the Compositional Variety of Impactors at 1AU Over the Last ~3.5 Ga: In Situ Identification and Analysis of >200 Meteoritic Grains in a Lunar Soil.

Conference Abstract from the 45th Lunar and Planetary Science Conference (2014).

Forman, L.V., Bland, P.A., Dyl, K.A., Daly, L., Ryan, C.G. and Paxman, J., 2014, Constraining the Compositional Variety of Impactors at 1AU Over the Last ~3.5 Ga: In Situ Identification and Analysis of> 200 Meteoritic Grains in a Lunar Soil: In Lunar and Planetary Science Conference v. 45, p. 2680.

STATEMENT OF AUTHORSHIP

I hereby confirm the primary author, Miss L. V. Forman, conducted the majority of this study and give my permission for this to be included in the candidate's PhD thesis.

MISS LUCY. V. FORMAN

- Lead on planning, data collection and analysis
- Drafted & formatted manuscript

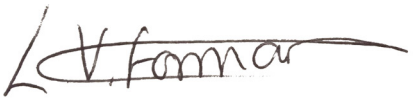

Contribution: *80%* ***Date:*** *22.2.17*

PROF. PHIL BLAND

- Assisted with initial concept and planning
- Manuscript editing

Contribution: *10%* ***Date:*** *23.2.17*

DR KATIE DYL

- Assisted with data collection
- Manuscript editing

Contribution: *2%* ***Date:*** *20.2.17*

MR LUKE DALY

- Assisted with data collection
- Manuscript editing

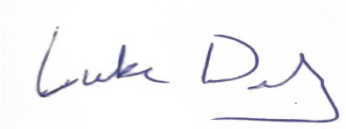

Contribution: *4%* ***Date:*** *22.2.17*

DR CHRIS RYAN

- Assisted with XRF Synchrotron imaging
- Manuscript editing

Contribution: *2%* ***Date:*** *26.2.17*

DR JONATHAN PAXMAN

- Manuscript editing

Contribution: *2%* ***Date:*** *5.3.17*

45th Lunar and Planetary Science Conference (2014) **2680.pdf**

CONSTRAINING THE COMPOSITIONAL VARIETY OF IMPACTORS AT 1AU OVER THE LAST ~3.5 GA: IN SITU IDENTIFICATION AND ANALYSIS OF >200 METEORITIC GRAINS IN A LUNAR SOIL

L. V. Forman[1], P. A. Bland[1], K. A. Dyl[1], L. Daly[1], C. G. Ryan[2] & J. Paxman[3]. [1]Dept. of Applied Geology, Curtin University, GPO Box U1987, Perth, WA, 6845, email: lucy.forman@postgrad.curtin.edu.au [2]Earth Science and Resource Engineering, Commonwealth Scientific and Industrial Research Organisation (CSIRO), Clayton, Victoria, Australia [3]Dept. of Mechanical Engineering, Curtin University, GPO Box U1987, Perth, WA, 6845.

Introduction: On their return from the moon, bulk chemistry of Apollo soil samples revealed an extralunar component, evidenced by an excess of siderophile and volatile elements consistent with primitive meteoritic material [1, 2]. Meteoritic material has been found *in situ* in regolith breccias [3, 4]. The most recent study involved a detailed analysis of 8 lunar regolith breccias and a lunar meteorite. 30 anomalous particles (identified by authors as ultramagnesian chondrule fragments) were identified by optical microscopy and SEM in older regolith samples; 5 more diverse projectile relics were found in younger breccias. But given its abundance in soils (in the case of Apollo 14 soil 14163, bulk chemistry indicated 2.5wt% of extralunar material is present) it is surprising that no detailed *in situ* characteristion of the meteoritic component in soils has been attempted. Aside from the Bench Crater [5] and Hadley Rille [6] meteorites, the collection of studied exogenous materials found within lunar settings, consists of a mesosiderite fragment [7] and iron meteorite fragments [8, 9]. The range of meteoritic hosts for the anomalous signature elements observed in bulk chemical analyses has not been determined.

In this study we apply a range of microanalytical techniques to the detection and characterisation of extralunar material in Apollo 14 soil 14163. It has been recording impacts for an extended period based on regolith grain size distribution [10], much longer than the expected half-life of asteroid families. As such, within the 2.5wt% extralunar component that is known to be present, we might expect to find fragments of meteorites derived from asteroids that are not currently delivering material to the Earth- Moon system.

Materials and Methods: Fine and coarse portions of 14163 were mounted onto cylindrical epoxy resin stubs of 25mm diameter. Fines were set in wells of approximately 50μm depth and both 3mm and 12mm diameters, whilst coarse seperates were mounted into wells 15mm in diameter and one grain deep.

For the purposes of initial analysis, a range of scanning electron microscopy (SEM) instrumentation was employed (Zeiss 1555 VP-FESEM, TESCAN VEGA3 & Phillips XL30 ESEM) at the Centre for Microscopy, Characterisation and Analysis (CMCA) at the University of Western Australia (UWA), and secondary electron, backscatter electron and energy dispersive X-ray spectroscopy (EDS) images were generated to examine the elemental make-up of the grains. In addition, the laser ablation inductively coupled plasma mass spectrometry (LA-ICP-MS) facility at Curtin University, Western Australia, was evaluated as a trace element mapping tool.

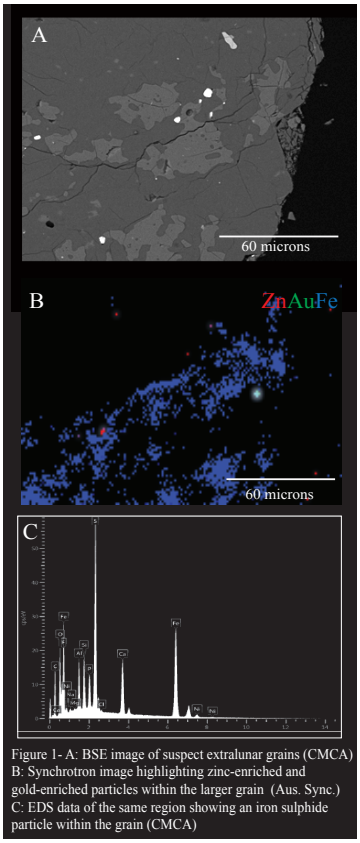

Figure 1- A: BSE image of suspect extralunar grains (CMCA) B: Synchrotron image highlighting zinc-enriched and gold-enriched particles within the larger grain (Aus. Sync.) C: EDS data of the same region showing an iron sulphide particle within the grain (CMCA)

For whole-sample mapping of trace and minor elements at high spatial resolution we employed the X-ray Fluorescence Microscopy (XFM) facility at the Australian Synchrotron, Victoria, Australia. This technique allowed us to create quantitative, micron-

scale resolution elemental maps from a variety of lunar fine and coarse samples of soil 14163. The Maia detector allows comprehensive and rapid data collection within a large energy range of 4-18 keV [11], detecting elements with Kα peaks within this range (including elements with an atomic number up to that of Zr-40). The 384-array Si-diode detector system is energy dispersive, meaning it allows this large range of minor and trace elements to be detected at high sensitivity, down to the 10s-1000s ppm scale depending upon peak energy [12], which is highly significant with respect to the initial goal of this research: identification and characterization of extralunar material. Post data collection spectral analysis was performed using the GeoPIXE software. GeoPIXE uses a dynamic analysis method allowing for spectral deconvolution and analysis of spatial distribution of trace and major elements [13].

Results: Using the Synchrotron facility and GeoPIXE software, areas and grains were highlighted that were highly enriched in siderophile, chalcophile or volatile elements. From the Synchrotron data alone, fine grained samples show approximately 50-100 anomalous grains per mount. Coarse grains often appear in the samples as microbreccias, and also provide some anomalous grains, with up to 30 grains/ mount.

Broad Classification	*Approximate Proportion*
Metals	60%
Sulphides	20%
Matrix	10%
Other	10%

Table 1- Approximate summary table of types of extralunar grains present within coarse samples of 14163.

'Hotspots' can be identified within the Synchrotron data, containing anomalously high siderophile, chalcophile and volatile elements. Characteristic elements were identified from previous research techniques, such as those outlined in [14-19], and based upon conclusions drawn from [20] a suite of suitable elements for identification of extralunar fragments was generated. These include Fe, Mn, Zn, Cu, Ni, Ge, Au, Ir, As and Pt; images of which can be seen in Figure 1.

Of the grains of the coarse samples examined thus far, Table 1 indicates the proportions of each broad compositional classification, of which the dominant classification is metallic. Fine grained soils contain a greater variety of grains; a study of which is ongoing.

Discussion: Our analytical protocol has detected large numbers of non-lunar fragments. Our preliminary analysis focused on the diagnostic elements listed above, restricting us to metal, sulphide, and volatile materials. Metallic grains are the most common of the extralunar grain types present in the coarse soils, simply due to the ease with which they are identified in the Synchrotron data and under SEM. However, these meteoritic materials will be associated with a larger fraction of silicates. Refining our data reduction protocol will allow us to characterise meteoritic silicates, extending the suite of identified extralunar particles beyond the ~200 grains already seen. This will be aided by the application of a new machine learning approach, which will enable multi-dimensional (25 element) automated identification and classification of grains.

Conclusions: This work has identified and analysed a large number of primarily metallic, sulphide and matrix grains within lunar soil 14163. Our technique, combining whole-sample mapping at high spatial resolution, with high sensitivity for a range of minor and trace elements, facilitates both the identification of anomalous grains and the generation of a detailed classification system. Future work will aim to further classify and characterise grains in terms of their origin, in a range of soils, based on geochemical signature and texture, supplementing Synchrotron analyses with additional techniques such as oxygen isotope analysis; TEM on FIB sections; and LA-ICP-MS mapping. The promising results from this initial study will contribute towards mapping the distribution of impact debris on the lunar surface, and constraining the compositional variety of impactors arriving at 1AU over the last ~3.5 Ga.

Acknowledgments: This work was funded by the Australian Research Council via their Australian Laureate Fellowship programme**.** The authors acknowledge the facilities, and the scientific and technical assistance of the Australian Microscopy & Microanalysis Research Facility at the Centre for Microscopy, Characterisation & Analysis, The University of Western Australia, a facility funded by the University, State and Commonwealth Governments. This research was also undertaken on the XFM beamline at the Australian Synchrotron, Victoria, Australia. We also acknowledge assistance provided by the LA-ICP-MS lab (Curtin University).

References: [1] Ryder G. (1990) *Eos, 71,* 313-323 [2] Hartmann W. K. (2003) *Met. Planet. Sci., 38,* 579-593 [3] Day J. M. D. et al (2006) *Geochim. Cosmochim. Ac., 70,* 5957-5989 [4]] Joy K. H. et al. (2012) *Science, 336,* 1426-1429 [5] Zolensky M. E. (1997) *Meteoritics & Planet. Sci., 32,* 15-18 [6] Rubin A. E. (1997) *Met. Planet. Sci., 32,* 231-247 [7] Wood J. A. et al (1970) *Smith. Astro. Obs. Spec. Report, 307* [8] Quaide W. & Bunch T. (1970) *Geochim. Cosmochim. Ac. Supp., 1,* 711-729 [9] Jolliff B. L. (1993) *LPSC XXIV,* 729-730 [9] Day J. M. D. et al (2006) *Geochim. Cosmochim. Ac., 70,* 5957-5989 [10] McKay. D. S. et al (1972) *Geochim. Cosmochim. Ac., 1,* 983-994 [11] Ryan C. G. et al. (2010) *AIP Conf. Proc., 1221,* 9-17 [12] Cleverly J. S. et al. (2012) *Meteoritics Planet. Sci. Supp., 75,* 5175 [13] GeoPIXE url:http://www.nmp.csiro.au/GeoPIXE.html [14] Wasson J. T. & Baedecker P. A. (1970) *Geochim. Cosmochim. Ac. Supp. 1,* 1741-1750. [15] Baedecker P. A. Chou C. L. & Wasson J. T. (1972) *LPSC Proc. II,* 1343-1359 [16] Ehmann W.D. & Chyi L. L. (1974) *LSC V, 2,* 1015-1024 [17] Wänke H. & Baddenhausen H. (1973) *LSC V, 2,* 1307-1335 [18] Laul J. C. & Schmitt R. A. (1973) *LSC IV, 2,* 1349-1367 [19] Wasson J. T. et al. (1975) *The Moon, 13,* 121-141 [20] Lodders K. (2003) *APJ, 591,* 1220- 1247.

Appendix B5

Impact-Induced Compaction in CV Chondrites: Exploring a Hidden Record with EBSD

(ASRC Abstract)

Conference Abstract from the 14th Australian Space Research Conference (2014).

Forman, L. V. , Bland, P. A., Timms, N. E., Benedix, G. K., 2014.

STATEMENT OF AUTHORSHIP

I hereby confirm the primary author, Miss L. V. Forman, conducted the majority of this study and give my permission for this to be included in the candidate's PhD thesis.

MISS LUCY. V. FORMAN

- Lead on planning, data collection and analysis
- Drafted & formatted manuscript

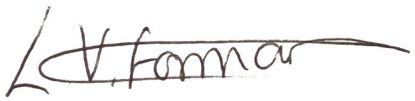

Contribution: *80%* ***Date:*** *22.2.17*

PROF. PHIL BLAND

- Assisted with initial concept and planning
- Manuscript editing

Contribution: *5%* ***Date:*** *23.2.17*

DR. NICK TIMMS

- Assisted with initial concept
- Assisted with data interpretation
- Manuscript editing

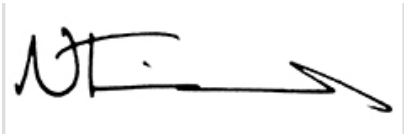

Contribution: *10%* ***Date:*** *23.2.17*

DR. GRETCHEN BENEDIX

- Manuscript editing

Contribution: *5%* ***Date:*** *28.2.17*

14th Australian Space Research Conference

Impact-Induced Compaction in CV Chondrites: Exploring a Hidden Record with EBSD.

L. V. Forman[1], P. A. Bland[1], N. E. Timms[1], & G. K. Benedix[1]
[1]Department of Applied Geology, Curtin University, GPO Box 1987, Western Australia, 6845

Abstract

The oxidised CV chondrite, Allende, has been thoroughly examined and robustly classified in terms of its geochemistry and textural features since it fell in 1969. Prior studies concluded Allende had undergone minimal metamorphic alteration as is portrayed through examination of the interiors of olivine chondrules and large grains within the matrix. Allende has therefore been classified as an S1- practically unshocked- signifying no chondrule flattening, and uniformly extinct olivine grains showing little to no strain across them.

However, recent modelling performed by Bland et al. (2012) has indicated that the effects of compaction and shock are likely to be observed much more strongly within matrix, owing to the greater porosity and greater variance in composition within it.

This study focuses upon the textural and crystallographic relationships between chondrules and matrix, and examines the strain observed across different meteoritic components using EBSD (Electron Backscatter Diffraction) analyses. We conclude Allende has indeed experienced some degree of shock, as is indicated by the large degree of intragrain strain observed within matrix grains (up to 20°). As is predicted by the modelling performed, the olivine chondrules present no deformation in their interiors, but up to 8° of intragrain strain at the edges, demonstrating the olivine chondrules only reveal the shock experienced at their edges.

Allende is therefore unlikely to fit into the S1 category, contrary to classification by Edward et al. (1992). Our evidence indicates there is a dominant compaction direction, as shown by mildly elongate chondrules, and the alignment of low-angle boundaries within matrix grains. Further investigation will seek to improve accuracy of the crystallographic analysis, and collect further data to investigate and confirm the shock properties seen so far within Allende.

Appendix C

Co-authored Publications

Appendix C1

In Situ Analysis of Refractory Metal Nuggets in Carbonaceous Chondrites

Daly et al., 2016, *in press*.

Daly, L., Bland, P.A., Dyl, K.A., Forman, L.V., Evans, K.A., Trimby, P.W., Moody, S., Yang, L., Liu, H., Ringer, S.P. and Ryan, C.G., 2016, In situ analysis of Refractory Metal Nuggets in carbonaceous chondrites: Geochimica et Cosmochimica Acta, in press.

STATEMENT OF AUTHORSHIP

As the primary author of the folloiwng manuscript, I hereby confirm the candidate's contributions and confirm my permission to include the manuscript in the candidate's PhD thesis.

MR LUKE DALY

- Lead investigator

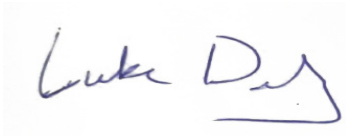

Date: ***22.2.17***

MISS LUCY. V. FORMAN

- Data Collection
- Manuscript editing

Contribution: ***2%*** ***Date:*** ***22.2.17***

Copyright Clearance Center RightsLink®

Account Info | Help

Title: In situ analysis of Refractory Metal Nuggets in carbonaceous chondrites

Author: Luke Daly,Phil A. Bland,Kathryn A. Dyl,Lucy V. Forman,Katy A. Evans,Patrick W. Trimby,Steve Moody,Limei Yang,Hongwei Liu,Simon P. Ringer,Christopher G. Ryan,Martin Saunders

Publication: Geochimica et Cosmochimica Acta

Publisher: Elsevier

Date: Dec 31, 1969

Logged in as:
Lucy Forman
Account #:
3001120586

LOGOUT

Order Completed

Thank you for your order.

This Agreement between Lucy Forman ("You") and Elsevier ("Elsevier") consists of your order details and the terms and conditions provided by Elsevier and Copyright Clearance Center.

License number	Reference confirmation email for license number
License date	Mar, 09 2017
Licensed Content Publisher	Elsevier
Licensed Content Publication	Geochimica et Cosmochimica Acta
Licensed Content Title	In situ analysis of Refractory Metal Nuggets in carbonaceous chondrites
Licensed Content Author	Luke Daly,Phil A. Bland,Kathryn A. Dyl,Lucy V. Forman,Katy A. Evans,Patrick W. Trimby,Steve Moody,Limei Yang,Hongwei Liu,Simon P. Ringer,Christopher G. Ryan,Martin Saunders
Licensed Content Date	Available online 25 November 2016
Licensed Content Volume	n/a
Licensed Content Issue	n/a
Licensed Content Pages	1
Type of Use	reuse in a thesis/dissertation
Portion	full article
Format	both print and electronic
Are you the author of this Elsevier article?	Yes
Will you be translating?	No
Order reference number	
Title of your thesis/dissertation	Impactors and the Impacted: Analytical Techniques to Identify and Understand the Impact Evolution of Extraterrestrial Materials
Expected completion date	Mar 2017
Estimated size (number of pages)	250
Elsevier VAT number	GB 494 6272 12
Requestor Location	Lucy Forman 11 Peter Street Halls Head, Western Australia 6210 Australia Attn: Lucy Forman
Billing Type	Invoice
Billing address	Lucy Forman 11 Peter Street Halls Head, Australia 6210 Attn: Lucy Forman
Total	0.00 AUD

ARTICLE IN PRESS

Available online at www.sciencedirect.com

ScienceDirect

Geochimica et Cosmochimica Acta xxx (2016) xxx–xxx

Geochimica et Cosmochimica Acta

www.elsevier.com/locate/gca

In situ analysis of Refractory Metal Nuggets in carbonaceous chondrites

Luke Daly [a,*], Phil A. Bland [a], Kathryn A. Dyl [a], Lucy V. Forman [a], Katy A. Evans [a], Patrick W. Trimby [b], Steve Moody [b], Limei Yang [b], Hongwei Liu [b], Simon P. Ringer [c], Christopher G. Ryan [d], Martin Saunders [e]

[a] *Department of Applied Geology, Curtin University, GPO Box U1987, Perth, WA 6845, Australia*
[b] *Australian Centre for Microscopy and Microanalysis and ARC Centre of Excellence for Design in Light Metals, The University of Sydney, NSW 2006, Australia*
[c] *Australian Institute for Nanoscale Science and Technology, and School of Aerospace, Mechanical and Mechatronic Engineering, The University of Sydney, NSW 2006, Australia*
[d] *CSIRO Earth Sciences and Resource Engineering, 26 Dick Perry Avenue, Kensington, Perth, WA 6151, Australia*
[e] *Centre for Microscopy, Characterisation and Analysis, The University of Western Australia, WA 6009, Australia*

Accepted for publication 17 November 2016; available online xxxx

Abstract

Micrometre to sub-micrometre-scale alloys of platinum group elements (PGEs) known as Refractory Metal Nuggets (RMNs) have been observed in primitive meteorites. The Australian Synchrotron X-ray Fluorescence (XRF) beamline, in tandem with the Maia detector, allows rapid detection of PGEs in concentrations as low as 50–100 ppm at 2 μm resolution. Corroborating these analyses with traditional electron microscopy techniques, RMNs can be rapidly identified *in situ* within carbonaceous chondrites. These results dispute the assumption of most previous studies: that RMNs are unique to Ca–Al-rich inclusions (CAIs). We find that RMNs are, in fact, observed within all components of carbonaceous chondrites, such as the matrix, chondrules (consistent with observations from Schwander et al. (2015b) and Wang et al. (2007)), and sulphides; though the majority of RMNs are still found in CAIs. The chemistry of RMNs reveals a complex diversity of compositions, which nevertheless averages to CI chondrite abundance ratios. This implies that RMNs are the dominant, if not sole host phase for PGEs. One hundred and thirteen RMNs from this study are combined with reported compositions in the literature, and compared to condensation model compositions similar to Berg et al. (2009), RMNs derived experimentally by precipitation (Schwander et al., 2015a), host phase and host meteorite. Comparisons reveal only weak correlations between parent body processes (sulphidation) and nebular processes (condensation and precipitation) with RMN compositions. It appears that none of these processes acting in isolation or in tandem can explain the diversity observed in the RMN population. Our interpretation is that the Solar Nebula inherited an initially compositionally diverse population of RMNs from the Giant Molecular Cloud; that a variety of Solar System processes have acted on that population; but none have completely homogenised it. Most RMNs have experienced disk and asteroidal processing, but some may have retained a primordial composition. RMNs have been identified in pre-solar graphite grains (Croat et al., 2013). We anticipate that pre-solar RMNs will be present elsewhere in primitive meteorites.

Keywords: Refractory Metal Nuggets; Solar Nebula; Solar System; Origin; Meteorites; Carbonaceous chondrites

* Corresponding author.
E-mail address: luke.daly@postgrad.curtin.edu.au (L. Daly).

http://dx.doi.org/10.1016/j.gca.2016.11.030
0016-7037/

Please cite this article in press as: Daly L., et al. *In situ* analysis of Refractory Metal Nuggets in carbonaceous chondrites. *Geochim. Cosmochim. Acta* (2016), http://dx.doi.org/10.1016/j.gca.2016.11.030

1. INTRODUCTION

Ca–Al-rich inclusions (CAIs) are the oldest solids to have formed in the Solar System, with an age of 4567.30 ± 0.16 Ma (Connelly et al., 2012). CAIs have been interpreted as primary high-temperature condensates which formed close to the protosun during the initial stages of the Solar Nebula, although some inclusions have experienced some degree of remelting (MacPherson et al., 2005). Analyses of CAIs indicate a significant enrichment in the platinum group elements (PGEs) W, Re, Os, Ir, Ru and Pt of between 22.8 and 11.9 times the elemental abundance observed in carbonaceous Ivuna-type (CI) chondrites (Grossman, 1973; Wänke et al., 1974). This enrichment was predicted to manifest itself in the form of Refractory Metal Nuggets (RMNs) within these early condensates (Grossman and Ganapathy, 1976). This was confirmed by the observation of PGE-rich metal grains within CAIs in Allende (Palme and Wlotzka, 1976; Wark and Lovering, 1976).

Since this discovery, there has been ongoing debate over how RMNs formed. Initially Palme and Wlotzka (1976) found the composition of the RMN contained within a 20 μm CAI-hosted sulphide from Allende, plotted onto an ideal condensation curve for a nebular gas. These authors demonstrated that this RMN could form as a homogeneous primary condensate in the Solar Nebula, noting the high 50% condensation temperatures of the PGEs within the RMN would imply that these alloys should condense first. The RMN contained CI abundance ratios of the PGEs which indicated an equilibrium condensation temperature slightly higher than that of Fe. They also calculated that the expected abundance of RMN nucleation centres in the nebular would be sufficient, although this has been disputed by later studies (Petaev and Wood, 2005). However, subsequent studies have shown that these RMNs described by Palme and Wlotzka (1976) and Wark and Lovering (1976) had also been affected by secondary alteration on the parent body, including oxidation, sulphurisation, and exsolution (Bischoff and Palme, 1987; Blum et al., 1988; Palme and Wlotzka, 1976). These RMNs, therefore, cannot be considered primary nebular condensates (Bischoff and Palme, 1987; Blum et al., 1988).

To ascertain whether such grains could be produced from condensation in the Solar Nebula, Grossman (1973) calculated the chemical composition of the solid phases that would condense from a cooling solar gas. This work has been developed and refined with more recent calculations for condensation in the Solar Nebula by Fegley and Palme (1985) and Lodders (2003). These studies indicated that the PGEs should condense between 1392 K and 1821 K at 10^{-4} bar. However, it should be noted that local variability in the nebula dust component may cause these predicted condensation temperatures to vary (Petaev and Wood, 2005). RMNs appear to be the host for these elements in primitive carbonaceous chondrites. These predictions were supported by observations of sub-μm RMNs hosted within unaltered 'fluffy' type A CAIs from Allende. These RMNs had compositions consistent with a condensation origin, particularly, the presence of elements such as Mo and W, which are easily lost with even minor degrees of alteration (Palme et al., 1998). These RMNs also exhibited none of the secondary alteration textures observed in previous studies (Blander et al., 1980; Eisenhour and Buseck, 1992). Individual RMNs with compositions consistent with condensation origin have also been described by Eisenhour and Buseck (1992).

Further analysis of RMNs divided them into two distinct families within CAIs (El Goresy et al., 1978): large 1–1000 μm multiphase inclusions containing micrometre-sized grains of RMNs (Blum et al., 1988), and isolated micrometre to sub-micrometre RMNs (Wark, 1986). Studies by El Goresy et al. (1977) and El Goresy et al. (1978) suggested that RMNs in multiphase inclusions had non-solar abundance ratios of PGEs and that isolated RMNs had solar abundance ratios. This indicated, alongside the condensation sequence of minerals which hosted the multiphase inclusions, that they could have had a pre-solar origin and conversely isolated grains may have had a nebular origin. However, such an origin for the multiphase inclusions is unlikely as these samples yielded solar isotopic ratios for Mg, Fe, Mo, Ru and W (Hutcheon et al., 1987). A pre-solar origin for RMNs has also been suggested by Wark and Lovering (1976) for non-solar PGE abundance ratios within isolated RMNs. Recent work has observed RMNs within pre-solar graphite (Croat et al., 2013) and a possible mechanism for the formation pre-solar-RMNs in asymptotic giant branch stars was discussed in Schwander et al. (2014). These are the only RMNs that can be interpreted as having a pre-solar origin with relative certainty, though due to their small size, isotopic analyses have not been possible.

The analysis of RMNs has been limited by the difficulty of finding sufficient numbers due to their small size. This has meant that the contextual work on RMNs has been restricted to CAIs. Anders et al. (1975) noted that PGEs were enriched in residue samples of Allende (CV3oxA) that have been dissolved with strong acids. This observation prompted Berg et al. (2009) to study similar residues from the Murchison (CM2) meteorite using an acid digestion technique devised by Amari et al. (1994). This procedure concentrated RMNs and permitted the analysis of several hundred grains rather than the < 20 analysed *in situ* in CAIs from previous studies. Following earlier work, Berg et al. (2009) proceeded with the assumption that RMNs in their residues had previously been associated with CAIs. The compositions of RMNs contained within these residues from energy-dispersive X-ray spectroscopy (EDS) were in agreement with theoretical equilibrium condensation calculations for similar grains (Campbell et al., 2001). This led Berg et al. (2009) to conclude that all the analysed grains were nebula condensates. However, later work by Schwander et al. (2014), who used an extra density separation to further concentrate RMNs, from Murchison, Allende and Leoville residues, showed that some, but not all RMNs from these residues have been affected by metamorphic oxidation and sulphidation on the parent body which resulted in the loss of W and Mo.

Please cite this article in press as: Daly L., et al. *In situ* analysis of Refractory Metal Nuggets in carbonaceous chondrites. *Geochim. Cosmochim. Acta* (2016), http://dx.doi.org/10.1016/j.gca.2016.11.030

The abundant grains found in acid residues have significantly expanded the number of analyses of RMNs, but the loss of contextual information during acid dissolution of the bulk sample severely limits interpretation of the data. The assumption that has arisen in prior studies is that RMNs are unique to CAIs (Berg et al., 2009; Bischoff and Palme, 1987; Blander et al., 1980; Eisenhour and Buseck, 1992; El Goresy et al., 1978; Fegley and Kornacki, 1984; Grossman et al., 1977; Palme and Wlotzka, 1976; Palme et al., 1982; Sylvester et al., 1990; Wark, 1986; Wark and Lovering, 1976). However, recent work by Wang et al. (2007) described RMNs within chondrules. Schwander et al. (2015) analysed over 200 RMNs *in situ* including the observation of RMNs within the matrix. This study suggests that the compositions of RMNs and their petrological context are inconsistent with a simple condensation model and that precipitation is a more likely mechanism for RMN formation, whereby the PGEs are dissolved into a silicate, or CAI melt. On quenching of this melt spherical RMNs are precipitated. This theory is supported by experimentally derived RMN-like precipitates from CAI melts in Schwander et al. (2015).

A diversity of terms can be found in the literature applied to these materials. In this study we will adopt the following terminology: RMNs will refer to any micrometre – sub-micrometre metal alloy grain that contains >1 atomic percent (at.%) of any PGE (Re, Os, Ir, Pt, Ru, Rh, Pd, W or Mo). If there is sufficient evidence to suggest a mechanism for how the RMN formed, a suitable precursor shall be attached to the start of the word i.e. pre-solar-RMN for an RMN with a demonstrably pre-solar origin similar to the naming scheme adopted by Croat et al. (2013). This can be extended to any process, e.g. sulphidation would produce sulphidation-RMNs, and primary nebular condensates would be designated condensation-RMNs, etc.

This paper presents a multidisciplinary study using the Australian Synchrotron (AS) X-ray Fluorescence (XRF) beamline alongside scanning electron microscopy (SEM) with EDS to facilitate rapid identification of RMNs *in situ*. The applications of these techniques allow rapid non-destructive quantification and determination at sub-micrometre scales whilst preserving context. The results of these analyses call into question the assumption that RMNs are unique to CAIs: we observe them in all chondritic components; reiterating and expanding upon observations made by Schwander et al. (2015) andWang et al. (2007). Comparing RMN compositions to equilibrium condensation models revealed a significant inconsistency. This suggests condensation in the nebular environment is unlikely for a large fraction of RMNs.

2. METHOD

The samples analysed in this study are thin and thick sections from the primitive carbonaceous chondrites: C2-ungrouped Acfer 094, C2-ungrouped Adelaide, CO3.0 ALH77307, CV3 Allende, CR2 Kaidun, CR2 Renazzo, and Murchison CM2, and CV3 Vigarano. Each thin sections has an area of approximately 1–4 cm^2.

2.1. X-ray fluorescence microscopy

The samples were analysed using the XRF beamline at the AS, combined with the Maia detector; a custom made 384 Si-diode detector (Ryan et al., 2010) with a dwell time of 0.488 ms per pixel. A more detailed discussion of the technique and its application to meteorites can be found in Dyl et al. (2014). This technique allows for rapid data collection over large areas with a resolution of 2 μm. The detector can analyse elements between the 4 and 18 keV range (Ryan et al., 2010). A particularly useful detail for this study is that PGE Lα, β, and γ energy peaks for Os, Ir and Pt lie in the most sensitive region of the spectrum (Fig. 1), with L-α peaks at 8.910, 9.174 and 9.441 keV, respectively (Dyl et al., 2014). This permits detection down to 50–100 ppm for these elements (Cleverley et al., 2012).

The data collected was interpreted using the GeoPIXE software, which uses a dynamic analysis matrix to deconvolve peaks of each individual element to generate elemental distribution maps (Ryan et al., 1995). The element maps are used to identify pixel-sized hotspots of PGEs as likely candidates for the location of RMNs with slight adjustments to contrast and brightness to make the most abundant regions stand out from the background.

The sample of Acfer 094 had been gold-coated for previous studies, and although this has been largely removed, a small residue remains. This generated a slight problem as the gold peak is in the same region of the spectrum as the Os, Ir, and Pt energy peaks. This interfered with the spectrum, and generated false positives. In the case of this sample, the problem was countered by analysing each spectrum on an individual basis to ensure true RMNs were observed rather than a residual gold particle.

Due to the penetrating nature of the X-ray beam employed (18.5 keV), fluorescence X-rays from elements are received from up to 100 μm depth into the sample (Dyl et al., 2014). This generates a problem when trying

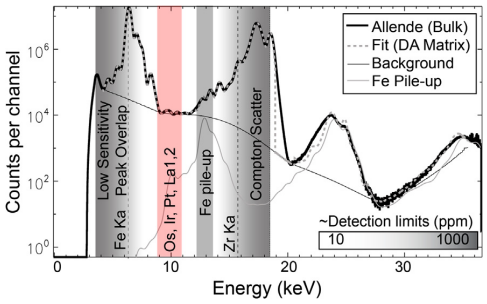

Fig. 1. Bulk Synchrotron spectrum from Allende; with the raw data depicted by the bold line and the fit calculated by GeoPIXE™ indicated by the dashed line. The solid and thinner black line signifies the background contribution to the spectra. Taking into account contributions such as the large iron peak and secondary pile up peak, along with the Compton scatter region, the detection limits are highlighted by the greyscale gradient map. The location of the Lα peaks for Os, Ir and Pt are highlighted in red and sit in the region of highest sensitivity and lowest detection limits. Image adapted after Dyl et al. (2014).

Please cite this article in press as: Daly L., et al. *In situ* analysis of Refractory Metal Nuggets in carbonaceous chondrites. *Geochim. Cosmochim. Acta* (2016), http://dx.doi.org/10.1016/j.gca.2016.11.030

to corroborate PGE hotspots with established techniques such as SEM and EDS, which only have penetration depths of ~1 μm. This, coupled with the size of the RMNs, which tend to be 90 nm–1.2 μm (Berg et al., 2009) means that any one PGE hotspot identified with the synchrotron has a 99% chance of being buried beneath the surface of the sample. However, this is also a benefit as a larger number of *in situ* grains are observed.

2.2. Scanning electron microscopy

The samples were analysed using two instruments: the Zeiss 1555 VP-FESEM at the Centre for Microscopy, Characterisation and Analysis (CMCA), University of Western Australia, and the Zeiss EVO50 LaB6 at the Australian Centre for Microscopy and Microanalysis (ACMM), the University of Sydney. Both instruments are equipped with 80 mm^2 high count rate silicon drift detector (SDD) EDS detectors. In both cases an accelerating voltage of 25 kV was used. Element maps derived from the AS data were geo-referenced with the live SEM image using the image overlay feature in Oxford Instrument's AZtec software. This method allowed rapid searching for RMNs present at the surface of the sample with high accuracy. This process was augmented by the feature mapping software in the Inca suite, which allowed whole thin section searches based on contrast bands. As RMNs are one of the densest phases in meteorites and backscatter microscopy reveals density differences in mineral phases; the brightest spots were refractory metal grains. This allowed us to analyse every metal grain at the surface of a sample. This method detected all the RMNs that were found using the combined synchrotron and EDS geo-referencing technique described above, along with a few others that were missed. The composition of the grains was derived using standardless quantitative analysis, using the standard database embedded within the Aztec software. Although a total of 145 RMNs were measured, the EDS spectra obtained through the feature mapping technique did not permit quantitative compositional measurements. 113 RMNs were relocated in the sample and a second EDS measurement was taken with a longer live time and with a process time of 5, enabling better energy resolution and detection limits. Elemental abundances for Ru, Mo, W, Re, Os, Ir and Pt were derived using the L-α X-ray lines in the spectra which are better separated than the M lines. Fe and Ni abundances were calculated using the K X-ray lines. Detection limits for elements within RMNs were <2 at.% for small RMNs and <1 at.% for larger RMNs. The relative uncertainty in these measurements is approximately ±10% providing sufficient accuracy to detect major and minor elements and draw comparisons between measured RMN compositions in different meteoritic components.

As the interaction volume of the EDS measurements is significantly larger than the RMN, we would expect some contribution from the surrounding phases in the spectra. Therefore, we have corrected and renormalised our data using a the same methodology as Schwander et al. (2015); removing elements present in the surrounding host phase such as Mg, Ca, O, Al, Si, etc, and only retaining elements present in RMNs: Fe, Ni, Ru, Rh, Mo, W, Re, Os, Ir, and Pt (Harries et al., 2012). As Schwander et al. (2015) described, it should be noted that Fe may be slightly overestimated in some samples due to small amounts of Fe in the surrounding phases, increasing the Fe signal. Also Ni and Fe are likely to be elevated in RMNs found in Fe–Ni sulphides due to the contribution of Fe and Ni in the host. RMN compositions were converted to atomic percent (at. %) and renormalised.

Some RMNs were extracted from the sample using a Focussed Ion Beam (FIB) technique using the Zeiss Auriga FIB-SEM at the ACMM, the University of Sydney. A thin protective layer of Pt was deposited using secondary electrons followed by a much thicker Pt layer deposited using Ga ions. The sample was then cut out using the Ga beam and extracted using a Kleindiek micromanipulator and welded to a Cu transmission electron microscopy mount by depositing more Pt. The sample was thinned down to 100 nm using a fine Ga beam. The samples were analysed using transmission Kikuchi diffraction (TKD) on a Zeiss ULTRA Plus FEG SEM at the ACMM, the University of Sydney. EDS data from the RMNs in each section were collected with an X-Max 20 mm^2 SDD EDS detector using an acceleration voltage of 30 kV. The same X-ray lines used to calculate elemental abundances, and the detection limits and uncertainty are similar to those described above. As Pt was used as a protective layer it is likely that we could observe an enrichment in the Pt signal from fluorescence in the chamber. Samples prepared in this way are denoted by a'*, in Table 3.

2.3. Condensation model and precipitation proxy

An exhaustive literature search was conducted in an attempt to produce a library of all previous RMN compositional data (Berg et al., 2009; Bischoff and Palme, 1987; Blander et al., 1980; Wark and Lovering, 1976; Wark, 1986; Palme et al., 1982; Croat et al., 2013; Schwander et al., 2014; Palme et al., 1994; Wark and Lovering, 1978; Harries et al., 2012; Schwander et al., 2015). We also include compositions of synthetic RMNs thought to be derived from precipitation processes (Schwander et al., 2015), as well as RMNs observed in cosmic spherules (Rudraswami et al., 2014). These analyses were plotted alongside observed RMN compositions from this study.

Compositions for hypothetical RMN condensates were calculated using the approach described in Palme and Wlotzka (1976) with slight modification. A set of ten non-linear equations were specified for the elements Fe, Ni, Ru, Pt, Rh, Mo, Ir, Os, Re and W, each of the form of Palme and Wlotzka (1976), equation [6]. Values for the cosmic abundances were taken from Lodders (2003). The equations were solved using a non-linear equation solver embedded in the Mathematica™ package at 10^{-3} and 10^{-4} bars for temperatures from 1200 to 1700 K with 10 K increments to produce a set of alloy compositions, *calc*, where *calc* is a 1 × 10 matrix consisting of the mole fractions of the ten specified elements. Residuals, $\Sigma(obs_i - calc_{i,T})^2$, were calculated where i represents each of the 10 elements, *obs* is the 1 × 10 matrix of the analysed

Please cite this article in press as: Daly L., et al. *In situ* analysis of Refractory Metal Nuggets in carbonaceous chondrites. *Geochim. Cosmochim. Acta* (2016), http://dx.doi.org/10.1016/j.gca.2016.11.030

alloy compositions for the 10 elements, obs_i is the mole fraction of element i in the alloy of interest, and $calc_{i,T}$ is the mole fraction of element i in the calculated alloy at specified temperature T. Residuals were calculated at each temperature for each alloy, and the temperature with the minimum residual for each alloy was chosen as the best guess of the temperature at which that alloy equilibrated with the fractionated Solar Nebula. Pressures of 10^{-4} bar provided smaller residuals and compositions calculated at this pressure were therefore used. Oxide compounds of W and Mo were excluded from the model, and all activity coefficients were set to 1, in accordance with other condensation models (Berg et al., 2009; Harries et al., 2012). Temperatures were calculated for analysed RMNs using the same methodology as Berg et al. (2009): using a least squares fit for each RMN composition to the predicted composition as a function of temperature for pressures 10^{-3} bar and 10^{-4} bar. The results of Harries et al. (2012) were used as a check for the method and were found to be generally consistent with the results obtained in this model.

3. RESULTS

.

3.1. Synchrotron

In depth analyses of the element maps derived from the AS were used to target and identify hotspots of PGEs. The vast majority of observed hotspots are pixel-sized, indicating grains are <2 μm. Each carbonaceous chondrite section analysed yielded an average of 10 hotspots per sample, with a maximum of 71 in Vigarano and a minimum of two in Adelaide and Acfer 094. The proximity of the Kα and Lα peaks of the PGEs to each other and major elements such as Zn, combined with the penetration depth, make it difficult to deconvolve the spectrum into individual element peaks. This means that the spectrum's shape is defined by the most abundant element in that energy range. Great care was taken in analysing the spectra to avoid misidentification due to peak overlaps; removing false positives. Most observed hotspots are located within CAIs as expected, however a number are observed within chondrules, sulphides, and matrix (Table 1). Kaidun and Renazzo seem to be dominated by matrix RMNs, although as these meteorites are brecciated and contain only rare small CAIs this may explain this preferred matrix association for RMNs in these meteorites.

Table 1
The number of PGE hotspots in each type of inclusion (CAI, chondrule, and matrix) observed within the Acfer 094, Adelaide, ALH 77307, Kaidun, Renazzo, and Vigarano meteorites, identified using the synchrotron XRF beamline.

Meteorite	Total RMNs	Host		
		CAI	Chondrule	Matrix
Acfer 094	2	0	1	1
Adelaide	2	1	0	1
ALH 77307	17	12	0	5
Kaidun	9	0	1	8
Renazzo	6	0	2	4
Vigarano	71	69	2	0

3.2. Synchrotron to SEM

Not all Synchrotron PGE hotspots yielded an RMN present on the surface of the sample in the SEM. This is expected due to the large penetration depth of synchrotron radiation. However, some hotspots revealed more than one RMN (Fig. 2). The feature mapping technique also increased the number of observed RMNs substantially, revealing several RMNs that the synchrotron data had not identified. Therefore, despite the low probability of observing RMNs at the surface with synchrotron radiation, the combination of these techniques, particularly the utilisation of the INCA feature mapping technique, identified 145 RMNs. These RMNs vary in size from 0.1 μm to 9.71 μm with an average of 1.2 μm, and a median of 0.88 μm. With the exception of two anomalously large (>5 μm) RMNs the vast majority are consistent with the size ranges described in other studies (Berg et al., 2009; Schwander et al., 2015). These RMNs were found across several meteorite samples; 2 in Adelaide, 86 in Allende, 37 in Vigarano, and 16 in ALH 77307. Most RMNs are found in CAIs (51) or sulphides which are hosted within CAIs, chondrules, and chondrule rims (79), but a number are observed within the matrix (9) and chondrules (6) of these meteorites (Fig. 3), Table 2). Of the 145 RMNs identified 113 have reliable EDS chemical analyses. The composition of the RMNs derived from EDS varies greatly between host and samples; Re and Rh were below detection limits for most RMNs analysed. The compositions of RMNs with reliable EDS data from this study are summarised in Table 3 and average compositions of RMNs for each inclusion and meteorite are detailed in Table 4.

4. DISCUSSION

4.1. Evaluation of the database

The deduction of elements such as Al, Ca, Mg, and O (which were present in the host phase and not from the RMN), from the RMN EDS measurement, resulted in small wt% totals. To evaluate whether this deduction and subsequent re-normalisation process has introduced any inherent biases or compound errors, each renormalised element was plotted in relation to the initial wt% total of PGEs + Fe + Ni before re-normalisation (Fig. 4). If the normalisation process was producing a systematic error, steep trends from small wt% totals to high wt% totals would be observed. However, these graphs had very shallow to flat trends indicating normalisation has not introduced significant bias.

4.2. RMNs within CAIs, chondrules and matrix

This study reveals that RMNs can be found within all components of carbonaceous chondrites. Current theories surrounding the origin of RMNs are tied to their assumed unique occurrence within CAIs e.g. Berg et al. (2009). CAIs

Please cite this article in press as: Daly L., et al. *In situ* analysis of Refractory Metal Nuggets in carbonaceous chondrites. *Geochim. Cosmochim. Acta* (2016), http://dx.doi.org/10.1016/j.gca.2016.11.030

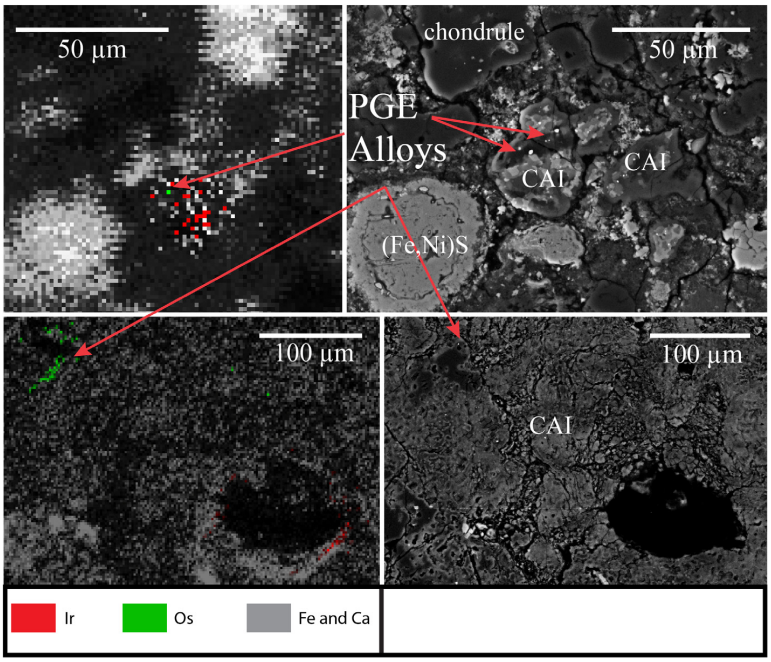

Fig. 2. Synchrotron element maps (left hand side) and corresponding SEM back scattered electron (BSE) images (right hand side) of the same regions in meteorites, indicating how elemental hotspots of PGEs in Synchrotron maps can be used to find RMNs on the surface of meteorite samples. Hotspots of the PGEs in synchrotron data (Ir in red and Os in green) relate to RMN localities on the surface of the thin section (bright points). The upper images were from the ALH 77307 meteorite and revealed RMNs within a Sc–Zr-rich CAI-like inclusion, and the lower images were from the Vigarano meteorite and revealed a single RMN within a zoned 'fluffy' type A CAI.

are thought to form initially as high temperature condensates (Grossman and Ganapathy, 1976; Wänke et al., 1974) (although most have experienced further processes such as remelting (MacPherson, 2005)). Therefore, the assumed model of formation for RMNs has been that they condensed at high temperatures in the same location and environment as CAIs (Grossman and Ganapathy, 1976). However, this single condensation event model is hard to reconcile with the myriad of compositions observed within RMNs (Grossman et al., 1977; Schwander et al., 2015). In addition, it should be borne in mind that CAIs affect the bulk composition of meteorites by enhancing refractory abundance above CI, indicating that CAIs were added to an approximately solar bulk 'background' composition. But in chemical analysis of matrix, or (CAI-absent) CI chondrite, we still observe PGEs. What then is the host phase of these elements? One possibility is finely comminuted CAI. However, if this were true, we would observe an enhancement in all refractory elements such as Ca and Al, which is not the case. Therefore RMNs in the matrix are unlikely to be broken fragments of CAIs as stipulated by Schwander et al. (2015) and are likely to have their own formation history. The chondrules that host the RMNs in this study do not appear to contain fragments of CAIs and the RMNs are contained within forsterite (Fig. 3), so similarly a CAI initial source for these chondrule-hosted RMNs is unlikely. The fact that we have now observed RMNs within matrix and chondrules demonstrates that CAIs are not a necessary factor in their formation. Indeed, their presence in chondritic components which formed at temperatures far below CAIs raises several new possibilities for RMN formation.

4.3. RMN compositional diversity

RMN PGE abundances compared to CI chondrite defined by (Lodders, 2003) (Fig. 5) show large enrichments and depletions relative to CI. Most RMNs are equally enriched or depleted in all refractory elements, however, some RMNs have significant relative depletions in Mo and W. The RMNs associated with this trend are principally hosted within sulphides, supporting the idea that sulphidation mobilises Mo and W (Palme et al., 1998). Nevertheless, the average RMN composition approximately follows a CI chondrite trend indicating that these refractory elements are primarily hosted within RMNs in meteorites. This expands the observation of Schwander et al. (2015): that the average composition of RMNs matches that of the PGE content of the bulk CAI to encompass the whole meteorite.

Please cite this article in press as: Daly L., et al. *In situ* analysis of Refractory Metal Nuggets in carbonaceous chondrites. *Geochim. Cosmochim. Acta* (2016), http://dx.doi.org/10.1016/j.gca.2016.11.030

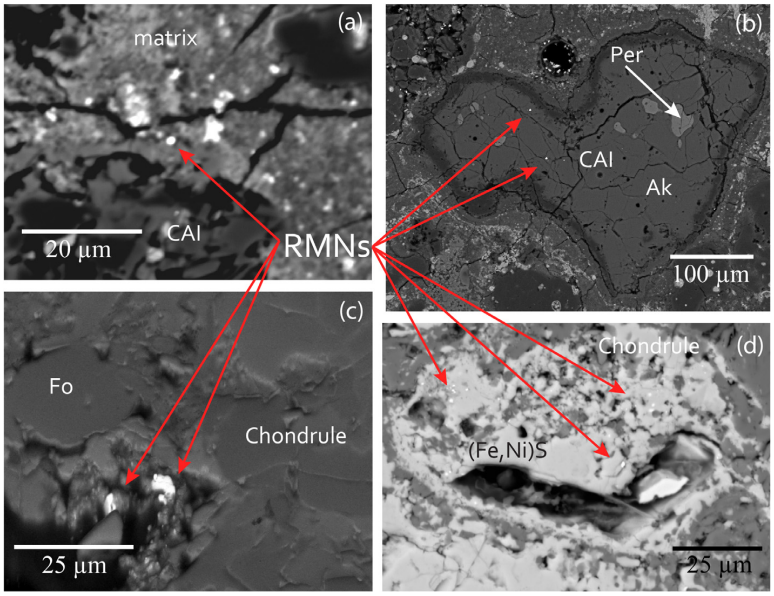

Fig. 3. SEM backscatter images of RMNs in all meteoritic components (a) RMN hosted in matrix from ALH 77307 in the vicinity of a CAI (b) RMN hosted in a åkermanite (Ak) and perovskite (Per)-rich CAI in ALH 77307, (c) RMN hosted in a chondrule in Allende within forsterite (Fo) (d) RMNs hosted within a (Fe-Ni) S rim around a chondrule in Allende.

Table 2
The abundance of RMNs in each type of inclusion (chondrule, matrix, sulphide and CAIs) observed within the Adelaide, ALH 77307, Allende, Murchison, and Vigarano meteorites. These RMNs were found by SEM and EDS analyses using the image overlay of synchrotron maps with PGE hotspots, and supplemented with RMNs identified using the INCA feature mapping software.

Meteorite	Total RMNs	Host			
		Chondrule	Matrix	Sulphide	CAI
Adelaide	2	1	0	0	1
ALH 77307	16	0	3	5	8
Allende	86	4	6	53	23
Murchison	4	0	0	2	2
Vigarano	37	1	0	19	17

4.3.1. RMN compositional diversity between inclusions

The total PGE contents of RMNs when compared with Fe and Ni (Fig. 6) reveal three main trends in the dataset: a Fe mixing line between 100 at.% PGE and 100 at.% Fe (black polygon); a Ni mixing line from 90 at.% PGE, 0 at.% Fe to 20 at.% PGE, 40 at.% Fe (red polygon); and a 'low PGE region' PGE < 30 at.% and 20–80 at.% Fe (green triangle). RMNs from acid residue studies were exclusively found within the high PGE portion of the Fe mixing line. These RMNs were significantly more PGE-rich and Fe and Ni-poor than most RMNs analysed *in situ*. RMNs in residues should contain RMNs from all meteoritic components which would include RMNs with high Ni and Fe contents. As this is not what we observe then it is likely that the process of concentrating RMNs in acid residues leaches RMNs of their Ni and Fe content. The low PGE region is primarily composed of matrix, chondrule and sulphide-hosted RMNs. CAI-hosted RMNs are evenly spread across all regions. The universal presence of CAI-hosted RMNs in all regions suggests that no single process equilibrated the composition of RMNs within CAIs.

Furthermore, the average chemical composition of RMNs within each host phase is significantly different (Table 4). Sulphide, matrix and chondrule hosted RMNs are depleted in most PGEs relative to CAI-hosted RMNs, and W and Mo are completely absent or in extremely low concentrations. There is a large range of RMN compositions observed within the dataset. We compared the observed spread of RMN compositions to the compositional distribution expected to be produced by proposed RMN forming processes, specifically: condensation, precipitation and sulphidation acting in isolation or in tandem.

Please cite this article in press as: Daly L., et al. *In situ* analysis of Refractory Metal Nuggets in carbonaceous chondrites. *Geochim. Cosmochim. Acta* (2016), http://dx.doi.org/10.1016/j.gca.2016.11.030

Table 3
RMN compositions from EDS in at.%, indicating the meteorite, inclusion, and host mineral phase. The data is also available in Supplementary Appendix 1.

Meteorite	Inclusion	Host	Fe	Ni	Ru	Rh	Mo	W	Re	Os	Ir	Pt
Adelaide	CAI	Anorthite	66.9	7.7	7.0	b.d.	14.1	b.d.	b.d.	b.d.	b.d.	4.3
Adelaide	Chondrule	Melilite	91.8	2.6	2.4	b.d.	b.d.	b.d.	b.d.	1.3	0.9	1.0
ALH 77307	CAI	ScZr-spinel	25.9	2.1	13.7	b.d.	21.0	2.6	b.d.	14.2	20.5	b.d.
ALH 77307	CAI	ScZr-spinel	43.0	3.4	13.9	b.d.	16.7	b.d.	b.d.	9.5	13.5	b.d.
ALH 77307*	CAI	Akermanite	46.3	6.7	13.1	3.2	14.8	b.d.	b.d.	4.6	2.9	8.3
ALH 77307*	CAI	Akermanite	40.0	3.8	9.1	b.d.	38.8	2.0	b.d.	2.8	1.4	2.0
Allende	CAI	Anorthite	58.5	2.7	10.9	b.d.	17.4	b.d.	b.d.	4.3	6.2	b.d.
Allende	CAI	Anorthite	46.4	13.6	15.0	b.d.	b.d.	b.d.	b.d.	7.7	12.9	4.5
Allende	CAI	Anorthite	16.1	29.2	14.4	b.d.	24.3	b.d.	b.d.	5.0	5.8	5.3
Allende	CAI	Forsterite	18.1	b.d.	44.5	b.d.	b.d.	b.d.	b.d.	22.6	14.8	b.d.
Allende	CAI	Forsterite	21.3	5.4	41.0	b.d.	6.0	b.d.	b.d.	12.4	13.9	b.d.
Allende	CAI	Forsterite	30.3	12.0	31.1	b.d.	2.7	b.d.	b.d.	10.2	13.6	b.d.
Allende	CAI	Forsterite	62.0	b.d.	19.1	b.d.	2.4	b.d.	b.d.	9.0	7.5	b.d.
Allende	CAI	Melilite	21.5	9.7	38.7	b.d.	b.d.	b.d.	b.d.	16.4	13.7	b.d.
Allende	CAI	Melilite	30.9	24.9	22.9	b.d.	b.d.	b.d.	b.d.	10.8	10.5	b.d.
Allende	CAI	Melilite	37.5	49.5	4.2	b.d.	b.d.	b.d.	b.d.	1.5	7.4	b.d.
Allende	CAI	Melilite	29.8	20.5	28.3	b.d.	b.d.	b.d.	b.d.	10.6	10.8	b.d.
Allende	CAI	Melilite	34.0	31.6	16.9	b.d.	b.d.	b.d.	b.d.	7.2	10.3	b.d.
Allende	CAI	Melilite	30.6	1.9	64.7	b.d.	b.d.	b.d.	b.d.	0.5	2.3	b.d.
Allende	CAI	Melilite	39.7	42.7	5.1	b.d.	b.d.	b.d.	b.d.	3.8	7.1	1.7
Allende	CAI	Melilite	33.7	59.5	b.d.	1.0	b.d.	b.d.	b.d.	0.2	0.9	4.7
Allende	CAI	Perovskite	44.5	b.d.	13.4	b.d.	22.8	b.d.	b.d.	9.1	10.2	b.d.
Allende	CAI	Perovskite	79.3	b.d.	20.7	b.d.	b.d.	b.d.	b.d.	b.d.	b.d.	b.d.
Allende	CAI	Pyroxene	35.3	5.5	26.3	b.d.	b.d.	b.d.	b.d.	18.8	14.2	b.d.
Allende	CAI	Pyroxene	21.7	1.3	43.2	b.d.	b.d.	b.d.	b.d.	16.9	16.9	b.d.
Allende	CAI	Pyroxene	20.3	b.d.	45.6	b.d.	b.d.	b.d.	b.d.	16.5	17.6	b.d.
Allende	CAI	Pyroxene	54.3	6.4	17.8	b.d.	b.d.	b.d.	b.d.	10.5	11.1	b.d.
Allende	CAI	Spinel	27.0	2.9	31.4	b.d.	17.0	b.d.	b.d.	11.4	10.4	b.d.
Allende	CAI	Spinel	49.4	3.6	15.6	b.d.	16.2	b.d.	b.d.	7.1	8.1	b.d.
Allende	Chondrule	Forsterite	32.4	64.4	0.5	b.d.	b.d.	b.d.	b.d.	b.d.	0.6	2.2
Allende	Chondrule	Forsterite	34.6	62.6	b.d.	b.d.	b.d.	b.d.	b.d.	b.d.	1.1	1.8
Allende	Chondrule	Forsterite	29.7	32.7	28.6	b.d.	b.d.	b.d.	b.d.	6.4	1.6	1.0
Allende	Chondrule rim	Forsterite	32.5	61.5	b.d.	b.d.	b.d.	b.d.	b.d.	b.d.	1.1	4.9
Allende	Chondrule rim sulphide	(Fe,Ni) S	68.9	28.6	b.d.	b.d.	b.d.	b.d.	b.d.	b.d.	b.d.	2.5
Allende	Chondrule rim sulphide	(Fe,Ni) S	71.5	27.7	b.d.	b.d.	b.d.	b.d.	b.d.	b.d.	b.d.	0.8
Allende	Chondrule rim sulphide	(Fe,Ni) S	65.9	29.2	b.d.	b.d.	b.d.	b.d.	b.d.	b.d.	0.8	4.2
Allende	Chondrule rim sulphide	(Fe,Ni) S	71.2	26.7	b.d.	b.d.	b.d.	b.d.	b.d.	0.2	0.3	1.5
Allende	Chondrule rim sulphide	(Fe,Ni) S	70.0	25.5	b.d.	b.d.	3.7	b.d.	b.d.	0.8	b.d.	b.d.
Allende	Chondrule rim sulphide	(Fe,Ni) S	71.8	26.6	b.d.	b.d.	b.d.	b.d.	b.d.	b.d.	b.d.	1.6
Allende	Chondrule rim sulphide	(Fe,Ni) S	84.2	11.1	b.d.	b.d.	3.4	b.d.	b.d.	b.d.	b.d.	1.3
Allende	Chondrule rim sulphide	(Fe,Ni) S	66.3	30.6	b.d.	b.d.	b.d.	b.d.	b.d.	b.d.	b.d.	3.0
Allende	Chondrule rim sulphide	(Fe,Ni) S	70.9	28.6	b.d.	b.d.	b.d.	b.d.	b.d.	b.d.	b.d.	0.5
Allende	Chondrule rim sulphide	(Fe,Ni) S	68.7	28.2	b.d.	b.d.	b.d.	b.d.	b.d.	b.d.	b.d.	3.1
Allende	Chondrule rim sulphide	(Fe,Ni) S	68.5	28.3	b.d.	b.d.	b.d.	b.d.	b.d.	0.2	0.5	2.4
Allende	Chondrule rim sulphide	(Fe,Ni) S	69.8	28.9	b.d.	b.d.	b.d.	b.d.	b.d.	b.d.	b.d.	1.3
Allende	Chondrule rim sulphide	(Fe,Ni) S	67.4	30.4	b.d.	b.d.	b.d.	b.d.	b.d.	b.d.	b.d.	2.2
Allende	Chondrule rim sulphide	(Fe,Ni) S	73.5	26.1	b.d.	b.d.	b.d.	b.d.	b.d.	b.d.	b.d.	0.4
Allende	Chondrule rim sulphide	(Fe,Ni) S	70.7	29.0	b.d.	b.d.	b.d.	b.d.	b.d.	b.d.	b.d.	0.3
Allende	Chondrule rim sulphide	(Fe,Ni) S	44.1	3.1	b.d.	b.d.	b.d.	b.d.	1.4	49.1	2.3	b.d.
Allende	Chondrule rim sulphide	(Fe,Ni) S	44.1	40.8	b.d.	b.d.	b.d.	b.d.	b.d.	b.d.	6.0	9.1
Allende	Chondrule rim sulphide	(Fe,Ni) S	57.8	35.3	b.d.	b.d.	b.d.	b.d.	b.d.	b.d.	4.1	2.8
Allende	Chondrule rim sulphide	(Fe,Ni) S	60.1	34.9	b.d.	b.d.	b.d.	b.d.	b.d.	b.d.	2.6	2.4
Allende	Chondrule rim sulphide	(Fe,Ni) S	63.5	29.9	b.d.	b.d.	b.d.	b.d.	b.d.	5.8	0.8	b.d.
Allende	Chondrule rim sulphide	(Fe,Ni) S	42.8	41.5	b.d.	b.d.	b.d.	b.d.	b.d.	b.d.	2.2	13.5
Allende	Chondrule rim sulphide	(Fe,Ni) S	49.1	48.2	b.d.	b.d.	b.d.	b.d.	b.d.	b.d.	1.8	0.9
Allende	Chondrule rim sulphide	(Fe,Ni) S	49.3	37.5	b.d.	b.d.	b.d.	b.d.	b.d.	b.d.	1.4	11.9
Allende	Chondrule rim sulphide	(Fe,Ni) S	46.2	40.5	b.d.	b.d.	b.d.	b.d.	b.d.	b.d.	2.6	10.7
Allende	Chondrule rim sulphide	(Fe,Ni) S	49.6	31.4	b.d.	b.d.	b.d.	b.d.	b.d.	b.d.	2.3	16.7
Allende	Chondrule rim sulphide	(Fe,Ni) S	39.1	46.7	b.d.	b.d.	b.d.	b.d.	b.d.	b.d.	3.3	10.9
Allende	Chondrule rim sulphide	(Fe,Ni) S	51.0	33.8	b.d.	b.d.	b.d.	b.d.	b.d.	b.d.	3.5	11.6

Please cite this article in press as: Daly L., et al. *In situ* analysis of Refractory Metal Nuggets in carbonaceous chondrites. *Geochim. Cosmochim. Acta* (2016), http://dx.doi.org/10.1016/j.gca.2016.11.030

Table 3 (*continued*)

Meteorite	Inclusion	Host	Fe	Ni	Ru	Rh	Mo	W	Re	Os	Ir	Pt
Allende	Chondrule rim sulphide	(Fe,Ni) S	62.6	34.5	b.d.	b.d.	b.d.	b.d.	b.d.	b.d.	1.3	1.6
Allende	Chondrule rim sulphide	(Fe,Ni) S	71.3	23.3	b.d.	b.d.	b.d.	b.d.	b.d.	b.d.	2.9	2.6
Allende	Chondrule rim sulphide	(Fe,Ni) S	47.1	39.1	b.d.	b.d.	b.d.	b.d.	b.d.	b.d.	7.7	6.2
Allende	Chondrule rim sulphide	(Fe,Ni) S	58.4	32.6	b.d.	b.d.	b.d.	b.d.	b.d.	b.d.	2.0	7.1
Allende	Chondrule rim sulphide	(Fe,Ni) S	66.3	32.5	b.d.	b.d.	b.d.	b.d.	b.d.	b.d.	b.d.	1.3
Allende	Chondrule rim sulphide	(Fe,Ni) S	61.3	32.4	b.d.	b.d.	b.d.	b.d.	b.d.	b.d.	2.5	3.8
Allende	Chondrule rim sulphide	(Fe,Ni) S	54.6	39.0	b.d.	b.d.	b.d.	b.d.	b.d.	b.d.	4.1	2.2
Allende	Chondrule rim sulphide	(Fe,Ni) S	46.2	39.4	b.d.	b.d.	b.d.	b.d.	b.d.	b.d.	3.7	10.7
Allende	Chondrule rim Sulphide	(Fe,Ni) S	56.7	36.1	b.d.	b.d.	b.d.	b.d.	b.d.	b.d.	2.5	4.7
Allende	Chondrule rim sulphide	(Fe,Ni) S	47.9	37.4	b.d.	b.d.	b.d.	b.d.	b.d.	0.5	11.1	3.1
Allende	Chondrule rim sulphide	(Fe,Ni) S	59.5	31.0	b.d.	b.d.	b.d.	b.d.	b.d.	b.d.	5.2	4.3
Allende	Chondrule rim sulphide	(Fe,Ni) S	67.7	27.4	b.d.	b.d.	b.d.	b.d.	b.d.	b.d.	5.0	b.d.
Allende	Chondrule rim sulphide	(Fe,Ni) S	47.8	35.4	b.d.	b.d.	b.d.	b.d.	b.d.	b.d.	9.1	7.6
Allende	Chondrule sulphide	(Fe,Ni) S	62.4	27.8	b.d.	b.d.	b.d.	b.d.	b.d.	b.d.	2.0	7.8
Allende	Chondrule sulphide	(Fe,Ni) S	61.3	32.8	b.d.	b.d.	b.d.	b.d.	b.d.	b.d.	b.d.	5.8
Allende	Chondrule sulphide	(Fe,Ni) S	62.2	30.8	b.d.	b.d.	b.d.	b.d.	b.d.	b.d.	6.1	0.9
Allende	Chondrule sulphide	(Fe,Ni) S	38.3	4.1	b.d.	b.d.	b.d.	b.d.	4.9	52.8	b.d.	b.d.
Allende	Chondrule sulphide	(Fe,Ni) S	65.5	28.1	b.d.	b.d.	b.d.	b.d.	b.d.	2.6	3.7	b.d.
Allende	Chondrule sulphide	(Fe,Ni) S	53.3	36.5	b.d.	b.d.	b.d.	b.d.	b.d.	1.2	4.1	4.9
Allende	Chondrule sulphide	(Fe,Ni) S	67.1	21.9	b.d.	b.d.	b.d.	b.d.	b.d.	9.3	1.8	b.d.
Allende	Chondrule sulphide	(Fe,Ni) S	54.1	34.2	b.d.	b.d.	b.d.	b.d.	b.d.	b.d.	3.9	7.7
Allende	Matrix	Melilite	51.4	46.5	b.d.	b.d.	b.d.	b.d.	b.d.	0.7	b.d.	1.3
Allende	Matrix	Melilite	40.6	58.4	b.d.	b.d.	b.d.	b.d.	b.d.	0.2	0.4	0.4
Allende	Matrix	Melilite	48.9	47.2	1.7	b.d.	b.d.	b.d.	b.d.	0.5	0.6	1.0
Allende	Matrix	Melilite	74.5	21.4	1.3	b.d.	b.d.	b.d.	b.d.	0.6	1.0	1.2
Allende	Matrix	Melilite	60.7	38.5	b.d.	b.d.	b.d.	b.d.	b.d.	b.d.	b.d.	0.8
Allende	Matrix	Melilite	66.3	33.5	b.d.	b.d.	b.d.	0.2	b.d.	b.d.	b.d.	b.d.
Allende*	Chondrule sulphide	Pentlandite	45.2	33.5	b.d.	b.d.	b.d.	b.d.	b.d.	b.d.	1.8	19.6
Allende*	Chondrule sulphide	Pentlandite	45.4	32.3	b.d.	b.d.	b.d.	b.d.	b.d.	0.7	4.8	16.8
Allende*	Chondrule sulphide	Pentlandite	51.9	31.8	b.d.	b.d.	b.d.	b.d.	b.d.	b.d.	6.7	9.7
Allende*	Chondrule sulphide	Pentlandite	29.0	63.6	b.d.	b.d.	b.d.	b.d.	b.d.	b.d.	7.4	b.d.
Allende*	Chondrule sulphide	Pentlandite & troilite	43.5	34.2	b.d.	b.d.	b.d.	b.d.	b.d.	b.d.	6.0	16.3
Murchison	CAI	Forsterite	77.5	4.7	7.9	b.d.	b.d.	b.d.	b.d.	2.2	3.3	4.4
Murchison	CAI	Perovskite	57.3	5.1	5.3	b.d.	24.3	1.6	b.d.	3.6	1.5	1.4
Murchison	CAI sulphide	(Fe,Ni) S	47.0	29.0	b.d.	b.d.	b.d.	b.d.	b.d.	15.7	7.2	1.1
Murchison	Matrix sulphide	(Fe,Ni) S	40.8	35.8	b.d.	b.d.	b.d.	b.d.	b.d.	2.5	3.8	17.0
Vigarano	CAI	Anorthite	53.0	40.8	4.4	b.d.	b.d.	b.d.	b.d.	0.5	0.6	0.7
Vigarano	CAI	Anorthite	55.8	40.6	2.9	b.d.	b.d.	b.d.	b.d.	b.d.	b.d.	0.7
Vigarano	CAI	Melilite	67.3	30.1	1.7	b.d.	b.d.	b.d.	b.d.	b.d.	b.d.	0.9
Vigarano	CAI	Pyroxene	72.2	1.8	b.d.	b.d.	7.5	4.6	b.d.	9.5	4.4	0.0
Vigarano	CAI	Pyroxene	61.1	34.2	2.0	b.d.	b.d.	b.d.	b.d.	0.5	0.5	1.6
Vigarano	CAI	Pyroxene	63.9	31.0	1.9	b.d.	b.d.	b.d.	b.d.	0.6	0.8	1.9
Vigarano	CAI	Pyroxene	67.5	28.2	1.8	b.d.	b.d.	b.d.	b.d.	b.d.	b.d.	2.5
Vigarano	CAI	Spinel	50.5	15.5	15.3	b.d.	11.8	b.d.	b.d.	3.1	2.6	1.2
Vigarano*	CAI	Anorthite	62.9	29.5	5.6	b.d.	b.d.	b.d.	b.d.	1.1	0.9	b.d.
Vigarano*	CAI	Anorthite	67.4	15.5	11.7	b.d.	b.d.	b.d.	b.d.	2.6	2.8	b.d.
Vigarano*	CAI	Anorthite	61.5	30.1	4.6	b.d.	b.d.	b.d.	b.d.	1.0	2.0	0.9
Vigarano*	CAI	Anorthite	65.7	14.1	14.2	b.d.	b.d.	b.d.	b.d.	2.4	3.7	b.d.
Vigarano*	CAI	Anorthite	55.4	39.2	2.4	b.d.	b.d.	b.d.	b.d.	0.7	1.0	1.4
Vigarano*	CAI	Anorthite	57.0	36.4	3.5	b.d.	b.d.	b.d.	b.d.	1.1	1.1	0.9
Vigarano*	CAI	Anorthite	64.4	17.7	10.8	b.d.	b.d.	b.d.	b.d.	3.4	3.7	b.d.
Vigarano*	CAI	Spinel	38.3	14.5	23.2	b.d.	13.1	b.d.	1.1	4.8	3.0	2.1
Vigarano*	CAI	Spinel & anorthite	48.8	48.6	1.7	b.d.	b.d.	b.d.	b.d.	0.4	b.d.	0.5

b.d., element was below detection limits for this RMN.
*RMNs prepared using FIB techniques.

4.3.2. Sulphidation as a RMN forming process

The high abundance of Fe–Ni-sulphide hosted RMNs contained within the low PGE region (Fig. 6) potentially allows us to interpret RMNs within this region as derived from, or affected by, sulphidation. If we assume that sulphide hosted RMNs were formed or had their composition modified by sulphidation, then either these RMNs have been affected by exposure to a S-rich gas in the nebula (Lauretta et al., 1996), and/or a parent body process has imposed a compositional fingerprint on these grains. The

Please cite this article in press as: Daly L., et al. *In situ* analysis of Refractory Metal Nuggets in carbonaceous chondrites. *Geochim. Cosmochim. Acta* (2016), http://dx.doi.org/10.1016/j.gca.2016.11.030

Table 4
Average RMN compositions in at.%, for each meteorite analysed in this study and and for each inclusion type.

Average RMNs	Fe	Ni	Ru	Rh	Mo	W	Re	Os	Ir	Pt
All RMN	39.1	20.9	11.9	1.6	10.9	1.6	1.8	5.3	3.8	3.3
Adelaide	73.4	4.7	4.4	b.d.	13.0	b.d.	b.d.	1.2	0.9	2.4
ALH 77307	36.6	3.7	11.7	3.0	21.5	2.2	b.d.	7.3	9.0	4.9
Allende	36.3	21.6	16.5	0.7	8.8	0.2	2.2	6.4	3.9	3.4
Murchison	45.4	15.2	5.4	b.d.	19.8	1.3	b.d.	4.9	3.2	4.9
Vigarano	51.4	23.7	5.8	b.d.	9.3	4.0	0.9	1.9	1.8	1.1
CAI	38.7	16.1	13.7	1.7	13.1	2.2	0.9	5.5	5.9	2.0
Chondrule	41.5	42.0	9.8	b.d.	b.d.	b.d.	b.d.	3.6	1.0	2.0
Sulphide	49.5	27.2	b.d.	b.d.	3.1	b.d.	2.7	9.3	3.2	5.0
Matrix	56.2	40.2	1.5	b.d.	b.d.	b.d.	b.d.	0.5	0.6	0.9

b.d., element was below detection limits for this RMN.

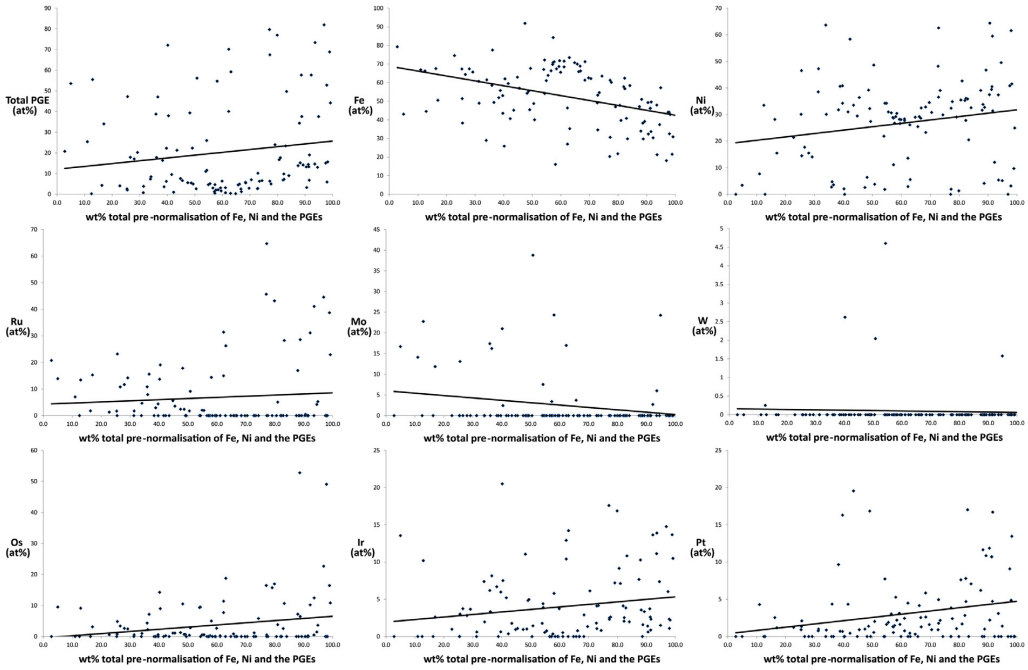

Fig. 4. At.% abundances of Fe, Ni and PGE elements vs the wt% total pre-normalisation of the RMN component in the EDS spectra for all samples from this study. The line in each graph represents a line of best fit through the data. These show relatively shallow trends which are significantly smaller than the overall compositional variability in at.% for each element. Therefore, it is unlikely that our re-normalisation calculations have introduced any significant bias to our dataset.

RMNs from this study are hosted in Fe-Ni sulphides and are therefore likely to be affected by parent body processes altering the chemistry of the sulphides from stochiometric troilite. It has been suggested that the presence of W and Mo could be used as an indicator for primitive RMNs as even low degrees of alteration would remobilise these two elements (Eisenhour and Buseck, 1992). Therefore, the fact that no W or Mo is observed in sulphide-hosted RMNs may be taken as evidence that these grains have been altered. We also do not observe any associated Mo or W dominated sulphide phases with these RMNs. We therefore expect that as the Fe-Ni-sulphide is significantly larger than the RMNs, the mobilised W and Mo become disseminated throughout the host sulphide during sulphidation, replacing Fe or Ni.

The fact that matrix, CAI and chondrule RMNs are also found within this region, that are not associated with sulphides suggests that this region is not a unique expression of sulphidation and other processes can produce RMNs with low PGE abundances. Therefore the compositional variance in the whole region cannot be explained completely by sulphidation.

Please cite this article in press as: Daly L., et al. *In situ* analysis of Refractory Metal Nuggets in carbonaceous chondrites. *Geochim. Cosmochim. Acta* (2016), http://dx.doi.org/10.1016/j.gca.2016.11.030

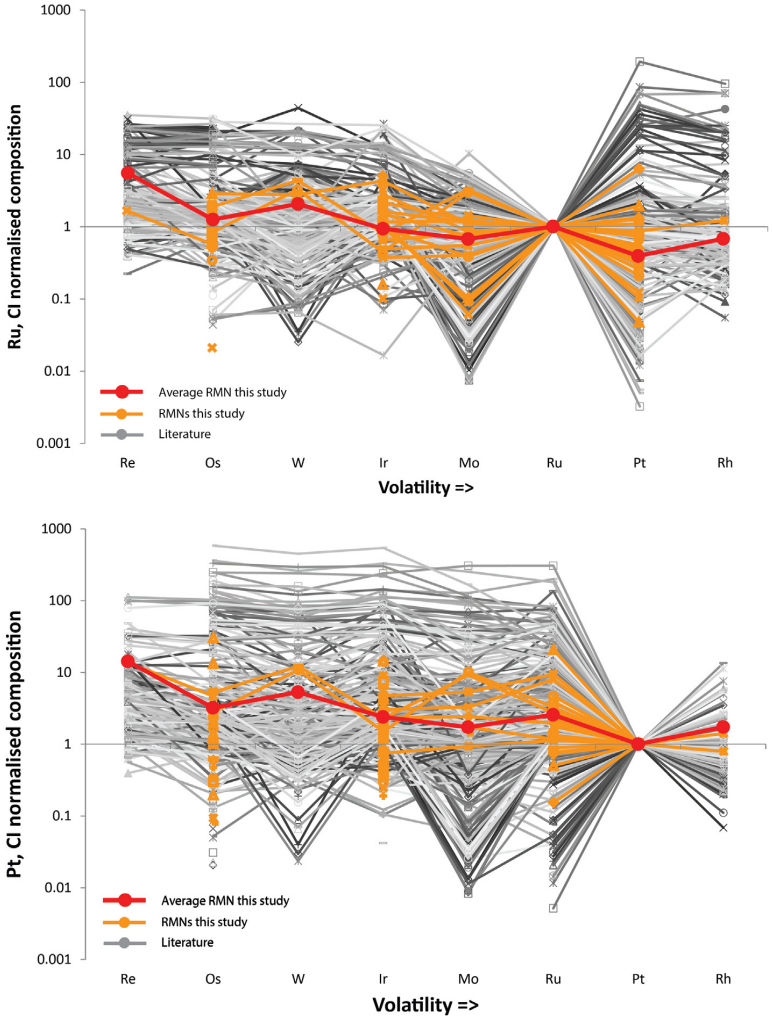

Fig. 5. RMN compositions from this study (orange), the average RMN from this study (red) and RMNs from our literature database (greyscale). PGEs have been plotted in order of increasing volatility and have been normalised to Ru then CI (top), or Pt then CI (bottom). These RMNs show a wide range of individual RMN compositions. However, the average RMN from this study has approximately CI chondrite relative abundance for these elements.

4.3.3. Condensation as a RMN forming process

Calculated RMN condensation temperatures show a reasonable agreement with condensation models for some elements, particularly Fe. However, other elements, such as Ru, Ir, Pt, and particularly Ni deviate substantially from the expected curve (Fig. 7).

To evaluate how closely the measured compositions of RMNs agree with modelled compositions, RMNs were grouped where every element is within 5 or 15 at.% agreement of the best fit calculated condensation composition (Fig. 8). As the tolerance is raised from 5 to 15 at.%, the number of RMNs consistent with condensation models increases from 5% to 50%. These RMNs are clustered exclusively along the Fe-mixing line. However, a significant portion of RMNs within the Fe-mixing line do not conform to the condensation model even at high tolerance levels. This indicates that condensation is not exclusively responsible for RMNs within the Fe mixing line. The abundance of RMNs consistent with our equilibrium condensation model in this study is similar to the abundance calculated in Schwander et al. (2014) in which only 4 out of 123 RMNs were consistent with

Please cite this article in press as: Daly L., et al. *In situ* analysis of Refractory Metal Nuggets in carbonaceous chondrites. *Geochim. Cosmochim. Acta* (2016), http://dx.doi.org/10.1016/j.gca.2016.11.030

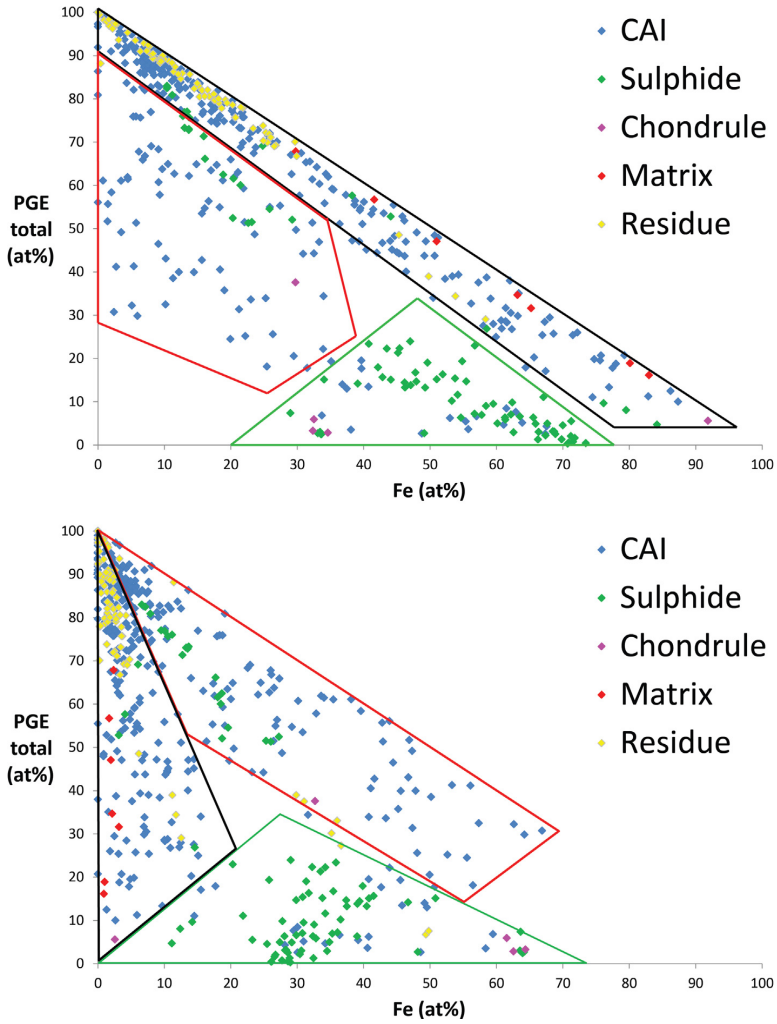

Fig. 6. Total PGE vs Fe and total PGE vs Ni plots by host phase (this study and the literature) indicating a well defined Fe-mixing trend (black polygon) a more dispersive Ni-mixing trend (red polygon) and a low PGE cluster (green triangle), which is dominated by sulphide phases.

an equilibrium condensation model. Interestingly, the 5% of RMNs that are consistent with condensation are hosted within opaque assemblages from Palme et al. (1994), cosmic spherules from Rudraswami et al. (2014), several CAIs with melting textures from Schwander et al. (2015), as well as a RMN from a chondrule rim sulphide (this study), all of which do not have textures consistent with condensation.

It is clear that predicted RMN compositions from current equilibrium condensation models cannot be reconciled with observations. Alternative condensation models, namely non-equilibrium condensation, fractional condensation and the effect of the activity coefficient will now be considered.

Previous equilibrium condensation models have assumed that the activity coefficients for each element are 1 (Berg et al., 2009). Schwander et al. (2014), noted that varying the activity coefficient would result in a migration of the condensation curve for each element. However, the systematic trend in RMN compositions would be maintained and therefore cannot account for the spread of observed RMN compositions.

Fractional condensation would result from successive periods of condensation followed by removal of RMNs from the reservoir, depleting it in the elements that had already condensed. The expected observations of this process would depend on the mechanism for isolating the RMNs from the condensing gas. If the RMNs were

Please cite this article in press as: Daly L., et al. *In situ* analysis of Refractory Metal Nuggets in carbonaceous chondrites. *Geochim. Cosmochim. Acta* (2016), http://dx.doi.org/10.1016/j.gca.2016.11.030

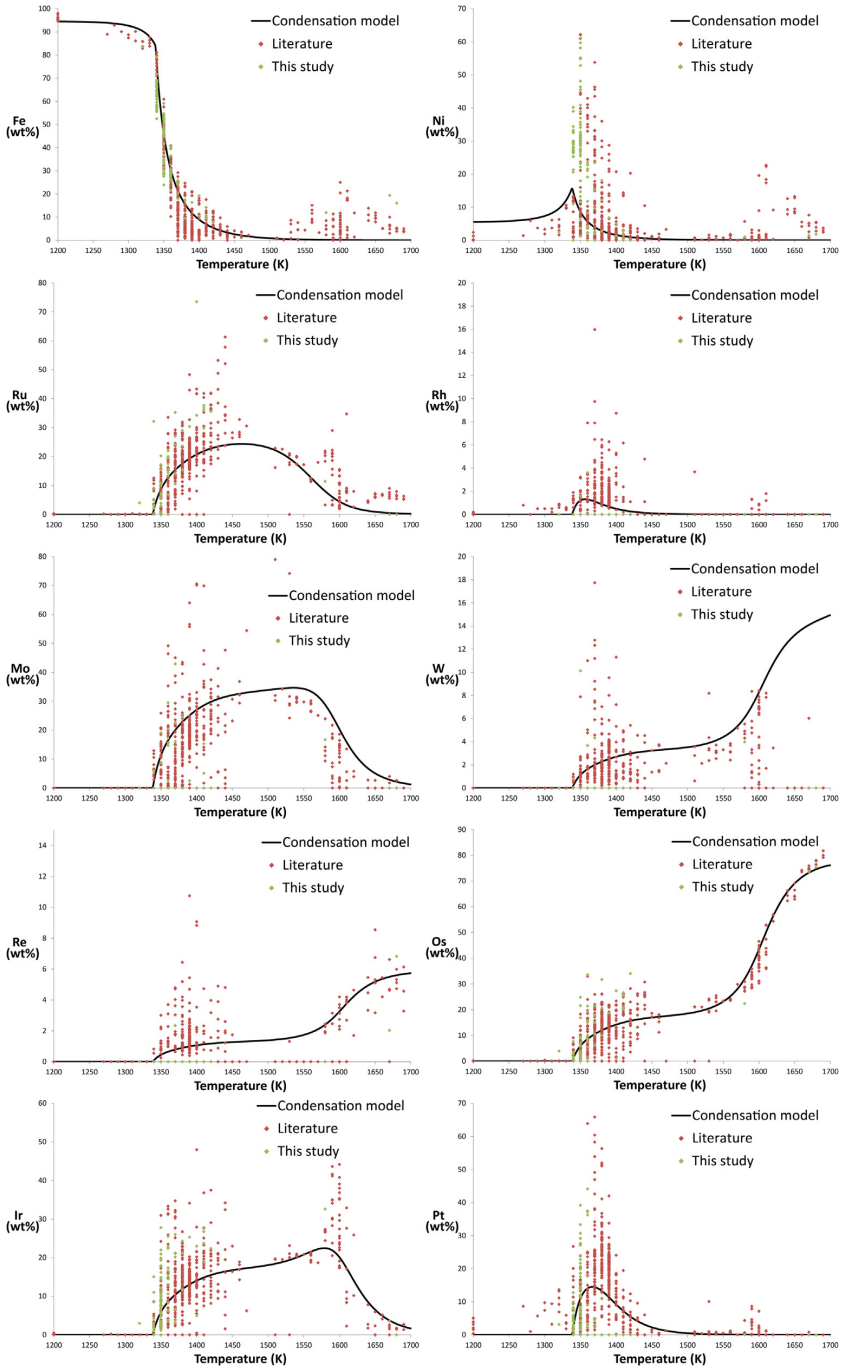

Fig. 7. A comparison of Fe, Ni and PGE abundance in wt% vs calculated equilibrium condensation temperature at 10^{-4} bar for RMNs from this study (green), and the literature (red). The data are plotted in the same format as Berg et al. (2009). RMN compositions exhibit good correlations with Fe and Mo but very poor correlations with Ni, Ru, Rh, Ir and Pt.

Please cite this article in press as: Daly L., et al. *In situ* analysis of Refractory Metal Nuggets in carbonaceous chondrites. *Geochim. Cosmochim. Acta* (2016), http://dx.doi.org/10.1016/j.gca.2016.11.030

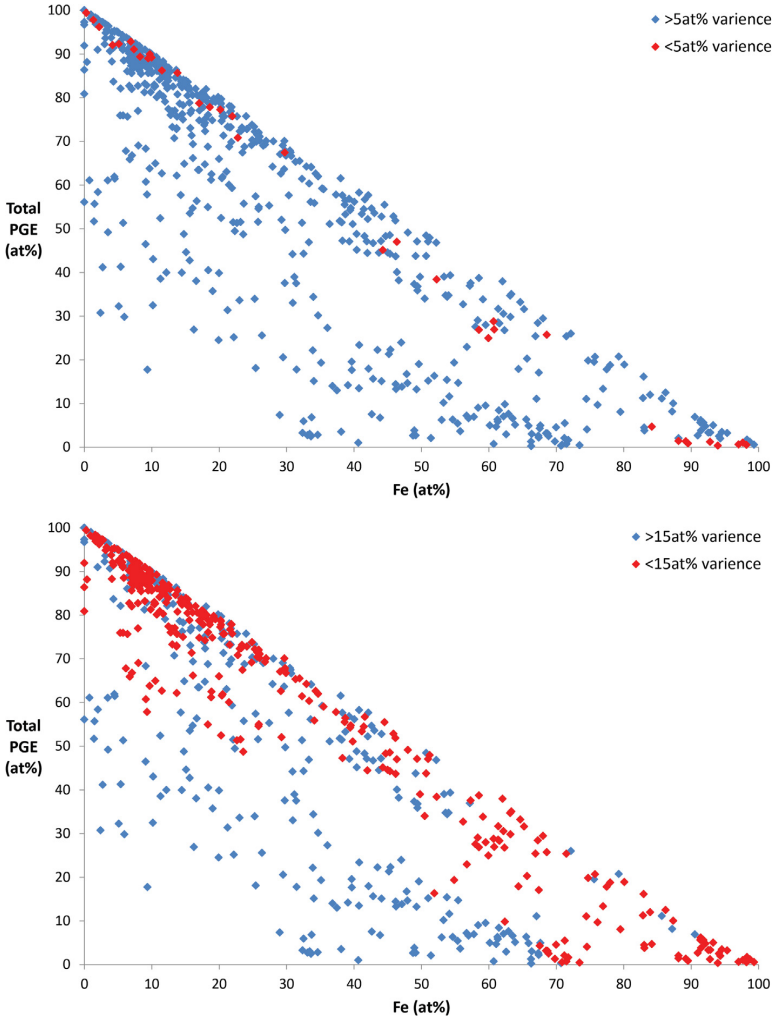

Fig. 8. Total PGE vs Fe abundance in at.%. These show all RMNs from this study and the literature are indicated by blue diamonds. The RMNs which match predicted equilibrium condensation compositions at 10^{-4} bar to within 5 at.% (top graph), and 15 at.% (bottom graph) are indicated with red diamonds.

removed by encapsulation within other condensing phases, we would expect to observe a mineralogical association with RMNs enriched in certain PGEs. For example, high temperature phases such as hibonite and corundum would be expected to bear RMNs enriched in the more refractory PGEs such as Os, Re, and W, while lower temperature phases such as Mg-spinel and anorthite would contain RMNs enriched in the more volatile PGEs such as Pt. Schwander et al., 2015 demonstrated that there is no systematic variability of RMN compositions with host phase. Therefore, this mechanism is unlikely. If the RMNs are physically removed from the reservoir we may expect to observe a chemically distinct RMN population within different host inclusions such as chondrules and CAIs. Fig. 6 revealed that the abundance of Fe and Ni in CAI hosted RMNs encompass the whole range of chemical compositions, including those occupied by sulphides, chondrules and matrix. This indicates that this mechanism for fractional condensation is also unlikely. We would also expect to observe clusters of RMNs with similar compositions which relate to the temperature they were fractionated from the condensing gas. However, no such clustering of RMN compositions is observed (see Fig. 6).

Non-equilibrium condensation, similar to other condensation models, is expected to produce a systematic trend in RMN compositions. The non-equilibrium condensation model produced by Tanaka et al. (2002) revealed that although the condensation temperatures

Please cite this article in press as: Daly L., et al. *In situ* analysis of Refractory Metal Nuggets in carbonaceous chondrites. *Geochim. Cosmochim. Acta* (2016), http://dx.doi.org/10.1016/j.gca.2016.11.030

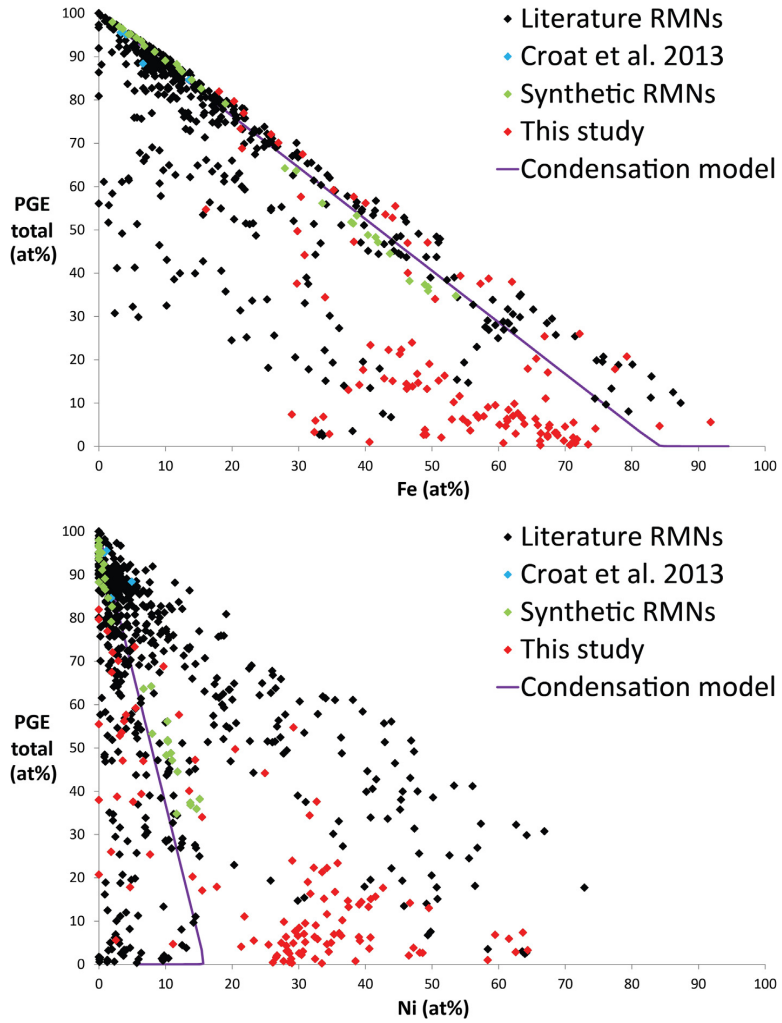

Fig. 9. Total PGEs vs Fe abundance in at.% for RMNs detailed in this study (red) and the literature (black) as well as pre-solar RMNs from Croat et al. (2013) (blue), synthetic RMNs produced by precipitation from Schwander et al. (2015) (green), and our condensation model calculated at 10^{-4} bar.

for certain PGEs may vary significantly, the overall condensation sequence for the elements within RMNs remains the same as that predicted for equilibrium condensation. Furthermore, we may expect to observe zonation in RMNs that condensed in this manner. However, zoning has not been reported in previous transmission electron microscopy studies of RMNs (Harries et al., 2012; Eisenhour and Buseck, 1992).

It is apparent that more complex nebular condensation models still result in RMNs with a systematic compositional trend. This cannot be reconciled with the large spread in the compositional data reported for RMNs. Therefore, nebular condensation is unlikely to be a dominant process in RMN formation.

4.3.4. Precipitation as a potential RMN forming process

Some RMNs have been demonstrably attributed to precipitation processes, where an RMN has crystallised from a melt; either in experimental studies (Schwander et al., 2015), or observed in cosmic spherules (Rudraswami et al., 2014). Although as cosmic spherules have a complex history of evaporation and remelting it is unclear whether these RMN compositions are derived from a pure precipitation process. When the synthetic RMNs are superim-

Please cite this article in press as: Daly L., et al. *In situ* analysis of Refractory Metal Nuggets in carbonaceous chondrites. *Geochim. Cosmochim. Acta* (2016), http://dx.doi.org/10.1016/j.gca.2016.11.030

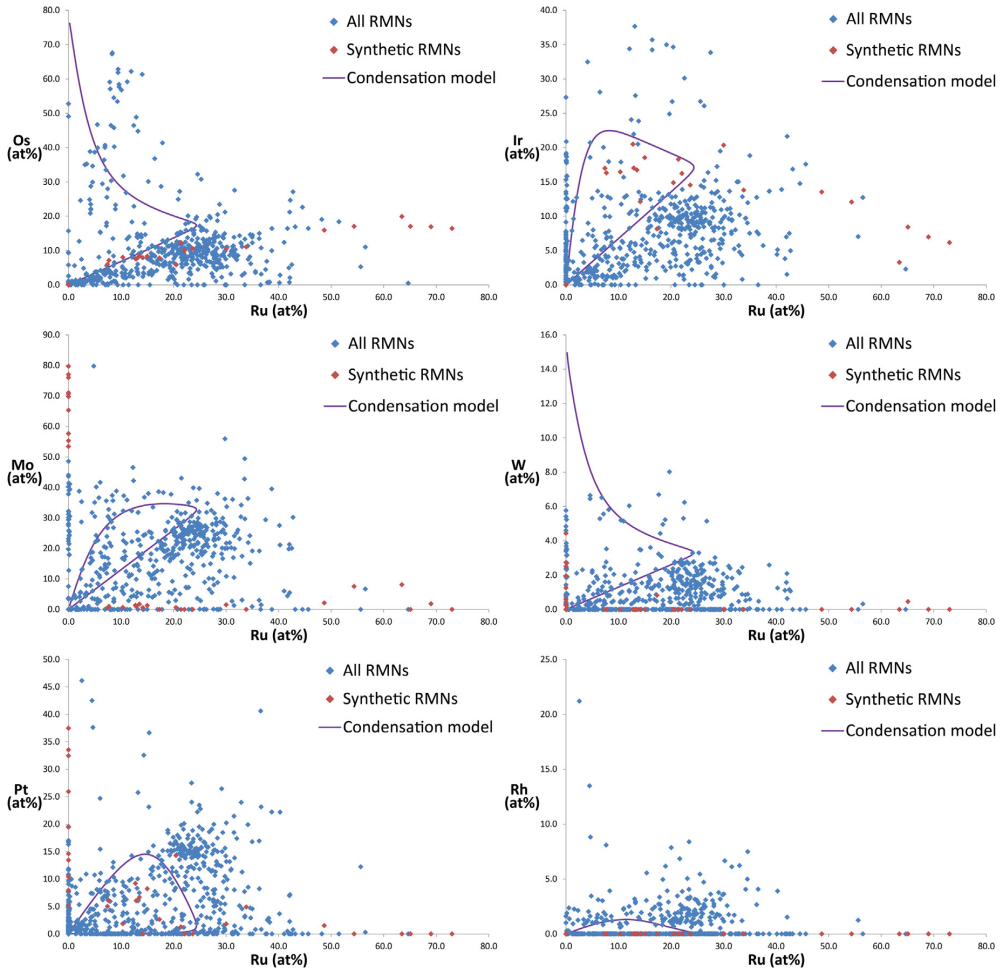

Fig. 10. Elemental ratio plots of each PGE vs Ru comparing RMNs from this study and the literature (blue) with precipitation derived RMNs from Schwander et al. (2015) (red) and our equilibrium condensation model at 10^{-4} bar (purple curve). These graphs show very weak or absent correlations of observed RMNs with predicted condensation model curves or synthetic RMNs formed by precipitation.

posed over RMNs analysed in this study and the literature (Fig. 9), precipitation RMNs fall along the Fe-mixing line in a similar trend to the condensation model curve. Therefore, even if we assume that the Fe-mixing line can be reconciled by a combination of condensation and precipitation processes there is still the Ni-mixing line which is inconsistent with all the processes we have described.

Considering each element in isolation, overlaying precipitation derived RMNs and our equilibrium condensation model curve over observed RMNs, from this study and the literature (Fig. 10), we reveal a further disparity. The spread of RMN compositions cannot be fully explained by precipitation Mo/Ru, W/Ru, Pt/Ru and Ir/Ru ratios for example do not match synthetic precipitates. Os/Ru at low Os concentrations does approximately follow a trend defined by synthetic precipitation derived RMNs, however there is also a population with very high Os abundances which is not consistent. Furthermore these RMN elemental ratios do not exhibit any association with the equilibrium condensation curve, except for a weak association in Os and Ir. Precipitation encounters the same problem as condensation; whilst it can produce compositions consistent with some RMN observations, it cannot explain them all. Furthermore, the population of RMNs that are consistent with condensation and precipitation are not complementary, and therefore cannot be an expression of both processes acting in tandem.

The synthetic RMNs derived from precipitation in Schwander et al. (2015) represent a single experiment, which naturally may not perfectly match nebula conditions. It is possible that precipitation could explain all RMN compositions if the experiments were carried out under different

Please cite this article in press as: Daly L., et al. *In situ* analysis of Refractory Metal Nuggets in carbonaceous chondrites. *Geochim. Cosmochim. Acta* (2016), http://dx.doi.org/10.1016/j.gca.2016.11.030

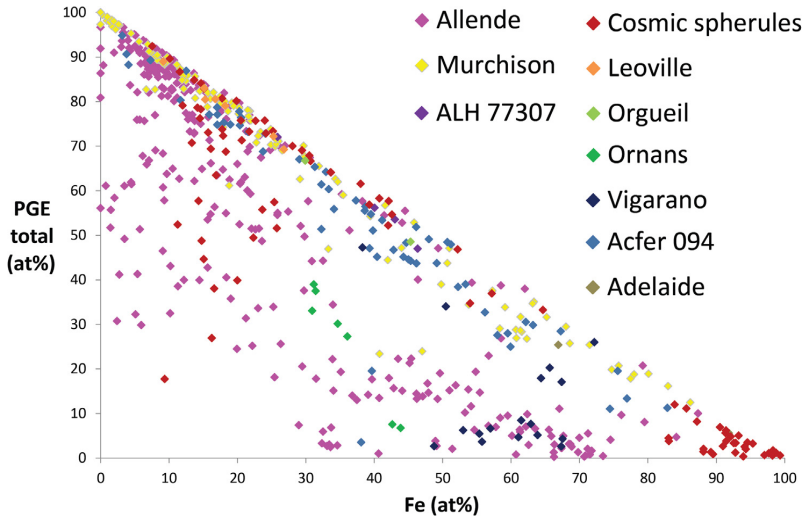

Fig. 11. Variability of total PGE vs Fe abundances (at.%) of RMNs in this study and the literature from the meteorites Allende, ALH 77307, Murchison, Leoville, Orgueil, Ornans, Vigarano, Acfer 094, Adelaide and those found in cosmic spherules.

conditions. However, there is a significant logical problem with the model. If all the PGEs are dissolved into a silicate or CAI-like melt, over time these elements will naturally become homogeneously distributed. Upon quenching the RMNs that do form should have homogeneous compositions within each inclusion. Heterogeneous RMNs would form only if PGEs are still heterogeneously distributed within the inclusion and were not molten for sufficient time to equilibrate. Therefore heterogeneous RMNs within remelted inclusions may not derive their heterogeneity from precipitation, but from an inherited heterogeneous distribution of the PGEs within the inclusion that did not equilibrate.

4.3.5. Other parent body processes

To ascertain if there is any variation between RMNs from different parent bodies, RMNs were separated according to meteorite (Fig. 11). Allende seems to encompass the whole range of RMN compositions. However, other meteorites cluster into certain regions. Murchison, Leoville, Orgueil, ALH 77307 and Adelaide represent certain portions of the Fe-mixing line. Ornans follows the Ni-mixing line into the low PGE region, and Vigarano contains RMNs from the low PGE region and the mid-section of the Fe-mixing line.

It is possible that this spread is due to a small dataset for some meteorites. However, the methodology used in this study would find most, if not all RMNs in a thin section, and all observed RMNs were analysed. Therefore it is possible that RMN populations may vary between parent bodies. In particular, the clustering of RMNs within Vigarano suggests this may be the case as several RMNs are observed and yet the spread of RMNs remains constrained.

Average abundances of PGEs in RMNs between meteorites have approximately chondritic trends (Fig. 12). Vigarano exhibits an enrichment in W, whereas Allende exhibits a depletion in W and Mo. This may be interpreted as a real compositional difference related to the formation history and oxidation state of the meteorite. However, as very few RMNs contain Mo or W these anomalies are therefore likely to be caused primarily by the averaging of a few W-rich RMNs in the case of Vigarano and a few Mo and W-poor RMNs in Allende.

PGEs are predominantly siderophile and generally unreactive, with the exception of W and Mo which have been shown to be mobile under low degrees of alteration (Palme et al., 1998). It has been shown by experiment that Pt, Mo and W will mobilise under reducing conditions at 1600 K before Os and Ir (Schwander et al., 2015). Therefore, to alter the entire PGE content in RMNs on the parent body would require significantly higher temperatures than all carbonaceous chondrite parent bodies have experienced. The heterogeneity in the PGE content of RMNs must therefore be present prior to accretion. Therefore, a parent body process producing heterogeneous RMNs is unlikely.

4.3.6. Petrological context

Finally, the context of the RMN is taken into account. RMNs have been shown to occur throughout carbonaceous chondrites. The methodology described in this study retains their context and mineralogical association. Therefore, we can check if the formation process implied by evaluation of the chemical data is plausible. Indeed, it is the case that some RMNs with compositions consistent with a condensation origin are located within a mineral assemblage that has an igneous history, such as the RMNs in cosmic spherules

Please cite this article in press as: Daly L., et al. *In situ* analysis of Refractory Metal Nuggets in carbonaceous chondrites. *Geochim. Cosmochim. Acta* (2016), http://dx.doi.org/10.1016/j.gca.2016.11.030

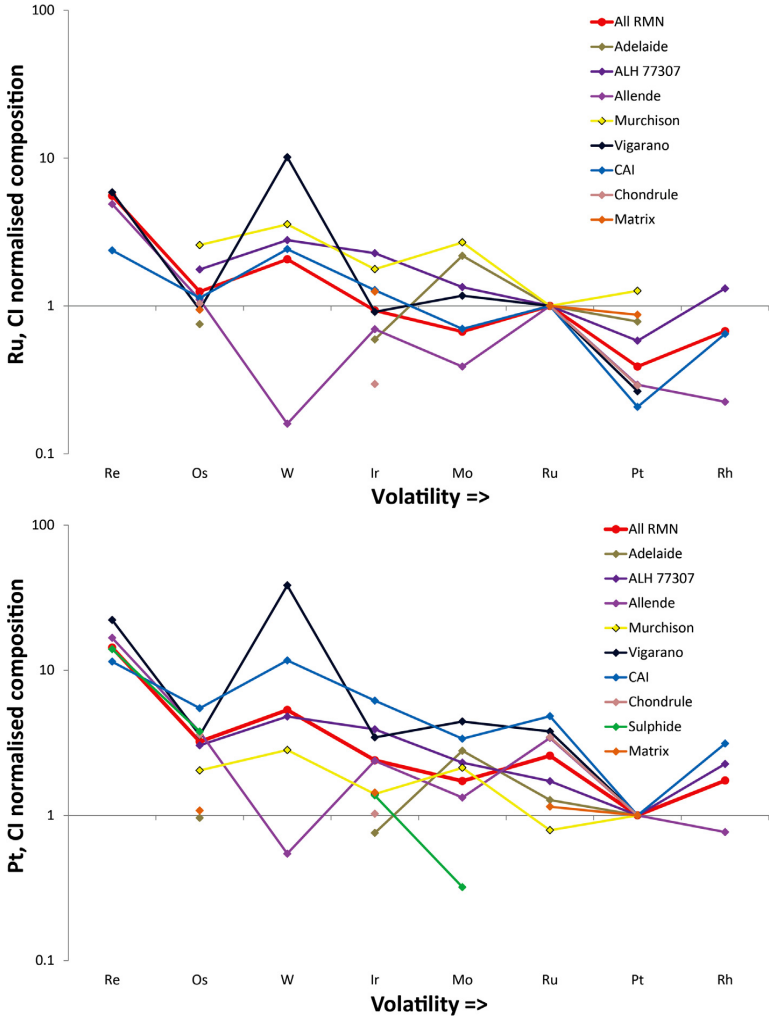

Fig. 12. RMN average compositions by host phase and meteorite from this study (Table 4). PGEs have been plotted in order of increasing volatility and have been normalised to Ru then CI (top), or Pt then CI (bottom). The average compositions of each meteorite exhibit approximately CI trends. Allende exhibits a slight depletion in Mo and W, while Vigarano shows a large W enrichment.

from Rudraswami et al. (2014). Cosmic spherules are thought to experience a very complex succession of heating, melting, and evaporation (Brownlee et al., 1997; Taylor et al., 2000; Genge et al., 2008) and therefore cannot have a condensation origin. Furthermore, although precipitation is thought to produce a diversity of chemical compositions in RMNs Schwander et al., 2015, not all inclusions in meteorites have an igneous history. Therefore, some RMNs cannot have formed via this process.

4.3.7. A combination of Solar System processes

No single process is responsible for the RMN variability we observe. However, it may be possible to produce this diversity through a combination of these processes. Indeed RMNs within cosmic spherules (Rudraswami et al., 2014) which do have a complex thermal history including heating, melting, and evaporation (Brownlee et al., 1997; Taylor et al., 2000; Genge et al., 2008), nearly cover the whole range of observed RMN compositions (Fig. 11). However, RMNs hosted within different meteoritic inclusions have a similar diversity of Ir/Os and Ir/Pt ratios (Fig. 13). The overlap of sulphide hosted RMNs in particular indicates that sulphidation does not significantly alter the original elemental ratio. Therefore the diversity of RMN compositions cannot be related to precipitation or condensation derived RMNs being suphidised. We have already dis-

Please cite this article in press as: Daly L., et al. *In situ* analysis of Refractory Metal Nuggets in carbonaceous chondrites. *Geochim. Cosmochim. Acta* (2016), http://dx.doi.org/10.1016/j.gca.2016.11.030

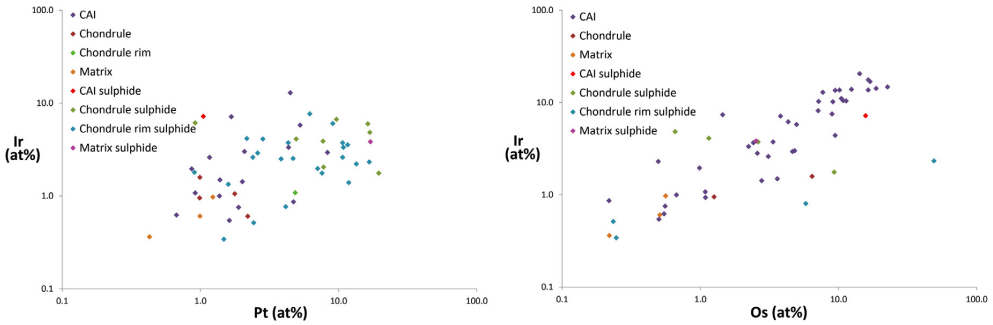

Fig. 13. Ir/Os (left) and Ir/Pt (right) plots of RMNS from this study with respect to their host phase. These plots reveal that sulphide CAI and chondrule hosted RMNs have a similar spread of PGE abundance ratios.

cussed how equilibrium condensation is not capable of producing the diversity of RMNs observed, and precipitation is unlikely to generate the observed diversity. Synthetic RMN compositions from precipitates and equilibrium condensation RMN compositions are not complementary. Therefore even a combination of these proposed formation mechanisms will not result in the suite of compositions we observe. This leaves three possibilities. Firstly, it may be possible to imagine a complex sequence of condensation, re-melting, evaporation, vaporisation, sulphidation, and oxidation that could produce a single RMN composition. However, the diversity of RMN compositions we observe would require almost every single RMN to experience a unique but complex formation history similar to cosmic spherules. This is inconsistent with textual observations of some RMN hosts, such as the RMN in a fuffy type A CAI in (Palme et al., 1998) and RMNs within a 'fluffy' type A CAI from Vigarano in this study (Fig. 2). These RMNs do not have compositions consistent with a single event equilibrium condensation model and yet are contained within a 'pristine' inclusion and therefore are unlikely to have been significantly altered by subsequent processes. It is also inconsistent with RMNs with variable compositions within the same inclusions Schwander et al., 2015. Secondly there may be a nebula or parent body process which has not yet been identified which is capable of producing the observed heterogeneity within RMNs either individually, or in tandem with the previously discussed processes. Finally, there is a possibility that this diversity of RMN compositions could be produced by inheriting an initially heterogeneous assemblage of pre-solar RMNs which were never completely equilibrated by subsequent nebular processing.

4.3.8. A pre-solar initial origin?

We have to accept that neither condensation (primary nebula), precipitation (secondary nebula), nor sulphidation (secondary asteroidal) and parent body processes can produce individually or in tandem the myriad of compositions of RMNs we observe in meteorites. We cannot currently produce the diversity of RMNs via a combination of known nebular and/or parent body processes, therefore we are required to look elsewhere.

The Solar System formed from a Giant Molecular Cloud fragment which would have included refractory metals from a variety of stellar sources. These are likely to be hosted in metal alloys. The resulting diversity of RMN compositions represents the initial condition of the protoplanetary disk. Our data indicate that while RMNs have been affected by condensation, precipitation, sulphidation and (possibly other) parent body processes, none of these processes are dominant, and together, they have not homogenised or equilibrated the RMN population and removed that initial compositional diversity. If this interpretation is correct, a prediction would be that pre-solar RMNs are present as discrete grains within primitive chondrites and IDPs, rather than solely hosted in pre-solar graphite (Croat et al., 2013). Therefore, some of the grains analysed in the course of this study belong to that pre-solar population. The most likely candidates for this are those RMNs found within the Ni-mixing line which is not readily explained by any process discussed in this study. Isotopic analysis is required to support this.

5. CONCLUSIONS

Observing RMNs in multiple components in meteorites, not just in CAIs, directly contradicts the assumption made by many studies that RMNs are unique to CAIs. Each RMN host has its own characteristic RMN compositional suite. However, the average RMN composition across all minerals averages to the bulk Solar System and CI chondrite implying that PGEs are primarily, if not uniquely, hosted within RMNs. Condensation models, experimentally derived RMNs from precipitation, and parent body processes such as sulphidation are unable to produce the suite of RMN compositions observed, either in isolation or in tandem. It may be possible to derive the suite of RMN compositions through complex sequences of condensation evaporation and remelting as we obverse a similar diversity in cosmic spherules. However, such a complex thermal sequence is not plausible for all meteoritic components. The Solar Nebula inherited a vast diversity of RMN compositions from a variety of stellar sources. Our data suggests that this initial RMN population was never fully homogenised. While some RMNs have been modified by

Please cite this article in press as: Daly L., et al. *In situ* analysis of Refractory Metal Nuggets in carbonaceous chondrites. *Geochim. Cosmochim. Acta* (2016), http://dx.doi.org/10.1016/j.gca.2016.11.030

nebular and asteroidal processes, the compositional diversity of the RMN population observed in this study indicates that the original pre-solar signature was never completely erased. If this assumption is correct, some RMNs may have escaped Nebula processing and will retain their pre-solar composition. Therefore, we should observe some demonstrably pre-solar RMNs not just within pre-solar graphite, but in other components as well. These conclusions could only be drawn by analysis of RMNs *in situ* highlighting the importance of retaining context and petrological associations.

ACKNOWLEDGEMENTS

This work was funded by the Australian Research Council via their Australian Laureate Fellowship program. This research was undertaken on the XFM beamline at the Australian Synchrotron, Victoria, Australia. The authors acknowledge the facilities, and the scientific and technical assistance, of the Australian Microscopy & Microanalysis Research Facility at the Australian Centre for Microscopy and Microanalysis, the University of Sydney and the Centre for Microscopy, Characterisation and Analysis, University of Western Australia. The authors would also like to thank the rest of the Desert Fireball Network research group as well as Mr. Timmons Erikson, Mr. Mark Daly, Ms. Mary Munroe, Ms. Sarah Hayes and Ms. Jennifer Porter for their assistance. Finally the authors would like to thank the three reviewers, as well as associate editor Nicolas Dauphas for their constructive comments and suggestions which significantly improved this manuscript.

APPENDIX A. SUPPLEMENTARY DATA

Supplementary data associated with this article can be found, in the online version, at http://dx.doi.org/10.1016/j.gca.2016.11.030.

REFERENCES

Amari S., Lewis R. S. and Anders E. (1994) Interstellar grains in meteorites: I. Isolation of SiC, graphite and diamond; size distributions of SiC and graphite. *Geochimica et Cosmochimica Acta* **58**, 459–470.

Anders E., Gros J., Takahashi H., Morgan J. and Higuchi H. (1975) Extinct superheavy element in the Allende meteorite. *Science* **190**, 459–470.

Berg T., Maul J., Schönhense G., Marosits E., Hoppe P., Ott U. and Palme H. (2009) Direct evidence for condensation in the early solar system and implications for nebular cooling rates. *The Astrophysical Journal Letters* **702**, L172–L176.

Bischoff A. and Palme H. (1987) Composition and mineralogy of refractory-metal-rich assemblages from a Ca, Al-rich inclusion in the Allende meteorite. *Geochimica et Cosmochimica Acta* **51**, 2733–2748.

Blander M., Fuchs L., Horowitz C. and Land R. (1980) Primordial refractory metal particles in the Allende meteorite. *Geochimica et Cosmochimica Acta* **44**, 217–223.

Blum J. D., Wasserburg G., Hutcheon I. D., Beckett J. R. and Stolper E. M. (1988) 'Domestic' origin of opaque assemblages in refractory inclusions in meteorites. *Nature* **331**, 404–409.

Brownlee D., Bates B. and Schramm L. (1997) The Leonard Award Address Presented 1996 July 25, Berlin, Germany: the elemental composition of stony cosmic spherules. *Meteoritics & Planetary Science* **32**, 157–175.

Campbell A. J., Humayun M., Meibom A., Krot A. N. and Keil K. (2001) Origin of zoned metal grains in the QUE94411 chondrite. *Geochimica et Cosmochimica Acta* **65**, 163–180.

Cleverley J., Ryan C., Hough R., Bland P., Fisher L. and Dyl K. (2012) Quantified, whole section, Maia XRF mapping of trace elements in allende. *Meteoritics and Planetary Science Supplement* **75**, 5175.

Connelly J. N., Bizzarro M., Krot A. N., Nordlund Å., Wielandt D. and Ivanova M. A. (2012) The absolute chronology and thermal processing of solids in the solar protoplanetary disk. *Science* **338**, 651–655.

Croat T., Berg T., Bernatowicz T., Groopman E. and Jadhav M. (2013) Refractory metal nuggets within presolar graphite: First condensates from a circumstellar environment. *Meteoritics & Planetary Science* **48**, 686–699.

Dyl K. A., Cleverley J. S., Bland P. A., Ryan C. G., Fisher L. A. and Hough R. M. (2014) Quantified, whole section trace element mapping of carbonaceous chondrites by Synchrotron X-ray Fluorescence Microscopy: 1. CV meteorites. *Geochimica et Cosmochimica Acta* **134**, 100–119.

Eisenhour D. and Buseck P. (1992) Transmission electron microscopy of RMNs: implications for single-phase condensation of the refractory siderophile elements. *Meteoritics* **27**, 217–218.

El Goresy A., Nagel K., Dominik B. and Ramdohr P. (1977) Fremdlinge: potential presolar material in Ca–Al-rich inclusions of Allende. *Meteoritics* **12**, 215–216.

El Goresy A., Nagel K., and Ramdohr P. (1978) Fremdlinge and their noble relatives. In *Lunar and Planetary Science Conference Proceedings*. pp. 1279–1303. 9.

Fegley B. and Kornacki A. S. (1984) The geochemical behavior of refractory noble metals and lithophile trace elements in refractory inclusions in carbonaceous chondrites. *Earth and planetary science letters* **68**, 181–197.

Fegley B. and Palme H. (1985) Evidence for oxidizing conditions in the solar nebula from Mo and W depletions in refractory inclusions in carbonaceous chondrites. *Earth and Planetary Science Letters* **72**, 311–326.

Genge M., Engrand C., Gounelle M. and Taylor S. (2008) The classification of micrometeorites. *Meteoritics & Planetary Science* **43**, 497–515.

Grossman L. (1973) Refractory trace elements in Ca–Al-rich inclusions in the Allende meteorite. *Geochimica et Cosmochimica Acta* **37**, 1119–1140.

Grossman L. and Ganapathy R. (1976) Trace elements in the Allende meteorite – I. Coarse-grained, Ca-rich inclusions. *Geochimica et Cosmochimica Acta* **40**, 331–344.

Grossman L., Ganapathy R. and Davis A. M. (1977) Trace elements in the Allende meteorite – III. Coarse-grained inclusions revisited. *Geochimica et Cosmochimica Acta* **41**, 1647–1664.

Harries D., Berg T., Langenhorst F. and Palme H. (2012) Structural clues to the origin of refractory metal alloys as condensates of the solar nebula. *Meteoritics & Planetary Science* **47**, 2148–2159.

Hutcheon I. D., Armstrong J. T. and Wasserburg G. (1987) Isotopic studies of Mg, Fe, Mo, Ru and W in Fremdlinge from Allende refractory inclusions. *Geochimica et Cosmochimica Acta* **51**, 3175–3192.

Lauretta D. S., Kremser D. T. and Fegley Jr B. (1996) The rate of iron sulfide formation in the solar nebula. *Icarus* **122**, 288–315.

Lodders K. (2003) Solar system abundances and condensation temperatures of the elements. *The Astrophysical Journal* **591**, 1220–1247.

MacPherson G., Simon S., Davis A., Grossman L., and Krot A. (2005) Calcium–Aluminum-Rich inclusions: major unanswered

Please cite this article in press as: Daly L., et al. *In situ* analysis of Refractory Metal Nuggets in carbonaceous chondrites. *Geochim. Cosmochim. Acta* (2016), http://dx.doi.org/10.1016/j.gca.2016.11.030

questions. In *Chondrites and the Protoplanetary Disk, 341*. p. 225.

MacPherson G. J. (2005) Calcium–Aluminum-Rich inclusions in chondritic meteorites. In *Meteorites, Comets and Planets: Treatise on Geochemistry*, vol. 1 (ed. A. M. Davis), ISBN 0-08-044720-1, p. 201, Executive Editors: HD Holland and KK Turekian.

Palme H. and Wlotzka F. (1976) A metal particle from a Ca, Al-rich inclusion from the meteorite Allende, and the condensation of refractory siderophile elements. *Earth and Planetary Science Letters* **33**, 45–60.

Palme H., Borisov A., and Wulf A. (1998) Experimental determination of the oxidation sequence of refractory metals. In *Lunar and Planetary Science Conference, 29*. p. 1611.

Palme H., Hutcheon I. and Spettel B. (1994) Composition and origin of refractory-metal-rich assemblages in a Ca, Al-rich Allende inclusion. *Geochimica et Cosmochimica Acta* **58**, 495–513.

Palme H., Wlotzka F., Nagel K. and El Goresy A. (1982) An ultra-refractory inclusion from the Ornans carbonaceous chondrite. *Earth and Planetary Science Letters* **61**, 1–12.

Petaev M. I. and Wood J. (2005) Meteoritic constraints on temperatures, pressures, cooling rates, chemical compositions and modes of condensation in the solar nebula. In *Chondrites and the protoplanetary disk, 341*. p. 373.

Rudraswami N., Prasad M. S., Plane J., Berg T., Feng W. and Balgar S. (2014) Refractory metal nuggets in different types of cosmic spherules. *Geochimica et Cosmochimica Acta* **131**, 247–266.

Ryan C., Jamieson D., Churms C. and Pilcher J. (1995) A new method for on-line true-elemental imaging using PIXE and the proton microprobe. *Nuclear Instruments and Methods in Physics Research Section B: Beam Interactions with Materials and Atoms* **104**, 147–165.

Ryan C., Siddons D., Kirkham R., Dunn P., Kuczewski A., Moorhead G., De Geronimo G., Paterson D., De Jonge M. and Hough R., et al. (2010) The new Maia detector system: methods for high definition trace element imaging of natural material. In *X-Ray Optics and Microanalysis: Proceedings of the 20th International Congress*, vol. 1221, pp. 9–17. X-Ray Optics and Microanalysis: Proceedings of the 20th International Congress. AIP Publishing.

Schwander D., Berg T., Harries D., Schönhense G. and Ott U. (2014) Composition and clues to the origin of refractory metal nuggets extracted from chondritic meteorites. *Meteoritics & Planetary Science* **49**, 1888–1901.

Schwander D., Berg T., Schönhense G. and Ott U. (2014) Condensation of Refractory Metals in Asymptotic Giant Branch and Other Stellar Environments. *The Astrophysical Journal* **793**, 1–5.

Schwander D., Buhre S., Schönhense G. and Ott U. (2015) Synthesis of refractory metal nuggets and constraints on the thermal histories of nugget-bearing Ca–Al-rich inclusions. *Meteoritics & Planetary Science* **50**, 893–903.

Schwander D., Kööp L., Berg T., Schönhense G., Heck P., Davis A. and Ott U. (2015) Formation of refractory metal nuggets and their link to the history of CAIs. *Geochimica et Cosmochimica Acta* **168**, 70–87.

Sylvester P. J., Ward B. J., Grossman L. and Hutcheon I. D. (1990) Chemical compositions of siderophile element-rich opaque assemblages in an Allende inclusion. *Geochimica et Cosmochimica Acta* **54**, 3491–3508.

Tanaka K. K., Tanaka H. and Nakazawa K. (2002) Non-equilibrium Condensation in a Primordial Solar Nebula: Formation of Refractory Metal Nuggets. *Icarus* **160**, 197–207.

Taylor S., Lever J. H. and Harvey R. P. (2000) Numbers, types, and compositions of an unbiased collection of cosmic spherules. *Meteoritics & Planetary Science* **35**, 651–666.

Wang Y., Hua X. and WeiBiao H. (2007) Petrogenesis of opaque assemblages in the Ningqiang carbonaceous chondrite. *Science in China Series D: Earth Sciences* **50**, 886–896.

Wänke H., Baddenhausen H., Palme H. and Spettel B. (1974) On the chemistry of the Allende inclusions and their origin as high temperature condensates. *Earth and Planetary Science Letters* **23**, 1–7.

Wark D. (1986) Evidence for successive episodes of condensation at high temperature in a part of the solar nebula. *Earth and Planetary Science Letters* **77**, 129–148.

Wark D. and Lovering J. (1976) Refractory/platinum metal grains in Allende calcium-aluminium-rich clasts (CARC's): possible exotic presolar material? In *Lunar and Planetary Science Conference, 7*. p. 912.

Wark D., and Lovering J. (1978) Refractory/platinum metals and other opaque phases in Allende Ca–Al inclusions. In *Lunar and Planetary Science Conference, 9*. pp. 1214–1216.

Associate editor: Nicolas Dauphas

Please cite this article in press as: Daly L., et al. *In situ* analysis of Refractory Metal Nuggets in carbonaceous chondrites. *Geochim. Cosmochim. Acta* (2016), http://dx.doi.org/10.1016/j.gca.2016.11.030

Appendix C2

Composition of Refractory Metal Nuggets: Implications for Their Origins

Daly et al., 2016

47th Lunar & Planetary Science Conference

Daly, L., Bland, P.A., Evans, K., Dyl, K.A., Forman, L.V., Trimby, P.W., Moody, S., Yang, L., Liu, H.W., La Fontaine, A. and Cairney, J.M., 2016, Composition of Refractory Metal Nuggets: Implications for Their Origins: In Lunar and Planetary Science Conference, v. 47, p. 1880.

STATEMENT OF AUTHORSHIP

As the primary author of the folloiwng manuscript, I hereby confirm the candidate's contributions and confirm my permission to include the manuscript in the candidate's PhD thesis.

MR LUKE DALY

- Lead investigator

Date: ***22.2.17***

MISS LUCY. V. FORMAN

- Manuscript editing

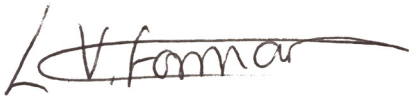

Contribution: ***1%*** ***Date:*** ***22.2.17***

COMPOSITION OF REFRACTORY METAL NUGGETS: IMPLICATIONS FOR THEIR ORIGINS. L. Daly[1], P. A. Bland[1], K. Evans[1], K. A. Dyl[1], L. V. Forman[1], P. W. Trimby[2], S. Moody[2], L. Yang[2] , H.W. Liu[2], A. La Fontaine[2], J. M. Cairney[2], S. P. Ringer[3] and M. Saunders[4], [1]Department of Applied Geology, Curtin University, GPO Box U1987, Perth, WA, 6845, Australia. E-mail luke.daly@postgrad.curtin.edu.au, [2]Australian Centre for Microscopy and Microanalysis and ARC Centre of Excellence for Design in Light Metals, The University of Sydney, NSW, 2006, Australia, [3]Australian Institute for Nanoscale Science and Technology, and School of Aerospace, Mechanical & Mechatronic Engineering The University of Sydney NSW, 2006, Australia. [4] Centre for microscopy, Characterisation and Analysis, The University of Western Australia, WA 6009, Australia

Introduction: Refractory metal nuggets (RMNs) are composed primairily of Fe, Ni, and platinum group elements (PGEs). They are thought to form by condensation in the early Solar Nebula [1]. However, it has also been suggested that RMNs can form via crystallisation from a silicate melt [2]. Here we combine *in situ* analysis of RMNs, RMN compositions reported in the literature, and predicted compositions from a condensation model to define populations of RMNs based on their chemistry.

Methodolgy: 109 RMNs were analysed *in situ* from Allende, Murchison, Vigarano, ALH 77307, and Adelaide, using energy dispersive X-Ray spectroscopy (EDS) at the University of Sydney, Curtin University, and the University of Western Australia. These observations were supported by analyses from EDS during Transmission Kikuchi Diffraction (TKD), and EDS obtained in transmission electron microscopes (TEMs).

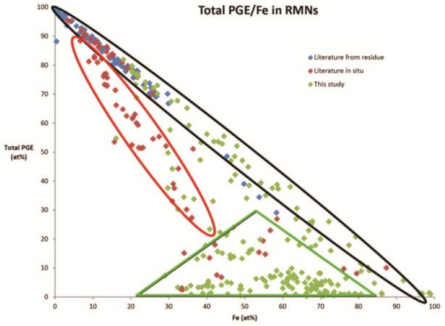

Figure 1: Total PGE/Fe in RMNs from this study and the literature. Showing a Fe mixing trend (black oval), a Ni mixing trend (red oval) and a low PGE region (green triangle).

An exhaustive literature search was performed in an attempt to include all published RMN compositions [1, 3-12], as well as RMNs thought to have formed via crystallisation in a silicate melt [2, 13], giving a sum total of 380 RMNs for this study.

All compositions have been converted to atomic percent and renormalised, only taking into account the elements Fe, Ni, Ru, Rh, Mo, W, Re, Os, Ir, and Pt. RMN compositions were compared to a condensation model similar to that detailed in [1].

Results and discussion: Plots of total PGE vs Fe (Fig 1), and total PGE vs Ni (Fig 5) show three distinct trends which can be defined by a Fe mixing line, a Ni mixing line and a cluster of low PGE concentrations (Fig 1). To check this is not an artifact of data processing, the data was plotted by original wt%, meteorite, author, technique, and inclusion type; revealing no systematic errors due to these factors.

Plotting the data in a similar vein to [1] (Fig 2) indicates that RMNs do approximately follow a condensation trend.

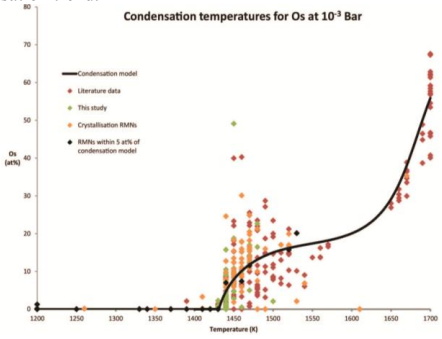

Figure 2: Composition of Os in RMNs compared to model condensation temperatures, RMNs within 5 at% of the condensation model for all elements are highlighted in black.

However, when the abundance of every element in each individual RMN was compared to the predicted composition from the condensation model, of the 380 RMNs analysed, only 29 were consistent to within 5 at% for every element. Of these 29, 22 were cosmic spherule-hosted RMNs from [13], which are thought to form by crystallisation. Of the remaining 7, only 2 had condensation temperatures >1500 K (Fig 2). In fact, when RMNs that formed via crystallisation are superimposed onto elemental plots (Fig 3) the spread is much more consistent with this mechanism of formation. Therefore, it is likely that most, if not all

RMNs formed by crystallisation, not condensation. Current condensation models cannot explain the full elemental composition of individual RMNs. This could be due to a lack of accurate activity coefficients for PGEs, this is required if we are to completely discount condensation as a possible mechanism for RMN formation.

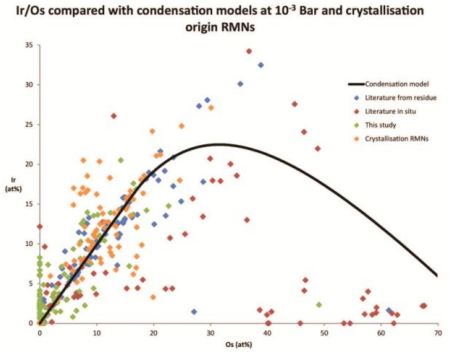

Figure 3: Ir/Os RMN compositions with condensation model and crystallisation RMNs. Indicating a crystallisation origin is more consistent with the spread of most RMN compositions.

Nevertheless, a crystallisation origin can only account for RMNs that follow the Fe mixing line (Fig 4).

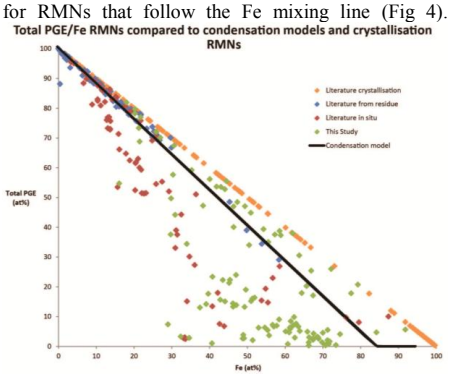

Figure 4: Total PGE/Fe with the condensation model and crystallisation RMNs. Indicating crystallisation or condensation cannot derive all RMNs.

Plotting RMNs relative to their host phase (Fig 5) reveals the low PGE cluster is dominated primarily by sulphide-hosted RMNs. Therefore, these grains are likely to have been affected by, if not formed due to sulphidation. However, the Ni mixing line remains an enigma. Fig 5 reveals the sulphide cluster is situated towards the end of the Ni mixing line. Therefore, the Ni trend and the sulphide cluster are potentially an expression of varying degrees of sulphidation of RMNs, or sulphidation of RMNs with variable compositions produced by crystallisation; with Fe being replaced by Ni, dragging the Fe mixing line down towards the Ni mixing line.

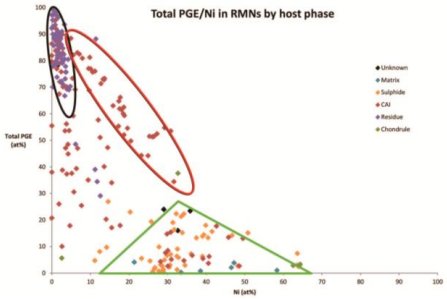

Figure 5: Total PGE/Ni RMNs by host. Indicating a relationship between the Ni mixing line (red) and the sulphide dominated region (green).

If every RMN can be interpreted as a product of crystallisation this presents a problem: RMNs are found in every component in carbonaceous chondrites [14]. This includes components which are not thought to have undergone igneous processes such as fluffy CAIs. This could call into question our current understanding of how these components form.

Conclusion: *In situ* analysis of RMN compositions reveals two populations of RMNs. The first follows a Fe mixing line, derived by crystallisation of RMNs from a silicate melt as described by [2]. The second follows a Ni mixing line produced by secondary sulphidation of crystallisation derived RMNs. A condensation origin for RMNs seems unlikely, but a crystallisation origin questions our current understanding of how meteoritic components form.

References: [1] Berg T. et al. (2009) *The Astrophys. Jour.*, 702, 172-176. [2] Schwander D. et al. (2015) *Met. & Planet. Sci.*, 50, 5, 893-903. [3] Bischoff A. & Palme H. (1987) *Geochim. et chosmochim. Ac.*, 51, 2733-2748. [4] Blander M. et al. (1980) *Geochim. et chosmochim. Ac.*, 44, 217-223. [5] Palme H. et al. (1994) *Geochim. et chosmochim. Ac.*, 58, 495-513. [6] Wark D.A. & Lovering J.F. (1976) *LPSC*, 7, 912 [7] Wark D.A. (1986) *Earth & planet. Sci. Let.*, 77, 129-148. [8] Palme H. et al. (1982) *Earth & planet. Sci. Let.*, 61, 1-12. [9] Wark D.A. & Lovering J.F. (1978) *LPI*, 9, 1214-1216. [10] Croat T.K. et al. (2013) *Met. & Planet. Sci.*, 48, 686-699. [11] Harries D. et al. (2012) *Met. & Planet. Sci.*, 47, 2148-2159. [12] Schwander D. et al. (2014) *Met. & Planet. Sci.*, 49, 1888-1901. [13] Rudraswami N.G. et al. (2014) *Geochim. et chosmochim. Ac.*, 131, 247-266. [14] Daly L. et al. (2014) *LPSC XLV*, Abstract #2071.

Appendix C3

Atom Probe Tomography and Its Application to Refractory Metal Nuggets

Daly et al., 2016

79th Annual Meeting of the Meteoritical Society

Daly, L., Bland, P.A., Forman, L.V., Reddy, S.M., Rickard, W.D.A., Saxey, D.W., La Fontaine, A., Yang, L., Trimby, P.W., Cairney, J. and Ringer, S., 2016: Atom Probe Tomography and Its Application to Refractory Metal Nuggets: LPI Contributions, Abstract #6241.

STATEMENT OF AUTHORSHIP

As the primary author of the folloiwng manuscript, I hereby confirm the candidate's contributions and confirm my permission to include the manuscript in the candidate's PhD thesis.

MR LUKE DALY

- Lead investigator

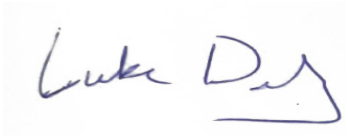

Date: ***22.2.17***

MISS LUCY. V. FORMAN

- Manuscript editing

Contribution: ***1%*** ***Date:*** ***22.2.17***

79th Annual Meeting of the Meteoritical Society (2016) **6241.pdf**

Atom probe tomography and its application to refractory metal nuggets.

L. Daly[1], P. A. Bland[1], L. V. Forman[1], S. M. Reddy[1,2], W. D. A. Rickard[2], D. W. Saxey[2], A. La Fontaine[3], L. Yang[3], P. W. Trimby[3], J. Cairney[3], S. Ringer[4] and B. F. Schaefer[5]

[1]Department of Applied Geology, Curtin University, GPO Box U1987, Perth, WA 6845, Australia. Luke.daly@postgrad.curtin.edu.au, [2] Geoscience Atom Probe, Advanced Resource Characterisation Facility, John de Laeter Centre, Curtin University, GPO Box U1987, Perth, WA 6845, Australia. [3]Australian Centre for Microscopy and Microanalysis, The University of Sydney, NSW 2006, Australia. [4]Australian Institute for Nanoscale Science and Technology, and School of Aerospace, Mechanical and Mechatronic Engineering, The University of Sydney, NSW, 2006, Australia. [5] Department of Earth and Planetary Sciences, Macquarie University NSW, 2109, Australia.

Introduction: Refractory metal nuggets (RMNs) are sub-micron metal alloys composed of highly siderophile elements found within primitive carbonaceous chondrites. Their unique occurrence within Ca-Al-rich inclusions (CAIs), has recently been questioned using synchrotron XFM observing RMNs in all meteoritic components [1]. RMNs are thought to form by condensation in the nebula [2] and/or crystallisation from a silicate melt [3]. However, a combined data set of 109 *in situ* RMN compositions, combined with a literature database have revealed a large diversity of compositions that cannot be produced by any single process. Therefore, we suggest that an inherently diverse population of RMNs was incorporated into the protoplanetary disk. These RMNs have undergone some processing but the inherited compositional diversity was never completely overprinted by subsequent solar system processes. Therefore, we might expect some RMNs to preserve a pre-solar isotopic and chemical signature [1].

Method and results: Candidate RMNs were identified in CAIs in ALH 77307 and Allende. These RMNs were extracted, mounted, and shaped to a 100 nm wide needle using a Focussed Ion Beam. The samples were placed into the CAMECA Local Electrode Atom Probe (LEAP) 4000X Si, Australian Centre of Microscopy and Microanalysis, Sydney University or the Geoscience Atom Probe CAMECA LEAP 4000X HR, Advanced Resource Characterisation Facility, Curtin University. Single atoms were ionised using field evaporation by high frequency laser (Curtin) pulses and accelerated towards the detector by the surrounding electric field. Time of flight measurements of ions hitting a position sensitive detector determined the elemental identity and its initial position in the tip [4]. IVAS software interpreted the data and generated a 3D reconstruction of the tip denoting the position of every detected atom. This revealed atomic scale chemical variations RMNs indicating they are not all chemically homogeneous (Figure 1). The RMN in ALH 77307 contained sulphur, a potential indicator for nebula sulphidation.

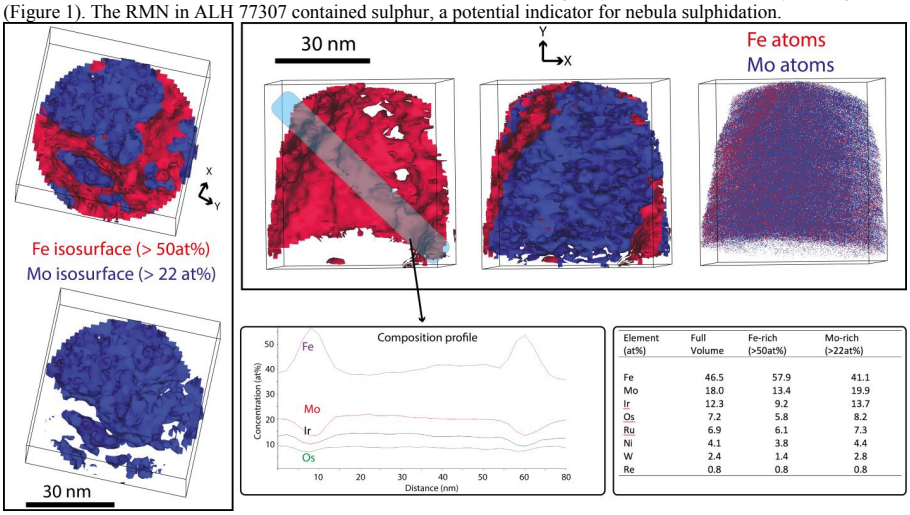

Figure 1: Allende RMN atom probe tip, indicating nanometer variations between Fe rich and Mo rich sub-volume.

References: [1] Daly L. et al., 2016. *Gechimica et Cosmocimica Acta*, (in review) [2] Berg T. et al., 2009. *The Astrophysical Journal Letters* 702, L172 [3] Schwander D. et al., 2015. *Geochimica et Cosmochimica Acta* 186, 70–87. [4] Gault B. et al., 2009, *Journal of Applied Physics*, 105, 3, 034913.

Appendix C4

Mineralogy and Petrology of the Murrili Meteorite

Benedix et al., 2016

79th Meteoritics & Planetary Science Conference

Benedix, G.K., Forman, L.V., Daly, L., Greenwood, R.C., Franchi, I.A., Friedrich, J.M., Meier, M.M., Maden, C., Busemann, H., Welten, K.C. and Caffee, M.W., 2016, Mineralogy and petrology of the Murrili meteorite: LPI Contribution No. 6237.

STATEMENT OF AUTHORSHIP

As the primary author of the folloiwng manuscript, I hereby confirm the candidate's contributions and confirm my permission to include the manuscript in the candidate's PhD thesis.

DR GRETCHEN BENEDIX

- Lead investigator

Date: ***28.2.17***

MISS LUCY. V. FORMAN

- Manuscript editing
- Characterisation of meteorite

Contribution: ***10%*** ***Date:*** ***22.2.17***

79th Annual Meeting of the Meteoritical Society (2016) **6237.pdf**

Mineralogy and Petrology of the Murrili Meteorite

G.K. Benedix[1], L.V. Forman[1], L.Daly[1], R.C. Greenwood[2], I. A. Franchi[2], J.M. Friedrich[3], M.M.M. Meier[4], C. Maden[4], H. Busemann[4], K.C. Welten[5], M.W. Caffee[6], P.A. Bland[1], J. Paxman[1], M. Towner[1], M. Cupak[1], E.K. Sansom[1], R. Howie[1], H. Devillepoix[1], M. A. Cox, T. Jansen-Sturgeon, K. Merigot[7], D. Stuart[8], and D. Strangway[8].
[1]Dept. Applied Geology, Curtin University, GPO Box U1987, Perth, WA 6845, Australia (g.benedix@curtin.edu.au), [2]PSSRI, Open University, Milton Keynes, UK MK7 6AA; [3]Dept. of Chemistry, Fordham University, Brooklyn, NY, USA; [4]ETH Zurich, Institute for Geochemistry and Petrology, Zurich, Switzerland. [5]Space Sciences Laboratory, University of California, Berkeley, CA 94720, USA. [6]Department of Physics, Purdue University, West Lafayette, IN 47907, USA. [7]John de Laeter Centre, Bldg 301, Curtin University, Bentley, 6845. Western Australia; [8]23 Main Street, Port Augusta, South Australia

Introduction: Murrili (pronounced moo-RRil-y) is the 3rd meteorite recovered by the Desert Fireball Network (for details of the fall and orbit see [1]). It fell as a single, heart-shaped, 1.68 kg stone, measuring ~13 × 7 × 6 cm, and was entirely fusion crusted. Two small wedges and a thin slab were cut from the main mass for examination and analyses. Cut surfaces reveal pervasive alteration with rusty staining heterogeneously distributed in a wormy pattern. Chips and powders of both altered and unaltered sample were sent for oxygen isotope, bulk composition, cosmogenic nuclide, porosity/density, and Mössbauer analyses.

Analytical techniques: Mineral compositions were determined on a thick section with a JEOL 8530F electron microprobe (20kV, 20nA). Modal mineralogy was determined using a Tescan Integrated Mineral Analyzer. Oxygen isotopes were measured using the method described in [2]. Bulk trace and major element compositions were determined using the method described in [3,4]. Cosmogenic nuclides were measured as described in [5,6].

Results: Mössbauer and porosity/density results are reported elsewhere in this volume [7,8]. We focus here on the classification, mineralogy and a preliminary petrologic description of the meteorite.

Physical characteristics: Distinct chondrule (barred olivine, the remnants of porphyritic olivine, and possible radiating pyroxene) outlines, as well as large single mineral crystal clasts, are set in a relatively coarse-grained matrix. The section is dominated (all in vol%) by olivine (32%) and orthopyroxene (32%), with smaller amounts of plagioclase (7%), metal and Fe-oxides (10%) and sulfides (6.5%). Phosphate and chromite make up < 1% of the section. Examination of the minerals in thin section shows no evidence of shock – olivine has normal extinction across the section indicating a shock stage of 1 [9].

Geochemistry: Olivine has an average composition of $Fa_{18.8\pm0.5}$ (n=15). The orthopyroxene average is $Fs_{16.4\pm0.3}Wo_{1.1\pm0.3}$ (n=8). Chromite (n=7) Cr/Cr+Al ranges from 0.85 to 0.87 and Fe/Fe+Mg varies from 0.84 to 0.86. The oxygen isotopic composition of the unaltered material is $\delta^{17}O$=2.76±0.02‰, $\delta^{18}O$=3.99±0.06‰. The isotopic composition of the altered material is shifted to slightly higher $\delta^{17}O$ (2.85±0.02‰) and $\delta^{18}O$ (4.18±0.04‰). Bulk elemental data and cosmogenic nuclide results will be reported at the meeting.

Discussion: The overall texture of the sample indicates that the meteorite is a type 5 ordinary chondrite, which is consistent with the chromite [10] and OPX Wo values [11]. The average olivine, orthopyroxene and oxygen isotope compositions indicate the meteorite is chemically classified as an H chondrite [12,13]. The cosmic ray exposure (CRE) age of ~7 Ma coincides with the main CRE age cluster for H-chondrites. Cosmogenic nuclide ratios are compatible with a small pre-atmospheric size (few 10 cm).

The alteration of the meteorite is extensive due to the time spent in the lake bed. The lake is generally a dry salt bed, but the area had experienced some precipitation between the fall and collection of the meteorite. Cut surfaces revealed red staining of the silicates and significant rusting of metal grains. However, the alteration does not seem to have affected the interiors of silicate minerals. Mineral and oxygen isotopic composition of unaltered areas are within error of the altered material.

Conclusions: The Murrili meteorite is classified as an H5 chondrite, based on olivine, orthopyroxene and oxygen isotope compositions, as well as textural features. It has a shock stage of S1. It is weathered due to exposure to the lake bed mud, but the alteration has not completely pervaded the rock.

References: [1] Bland P.A. et al. 2016, this conference. [2] Miller M.F. et al. (1999) *Rapid. Comm. Mass Spec.* 13, 1211-1217. [3]Friedrich et al. 2003, *GCA*, 67, 2467-2479. [4] Wolf et al. 2012, *Talanta* 1000, 276-281.[5] Welten et al., 2011, *MAPS* 46, 177-198. [6] Meier M. M. M. et al., 2016, *MAPS* submitted. [7] Cadogen S. et al. 2016, this conference. [8] Macke, R. Et al., 2016, this conference. [9] Stöffler D. et al., 1991, *GCA*, 55, 3845-3867. [10] Bunch et al., 1967, *GCA* 31, 1569-1582. [11] Scott et al., 1986, *Proc. Lunar Planet. Sci. Conf.* 17, E115-E123. [12] Gomes C.B. and Keil K. 1980, *Brazilian Stone Meteorites*, Univ. New Mexico Press, 161pp. [13] Clayton et al. 1991 *GCA* 55, 2317-2337.

Appendix C5

In Situ Analysis of Refractory Metal Nugget Crystallography Providing Clues to Early Solar System Events.

Daly et al., 2015

78th Annual Meeting of the Meteoritical Society

Daly, L., Bland, P.A., Forman, L.V., Trimby, P.W., Moody, S., Yang, L., Liu, H.W., Ringer, S.P. and Saunders, M., 2015. In Situ Analysis of Refractory Metal Nugget Crystallography Providing Clues to Early Solar System Events: In 78th Annual Meeting of the Meteoritical Society, v. 1856, p. 5061.

STATEMENT OF AUTHORSHIP

As the primary author of the folloiwng manuscript, I hereby confirm the candidate's contributions and confirm my permission to include the manuscript in the candidate's PhD thesis.

MR LUKE DALY

- Lead investigator

Date: 22.2.17

MISS LUCY. V. FORMAN

- Manuscript editing

Contribution: 1% ***Date: 22.2.17***

78th Annual Meeting of the Meteoritical Society (2015) **5061.pdf**

IN SITU ANALYSIS OF REFRACTORY METAL NUGGET CRYSTALLOGRAPHY PROVIDING CLUES TO EARLY SOLAR SYSTEM EVENTS.

L. Daly[1], P. A. Bland[1], L. V. Forman[1], P. W. Trimby[2], S. Moody[2], L.Yang[2], H.W. Liu[2], S. P. Ringer[2], and M. Saunders[3] [1]Department of Applied Geology, Curtin University, GPO Box U1987, Perth, WA 6845. E-mail: luke.daly@postgrad.curtin.edu.au. [2]Australian Key Centre for Microscopy and Microanalysis and ARC Centre of Excellence for Design in Light Metals, University of Sydney, NSW 2006, Australia. [3]Centre for Microscopy, Characterisation and Analysis, University of Western Australia, WA 6009, Australia.

Introduction: Refractory metal nuggets (RMNs) are thought to be the first solids to condense from a cooling nebular gas [1]. Here we present *in situ* analysis of RMNs revealing new observations, which may assist in the interpretation of how they form.

Method: RMNs were extracted from samples of Allende, Vigarano, and ALH77307 in the form of a 100 nm thick TEM lamella using a Focused Ion Beam (FIB). The samples were analysed using Transmission Kikuchi Diffraction (TKD) and Transmission Electron Microscopy (TEM) techniques.

Results and discussion: Analyses of RMNs *in situ* revealed new textures that have not previously been documented:

Twinning in Vigarano RMNs: We observed twins in RMNs hosted within a 'fluffy' Type A CAI. They are most likely annealing twins due to the 60° misorientation about the [111] axis across the twin boundary. Annealing twins form under high-temperature, low-pressure conditions. No experimental data exists for the compositions of interest; in FePt nanoparticles annealing begins around ~500 °C [2]. Assuming similar or higher temperatures were required for Vigarano RMNs, we can say that this is significantly higher than estimates for Vigarano parent body metamorphism [3], and therefore that annealing must have occurred before the CAI was incorporated into the chondrite. The mineral phase hosting the RMNs also exhibits annealing textures, but the whole CAI does not. We suggest a very short-lived nebular heating event as a mechanism.

RMN alignment in Allende and ALH 77307: RMNs found in ALH 77307 CAIs and Allende chondrules exhibit a crystallographic relationship with their host phase. In ALH 77307 the RMN [002] axis is parallel to the [201] axis in the host Åkermanite phase. The RMN <c> axis is parallel to a secondary FeMoOs phase exhibiting apparent super-cooling textures. The origin of this preferred alignment is interpreted as nucleation of CAI phases around the RMN. A secondary heating event followed by very rapid cooling formed the new mineral phase. The orientation in Allende is more complex; the RMNs are perfectly aligned with each other but exhibit no crystallographic relationship with the host sulphide phase. However, they do share a [100] axis with the neighboring forsterite. This is tentatively interpreted as nucleation of forsterite about RMNs producing a shared alignment via a minimisation of surface energy. This alignment is preserved during secondary sulphidisation.

Conclusion: *In situ* analysis of RMNs is providing us with a detailed picture of how these most refractory materials, and their host inclusions formed and were subsequently altered.

References: [1] Grossman L. and Ganapathy R. 1976. *Geochimica et Cosmochmica Acta* 40:331-344. [2] Dai Z., Sun S. and Wang Z. 2001. *Nano Letters* 1:443-447. [3] Cody G. et al. 2008. *Earth and Planetary Science Letters* 272:446-455

Appendix C6

Catching a Falling Star (or Meteorite)- Fireball Camera Networks in the 21st Century

Bland et al., 2015

Bland, P. A., Benedix, G. K. & Desert Fireball Network Team, 2015, June. Catching a Falling Star (or Meteorite)- Fireball Camera Networks in the 21st Century: Elements, p.160-161.

MINERALOGICAL SOCIETY OF AMERICA
3635 Concorde Pkwy Ste 500 • Chantilly VA 20151-1110 • USA
Tel: 1 (703) 652-9950 • Fax: 1 (703) 652-9951 • Internet: www.minsocam.org

March 7, 2017

Miss Lucy Forman
11 Peter Street
Halls Head WA 6210
Australia

Email: lucy.forman@curtin.edu.a

Dear Miss Forman:

I received your e-mail message of 2017-03-06 requesting permission to reproduce the following article, on which you are a co-author as a member of the Desert Fireball Network, in its entirety as part of your Ph.D. thesis, *Impactors and the Impacted: Analytical Techniques to Identify and Understand the Impact Evolution of Extraterrestrial Materials*, submission for Curtin University:

- Philip A. Bland, Gretchen K. Benedix, and the Desert Fireball Network (DFN) Team (2015) CosmoELEMENTS, *Elements*, v. 11, i. 3, p. 160-161.

It is with pleasure that we grant you permission to reproduce this article without cost and all subsequent editions of the work, its ancillaries, and other derivative works, in any form or medium, whether now known or hereafter developed, in all languages, for distribution throughout the world on the conditions that reference is given to the original publication of the Mineralogical Society of America.

Sincerely,

J. Alex Speer

J. Alexander Speer
Executive Director, MSA

STATEMENT OF AUTHORSHIP

As the primary author of the folloiwng manuscript, I hereby confirm the candidate's contributions and confirm my permission to include the manuscript in the candidate's PhD thesis.

PROF. PHIL BLAND

- Lead investigator

Date: ***23.2.17***

MISS LUCY. V. FORMAN

- Manuscript editing
- Community outreach/ engagement

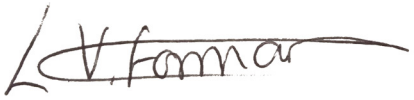

Contribution: ***5%*** ***Date:*** ***22.2.17***

CosmoELEMENTS

CATCHING A FALLING STAR (OR METEORITE) – FIREBALL CAMERA NETWORKS IN THE 21st CENTURY

Philip A. Bland[1], Gretchen K. Benedix[2], and the Desert Fireball Network (DFN) Team[3]

Have you ever seen a shooting star? Have you ever seen a fireball? They are the spectacular fiery result when space dust and rocks enter our atmosphere. Meteors (also known as shooting stars) are specks of dust that leave a trail of light as they burn up in the atmosphere. Fireballs are caused by larger bits of material, making them significantly brighter, and can last several seconds in duration. Fireballs and meteors hit the atmosphere at velocities of tens of kilometres per second. Friction from the air heats the surface of the rock, melting and ablating it, giving the impression of a ball of fire. A meteorite is the surviving material from a fireball. Meteorites give planetary scientists information about the origin and evolution of the Solar System: from how the first solids formed all the way through to the accretion of planets. Meteorites provide a scientifically priceless record, but their impact is reduced because we have no spatial context to interpret their compositional data. Imagine trying to understand the geology of a continent if all you had to work with was a collection of random rocks dumped in your yard. That is where we are with meteorites. We know meteorites come from space, mostly from the asteroid belt. We can pinpoint their precise origin in the Solar System by determining the orbit that they were on before they hit our atmosphere. However, this is only possible if we are able to track the fireball before it lands. Combining the orbit with the recovered meteorite is a major step towards interpreting the record of early Solar System processes that meteorites contain.

Camera Networks

Fireball camera networks are designed to recover meteorites with orbits. The first network, based in the Czech Republic, became active in 1959 and continues to operate as part of the European Fireball Network (Oberst et al. 1998). In the 60s, 70s, and 80s, two other networks were operational in North America, covering parts of the US (Prairie Meteorite Network; McCrosky et al. 1978) and Canada (Meteorite Observation and Recovery Project; Halliday et al. 1996). Despite covering over a million square kilometers of the Earth's surface, only a handful of meteorites have been recovered. This is unfortunate because the promise of these camera networks is very great—knowing the spatial context (an orbit) bridges the gap between meteorite and asteroid research, with the potential to revolutionize both fields. Although the methodology employed in these earlier networks is sound, they are limited by their location: temperate zones where vegetation and weather conditions are not well suited for meteorite preservation or retrieval. It is hard to spot a meteorite in a cornfield, on the tundra, or in a forest. Moreover, meteorites weather away quite rapidly on Earth (Bland et al. 1998); even brief exposure to rain will affect the primordial record they hold (Jenniskens et al. 2012).

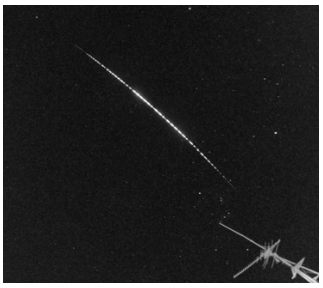

Figure 1 Fireball over Perenjori, 260 km north of Perth (Western Australia). The camera was set up on Perenjori Primary School as part of the Fireballs in the Sky outreach program.

The Desert Fireball Network

Deserts are exceptionally suited to finding meteorites due to the lack of plant cover and because the environmental conditions limit degradation (Bland et al. 2000). Around 80% of all meteorites have been found in deserts. Could a network sited in a desert deliver greater numbers of meteorites with orbits? The benefit is that searching should be easier. The major difficulty is building hardware to survive and operate autonomously for extended periods in a harsh environment. To test the concept, a trial network of four film cameras in the Nullarbor desert of Western Australia was established in 2007 (Bland et al. 2012). Australia was considered ideally suited for the network because of clear skies and arid environmental conditions. Prior to this project, there were no known southern hemisphere meteorites with orbits, or indeed any extended campaigns observing southern hemisphere fireballs (Fig. 1). The initial Desert Fireball Network (DFN) covered only a small area (172,000 km^2), but by 2010, two meteorites had already been recovered (Bunburra Rockhole and Mason Gully) using trajectory information calculated from fireball images. The images also allowed us to determine the precise pre-atmosphere orbits for these rocks (Bland et al. 2009; Towner et al. 2011). Bunburra Rockhole was an especially interesting find—a unique basaltic achondrite with an Aten-type near-Earth object orbit (Bland et al. 2009). This achievement has allowed us to upgrade and expand the DFN.

Currently, DFN has 32 camera stations covering ~1.3 million km^2. The cameras are fully autonomous systems, capable of operating for 12 months without maintenance and storing all images collected over that period. Each station incorporates a 36-megapixel full-format digital and low-light video camera run by an embedded computer. The package is an intelligent imaging system, which calibrates its own optics, modifies observations based on cloud conditions, automatically recognizes fireball events, and pre-processes the data prior to uploading it to the project server. The data pipeline includes image processing to determine fireball position at sub-pixel level, triangulation and fireball trajectory modelling, and dark flight trajectory modified by weather and forecast climate modelling. The final facility will incorporate 70 stations extending over twice the present area to record meteorite falls, track re-entry of space debris, and determine landing sites for each.

Citizen Science

DFN is a natural outlet for community outreach/engagement because of the widespread interest in fireballs and meteorites. Fireballs get more and more media coverage, especially in the age of expanding use of dashboard and security cameras. Fireballs in the Sky (FITS) is a citizen science project linked to the DFN (www.fireballsinthesky.com.au) with the goal of sharing the research and involving the global public. School students and the general public are encouraged to contribute and interact with scientists as the program develops, essentially becoming members of Fireballs in the Sky community. There are a number of ways to engage with the team: e-newsletters, a blog, Facebook (www.facebook.com/fireballsinthesky), and Twitter (@fireballssky). A smartphone app (www.fireballsinthesky.com.au/download-app) has been developed so that the public can record and share their fireball sightings with scientists, participating in real-time research (Fig. 2). The app works around the world, allowing orbital data to be confirmed from anywhere on the planet, even if no meteorite is found. Users receive updates on the specific event that they witnessed. A recent upgrade adds details on meteor showers throughout the year and provides users a display directing them to the specific location in the sky for that shower.

1 Curtin University, Department of Applied Geology, Perth, WA, Australia
E-mail: P.Bland@curtin.edu.au

2 E-mail: G.Benedix@curtin.edu.au

3 DFN Team members: Martin Towner, Jonathan Paxman, Martin Cupak, Robert Howie, Eleanor Sansom, Jay Ridgewell, Kathryn Dyl, Luke Daly, Lucy Forman, Hadrien Devillepoix, and Monty Galloway

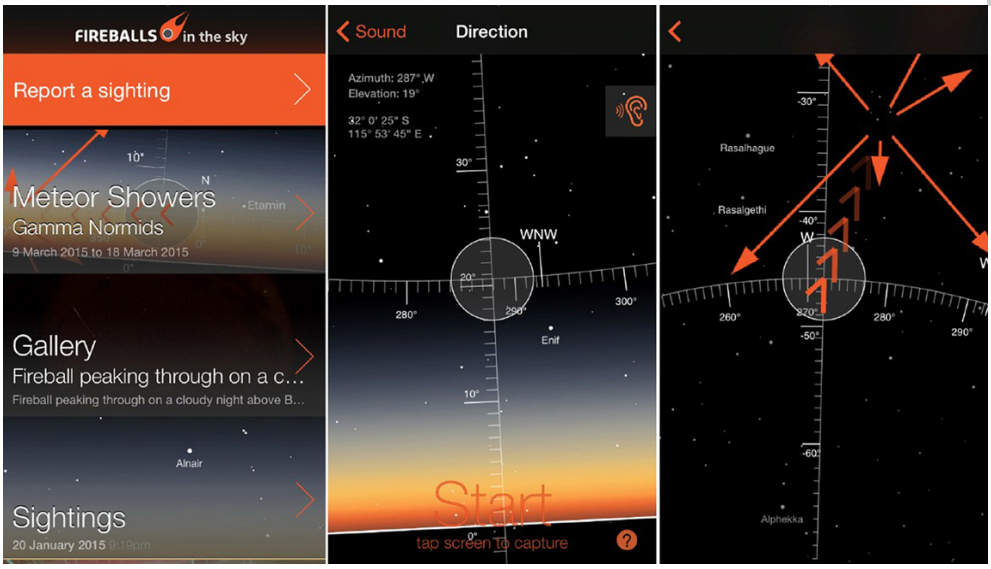

FIGURE 2 Three screenshots illustrating the main features of the Fireballs in the Sky smartphone app. (**LEFT**) The menu screen allows a user to report a sighting, to find current and upcoming meteor showers in their area, and get up-to-date news on what's happening with the DFN research team. (**MIDDLE**) To record a sighting, the user points the phone at the start and end positions in the sky and "draws" the path of the fireball. The user is then prompted to edit the created simulation by adjusting duration, brightness, shape, and colour of the fireball before reaching a summary page. Because it is a simulation, not a video, this is done after the fireball has burned out. With multiple reports, a sighting can be confirmed and will be listed on the app for users to check. (**RIGHT**) Once a user selects a meteor shower, the app will provide data such as expected peak, zenith hourly rate, and Moon phase. The app will then direct the user to the best area to look in the sky, in real time.

Finally, with technologies invented for the next generation digital observatories, we are developing an inexpensive "kit" fireball camera station that would allow interested amateurs to plug in a digital camera and have their own advanced fireball observatory. A versatile interface will allow users to customize camera settings, schedule operations, and download imagers using Wi-Fi. The ability to use it for daytime photography means that the system can be adapted for multiple functions outside of fireball observations.

The goal of DFN is to increase recovery of meteorites with orbits: a growing, lasting resource for the research community. It is our hope that with the smartphone app and new home kit hardware, the public can make a real contribution to the field and participate in this research as it happens.

REFERENCES

Bland PA, Berry FJ, Pillinger CT (1998) Rapid weathering in Holbrook: an ^{57}Fe Mössbauer spectroscopy study. Meteoritics and Planetary Science 33: 127-129

Bland PA, Bevan AWR, Jull AJT (2000) Ancient meteorite finds and the Earth's surface environment. Quaternary Research 53: 131-142

Bland PA and 17 coauthors (2009) An anomalous basaltic meteorite from the innermost main belt. Science 325: 1525-1527

Bland PA and 13 coauthors (2012) The Australian Desert Fireball Network: a new era for planetary science. Australian Journal of Earth Science 59: 177-187

Halliday I, Griffin, AA, Blackwell AT (1996). Detailed data for 259 fireballs from the Canadian camera network and inferences concerning the influx of large meteoroids. Meteoritics and Planetary Science 31: 185-217

Jenniskens P and 70 coauthors (2012) Radar enabled recovery of the Sutter's Mill meteorite, a carbonaceous chondrite regolith breccia. Science 338: 1583-1587

McCrosky RE, Shao C-Y, Posen A (1978) Prairie Network Fireball Data. I. Summary and orbits. Meteoritika 37: 44-59

Oberst J and 8 coauthors (1998) The "European Fireball Network": current status and future prospects. Meteoritics and Planetary Science 33: 49-56

Towner MC and 10 coauthors (2011) Mason Gully: the second meteorite recovered by the Desert Fireball Network. 74th Meteoritical Society Meeting: Abstract #5124

Appendix C7

A New Unequilibrated Chondrite Lithology Discovered in the Murchison CM2 Meteorite

Benedix et al., 2015

46th Lunar and Planetary Science Conference

Benedix, G.K., Russell, S.S., Forman, L.V., Bevan, A.W.R. and Bland, P.A., 2015, A New Unequilibrated Chondrite Lithology Discovered in the Murchison CM2 Meteorite: In Lunar and Planetary Science Conference, v. 46, p. 1143.

STATEMENT OF AUTHORSHIP

As the primary author of the folloiwng manuscript, I hereby confirm the candidate's contributions and confirm my permission to include the manuscript in the candidate's PhD thesis.

DR GRETCHEN BENEDIX

- Lead investigator

Date: ***28.2.17***

MISS LUCY. V. FORMAN

- Manuscript editing

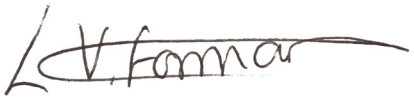

Contribution: ***2%*** ***Date:*** ***22.2.17***

46th Lunar and Planetary Science Conference (2015) **1143.pdf**

A NEW UNEQUILIBRATED CHONDRITE LITHOLOGY DISCOVERED IN THE MURCHISON CM2 METEORITE G.K. Benedix[1,2], S.S. Russell[3], L.V. Forman[1], A.W.R. Bevan[2], and P.A.Bland[1,2], [1]Dept of Applied Geology, Curtin Univeristy, GPO Box U1987A, Perth, Western Australia, 6845 Australia (g.benedix@curtin.edu.au), [2]Western Australian Museum, Locked Bag 49, Welshpool, WA, 6986, Australia, [3]Department of Earth Sciences, Natural History Museum, Cromwell Road, London, SW7 5BD, U.K

Introduction: The Murchison meteorite fell in Victoria, Australia in 1969 and is probably the most studied CM2 meteorite because of the amount of material available (~100kg in a number of stones) as well as the fact that it is a fall [1]. The major texture of the meteorite is dominated by a fine-grained matrix of aqueously altered minerals in which chondrules and CAIs are heterogeneously distributed [1 and references therein]. In addition, it was one of the first meteorites from which organics were reported [2].

The first comprehensive study of Murchison [3], noted the occurrence of four types of inclusion distributed through the dark, fine-grained matrix material; A) fragments or whole single mineral crystals, B) 'white inclusions' (probably CAIs and/or partly characterised phases), C) chondrules, and D) fragments of xenoliths. The fragmental xenoliths were described as being lighter in color and ranging in size up to 13mm. It was suggested that they represent a 'unique kind of C3 chondrite'[3], containing mostly troilite and pentlandite with little to no metal or 'true' chondrules.

The main 'mass', consisting of many stones comprising 65kg of Murchison was acquired through private sale by the Field Museum of Natural History in Chicago. A 691.7g, nearly complete, crusted individual was exchanged with the Western Australian Museum (WAM 13323) by the FMNH (through Ed Olsen) in 1974. One end of the stone was cut and two thin sections were made. Upon recent detailed examination, the texture of one of the thin sections (WAM13323-1) was found to be completely unlike normal Murchison and, further, does not seem to be one of the xenolithic inclusions described by [3].

We present here analytical data on this new textural/chemical lithology in Murchison that is best described as an ungrouped, unequilibrated chondrite.

Analytical techniques: Mineral compositions were determined using a JEOL 8530F microprobe at the University of Western Australia Centre for Microscopy, Characterisation, and Analysis (CMCA). High resolution quantitative maps were acquired on the same system. Operating conditions for mineral analyses were 20kv and 20nA; for imaging, the beam current was 80nA.

Low resolution back-scatter and element maps of the entire thin section (measuring 15.7 x 40 mm) were obtained on the Tescan Mira3 FESEM in the John de Laeter Centre (JdLC) of Isotope Studies at Curtin University. Operating conditions were 20kv and a beam intensity of 10.

Results and Discussion: The thin section has an unequilibrated chondritic texture and is dominated by whole and broken chondrules ranging in size from <150 to >1500 μm in diameter (Fig. 1) dispersed amongst broken bits of anhydrous mineral crystals. Olivine shows slight undulatory extinction in a number of different chondrules, indicating low shock levels across the section. Metal (both Ni-rich and poor) and sulfide are heterogeneously distributed across the thin section. Several chondrules have sulfide rims. Modally, sulfide and metal are ~8 and ~3 vol%, respectively. The metal content falls within the LL-type ordinary chondrites (OC) range, but the sulfide/metal ratio is higher than H and L, and lower than LL. There is no evidence for pentlandite in the section.

A random sampling of 12 olivine grains from seven chondrules gives an average Fa value of 23.0 ± 1.7, with a variance of 2.9. If the minimum (17.7) and maximum (24.1) Fa values are removed, the average value of the remaining grains is 23.4 ± 0.02 with a variance of 0.05. This value falls in the range for L chondrites. However, the pyroxene and plagioclase compositions are not so diagnostic.

Analysis of 13 pyroxenes from 7 chondrules reveals 8 high-Ca pyroxene with a mean value of $Fs_{7\pm4}Wo_{44\pm4}$; the 5 low-Ca pyroxenes have a mean value of $Fs_{13\pm2}Wo_{8\pm6}$ (Fig. 2). The variance for these analyses is significantly larger than for olivine and is more consistent with the unequilibrated texture.

In most unequilibrated (type 3) ordinary chondrites, plagioclase is a rare phase; where found it is typically anorthositic [e.g. 4]. In thin section WAM 13323-1, plagioclase is abundant; compositions of 27 grains in 8 chondrules span the range from nearly pure anorthite to virtually pure albite (Fig. 3). In our preliminary examination, Na-rich plagioclase compositions occur in 5 different chondrules or chondrule fragments. These overlap with all mean OC plagioclase compositions.

Finally, a few grains of Cr-poor spinel were found with compositions roughly between spinel ($MgAl_2O_4$) and hercynite ($FeAl_2O_4$). Fe-rich spinel can be an indicator of parent body metamorphism [5], but seems unlikely in this sample given the highly unequilibrated silicates.. Spinel is more common in carbonaceous chondrites (CC) than OC, where it is more likely to be in the form of chromite.

Conclusions: This sample appears to be a rather large unequilibrated chondritic xenolith found in the Murchison meteorite. Based on the above information, it does not fit Fuchs' [3] description of a unique C3 type (no metal, rare chondrules, lots of sulfide/pentlandite) found in Murchison previously and, thus, is a new xenolith type that has not been sampled before. It has affinities to both OC and CC, as well as features that are not indicative of any known chondritic groups. The paucity of matrix may rule out any similarity to C types. The olivine and pyroxene compositions are contradictory. The plagioclase compositions span the whole range of ordinary and carbonaceous chondrites. Based on this current work, we consider this to be an ungrouped Type 3 chondritic rock.

Future work: Of note in the large area element maps were several small (~300 µm diameter) Na-rich, Ca-poor chondrules. These are the source of the albitic compositions reported above. We will study these in detail to determine how they formed and what they might mean for chondrule formation theories. We will use electron backscatter diffraction (EBSD) to ascertain the mineralogy of these Na-rich chondrules as well as quantify the level of shock in the meteorite.

We will also explore the relationship of this lithology to the rest of Murchison by analyzing the oxygen isotopic compositions of the minerals.

Acknowledgments: We thank Dr. Malcolm Roberts for help with the quantitative mapping at the CMCA.

References: [1] Hutchison R. (2004) Meteorites: A Petrologic, Chemical, and Isotopic Synthesis. Cambridge University Press, 506pp. [2] Kvenvolden, K. et al. (1970) Nature, 228, 923-926. [3] Fuchs et al. (1973) Smithsonian Contrib. to Earth Sci., 10. [4] Huss et al. (2001) 36 975-997 [5] Russell et al. (1998) Geochimica et Cosmochimica Acta 62 689-714.

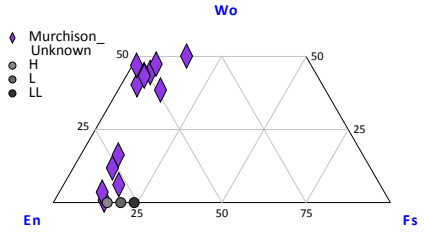

Figure 2. Pyroxene quadrilateral diagram showing compositional range in Murchison unknown. Average compositions of equilibrated ordinary chondrite low-Ca pyroxenes are also shown. Data for OC from [1].

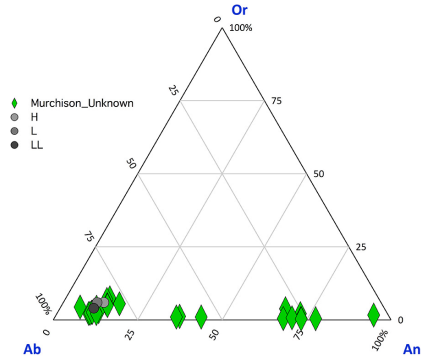

Figure 3. Plagioclase ternary diagram illustrating the range of plagioclase compositions. Average compositions of plagioclase in equilibrated ordinary chondrites are also shown. Data for OCs from [1]

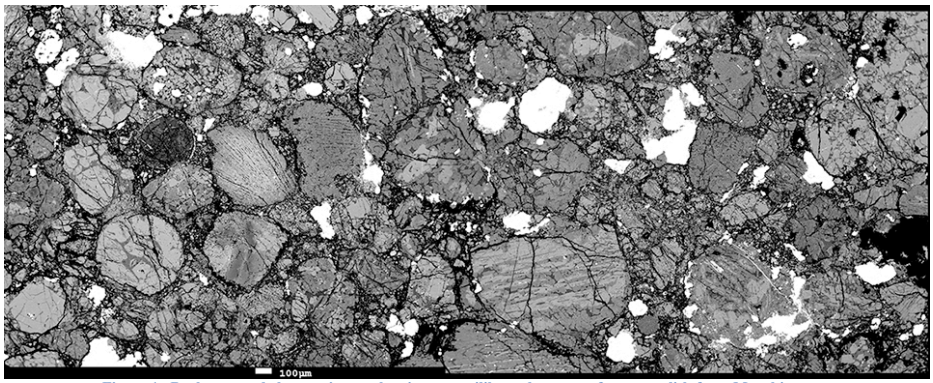

Figure 1. Backscattered electron image showing unequilibrated texture of new xenolith from Murchison meteorite.

Appendix C8

Crystallography of Refractory Metal Nuggets Identified Within Ca-Al-Rich Inclusions, Chondrules and Matrix of Carbonaceous Chondrites.

Daly et al., 2014

77th Annual Meeting of the Meteoritical Society

Daly, L., Bland, P.A., Dyl, K.A., Forman, L.V., Trimby, P.W., Moody, S. and Ringer, S.P., 2014, September. Crystallography of Refractory Metal Nuggets Identified Within Ca-Al-Rich Inclusions, Chondrules and Matrix of Carbonaceous Chondrites: In 77th Annual Meeting of the Meteoritical Society, v. 77, p 5207.

STATEMENT OF AUTHORSHIP

As the primary author of the folloiwng manuscript, I hereby confirm the candidate's contributions and confirm my permission to include the manuscript in the candidate's PhD thesis.

MR LUKE DALY

- Lead investigator

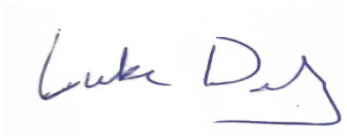

Date: ***22.2.17***

MISS LUCY. V. FORMAN

- Manuscript editing

Contribution: ***1%*** ***Date:*** ***22.2.17***

77th Annual Meteoritical Society Meeting (2014) **5207.pdf**

CRYSTALLOGRAPHY OF REFRACTORY METAL NUGGETS IDENTIFIED WITHIN CA-AL-RICH INCLUSIONS, CHONDRULES AND MATRIX OF CARBONACEOUS CHONDRITES.

L. Daly[1], P. A. Bland[1], K. A. Dyl[1], L. V. Forman[1], P. W. Trimby[2], S. Moody[2] and S. P. Ringer[2] [1]Department of Applied Geology, Curtin University, GPO Box U1987, Perth, WA 6845. E-mail: luke.daly@postgrad.curtin.edu.au. [2]Australian Centre for Microscopy and Microanalysis and ARC Centre of Excellence for Design in Light Metals, The University of Sydney, NSW 2006, Australia.

Introduction: Refractory metal nuggets (RMNs) as described by [1,2] are predicted to be some of the first Nebular condensates [3]. Previous work assumes these grains occur exclusively within Ca-Al-rich Inclusions (CAIs) [4]. Initial results utilising the Australian Synchrotron (AS) suggest this is not the case [5]. Here we present the combination of X-Ray Fluorescence (XRF) and scanning electron microscopy (SEM) techniques that positively identify RMNs within chondrules and matrix, as well as CAIs. We show for the first time the application of transmission Kikuchi diffraction (TKD) to a meteorite, defining nanometer-scale crystallographic and compositional variations of RMNs.

Method: Carbonaceous chondrites Vigarano and Allende were analysed with the AS XRF beamline and Maia detector. GeoPIXE software generated element maps, [6] identifying pixel-sized (2μm) hotspots of platinum group elements (PGEs). Analyses using electron back scatter diffraction (EBSD), and energy dispersive spectroscopy confirmed the presence of PGE alloys at the surface of the sample in the location of the hotspots. TKD analyses on focused ion beam generated sections of PGE alloys, using a 25nm step size, provided high spatial resolution data on the crystallography, orientation, and chemistry of RMNs *in situ*.

Results and Discussion: This approach has identified several RMNs in CAI material, and 6 RMNs within non-CAI material: 4 from Vigarano (3 within chondrules, and 1 within matrix), and 2 from chondrules in Allende. EBSD analysis of RMNs within Allende's chondrules indicate that the RMNs are single crystal cubic alloys with random crystal orientations. TKD analyses of 7 RMNs, between 80-500nm, in CAIs from Vigarano are also cubic alloys with random orientations, but in several cases exhibit polysynthetic twins with 20-130nm spacing. TKD Analysis of 3 PGE alloys, between 0.7-1.1μm, found within sulphide nodules enclosed within a chondrule of Allende reveal they are also single crystal cubic alloys; however the orientations of these grains are nearly identical. This heavily implies that these grains formed through parent body processes rather than condensation in the Nebula. However their similarity in appearance to RMNs highlights the importance of analysing these grains *in situ*.

Identifying RMNs enclosed within matrix and chondrules as well as CAIs has significant implications for how we interpret their formation. It is our aim with further research and analyses of RMNs *in situ* to develop a unifying theory of RMN formation.

References: [1] Blander M. et al. (1980) *Geochimica Et Cosmochimica Acta*, *44*, 2, 217-223. [2] Eisenhour D.D. and Buseck P.R. (1992) *Meteoritics*, *27*, 3, 217-218. [3] Lodders K. (2003) *The Astrophysical Journal*, *591*, 2, 1220-1247 [4] Berg T. et al. (2009) *The Astrophysical Journal*, 702, 172-176. [5] Daly L. et al. Abstract #2017 45th Lunar and Planetary Science Conference. [6] Ryan C.G. et al., (2010) *AIP Conference Proceedings*, *1221*, 1, 9-17.

Appendix C9

In Situ Analysis of Refractory Metal Alloys in Carbonaceous Chondrites: Implications for Early Solar System Processes

Daly et al., 2014

45th Lunar & Planetary Science Conference

Daly, L., Bland, P.A., Dyl, K.A., Forman, L.V. and Ryan, C.G., 2014, March. In Situ Analysis of Refractory Metal Alloys in Carbonaceous Chondrites: Implications for Early Solar System Processes: In Lunar and Planetary Science Conference, v. 45, p. 2071.

STATEMENT OF AUTHORSHIP

As the primary author of the folloiwng manuscript, I hereby confirm the candidate's contributions and confirm my permission to include the manuscript in the candidate's PhD thesis.

MR LUKE DALY

- Lead investigator

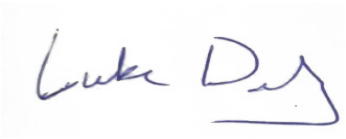

Date: ***22.2.17***

MISS LUCY. V. FORMAN

- Manuscript editing
- Data collection

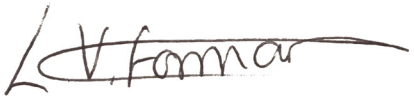

Contribution: ***2%*** ***Date:*** ***22.2.17***

45th Lunar and Planetary Science Conference (2014) 2071.pdf

IN SITU ANALYSIS OF REFRACTORY METAL ALLOYS IN CARBONACEOUS CHONDRITES: IMPLICATIONS FOR EARLY SOLAR SYSTEM PROCESSES. L. Daly[1], P. A. Bland[1], K. A. Dyl[1,2], L. V. Forman[1], and C. G. Ryan[2] [1]Department of Applied Geology, Curtin University, GPO Box U1987, Perth, WA 6845, luke.daly@postgrad.curtin.edu.au, [2]CSIRO Earth Sciences and Resource Engineering, 26 Dick Perry Avenue, Kensington, Perth, WA 6151, Australia.

Introduction: Refractory metal alloys are predicted to be the first solids to condense from the cooling Solar Nebula [1, 2]. Assemblages of refractory metals within carbonacous chondrites were first described by [3, 4]. These are composed of the transition elements W, Re, Os, Ir, Mo, Pt, Rh, Ru, Zr and Hf [3]. These opaque assemblages (OAs) or fremdlinge have been affected by oxidation, sulfidisation and re-mobilization into non metallic phases [5, 6]. Sub-µm refractory metal alloys known as refractory metal nuggets (RMNs) with compositions and crystal structures consistant with a condensation origin have also been described [2, 7]. These are similar in morphology and composition to the solids predicted by [1, 2] that condense primarily from a cooling gas of solar composition. RMNs therefore can potentially provide insights into processes acting at the advent of Solar System formation. The assumption has been RMNs occur exclusively within Ca-Al rich inclusions (CAIs) [8]: those insights have tended to be associated with CAI formation. Here we present results from *in situ* analyses of carbonacous chondrites that contradict this assumption. RMNs are found within all chondritic components.

Method: A suite of carbonaceous chondrites (Vigarano, Allende, Adelaide, Kaidun, ALH77307 Renazzo and Acfer 094) were analysed on the X-Ray Flourescence Microscopy (XFM) beamline at the Australian Synchrotron, using the Maia detector, which allows for rapid data collection and analysis at high resolution across a broad energy range (4-18 keV) [9], utilizing its custom-made 384 Si-diode detectors. This analytical protocol generated element maps covering whole thin sections (or large selected areas) at 2µm resolution and a sensitivity of 50-100ppm for elements such as Os, Ir, and Pt [10], allowing detection of a suite of trace and minor elements. The element maps were created with the GeoPIXE software, which utilizes a dynamic analysis matrix method to deconvolve the elements spectral peaks [11]. The high energy of the XFM beamline is such that diagnostic elemental X-rays are collected from ≥100µm into the sample.

The samples were subsequently analysed on the Zeiss 1555 VP-FESEM at the Centre for Microscopy, Characterisation and Analysis (CMCA) at the Univeristy of Western Australia. Energy-dispersive X-ray spectroscopy (EDS) at 25KeV confirmed the presence of some RMNs that were on the surface of the sample, validating the detection of these elements via two methods.

Results: The Synchrotron data was analysed targeting refractory element hotspots such as Os, Ir, and Pt. This method yielded an average of 20 potential RMNs per sample with a maximum of 70 in Vigarano and a minimum of two in Adelaide (Table 1). Due to the proximity of the Kα and Lα peaks for Os, Ir and Pt with both one another and more abundant elements (i.e., Zn), as well as the thickness of the sample, it is difficult to differentiate individual peaks from the peak of the most abundant element which overprints and defines the shape of the spectra in that energy range. A detailed analysis of potential peak overlaps was undertaken for every grain in order to avoid misidentification of PGEs, and any false positives removed. For confirmed RMNs, Synchrotron and EDS analyses show that these RMNs occur as alloys of several PGEs. The size of RMNs observed in the Synchrotron data for >95% of cases are pixel size, consistent with grains ≤2µm.

The depth variations between the two techniques (100µm for Synchrotron and 1µm for EDS) generates an issue when locating RMNs in EDS maps. Given their size ((90nm-1.2µm [8], sub- µm to µm-scale (this work)), the likelihood (99%) is that the grain will be buried beneath the sample surface. However, a follow-up study of each identified hotspot with detailed Backscattered electron (BSE) and EDS mapping revealed a number of cases where grains could be identified and analysed at the surface.

Table 1: Table showing the distribution of RMNs within carbonaceous chondrites as revealed by the XFM beamline at the Australian Synchrotron.

Meteorite	*Total RMNs*	*Host Material*		
		CAI	Chondrule	Matrix
Acfer 094	2	0	1	1
Adelaide	2	1	0	1
ALH77307	17	12	0	5
Kaidun	9	0	1	8
Renazzo	6	0	2	4
Vigarano	71	69	2	0

Discussion: The techniques applied here allow for rapid identification of RMNs *in situ* within carbonaceous chondrites at high spatial resolution. It is evident that the majority of RMNs are hosted in CAIs. But the combined data from the Synchrotron, SEM and EDS

analyses clearly show that RMNs can also be found within other components of carbonaceous chondrites such as chondrules, and matrix (Figure 1).

This observation may have some far reaching implications. The assumption that RMNs are unique to CAIs has limited interpretations about their origin to high temperature regions close to the proto-Sun. The fact that we observe RMNs in other components in carbonaceous chondrites raises questions about how they formed.

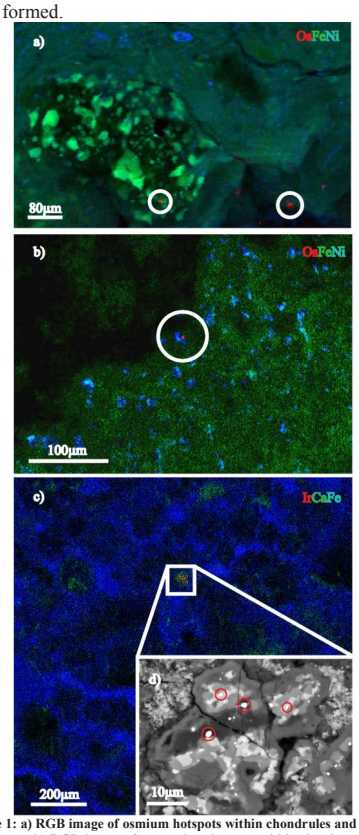

Figure 1: a) RGB image of osmium hotspots within chondrules and matrix in Renazzo b) RGB image of an osmium hotspot within the rim material of a CAI in Allende c) RGB image of PGE metals contained within a CAI in ALH77307 d) EBSD image of RMNs contained within an inclusion in ALH77307. The presence of PGEs were confirmed using EDS.

RMNs condense at high temperature [1]. Their prescence within relatively unaltered ('cold') matrix material has significant implications for conditions in the early Solar Nebula. There appear to be several possibilities regarding their formation: 1) disk temperatures exceeded ~1800K out to asteroidal distances; 2) localized high-temperature (>~1800K) events occurred at asteroidal distances (in excess of temperatures generally associated with chondrule formation); 3) materials condensing over the complete temperature range were extremely well mixed in the disk. We can test these possibilities using a range of additional techniques.

Following a similar approach to [8], we can use the specific mix of elemental abundances within each grain to define where that grain falls on an ideal condensation curve. With data gained from *in situ* analysis providing a spatial context, we can obtain cooling rates for grains in different chondritic components – allowing us to choose between formation mechanisms for non-CAI RMNs. By analyzing different components, in different meteorites, this approach offers the interesting possibility of tracking cooling rates at various points in space and time within the early Solar Nebula, generating a detailed thermal history to compare to disk models.

Conclusion: The combination of Synchrotron data with SEM and EDS analysis allows us to rapidly identify PGE hotspots within carbonaceous chondrites, generating a large dataset which retains its spatial context. This opens the way to a wider spectrum of possibilities when interpreting the origin of RMNs. RMNs are not unique to CAIs but can be observed in other components in carbonaceous chondrites that have not seen such extremes of temperature such as matrix and chondrules. This could provide insights into the thermal structure of the early Solar Nebula. Further analysis of these grains *in situ* utilizing LA-ICP-MS, FIB, transmission electron microscopy (TEM) and atom probe analysis will help establish their value as tracers of the thermal history of the inner Solar Nebula.

Acknowledgements: The authors acknowledge the facilities, and the scientific and technical assistance of the Australian Microscopy & Microanalysis Research Facility at the Centre for Microscopy, Characterisation & Analysis, The University of Western Australia, a facility funded by the University, State and Commonwealth Governments. This work was funded by the Australian Research Council via their Australian Laureate Fellowship program. This research was undertaken on the XFM beamline at the Australian Synchrotron, Victoria, Australia. We also acknowledge assistance provided by Mr Timmons Erikson.

References: [1] Lodders K. (2003) *Astrophys. Jour.*, *591*, 2, 1220-1247. [2] Blander M. et al. (1980) *Geochim. Et Cosmochim. Ac.*, *44*, 2, 217-223. [3] Palme H. and Wlotzka F. (1976) *Earth and Planet. Sci. Let.*, *33*, 1, 45-60. [4] Wark D.A. and Lovering J.F. (1976) *LPSC*, *7*, 912. [5] El Goresy A., et al. (1978) *LPSC IX*, *1*, 1279-1303. [6] Bischoff A. and Palme H. (1987) *Geochim. Et Cosmochim. Ac.*, *51*, 10, 2733-2748. [7] Eisenhour D.D. and Buseck P.R. (1992) *Met.*, *27*, 3, 217-218. [8] Berg T. et al. (2009) *The Astrophys. Jour.*, 702, 172-176. [9] Ryan C.G. et al., (2010) *AIP Conf. Proc.*, *1221*, 1, 9-17. [10] Cleverly J. et al. (2012) *Met. and Planet. Sci. Sup.*, *75*, 5175. [11] Ryan C.G. et al. (1995) *Nuc. Inst. & Meth. in Phys. Res. Sect. B: Beam Interact. with Mater. & Atom.*, *104*, 1–4, 157-165.

Mischief Managed.

- J. K. Rowling